NOVA SCHOOL OF
SCIENCE & TECHNOLOGY

DEPARTMENT OF ELECTRICAL
AND COMPUTER ENGINEERING

JOÃO JOSÉ MATIAS SANTOS

BSc in Sciences of Electrical and Computer Engineering

DESIGN, IMPLEMENTATION AND TEST OF AN IONOGEL SENSOR-BASED ELECTRONIC NOSE

MASTER IN ELECTRICAL AND COMPUTER ENGINEERING

NOVA University Lisbon
September, 2022

DEPARTMENT OF ELECTRICAL
AND COMPUTER ENGINEERING

DESIGN, IMPLEMENTATION AND TEST OF AN IONOGEL SENSOR-BASED ELECTRONIC NOSE

JOÃO JOSÉ MATIAS SANTOS
BSc in Sciences of Electrical and Computer Engineering

Adviser: João Pedro Abreu de Oliveira
Assistant Professor, NOVA University Lisbon

Co-advisers: Ana Cecília Afonso Roque
Associate Professor, NOVA University Lisbon
Hugo Filipe Silveira Gamboa
Associate Professor, NOVA University Lisbon

Examination Committee

Chair: Paulo da Costa Luís da Fonseca Pinto
Full Professor, NOVA University Lisbon

Rapporteurs: Jorge Manuel Correia Guilherme
Assistant Professor, ESTT-IPT
João Pedro Abreu de Oliveira
Assistant Professor, NOVA University Lisbon

MASTER IN ELECTRICAL AND COMPUTER ENGINEERING

NOVA University Lisbon
September, 2022

Design, Implementation and Test of an Ionogel Sensor-based Electronic Nose

---

This document was created with the (pdf/Xe/Lua)LaTeX processor and the NOVAthesis template (v6.9.15) [1].

For those who shaped me into what I am today.

ACKNOWLEDGEMENTS

During the past 5 years, I have learned that I am nothing less but a weighted sum, whose terms represent the most grateful and profound memories of different people. To these people, including teachers, colleagues, friends, and family, I profoundly thank the experiences, the knowledge and wisdom, the commitment and support, the help and concern, and above all, for having transformed my life and my person.

To FCT-NOVA as a whole, and to the Department of Electrical and Computer Engineering, I thank for the positive, welcoming, and inspiring ambient and spirit, and for the professional, demanding, and enriching knowledge provided.

To my thesis supervisor, professor João P. Oliveira, I thank for the immense degree of commitment and professionalism, both during the thesis supervision and the past 5 years as a (great) teacher. I, thereby, express my deepest respect for you, as a teacher, but also as a wise, calm, and respectful person, who, apart from the technical knowledge, has taught me how to talk, think, decide, and act as an engineer, which has set great foundations for the rest of my professional life.

To professor A. Cecilia Roque, I thank for the opportunity of being a part of the Biomolecular Engineering Laboratory, during almost 3 years, which impacted my personal and professional life in ways that I cannot quantify. Alongside your guidance, I learned to be responsible, professional, dedicated, self-demanding, creative, efficient, and ambitious, but also to be more calm, self-confident, and wiser. I also thank for always being a happy and joy-full person, who always seeks to provide those around you a sense of calm and positive thinking. Lastly, I express my gratitude for the friendship, which I will always remember with joy.

To professor Hugo Gamboa, I thank for raising the questions that lead to the motivation behind this thesis, and to the basis of the work I was fortunate to be part of, during the past 3 years. I also thank for the support and trust deposited on me, and for the wise and kind words throughout your guidance, which I immensely appreciate.

To Susana Palma, I cannot thank enough for the commitment, professionalism, and support during the past 3 years. Thanks to your calm, respectful, and friendly attitude, I was able to quickly feel integrated in the laboratory group. Without your constructive thinking, this thesis would exist, since you were fundamental in raising the necessary questions that lead to the creation of this work, which hopefully will benefit a lot of people.

To Carina Esteves, I owe the capacity of looking forward with a smile on the face, even on "cloudy" days, since that is something very characteristic of you. I will remember you as the happy, fun and joy-full person that was fundamental in motivating me to strive and achieve more and better, which is something that I will carry with me forever.

I thank the remaining colleagues of the Biomolecular Engineering Laboratory, especially to Gonçalo Santos, who opened my door to the group, by believing in my capabilities before I did. This thesis would not be possible without you.

To Fábio Pires and Pedro Barreira, I thank for the friendship, funny moments and memories, and countless arduous study hours together. To Pedro Albuquerque I thank for being such a humble and kind friend, who happily provided me study material and helpful counsels, and for the amazing performance as a monitor teacher in two distinct disciplines. For the remaining friends, I owe you no less, and thank for always being true and supportive.

To my girlfriend Cátia Simões, I thank for more that I could ever express in this section. Thanks to you, I am capable of surpassing my fears and insecurities, I am capable of looking forward with hope and confidence, I have become a lot of what I am today. To you, I owe more than words.

To my family, I thank for the unconditional support, love, appreciation, education, and wisdom. To my family, I am profoundly thankful. To "avô Parafuso", "avó Mila", "avô Matias", "avó Nazaré", "Camilo", and "tia Elvira" I express my love and gratitude.

Finally, and most importantly, I thank my parents, to whom I owe the majority of the "weighted sum" and cannot properly thank by any written or spoken means, other than trying to be the best of you, and carrying your love in my heart. To my dad, João, as you (and almost everyone) say, I owe you my way of being, my self-demanding, and my persistence. To my mother, Telma, I profoundly thank you for providing me the support, (extra) care, and for being what a son should have as a mother. To both, I hope I have made you proud doing things you would have liked to do, if life had given you the opportunity. To my parents, I thank for everything.

"Science can amuse and fascinate us all, but it is engineering that changes the world." (Isaac Asimov)

ABSTRACT

An electronic nose (E-nose) is a device that mimics the mammals olfactory system. An E-nose is typically constituted by a sample delivery system, an array of chemical sensors, an acquisition system, and machine learning algorithms trained to recognize signal patterns. Typical E-nose applications range from disease detection, food quality assessment, air pollution and water contamination measurements, as well as in numerous industries, such as cosmetics, coffee, tobacco, and wine.

In the medical field, such devices are becoming more popular, due to their potential for non-invasive diagnosis of various diseases, whilst being cheaper than most invasive medical procedures, and providing better comfort for the patient.

This thesis was developed within the context of an innovative class of E-nose sensors, known as hybrid gel and ionogel sensors, developed by the Biomolecular Engineering Laboratory, at FCT-NOVA. In addition, the group also developed a custom-made E-nose device. Due to their innovative nature, a characterization of such sensors, under different operating conditions, is mandatory to further improve the sensing accuracy. Thus, a multi-sensor frequency response analysis of an array of different sensor formulations is presented and discussed. Such analysis enables numerous optimizations, such as increased sensor sensitivity to analytes and reduced impact of environmental conditions, such as relative humidity.

Regarding the E-nose device optimization, a flexible, high-accuracy and high-precision analog front-end (AFE) circuit is designed, implemented, and tested. Such AFE circuit is based on a programmable system-on-a-chip (PSoC) device. The optimization is done in two parts: i) a fully PSoC-based AFE circuit is implemented, which operates at a fixed frequency; and ii) an add-on analog circuit to the latter implementation, enabling greater data acquisition accuracy, precision, and bandwidth. Lastly, a brand-new system architecture is designed and implemented, resulting in a fully-operational E-nose device. Real experimental data acquired with the device is presented, which validates its operation.

Keywords: Electronic Nose, Ionogel Sensor, Analog Front-End, System-on-a-Chip

RESUMO

Um nariz eletrónico (*E-nose*) é um dispositivo que replica o sistema olfativo dos mamíferos. Um *E-nose* é tipicamente constituído por um sistema de encaminhamento da amostra, um conjunto de sensores químicos, um sistema de aquisição, e algoritmos treinados para reconhecimento de padrões. Tipicamente, as aplicações de *E-noses* vão desde deteção de doenças, avaliação da qualidade de alimentos, medição de poluentes atmosféricos e contaminantes em água, até ao uso em diversas indústrias, tais como a cosmética, do café, do tabaco e do vinho.

Na área da medicina, estes dispositivos têm ganho popularidade, devido a possibilitarem métodos não-invasivos de deteção de várias doenças, sendo mais baratos do que a maioria dos procedimentos médicos, e providenciando um maior conforto ao paciente.

Esta tese foi desenvolvida com base num grupo inovador de sensores para *E-noses*, denominados por sensores de geis hibridos, ou sensores de ionogel, desenvolvidos pelo Laboratório de Engenharia Biomolecular, na FCT-NOVA. O mesmo grupo desenvolveu também o seu próprio *E-nose*. Devido à sua natureza inovadora, é indispensável uma caracterização da resposta elétrica dos sensores, em diferentes condições de operação. Desta forma, testes da resposta em frequência de um grupo de sensores foram elaborados e os resultados discutidos. Estes testes permitem otimizações como maior sensibilidade do sensor a analitos, e redução do impacto da humidade relativa nos sinais recolhidos.

Relativamente à otimização do *E-nose*, um circuito de interface analógico (AFE) flexível, de alta precisão e alta exatidão foi projetado, implementado e testado. Este circuito de interface é baseado num *programmable system-on-a-chip* (PSoC), e a sua otimização é feita em duas partes: i) um circuito AFE totalmente integrado num PSoC, que opera numa frequência de excitação fixa; e ii) um circuito adicional à implementação anterior, com ganhos a nível de exatidão, precisão e largura de banda. Por último, é projetada e implementada uma nova arquitetura de sistema. Dados recolhidos em experiências laboratoriais são apresentados, validando o funcionamento do *E-nose*.

Palavras-chave: Nariz eletrónico, Sensor Ionogel, Analog Front-End, System-on-a-Chip

CONTENTS

Appendices

List of Figures

List of Tables

ACRONYMS

ADC	Analog-to-Digital Converter
AFE	Analog Front-End
ARM	Advanced RISC Machine
CAD	Computer-Aided Design
CAN	Controller Area Network
CMOS	Complementary Metal–Oxide–Semiconductor
CMRR	Common-Mode Rejection Ratio
CPU	Central Processing-Unit
DAC	Digital-to-Analog Converter
DAQ	Data Acquisition System
DDS	Direct Digital Synthesizer
DMA	Direct Memory Access
DNL	Differential Non-Linearity
DSP	Digital Signal Processor
E-nose	Electronic Nose
EMC	Electromagnetic Compatibility
EMF	Electromotive Force
EMI	Electromagnetic Interference
ENOB	Effective Number of Bits
FFT	Fast-Fourier Transform
FIR	Finite Impulse Response
FPGA	Field-Programmable Gate Array
GBW	Gain-Bandwidth Product
GPIO	General Purpose Input/Output

GUI	Graphical User Interface
I2C	Inter-Integrated Circuit
IC	Integrated Circuit
IDE	Interdigitated Electrode
IIR	Infinite Impulse Response
IL	Ionic Liquid
INL	Integral Non-Linearity
LC	Liquid Crystal
LED	Light-Emitting Diode
LSB	Least Significant Bit
MFC	Mass-Flow Controller
MOS	Metal-Oxide Semiconductor
MOSFET	Metal-Oxide-Semiconductor Field-Effect Transistor
Op-amp	Operational Amplifier
OSNs	Olfactory Sensory Neurons
PCB	Printed Circuit Board
PM	Phase Margin
PSD	Power Spectral Density
PSoC	Programmable System-on-a-Chip
PSRR	Power-Supply Rejection Ratio
PWM	Pulse-Width Modulation
QCM	Quartz Crystal Microbalance
RH	Relative Humidity
RISC	Reduced Instruction Set Computer
RMS	Root Mean Square
SAR	Successive-Approximation Register
SINAD	Signal-to-Noise and Distortion Ratio
SMD	Surface Mount Device
SNR	Signal-to-Noise Ratio
SoC	System-on-a-Chip
SPI	Serial Peripheral Interface
SRAM	Single Random-Access Memory

THD	Total Harmonic Distortion
TIA	Trans-Impedance Amplifier
UART	Universal Asynchronous Receiver/Transmitter
USB	Universal Serial Bus
VOC	Volatile Organic Compound

1

INTRODUCTION

1.1 Motivation

For centuries, diseases and odors have been intimately linked. Hippocrates (born c. 460 BCE, island of Cos, Greece—died c. 375 BCE, Larissa, Thessaly), a renowned physician, proposed the miasma theory in the 5th century BC [2], where the bad quality of the air, due to decaying organic matter, was believed to be the main cause of plagues and deadly epidemics. Although more accurate theories emerged, the use of scent would still be prominent in disease diagnosing, for the next centuries.

In the second half of the 20th century, animal scent detection gained substantial significance in identifying human illness [3]. Studies have found that the canines odor detection capability is at least 10 000 times superior to that of the average human [4]. Their ultra-sensitive sense of smell is a powerful tool used by many research teams aimed to identify various diseases in humans. Some examples include the detection of hypoglycemia in patients with type-1 diabetes [5], bladder cancer [6], lung cancer and urinary tract infections [7]. Advances in electronics allowed the envision of a device that could mimic this biological sensing behavior, thus the term *electronic nose* was born.

The sense of smell is based on the detection of Volatile Organic Compounds (VOCs). Humans emit different kinds of body odors, which result from the combination of multiple VOCs derived from the normal (or abnormal) body metabolism. Such combinations can be used as “odor-signatures” [8]. Biological samples, such as breath, urine, or feces, constitute non-invasive samples for capturing the patient VOC profile, when compared to tissue biopsies. These samples can be used as an odor source by an Electronic Nose (E-nose) for disease diagnosis.

An E-nose is a sensing system composed of an array of semi-selective gas sensors that produce response patterns when exposed to different VOCs and VOC mixtures. The main goal is to mimic the behavior of biological olfactory receptors. Using different forms of pattern recognition based on artificial intelligence such as deep learning, decision trees or neural networks, it is possible to obtain quantitative or qualitative results which are used to detect diseases [9, 10]. The user-friendly, cost-effective, and time-effective approach of

E-noses makes them great candidates for applications where fast and accurate diagnostics are mandatory, such as cancer [11, 12].

1.2 Context and Aim

In the Biomolecular Engineering Laboratory, at the Chemistry Department of FCT-NOVA, a team of researchers (of which I am part) developed an E-nose that works with innovative ionogel, and hybrid gel sensors also developed by the team [13–18].

These ionogel materials are made of a mixture of gelatin and Ionic Liquid (IL) and have interesting electrical properties. When a liquid crystal component is added to the mixture, hybrid gels are obtained, with additional optical properties. The electrical properties of the ionogel sensors originate from the ionic conductivity of the material, which is a constructive parameter of each sensor, dictated by its formulation, namely the IL nature. Different formulations allow the sensors to present different levels of selectivity to different VOCs, which makes them semi-selective.

Even though the Relative Humidity (RH) in human breath can be used to detect diseases [19], variations in RH can change the sensing properties of a gas sensor, contributing as an unwanted signal [20, 21]. In typical E-nose operation, the ideal signal should only be dependent on the sensor response to analytes. However, in reality, both the parasitic signal due to RH variation, and the signal due to the sensor response to analyte, contribute to the obtained signal. This problem can lead to significant errors. Thus, it is imperative to characterize the sensor properties in different RH conditions.

In addition, the resulting detection accuracy of the E-nose device is highly dependent on the accuracy of its acquisition system. The latest E-nose version developed by the Biomolecular Engineering Laboratory requires improvements on the acquisition system, more specifically, its Analog Front-End (AFE) circuit. Moreover, improvements at the system level are mandatory to efficiently increase the performance of the device.

As such, a detailed frequency response characterization of an array of sensors, under different RH conditions, is performed. This characterization is useful is many ways, one of which is related to the optimization of the AFE circuit, and other being the possibility of compensating for the parasitic RH signal, as well as optimizing the operation point of the sensors. All of these outcomes are beneficial to the E-nose device, and sensor technology. Moreover, the improved AFE circuit enables greater accuracy, precision, repeatability, and flexibility, while the optimized system design improves user-experience, device stability and overall quality of the results.

1.3 Document Organization

This dissertation is divided in 6 chapters. In this chapter, chapter 1, an introduction to the E-nose technology was presented. Firstly, the relation between the biological scent capabilities and the detection of various human diseases was studied, which serves as a motivation for the artificial olfaction methods. In addition, the aim of the work is defined, and a number of specifications and objectives are set.

In the second chapter, chapter 2, the current E-nose technology is presented, as well as background theory that is the base for the work developed. Firstly, the biological olfaction system is introduced, enabling an understanding of the biological principles which are replicated by artificial olfaction methods. Afterwards, the innovative ionogel and hybrid gel sensors are introduced, and other mainstream sensor technologies are discussed. Furthermore, the E-noses developed by the Biomolecular Engineering Laboratory are presented, which includes previous work developed by the author of this dissertation. In addition, the background theory part covers the topics of data acquisition systems, analog circuit design, System-on-a-Chip (SoC) devices, and digital filtering.

In the third chapter, chapter 3, the working principle of the ionogel sensor is studied and presented, in the first section. A detailed study of the ionogel sensor is presented, which is divided in another two sections. In the first one, the effect of the RH on the sensor frequency response is studied. More specifically, a number of frequency response acquisitions were obtained, for various controlled RH levels. In the last section, the response of the sensor to different analytes is studied. For that, a second group of experiments is conducted, with the goal of determining the impact of the various analytes in the impedance of the sensor, for a given frequency range, while the RH was kept constant. Finally, the results from both parts enabled a detailed characterization of the sensor, which sets the specifications for the design of a dedicated AFE circuit, presented in the fourth chapter, chapter 4.

The design of the E-nose device, the Electrical E-nose V3, is presented in the fourth chapter, and is composed of a hardware part and a software part. In the hardware part, two sections are dedicated to the design of the E-nose AFE circuit. More specifically, in the first section, the design of an AFE circuit fully integrated in the PSoC 5LP is presented, while in the second section, the design of an optimized AFE circuit that can measure the impedance of the sensors in multiple frequencies is presented. The design of the E-nose delivery system is presented in a subsequent section, as well as the design of an electronics module, which includes the Printed Circuit Boards (PCBs) that implement the circuits and the respective Computer-Aided Design (CAD) models. Regarding the software part, the development of Python software that implements a Graphical User Interface (GUI), and a real-time plotter is presented. In addition, the design of a digital filter using Python is discussed.

The implementation of the Electrical E-nose V3 is discussed in the first section of the fifth chapter, chapter 5, which is based on the design presented in chapter 4. Three variations of the device were implemented, each one featuring a delivery system optimized for a specific application, while the electronic circuit is the same. After its implementation, researchers from the Biomolecular Engineering Laboratory used the E-nose to perform an array of experiments, throughout various days. This way, in the second section of the fifth chapter, signals acquired by the E-nose in laboratory experiments are presented and analyzed. Moreover, such tests were used to validate the correct working of the created

E-nose device.

Lastly, some conclusions of the work developed, as well as prospects for future work, are presented in the sixth chapter, chapter 6.

2

LITERATURE REVIEW AND BACKGROUND THEORY

In this chapter, the reader will find a brief presentation of the topics in which the work presented is based on, including the current state-of-the-art regarding sensor technologies for E-nose sensing. Additionally, an overview of the relevant technologies, circuit design theory and electronic circuit building blocks is presented.

2.1 Electronic Noses

This section aims to provide an overview of the current E-nose technology, in particular the one developed in the Biomolecular Engineering Laboratory [14–18, 22, 23]. A comparison between biological and artificial olfaction is presented, as well as the most relevant sensor technologies used in artificial olfaction systems.

2.1.1 Analogy with Human's Olfactory System

In the human olfactory system, two nasal cavities allocate millions of distinct Olfactory Sensory Neurons (OSNs), which interact with airborne volatile chemicals inhaled in the respiratory flow. This chemical interaction triggers various signals, from the different OSNs, which are sent to the olfactory bulb as unique patterns of neuronal signals, which the brain recognizes as odors [24].

In E-noses, in place of the human's nasal cavities and OSNs there is a set of semi-selective gas sensors, housed in a sealed chamber, which produce signals when exposed to different gases. A computer algorithm interprets the signals, trying to recognize patterns associated with distinct odors, mimicking the brain's job. In Figure 2.1, a side-by-side comparison between biological and artificial olfaction is shown.

2.1.2 Mainstream Sensor Technologies

Metal-Oxide Semiconductor (MOS), Liquid Crystal (LC), conductive polymer, and Quartz Crystal Microbalance (QCM)-based sensors are the most common sensor technologies

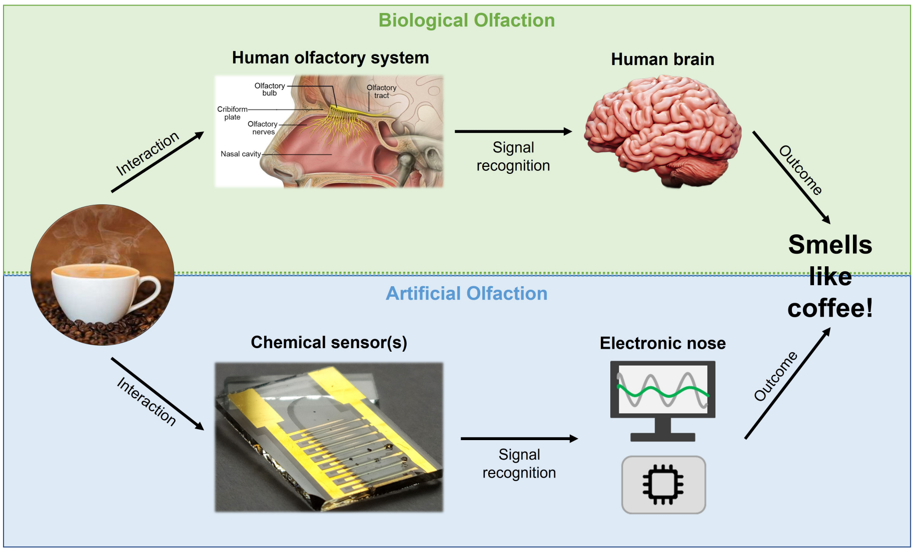

Figure 2.1: Comparison between biological and artificial olfaction. (Adapted from [25–27]).

used in E-nose sensing systems.

In the Biomolecular Engineering Laboratory, innovative ionogel and hybrid gel sensors formed by a mixture of gelatin (or peptides) and ILs, or a mixture of gelatin (or peptides), IL and LCs, yield two separate responses to analytes: optical and electrical. Thus, two families of sensors can be considered: optical sensors; and electrical sensors [14]. In this thesis the focus will be placed on the electrical sensors, also denominated as ionogel sensors, which are presented in detail in chapter 3.

MOS sensors [28–30] are typically based on an Interdigitated Electrode (IDE) structure, where a material such as tin oxide is deposited, forming a coat on the surface. When the sensor is exposed to ambient air, it features a high resistance, however, if a specific VOC interacts with the surface material a reduction process occurs, releasing electrons to the tin oxide. The adsorption of gases changes the resistance of the material. To measure it, a potential is applied to the sensor and the resulting current is measured. MOS sensors are very small and can easily be implement alongside electronic circuits. Metal-Oxide-Semiconductor Field-Effect Transistor (MOSFET)-based sensors are similar to MOS sensors, however, the interaction with analytes results in a change in the threshold voltage of the transistor, which is proportional to the gas concentration.

LC-based sensors [31] change their optical properties under the exposure to certain gases, *e.g.* the optical properties of hybrid gel sensors, which result in a modulation of the light transmitted through the material, which is dependent on the VOC [16].

Polymer-based sensors [32–34], more specifically conductive polymer sensors, are based on the measurement of the electric conductivity of the material, which changes when an interaction with an analyte occurs. Apart from considerable sensitivity and ease of production, one major disadvantage of this technology is its susceptibility to humidity.

QCM sensors' oscillating frequency is changed when an interaction with an analyte occurs [35]. These sensors are characterized by a nominal fundamental frequency. The adsorption of gases to the material changes its properties, resulting in a change of oscillating frequency.

2.1.3 Commercially Available E-noses

The E-nose technology is a relatively recent one. Since the 1980's, numerous research groups and entities have been developing it to suit a large range of applications. However, in the last 2 decades, the *technology boom* enabled rapid and efficient access to resources and methods required for the development of the E-nose technology. The result is a large number of in-house developed E-nose devices, targeted to the different applications in numerous fields and industries, such as the medical field, food and beverage industries, agriculture and forestry industries, quality assessment and control, environmental protection and monitoring, and others.

Furthermore, some of the in-house E-nose developers have taken their technology to the market. However, this is still a relatively small and limited one. Table 2.1 contains examples of commercially available E-noses, as well as their applications and sensor technology.

E-nose / Company	Industry	Applications	Sensor Technology
Aenose, The eNose Company [36]	Medical	Lung and colon cancer	MOS
Cyrano Sciences' Cyranose 320, Sensigent [37]	Medical	Respiratory diseases	Conductive Polymer
BH114, Bloodhound Sensors	Medical	Urinary tract infections [38], tuberculosis	Conductive Polymer
FreshSense	Food	Fish freshness [39]	Gas
Portable Electronic Nose, AirSense Analytics [40]	Food	Food and beverage quality control	MOS
The FOODsniffer [41], Peres	Food	Meat and fish spoilage	Gas
e-Nose 5000	Environmental	Water contamination [42]	Conductive Polymer
The JPL Electronic Nose [43]	Environmental	Air quality assessment	N.A

Table 2.1: Commercially available E-noses and their applications.

2.1.4 E-noses developed by Biomolecular Engineering Laboratory

At the current year of 2022, the Biomolecular Engineering Laboratory has developed two E-nose variations, whose most recent iterations are the Optical E-nose V4 and Electrical E-nose V2 [22, 23], which take advantage of the optical and electrical properties of the hybrid gel sensors, respectively.

As presented in Figure 2.2, the E-nose is composed of three main systems: a delivery system; a detection system; and an acquisition system. The delivery system is responsible to deliver the gas sample, or analyte, to the detection chamber. For that, a pump, or a set of pumps, pushes ambient air into the sample flask, thereby driving its saturated headspace out. A set of valves directs the analyte to the detection chamber, where the interaction with the sensors occurs. Additionally, this set of valves is also used to direct clean air to the detection chamber, for cleaning purposes.

In the detection chamber, the signals captured from the ionogel sensors are sampled by the acquisition system, more specifically by the AFE circuit. The AFE circuit amplifies and filters the signals, which are then converted into the digital domain. A micro-controller is implemented to manage the analog-to-digital conversion and provide control signals for the power control circuit, whose job is to switch the power to the delivery system.

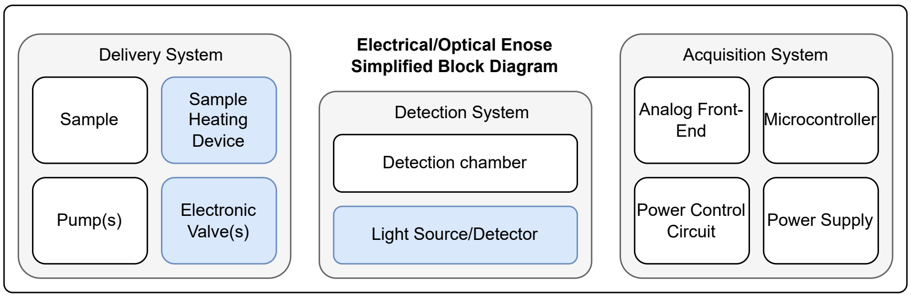

Figure 2.2: Biomolecular Engineering Laboratory E-nose simplified block diagram. The blue color identifies the components unique to the Optical E-nose version.

2.1.4.1 Electrical E-nose V2

The Electrical E-nose V2 is presented in Figure 2.3a. This E-nose is designed to work with an array of 12 ionogel sensors, simultaneously. A custom PCB, shown in Figure 2.3b, implements 12 independent channels, consisting of a conductivity meter, similar to the one proposed by [44]. The conductivity meter is based on a triangle-wave generator, a variable-gain Trans-Impedance Amplifier (TIA), a precision full-bridge rectifier, and a low-pass filter. The trans-impedance gain can be adjusted with a potentiometer, for a pair of channels.

An Arduino DUE [45] is used to sample each of the 12 analog outputs, offering 12-bit resolution. In Figure A.21, the simplified circuit of the Electrical E-nose V2 is presented. An additional relay-based circuit board is used to control the delivery system. The delivery system is composed of two mains-powered aquarium pumps connected to the sample flask (not shown), which is in a heated water bath, through the use of an external heating device. The gas media is forced into a detection chamber, and a temperature and humidity sensor is implemented at the outlet. The power is supplied by an external 12V switching power supply, and a complementary 5V power supply is also used to power the relay circuit.

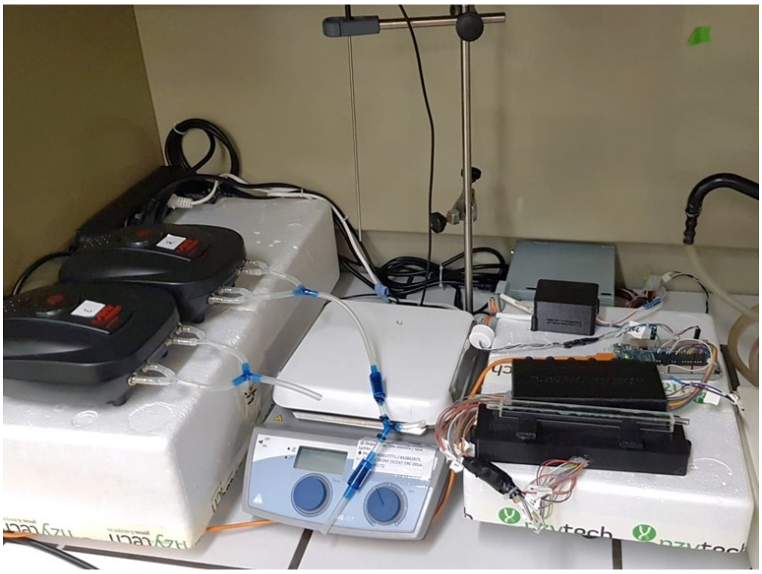

(a) Electrical E-nose V2 implementation.

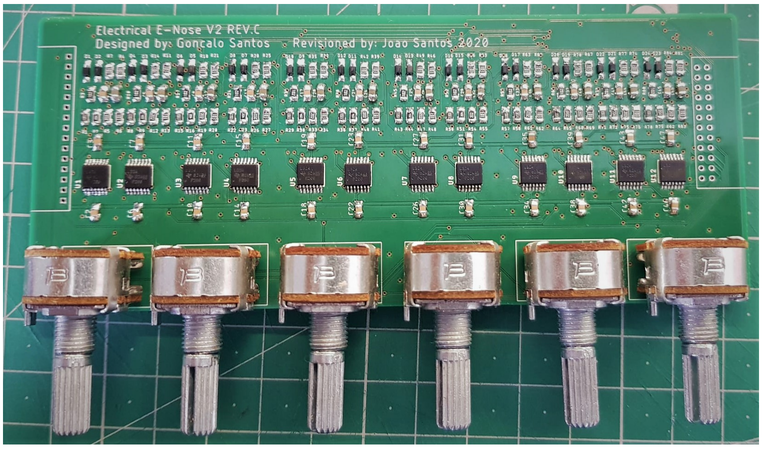

(b) Electrical E-nose V2 AFE PCB.

Figure 2.3: Electrical E-nose V2. In a) the complete device is shown. In b) the dedicated AFE circuit is presented.

2.1.4.2 Optical E-nose V4

The Optical E-nose V4 was designed and built by the author of this dissertation, under the scope of previous work developed for the ERC project SCENT (SCENT-ERC-2014-STG-639123, 2014-2022), in the Biomolecular Engineering Laboratory. This E-nose is shown in Figure 2.4a.

The Optical E-nose V4 is designed to work with an array of 12 optical sensors. For that, the AFE circuit is composed of 12 identical and independent channels, each one featuring a photo-diode and a programmable-gain TIA. The AFE circuit is shown in Figure 2.4b and corresponds to the PCB on the top. Due to the high dynamic range necessary to fulfill the requirements of the optical sensors, the trans-impedance gain is controlled with an analog multiplexer, and an array of resistors ranging from 100 kΩ to 300 MΩ , resulting in 16 discrete gain levels. In Figure A.22, the simplified circuit of the Optical E-nose V4 is

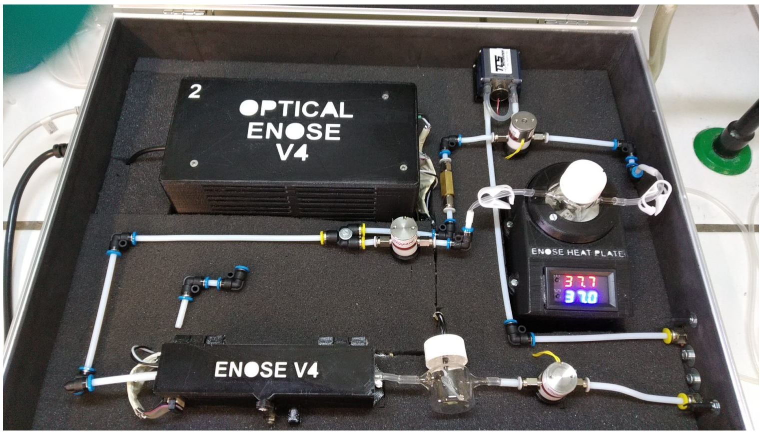

(a) Optical E-nose V4 implementation.

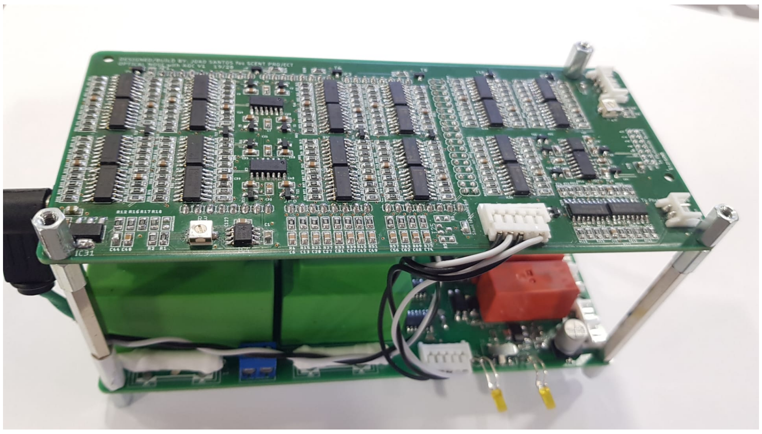

(b) Optical E-nose V4 AFE.

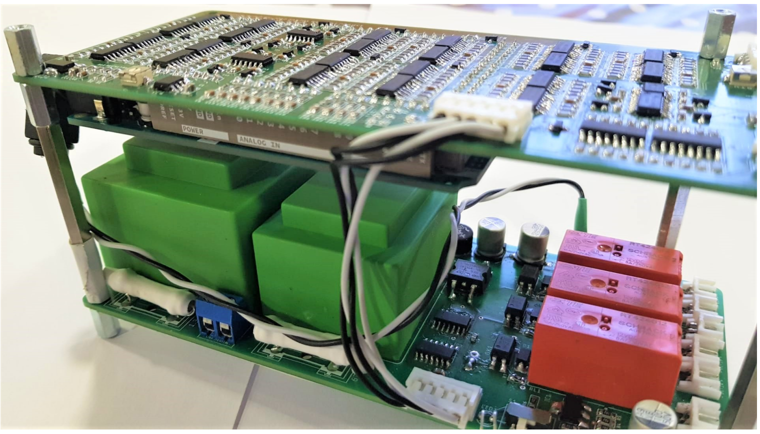

(c) Optical E-nose V4 power supply and control circuit.

Figure 2.4: Optical E-nose V4. In a) the hardcase implementation of the E-nose is shown. In b) and c) the circuitry on the top corresponds to the AFE circuit, and the circuitry on the bottom corresponds to the power supply and delivery system control circuit.

presented.

An Arduino DUE [45] is used to sample the 12 analog signals, corresponding to the amplified signal from each sensor, and its Analog-to-Digital Converter (ADC) offers a resolution of 12-bit. Due to the low-frequency nature of the optical signals, a sampling rate of 250 Hz is used. The Arduino was also used to control the multiplexers and the delivery system.

The delivery system is composed of 3 12V solenoid valves, a 3-6V miniature air pump, and a custom-built 22W resistive sample heating device. Additionally, 4mm PTFE tubing was used, as well as dedicated push-quick connectors . The power for the delivery system control circuit, presented in Figure 2.4c, was supplied from a custom-built linear power supply. However, a secondary power supply, also integrated in the power system, provides a very low-noise 9V for the sensitive AFE circuit.

The device is implemented in a portable aluminum hardcase, filled with foam. This way, the system is more stable and always ready to use, improving reliability and repeatability. The device was assembled manually, including the soldering process.

2.2 Analog Circuit Design Theory and Building Blocks

In this section, the most relevant analog and mixed-signal electronic circuit building blocks, in the scope of this work, are presented. Such building blocks include higher level Data Acquisition Systems (DAQs), SoCs, and AFE circuits, as well as the basic working principles of Operational Amplifiers (Op-amps), analog switches, and signal converters. Furthermore, an overview of noise in electronic circuits, and filters, are presented.

2.2.1 Data Acquisition Systems

DAQs are becoming ubiquitous in modern day electronics. Since their introduction in the market, in 1963, their applications range from infrastructure monitoring, manufacturing, medical devices, and can be found integrated in most of modern-day gadgets and appliances.

A DAQ can be defined as a measurement system targeted to acquire signals from multiple sources. A typical block diagram of a DAQ, represented in Figure 2.5, is composed of four main parts: a sensor or transducer; a signal conditioning stage, which may implement noise filtering and signal amplification; a data acquisition stage, which may include a hardware and software part; and a digital signal processing stage, which incorporates various forms of data processing, such as digital filtering or Fast-Fourier Transforms (FFTs) [46].

The bridge between the physical and the electrical world is made by sensors, which are a form of transducers [47]. A transducer is a device that operates via a transduction process, in which the input energy form is transformed in another energy form at the output. The transduction function describes the operation of the transducer, *i.e.* the form of input

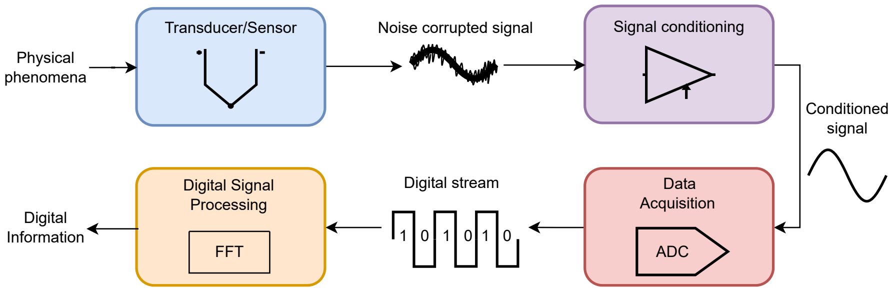

Figure 2.5: Generic data acquisition system block diagram (adapted from [46]).

energy, *e.g.* temperature, pressure or electrical energy, and the form of output energy, *e.g.* electrical energy, pressure or light. For example, an antenna has electromagnetic energy at its input and electrical energy at its output, while a speaker has electrical energy at the input and mechanical energy, in the form of acoustic waves, at the output.

A sensor is the particular case of a transducer [48], whose output is in the form of electrical energy, being a voltage, a current, a resistance or a capacitance. The input energy form of a sensor can be any other, such as mechanical energy in the form of vibration, acoustic waves, or elasticity of a material, or chemical energy such as the concentration of analyte in a chemical sample.

The measurement of real-word phenomena using sensors is a non-ideal process. Analog sensors such as photo-diodes generate very small electrical current signals, in the orders of pA. This is the case of the optical signals described in subsubsection 2.1.4.2. Most of the time, the problem arises when such small signals are to be measured and detected, since the environment is full of unwanted signals, such as electrical noise, radiation, and interference. Typically, to solve this problem, DAQs implement a signal conditioning stage.

Signal conditioning is required when a given analog signal doesn't comply with certain requirements, such as amplitude, bandwidth, or isolation, and aims to prepare that signal for the next processing stage. For example, the small electrical current of a photo-diode is amplified, and its bandwidth limited to reduce high-frequency noise and interference. An electrocardiogram is another great example of the importance of signal conditioning [49]. Generally, these medical exams consist in the measurement of μV level signals, which are easily corruptible by magnetic fields, switching noise from power supplies and high frequency pollution from all sorts of equipment. Thus, the acquired signal requires filtering and amplification before digitization [50]. Apart from that, these devices should comply with a number of safety regulations, including electrical isolation.

As the name implies, the conversion process is responsible to convert the analog domain signal into a digital domain signal. Decades ago, the conversion process did not include an analog-to-digital conversion, but rather a conversion of the electrical signal into the actuation of a dial in a measurement device, or light-rays in a display. In recent years, the integration of an analog-to-digital conversion process has become ubiquitous.

In addition, the conversion process has become increasingly more important, due to the increasing demand of higher-accuracy and higher-precision applications.

At the hardware level, DAQs include ADCs, which may be more suitable for high frequency signals or optimized for higher resolutions. Nowadays, it is common for ADCs to feature resolutions from 16-bit to 32-bit. The sampling rate and resolution are the most looked-after and important parameters when choosing the right ADC for the application, but other parameters such as linearity and Total Harmonic Distortion (THD) are also relevant [51].

To handle the data generated by the analog to digital conversion process, dedicated software is used, which can also be responsible to store and present it in real-time. Moreover, the acquisition software may also implement some sort of digital signal processing. Signal processing can be as simple as filtering data according to a set of parameters, or as complex as computing mathematical functions such as FFTs. In more advanced systems, the latter operation may be performed in hardware, presenting performance advantages over software implementations, by using dedicated Digital Signal Processors (DSPs).

2.2.2 System-on-a-Chip

SoC devices integrate a wide range of electronic building blocks in a single Integrated Circuit (IC), sharing a common silicon-die, including analog and digital components such as processors, memory, amplifiers, signal converters and configurable General Purpose Inputs/Outputs (GPIOs). These highly integrated circuits have lots of applications in mobile devices, due to a great balance between power-consumption and processing power. In [52], the authors developed a wearable body temperature monitoring system, in [53] a Field-Programmable Gate Array (FPGA) based SoC was designed for continuous blood pressure measurements, and in [54] a body-area-network system capable of acquiring data from multiple sensor nodes positioned along the body was developed.

Typically, SoCs feature a Reduced Instruction Set Computer (RISC)-based single or multi-core processors, due to their simplicity and computation efficiency, reducing power-consumption and price. In particular the Advanced RISC Machine (ARM) architecture is widely used.

Communication protocols such as Serial Peripheral Interface (SPI), Inter-Integrated Circuit (I2C), Ethernet, Universal Asynchronous Receiver/Transmitter (UART) and Universal Serial Bus (USB) are implemented, easing the inter-connection between sensor nodes. More recent iterations include internet-of-things oriented communication interfaces, such as Bluetooth Low Energy and Wi-Fi. To take full advantage of the mixed-signal architecture, DSPs are sometimes integrated in the SoC, eliminating the need for external processors.

Companies such as Infineon Technologies have improved the flexibility of typical SoC devices by introducing a configurable analog sub-system, creating their well-known Programmable System-on-a-Chip (PSoC) family. The most recent iteration of the PSoC family is the PSoC 6, however due to their success the PSoC 5LP [55] is still widely used.

At their core there is a Central Processing-Unit (CPU) and multiple configurable analog and digital peripherals, which differentiates them from typical micro-controllers and FPGAs [56]. Infineon Technologies also developed a dedicated integrated development environment, the PSoC Creator [57], which enables control, configuration and debugging of the devices.

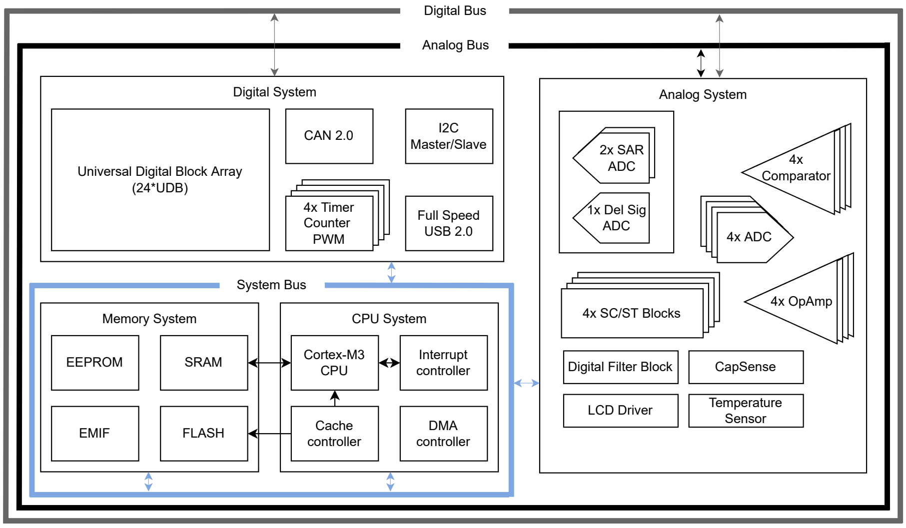

Figure 2.6: PSoC 5LP simplified block diagram (adapted from [55]).

The CY8C58LP is a family of ultra-efficient, flash programmable devices based on the PSoC 5LP platform. As presented in Figure 2.6, the simplified block diagram can be divided in four main parts: analog system; digital system; CPU system; and routing buses.

The analog sub-system includes two types of ADCs: two Successive-Approximation Register (SAR) ADCs; and a $\Sigma\Delta$ ADC. The SAR ADCs can be configured to a maximum of 12-bit of resolution and a sampling rate of 1 MHz, while the $\Sigma\Delta$ ADC can support from 8-bit up to 20-bit of resolution and a maximum sampling rate of 384 kHz, due to its 3^{rd} order modulator and programmable decimator filter. A high input impedance buffer with configurable gain is available. Both ADCs feature various power modes, single-ended or differential input, and internal or external voltage references.

The four available Digital-to-Analog Converters (DACs) are based on a current-DAC, which can either source or sink current. Optionally, the output of each current-DAC can be routed to a current-to-voltage converter, resulting in a voltage-DAC. Four Op-amps and comparators can be used for direct interface with GPIO ports or internal signals. Also, switched capacitor/continuous time amplifiers are available, in the forms of programmable-gain amplifiers, unity-gain buffers, TIAs, mixers and first order analog to digital modulators. Apart from this, the analog system also includes LCD drivers, CapSense technology and temperature sensors.

The digital sub-system is quite versatile, featuring 24 universal digital blocks, consisting in a combination of programmable logic devices and structured logic, enabling the implementation of digital hardware circuits, similarly to an FPGA. I2C and Controller Area Network (CAN) bus controllers are implemented in configurable blocks. Also, four timers are available for different purposes, such as Pulse-Width Modulation (PWM) functionality. One main advantage of the digital subsystem is the inclusion of a full-speed USB 2.0 transceiver, enabling easy data exchange with peripherals such as computers.

The PSoC 5LP features an RISC Cortex-M3 CPU, integrated with interrupt, cache, and Direct Memory Access (DMA) controllers. Temporary data storage is managed by an Single Random-Access Memory (SRAM), which can be simultaneously accessed by the CPU or a DMA controller. Flash memory provides storage for firmware and configurations, and an EEPROM is used to store user data. Apart from this, a flexible analog routing matrix enables the connection between GPIOs and different hardware blocks, which is a big advantage of this family of PSoCs.

2.2.3 Analog Front-End Circuits

One of the fundamental building blocks of a DAQ is the AFE circuit. The purpose of an AFE is to provide an interface between a sensor, or a set of sensors, and an ADC. Such circuit is responsible to implement analog signal conditioning, including amplification, attenuation, filtering, and also the signal conversion. For the conversion process, ADCs are typically found in AFE circuits, alongside a micro-controller. In some applications, the AFE circuit can also be responsible for driving a sensor, using a DAC. Thus, AFE circuits can be considered mixed-signal blocks of a DAQ.

Due to their complexity, AFE circuits are readily available in the form of an IC. IC technology provides cost reduction, improved performance, high levels of integration and high reconfigurability. Thus, AFE ICs are very popular in power-efficient and small-footprint electronic products, such as internet-of-things and medical devices. One example of a powerful AFE IC is the ADuCM355 [58], from Analog Devices, whose functional block diagram is presented in Figure 2.7.

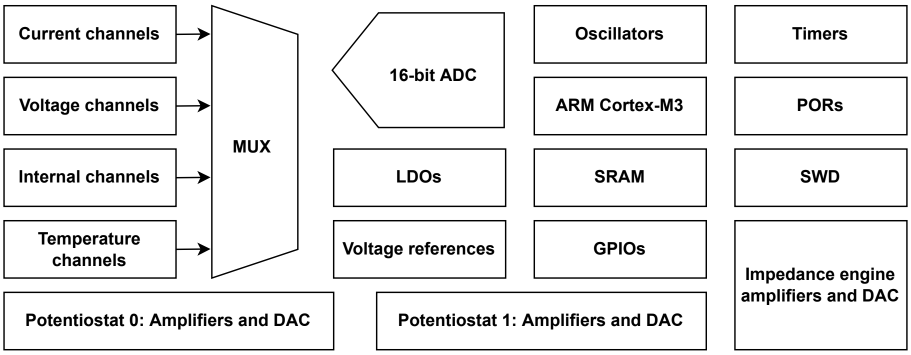

Figure 2.7: ADuCM355 simplified functional block diagram (adapted from [58]).

This on-chip system is best suited for electrochemical and biosensor applications, incorporating analog and digital elements in the same silicon die. A 32-bit ARM Cortex-M3 processor, running at 26 MHz, supporting DMA, independent SPI ports, I2C communication, UART, 128 kB of flash memory, 64 kB of SRAM is used as the main control and processing unit.

Seventeen GPIO ports are available, which implement PWM, a set of timers, and various configurable oscillators. A 16-bit multi-channel SAR ADC, capable of a sampling rate of 400 kHz, featuring built-in anti-aliasing filters and programmable gain amplifiers is available to use. Typical analog circuits are included, such as TIAs, potentiostat amplifiers, DACs, multiplexers, internal temperature sensor, voltage-regulators, and low-dropout regulators. Not coincidentally, such electronic circuits are basic building blocks off most high-performance bio-chemical focused devices, such as environmental sensing, impedance measurements, amperometry, voltammetry and spectroscopy.

As with many IC solutions, there are some disadvantages. Due to the integration of a high-number of circuit building blocks, these devices can be rather complex to configure. In addition, some applications may require just a few building blocks, making the IC approach over-priced and excessively complex.

2.2.4 Operational Amplifiers [59–64]

2.2.4.1 Ideal Model

Op-amps are versatile electronic building blocks, which are characterized by high-gain, high input impedance and low output impedance. An ideal Op-amp, whose model is represented in Figure 2.8, has infinite open-loop differential gain, zero common-mode gain, zero offset voltage, zero input bias currents and zero input capacitance.

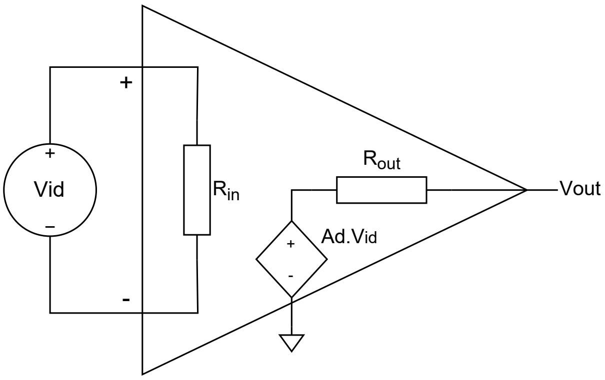

Figure 2.8: Ideal Op-amp model. R_{in} represents the open-loop input impedance, R_{out} represents the open-loop output impedance, A_d represents the open-loop differential voltage gain, and V_{id} represents the differential input voltage.

The open-loop differential gain of an Op-amp circuit relates the output voltage with the differential input voltage, and in the linear region of operation, is given by:

$$V_{out} = A_d \times V_{diff}, \tag{2.1}$$

where V_{out} is the output voltage, A_d is the open-loop differential voltage gain, and V_{diff} is the differential input voltage. Considering that the ideal differential voltage gain is infinite, in open-loop operation the Op-amp saturates on the supply rails, acting as a voltage comparator, and the output voltage, is described by,

$$V_{out} = \begin{cases} V_{sat+} & \text{if } V_{diff} > 0 \\ V_{sat-} & \text{if } V_{diff} < 0 \end{cases}, \tag{2.2}$$

where V_{sat+} and V_{sat-} are the positive and negative output saturation voltages of the Op-amp, respectively.

2.2.4.2 Feedback Theory

To provide amplification in precise amounts, to ensure stability, and control the bandwidth of the circuit, the loop of the Op-amp must be "closed". For that, a feedback path from the output of the Op-amp to its input is created, closing the loop. This feedback system is represented in Figure 2.9.

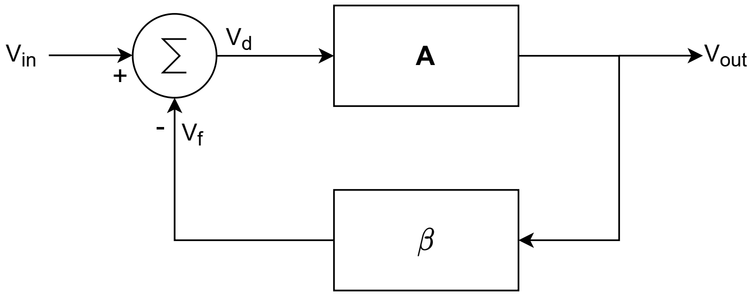

Figure 2.9: Negative feedback system.

The closed-loop system is composed by a forward gain block, and a feedback attenuation block, represented by A and β, respectively. By analyzing the feedback system, it is possible to conclude that,

$$\begin{cases} V_{\text{out}} = A \times V_{\text{d}} \\ V_{\text{f}} = \beta \times V_{\text{out}} \\ V_{\text{d}} = V_{\text{in}} - V_{\text{f}} \end{cases}, \tag{2.3}$$

where A is the forward gain and β is the feedback attenuation factor.

Solving Equation 2.3, the closed-loop gain (A_{cl}) of the system is given by:

$$A_{\text{cl}} = \frac{V_{\text{out}}}{V_{\text{in}}} = \frac{A}{1 + A\beta}. \tag{2.4}$$

In reality, Op-amps are non-ideal devices. Most notably, the open-loop gain of an Op-amp is finite. However, some modern technologies are capable of open-loop gains in the order of 140 dB, which can be approximated as tending to infinity. In this case, the approximate closed-loop gain is approximately given by:

$$A_{\text{cl}} \approx \lim_{A\to\infty}\left(\frac{A}{1+A\beta}\right) \approx \frac{1}{\beta}. \tag{2.5}$$

The latter statement regarding the scale of open-loop gain, can be considered a good approximation depending on the application. For typical applications, an open-loop gain greater than 60 dB provides reasonable gain error, while a minimum of 120 dB is required for higher-accuracy applications.

This derivation proves that a very high open-loop gain of the Op-amp results in a closed-loop gain that is almost independent of the absolute open-loop gain, which can vary significantly, either due to the manufacturing process, or temperature changes. Depending on the value of the loop-gain, $A\beta$, two feedback modes can be considered: negative feedback; and positive feedback. Positive feedback is commonly used to implement oscillator circuits. On the other hand, negative feedback enables the implementation of numerous forms of amplifiers, such as voltage amplifiers, current amplifiers, transconductance amplifiers and TIAs.

Other beneficial outcome of feedback is related with the input impedance and output impedance of the circuit. Generally, the open-loop input impedance and open-loop output impedance appears multiplied by $1 + A\beta$, if the circuit features a series-input or series-output, respectively. On the other hand, if the circuit presents parallel-input or parallel-output, the open-loop input impedance and the open-loop output impedance appears divided by $1 + A\beta$, respectively.

Voltage amplifiers are considered series-input and parallel-output circuits. Thus, the implementation of feedback results in the increase of input impedance and decrease in output impedance, which can be calculated as,

$$\begin{cases} Z_{\text{in,cl}} = Z_{\text{in,ol}} \times (1 + A\beta) \\ Z_{\text{out,cl}} = \frac{Z_{\text{out,ol}}}{1+A\beta} \end{cases}, \tag{2.6}$$

where $\text{Z}_{\text{in,cl}}$ and $\text{Z}_{\text{in,ol}}$ are the closed-loop and open-loop input impedances, and $\text{Z}_{\text{out,cl}}$ and $\text{Z}_{\text{out,ol}}$ are the closed-loop and open-loop output impedances.

2.2.4.3 Amplifiers Topologies

Some of the most common voltage amplifier topologies are the unity-gain buffer, inverting amplifier, non-inverting amplifier, and difference amplifier.

A unity-gain buffer is obtained when the feedback attenuation, β, is equal to unity. The respective circuit is presented in Figure 2.10a. Even though this topology does not provide amplification, it is useful in other applications, such as driving low impedance sources and providing isolation between signals.

A non-inverting amplifier is represented in Figure 2.10b. In this topology, the value of β is given by:

$$\beta = \frac{Rs}{Rs + Rf}, \tag{2.7}$$

thus, considering Equation 2.5, the approximated closed-loop gain is set by the ratio of two resistors, and is given by:

$$A_{\mathrm{cl}} = \frac{V_{\mathrm{out}}}{V_{\mathrm{in}}} \approx 1 + \frac{Rf}{Rs}. \tag{2.8}$$

Similarly, in an inverting typology, represented in Figure 2.10c, the gain is set by the ratio of two resistors, and is given by:

$$A_{\mathrm{cl}} = \frac{V_{\mathrm{out}}}{V_{\mathrm{in}}} \approx -\frac{Rf}{Rs}. \tag{2.9}$$

Unlike the inverting and non-inverting topologies, the difference amplifier, represented in Figure 2.10d, features two signal inputs, while its output is directly related to the differential voltage between them. However, both the differential and average voltages of the inputs, *i.e.* the common mode voltage (CMV), contribute to the output voltage of a difference amplifier, as given by:

$$V_{\mathrm{out}} = A_{\mathrm{d}}(V1 - V2) + A_{\mathrm{cm}}\left(\frac{V1 + V2}{2}\right), \tag{2.10}$$

where A_{cm} is the common mode gain of the Op-amp, and V1 and V2 are the input signals. Ideally, the differential voltage gain (A_{d}) should be considerably higher than the common mode gain (A_{cm}). If $A_{\mathrm{d}} = 1$, the difference amplifier can be denominated a voltage subtractor.

TIAs are commonly found in applications in which a current is converted to a voltage. Thus, the gain of a TIA is given in units of Ω. A TIA can be thought as being an inverting amplifier configuration with a current source at its input, as represented in Figure 2.10e. Applying the same analysis procedure, the trans-impedance gain ($\mathrm{Gain}_{\mathrm{TIA}}$) is given by:

$$Gain_{\mathrm{TIA}} = \frac{V_{\mathrm{out}}}{I_{\mathrm{in}}} = -R_{\mathrm{f}}, \tag{2.11}$$

where R_{f} is the feedback resistance. Thus, the output voltage of a trans-impedance is given by:

$$V_{\mathrm{out}} = V_{\mathrm{ref}} - I_{\mathrm{in}} \times R_{\mathrm{f}}, \tag{2.12}$$

where I_{in} is the input current.

2.2.4.4 Frequency Response and Stability

So far, the dependence of Op-amp open-loop gain with frequency has been neglected. However, the open-loop gain of any Op-amp is a function of frequency. Op-amps have inherent capacitance, which decreases their ability to provide gain at high-frequencies.

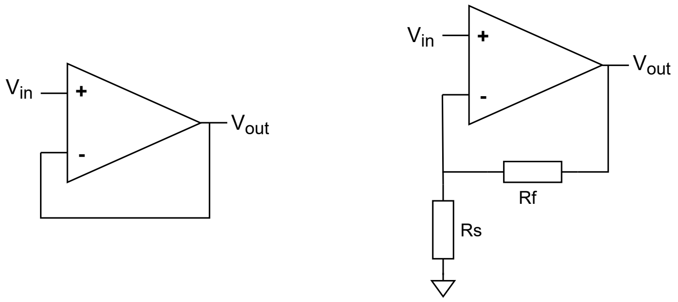

(a) Unity-gain buffer.

(b) Non-inverting amplifier.

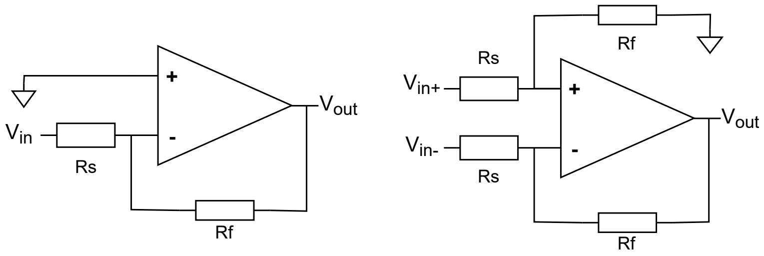

(c) Inverting amplifier.

(d) Difference amplifier.

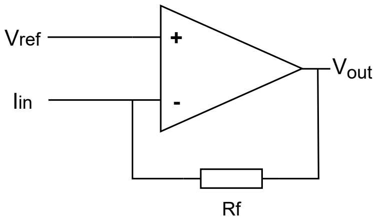

(e) Trans-impedance amplifier.

Figure 2.10: Op-amp voltage and trans-impedance amplifier topologies.

Typically, Op-amp manufactures include a built-in frequency compensation circuit, which simplifies the open-loop response of the Op-amp. Most commonly, Op-amps are characterized by a single low-frequency pole, however, some present a higher-number of poles. The lowest-frequency pole is denominated as dominant pole.

The Gain-Bandwidth Product (GBW) of an Op-amp is a figure of merit used to quantify the relation between open-loop gain and frequency. This value can be visually obtained, by analyzing the Op-amp open-loop gain characteristic and measuring the frequency at which the open-loop gain equals to unity.

The closed-loop bandwidth of an Op-amp circuit is dependent on the β factor and the GBW of the amplifier, as it remains constant and equal to, approximately, $\frac{1}{\beta}$, until the intersection frequency with the open-loop gain curve, f_{i}. After that, the closed-loop gain is equal to the open-loop gain, as the frequency response is dominated by the Op-amp itself. In Figure 2.11a, the later behavior is visually represented for two distinct β values. The GBW of the Op-amp is presented at two different frequencies, *i.e.* 1 kHz and 100 kHz, and has a value of 100 kHz.

In a single open-loop low-frequency pole Op-amp, the GBW is approximately constant and equal to the ratio between open-loop gain and frequency. Considering a straight-line approximation, the slope of the open-loop gain, as denoted in Figure 2.11a, is -20 dB/decade, whilst the gain is constant for frequencies lower than the dominant-pole frequency. The latter gain value is denominated as DC gain. At the pole frequency, the gain has dropped by 3 dB from the DC gain.

If the Op-amp has multiple poles, then each one contributes with an attenuation of 20 dB/decade. On the other hand, if the open-loop response has a zero, then the gain increases at a rate of 20 dB/decade. Thus, the interaction of poles and zeros dictates the open-loop gain characteristics of the Op-amp.

A highly important characteristic of a given frequency response is the phase response. The phase response gives a more concise understanding about the frequencies of poles and zeros, of a given system. When the system is under the effect of a pole, the phase decreases by 45° at the pole frequency, and further decreases another 45° , a decade after the pole frequency, remaining constant afterwards. On the other hand, the phase value increases if the system is under the effect of a zero. Similarly, the phase begins to increase a decade lower than the zero frequency, and stops a decade after it, resulting in a total increase of 90° .

In Op-amp circuits, the phase response is used to verify its stability. Considering the feedback system presented in Figure 2.9, if either A or β become highly-dependent on frequency, then negative feedback can turn into positive feedback, which can lead to instability. To assess the stability of an Op-amp circuit, a combination of visual interpretation of the bode plot and mathematical methods can be used. Considering Equation 2.4, when $A\beta = -1$, the open-loop gain is undefined. This is equivalent to an open-loop gain of unity, with a 180° phase shift. In this condition, the circuit becomes unstable.

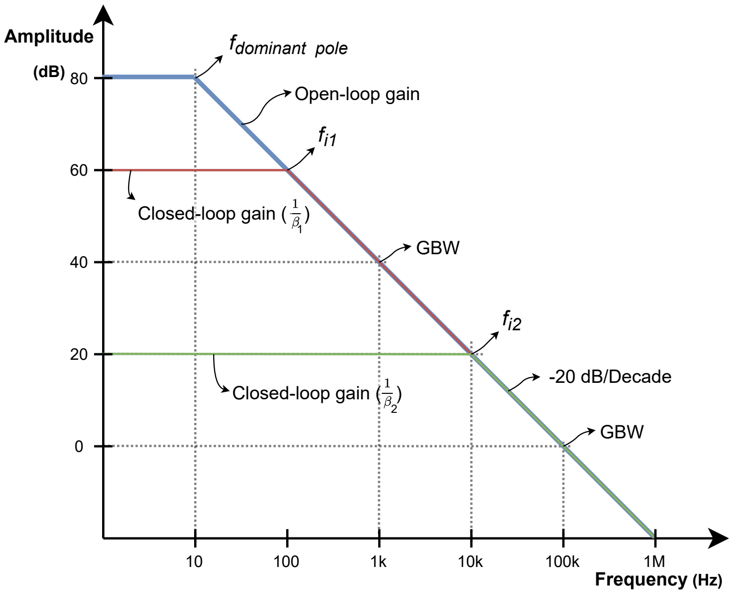

(a) Amplitude response.

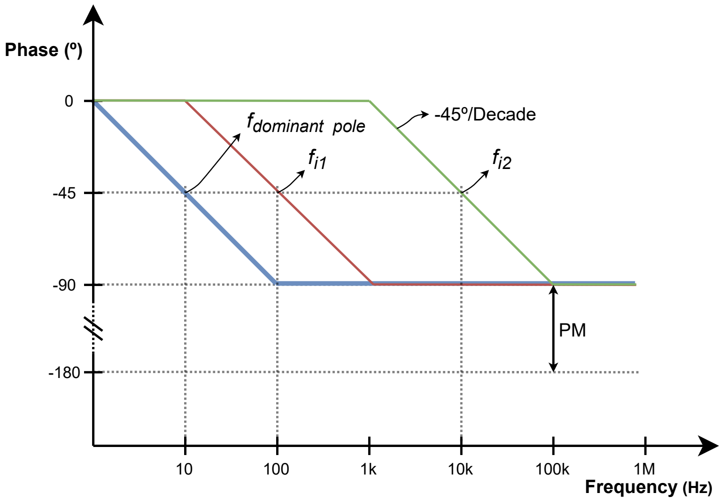

(b) Phase response.

Figure 2.11: Bode plot of Op-amp frequency response, as a function of β. $f_{\text{dominant pole}}$ is the Op-amp dominant pole frequency, f_{i1} and f_{i2} are the pole frequencies for closed-loop gains $\frac{1}{\beta 1}$ and $\frac{1}{\beta 2}$, respectively.

Thus, to ensure stability, the difference between the unity-gain phase value and 180°, relative to DC phase, must be greater or equal to zero. This is the definition of Phase Margin (PM). A PM of 45° is commonly used as a rule-of-thumb, to ensure that the circuit is marginally stable. Increasing the PM results in greater stability, while the opposite is true. Visually, the PM can be obtained by measuring the difference between the phase of closed-loop gain, at unity-gain, as shown in Figure 2.11b. The PM condition dictates the stability of the circuit.

2.2.4.5 Specifications and Non-Ideal Aspects of Op-amps

Being non-ideal devices, the performance of Op-amps can be assessed by particular properties. The most relevant specifications for Op-amps are the following:

- Input offset voltage and drift;
- Input bias currents and drift;
- Input impedance;
- Input and output dynamic range;
- Open-loop gain and gain linearity;
- GBW
- Slew-rate;
- Common-Mode Rejection Ratio (CMRR);
- Power-Supply Rejection Ratio (PSRR);
- Noise spectral density;
- Supply voltage and power dissipation.

Input offset voltage, $\mathrm{V_{off}}$, and input bias currents, $\mathrm{I_{bias}}$, generate static DC errors. However, $\mathrm{V_{off}}$ and $\mathrm{I_{bias}}$ are temperature dependent, which manifest as a drifting DC error. These errors are primarily due to manufacturing imperfections of the input-stage of the Op-amp. As presented in Figure 2.12, the $\mathrm{V_{off}}$ and $\mathrm{I_{bias}}$ are modeled through an ideal voltage and current sources, respectively, at the input of the Op-amp. The output voltage error due to $\mathrm{V_{off}}$ is given by:

$$Verror_{\mathrm{Voff}} = A_{\mathrm{cl}} V_{\mathrm{off}}. \tag{2.13}$$

The output voltage error due to $\mathrm{I_{bias}}$ is given by:

$$Verror_{\mathrm{Ibias}} = A_{\mathrm{cl}} Rin_{\mathrm{eq}} \left(I_{\mathrm{bias+}} - I_{\mathrm{bias-}} \right), \tag{2.14}$$

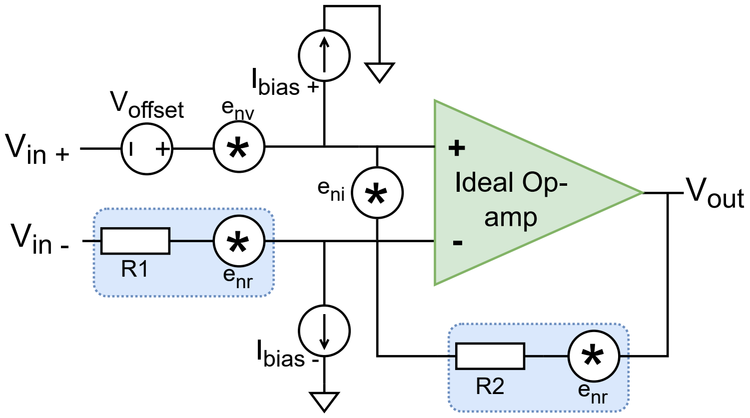

Figure 2.12: Non-ideal Op-amp model. e_{nv} and e_{ni} represent the voltage and current noise sources, respectively, e_{nr} represents the resistor thermal noise, R represents an ideal resistor, V_{offset} represents the input offset voltage, and I_{bias} represent the input bias currents of the Op-amp.

where Rin_{eq} is the equivalent resistance seen at the Op-amp input, which is particular for every circuit.

The input impedance of an Op-amp is composed of a resistive part and a capacitive reactance part. The resistive part is dominant, and depending on the technology, can be in the range of hundreds of kΩ up to several $G\Omega$. The capacitive part is given as a shunt capacitance from the inputs to ground, and is generally in the order of fA to hundreds of μA.

The dynamic range of an Op-amp can be expressed as the maximum and minimum voltage limits that guarantee linear circuit operation. This value is specified for both input and output part of the Op-amp, while each part has an upper limit, which is typically closer to the positive supply rail, and a lower limit, which is closer to the negative supply rail, or ground, depending on the type of supply used.

Most importantly, a high output dynamic range of an Op-amp is mandatory to maximize the output voltage swing, when a low supply voltage is used, such as 3V, or even as low as 1V. Most modern single-supply Op-amps are capable of limits that are as little as tens of mV of the supply rails.

As previously discussed in subsubsection 2.2.4.2, a high open-loop gain is mandatory to minimize closed-loop gain errors. However, it is as important that the open-loop gain is as linear as possible. Due to these factors, and also considering the gain frequency dependence, the resulting gain error is also a function of frequency.

The GBW is directly related to gain error, and slew-rate is related to other frequency-dependent errors. The slew-rate of an Op-amp is defined as the rate of change on the output, when the input is subjected to a ideally-fast voltage step. This specification considers the time it takes for the output of the Op-amp to go from 10% to 90% of the respective input signal voltage. Slew-rate limitations are due to the charging of the internal capacitances of the Op-amp, such as the Miller-capacitance. Thus, slew-rate limitations occur for fast signals, since the internal capacitances of the Op-amp have less time to charge and discharge.

CMRR is a measure of the ability of an Op-amp to suppress common-mode voltages, from the input to the output. Common-mode signals are present at both of the inputs of the Op-amp. Ideally, the Op-amp should only amplify differential signals, but in practice, a change in the common-mode voltage of the Op-amp has an effect on the output, as given by:

$$V_{\text{out}} = A_{\text{d}} V_{\text{d}} + A_{\text{cm}} V_{\text{cm}}, \tag{2.15}$$

where A_{d} and A_{cm} are the differential and common-mode voltage gains, and V_{d} and V_{cm} are the differential and common-mode signals, respectively. The CMRR, in dB, can be defined by,

$$CMRR = 20 \log_{10} \left(\frac{A_{\text{d}}}{A_{\text{cm}}} \right). \tag{2.16}$$

Thus, the error due to CMRR can be expressed as a voltage source in series with the Op-amp input, whose value is given by:

$$V_{\text{CMRR}} = \frac{\Delta V_{\text{out}}}{CMRR_{\text{V/V}}}. \tag{2.17}$$

Additionally, the CMRR of an Op-amp is also a function of frequency. Typically, the CMRR degrades as the frequency increases, which can lead to frequency related errors. The PSRR of an Op-amp measures the effect of a variation in the power supply voltage on its output. The mathematical description of the error due to PSRR is similar to Equation 2.17. Moreover, PSRR is frequency dependent. In practice, to compensate for this non-ideal property, a stable power supply, with local capacitive storage and decoupling, culminates in negligible error due to PSRR.

The previous specifications are mostly related to predictable error sources. However, some errors are random, such as those created by noise. Because of this, the error due to noise has to be calculated using some statistical calculus. Thus, the specifications for noise are given in units of spectral density, which are frequency dependent. For that, it is important to identify the major noise types in Op-amp circuits, which are:

- Resistor thermal noise, e_{nr};
- Op-amp voltage noise, e_{nv};
- Op-amp current noise, e_{ni}.

Both the Op-amp voltage and current noise are composed of two parts: $\frac{1}{f}$ voltage and current noise (e_{nvf} and e_{nif}, respectively); and broadband voltage and current noise (e_{nvBB} and e_{niBB}, respectively)

Commonly, in Op-amp datasheets, the noise voltage spectral density is presented in units of nV/$\sqrt{Hz}$ and current noise spectral density in units of pA/$\sqrt{Hz}$. High-performance Op-amps are capable of sub-10nV/$\sqrt{Hz}$ and dozens of pA/$\sqrt{Hz}$. Additionally, these values are given for a particular frequency, denominated noise corner-frequency, which corresponds to the frequency where broadband noise becomes dominant.

In subsection 2.2.7, a more detailed explanation about noise in circuits is presented.

2.2.5 Analog Switches

A switch is a device that connects an input to an output, or vice-versa. Switches can be mechanical, such a light switch, thermal, such as a thermostat, electro-mechanical, such as a relay, or electronic, such as a transistor. A multiplexer is a form of electronic switch, which can work with analog, digital, or both types of signals.

Analog multiplexers are formed by an array of analog switches. Analog switches are based on a single, or pairs of transistors. The most common analog switch technology is Complementary Metal–Oxide–Semiconductor (CMOS), where both an N-channel and P-channel transistor perform the switching action.

The N-type transistor conducts for negative voltages, while the P-type transistor does the opposite [65]. A control signal, applied to the gate of the transistors, defines the state of the switch. In Figure 2.13a, a typical CMOS analog switch is presented. A multiplexer features multiple switches, which might share a common control signal, or integrate some form of decoder logic to control each individual switch. Typically, a multiplexer has a number of switches that is a base of 2, *i.e.* 2, 4, or 8, featuring 1, 2, 3 or 4 control lines and an optional global enable signal.

In Figure 2.13a, the simplified model of an analog multiplexer is also presented. As CMOS transistors feature an on-resistance, R_{on}, so does an analog switch, which is a combination of the on-resistance of the P-type and N-type transistors and is shown in Figure 2.13b. It is possible to see that the on-resistance of the multiplexer is a function of the input voltage. Commonly, multiplexers are described by its nominal on-resistance and on-resistance flatness, which is the difference between the maximum and minimum on-resistance within the input voltage range. A multiplexer with a high on-resistance flatness introduces non-linear voltage error in a circuit.

An analog switch is characterized by a capacitance at the input terminal, C_{in}, and a capacitance at the (common) output terminal, C_{com}. Depending on the state of the switch, these capacitances may sum. These capacitances not only affect bandwidth, but also the settling time of the switch. Together with the on-resistance, the multiplexer is, effectively, a low-pass filter, whose cut-off frequency depends on its on-resistance and parasitic capacitance.

Moreover, for high-frequency switching applications, charge injection should be considered. This phenomenon is due to the parasitic gate to source capacitance of the switch transistors and can lead to unwanted currents flowing from the control signal to the output terminal of the switch.

Other source of error in analog multiplexers is due to leakage current. However, this error is only considerable at higher temperatures, while it can be neglected in most applications, at room temperature. Multiplexer leakage is due to transistor leakage currents, that flow when the transistor is off. This current can be divided in two sources, $I_{\text{leak in}}$, and $I_{\text{leak com}}$. When the switch is on both currents flow to the output terminal. When the switch is off, the $I_{\text{leak in}}$ flows to the input terminal, while the $I_{\text{leak com}}$ flows to the output terminal. The voltage error due to leakage current, $\text{V}_{\text{error leakage}}$, is given by:

$$V_{\text{error leakage}} = (R_{\text{on}} + R_{\text{source}})\,(I_{\text{leak in}} + I_{\text{leak com}})\,, \tag{2.18}$$

where R_{source} is the source impedance seen at the input terminal. Typically, leakage currents are in the orders of fA, for high-precision multiplexers, but can reach nA for lower-grade devices.

2.2.6 Signal Converters

Signal converters [51, 64] are the bridge between real-world analog signals and digital signals. For example, to talk on the phone, the human voice is captured by a microphone, which results in an analog signal. However, the communications network is digital, meaning that the analog voice signal needs to be converted to a digital stream. At the receiver end, the inverse happens, since the digital information needs to be converted to an analog signal that drives a cellphone speaker. For these tasks, an ADC and a DAC are employed, respectively.

ADCs convert an analog voltage signal to binary information, in the form of bits. A bit is the smallest unit of digital data. Multiple bits, or bytes, are used to store digital data. On the other hand, DACs convert digital data into analog signals, *e.g.* a voltage signal or a current signal.

2.2.6.1 Analog-to-Digital Converter Performance Metrics

The purpose of ADCs is to sample analog signals and to digitally encode them. For that, two consecutive steps are taken: sample and holding; and quantization and encoding [66].

In the sampling phase, the analog signal is sampled and hold, to guarantee that the signal doesn't change in the quantization process. Also, successive samples of the signal are taken in regular intervals, determined by the sampling rate. The quantization phase depends on the type of ADC used, but in general terms, a set of bits corresponding to the analog signal are obtained, resulting in a digital signal.

Independently of the ADC type, a number of parameters and metrics describe their performance, such as resolution, Effective Number of Bits (ENOB), sampling rate, Signal-to-Noise Ratio (SNR), THD, Differential Non-Linearity (DNL), Integral Non-Linearity (INL), offset and gain errors, and input type and dynamic range.

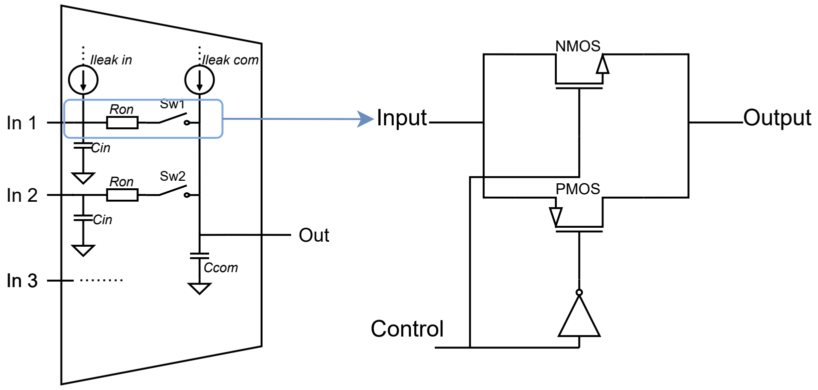

(a) CMOS analog multiplexer switch.

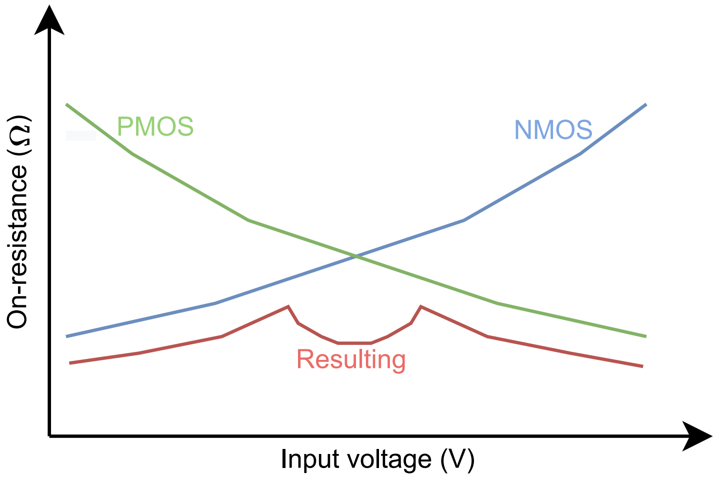

(b) On-resistance characteristic of an analog multiplexer.

Figure 2.13: Analog multiplexer architecture and characteristics.

The resolution of an ADC is given in bits. The Least Significant Bit (LSB) is the smallest voltage step size corresponding to a single bit, and is given by:

$$V_{\text{LSB}} = \frac{V_{\text{fs}}}{2^N}, \tag{2.19}$$

where V_{fs} is the full-scale voltage of the ADC, and N is the resolution (in bits) of the ADC. The sampling rate, or sampling frequency, f_s, of an ADC corresponds to the time interval between consecutive samples of the input signal. The sampling rate should comply with the Nyquist theorem, which states that:

$$f_s \geq 2B, \tag{2.20}$$

where B is the bandwidth of the signal. The latter condition ensures that aliasing does not occur. To prevent aliasing, ADCs may feature anti-aliasing filters, which are a form of low-pass filters, with a cut-off frequency equal to the Nyquist frequency, $f_{\text{Nyq}} = \frac{B}{2}$.

It is important to understand that the quantization process is inherently an error source in ADCs since the analog signal is approximated by a digital code. The quantization error can be seen as a noise source, V_{nq}, which is a random variable comprehended between $\frac{V_{\text{LSB}}}{2}$ and $-\frac{V_{\text{LSB}}}{2}$, and has a Root Mean Square (RMS) value given by:

$$V_{\text{nq,rms}} = \frac{V_{\text{LSB}}}{2\sqrt{12}}. \tag{2.21}$$

The SNR, in dB, of an ADC can be calculated by:

$$SNR = 20\log 10\left(\frac{V_{\text{fs,rms}}}{V_{\text{nq,rms}}}\right) = 6.02N + 1.76, \tag{2.22}$$

which is valid for a frequency range between 0 Hz and f_{Nyq}. Distortion is another major non-ideal property in ADCs. More specifically, in ADCs the THD describes the distortion in the frequency domain. Thus, the Signal-to-Noise and Distortion Ratio (SINAD) is given by:

$$SINAD = 20\log 10\left(\frac{S}{N + THD}\right), \tag{2.23}$$

where S is related to the signal, and N related to the noise. Thus, the ENOB, in dB, is obtained by considering the SINAD, and can be obtained from Equation 2.22, which is given by:

$$ENOB = \frac{SINAD - 1.76}{6.02}. \tag{2.24}$$

The DNL and INL are constructive properties of an ADC, which cannot be fully calibrated, and produce errors. The DNL is defined as the difference between the ideal binary code and the ADC resulting binary code and is measured in LSBs. If the DNL is within $\pm 1LSB$, then no error is produced. As the name implies, INL is the integral of the DNL errors and can be understood as the error between a linear transfer function and the ADC transfer function.

ADCs are also affected by gain and offset errors. The gain error describes the deviation between the ideal gain and the resulting ADC amplifier/buffer gain. This error can be visually interpreted as an error in the slope of the ADC transfer characteristic. Similarly, an offset error describes the amount of offset between the ideal an the ADC transfer characteristic. Both of these errors can be given in units of mV or LSBs. Contrary to DNL and INL errors, gain and offset errors can be calibrated by the user.

Regarding the input typology of the ADC, a single-ended input or differential-input are commonly used. The dynamic range of an ADC is the range of input voltages that it can convert to digital codes.

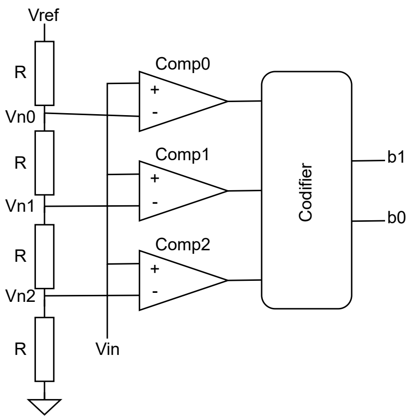

(a) Flash ADC.

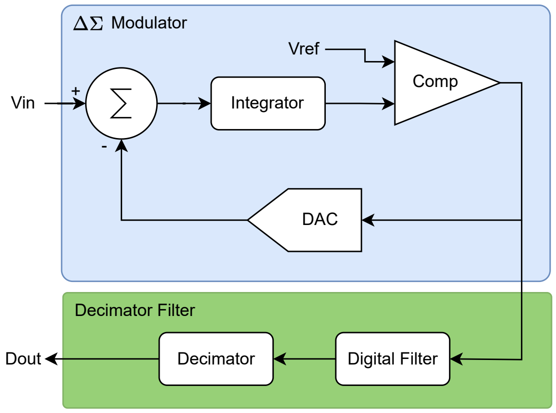

(b) ΣΔ ADC.

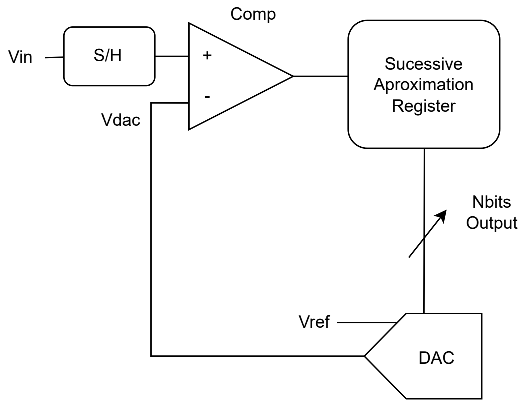

(c) SAR ADC.

Figure 2.14: Simplified ADC architectures.

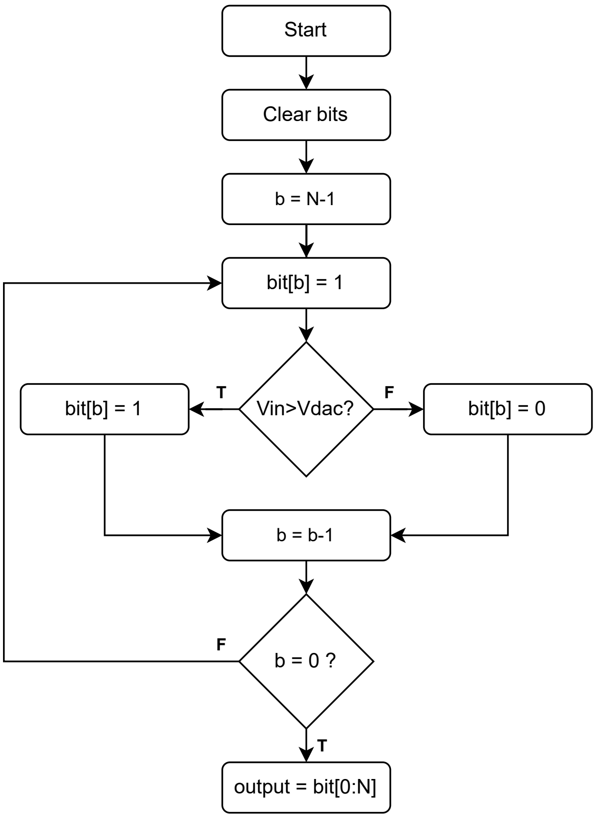

Figure 2.15: SAR algorithm flow-chart.

2.2.6.2 Analog-to-Digital Converter Types

The most common ADC types are the flash, the SAR and the sigma-delta ($\Sigma\Delta$). Different topologies are optimized for power consumption, sampling rate, resolution, or lower silicon implementation area.

The flash ADC, which is presented in Figure 2.14a, is composed of a resistive divider, an array of comparators and a decoder. The resistor divider generates precise voltage levels at the inverting terminal of each comparator. For a N-bit flash ADC, there are 2^N resistors and $2^N - 1$ comparators. The input voltage, which is applied to the non-inverting terminal of all the comparators, is compared with the respective voltage at the comparator inverting terminal. The output of the comparators is fed to an encoder, which outputs the digital code in its N output bits. It is easy to conclude that this typology becomes exponentially more complex, expansive, and power hungry as the number of bits increases, however, its simplicity makes it a very fast ADC.

The SAR ADC, which is presented in Figure 2.14c, is composed of a sample-and-hold circuit, a comparator, the SAR logic, and an N-bit DAC. The sample-and-hold circuit is mandatory to ensure that the input voltage is stable throughout the entire conversion process. A N-bit DAC generates a voltage, V_{DAC}, that is compared with the input sampled voltage. The SAR logic controls the DAC, following a successive approximation algorithm.

The SAR algorithm, presented in Figure 2.15, sets the binary input of the DAC, starting with the most significant bit, and comparing the DAC output voltage, V_{DAC}, with the input voltage, V_{in}. Depending on the comparator output, the remaining bits are set, and the voltage comparison is repeated. Thus, for a N-bit SAR ADC, a total of N conversion cycles are necessary. However, this also means that the conversion time is not a function of the input signal, which is a positive outcome. Comparatively, the SAR ADC is slower than the flash ADC but can be more efficient and accurate.

The ΣΔ ADC, presented in Figure 2.14b, achieves greater resolutions due to its over-sampling capabilities. This ADC is composed of a ΣΔ modulator and a decimator filter. The ΣΔ modulator works by over-sampling the input signal. The over-sampling ratio, OSR, can be defined by:

$$OSR = \frac{F_{\text{Modulator}}}{F_{\text{Dout}}}, \tag{2.25}$$

where $\text{F}_{\text{Modulator}}$ is the frequency at which the modulator samples the input signal, and F_{Dout} is the data rate of the ADC.

The over-sampling process enables the ADC to perform several averages of the input signal, increasing the accuracy and decreasing the quantization error. For that, the output of the modulator is a bit-stream in the form of pulse-code modulation, whose average can be digitally obtained. The modulator is constituted by an integrator, a comparator and a DAC. An error voltage, corresponding to the difference between the input voltage and the DAC output voltage, is integrated, resulting in a ramp signal. The comparator compares this ramp signal with a reference voltage. Considering a given time, the average of the output of the comparator results in the average of the signal.

Due to over-sampling, the bandwidth is increased, resulting in a distribution of the quantization noise over the frequency spectrum. In addition, due to the architecture of the modulator, the input signal is multiplied by a low-pass filter, and the noise is multiplied by a high-pass filter, resulting in less noise in the band of interest. Thus, the noise in the ΣΔ is greatly reduced. To eliminate the high frequency noise, outside the band of interest, a digital decimator filter is used.

2.2.7 Noise

Noise is a random, unpredictable, and unwanted signal that is the primary limitation in a system's resolution, since it limits the sensitivity of the system [60]. It is constituted by random frequencies and amplitudes, which makes it impossible to predict. However, it is possible to predict the probability of the occurrence of noise, due to the noise's Gaussian distribution, which is given by:

$$P(x) = \frac{1}{\sigma\sqrt{2\pi}} e^{-\frac{x-\mu}{2\sigma^2}}, \tag{2.26}$$

where $P(x)$ is the probability of the event x, σ is the standard deviation, and μ is the mean. A general rule-of-thumb is to consider that noise lies within 3σ of the μ, which is 99.7% accurate. Thus, the noise analysis is based on these statistical assumptions.

It is important to differentiate system generated noise and interference. The latter can come from nearby equipment, mains power interference, radio-frequency interference, magnetic coupling, electrostatic discharges, and others alike.

To minimize external interference, sensitive analog circuits are shielded, *e.g.* a low-noise amplifier is implemented inside a dedicated conductive shell, acting as a Faraday cage. If the signals are to be carried for long distances, twisted pairs are mandatory to make the noise a common-mode signal, which can be attenuated by the CMRR of an amplifier. A good and well-planned PCB layout is mandatory to avoid radio frequency interference, magnetic coupling, and other interference, as well as careful grounding [67].

However, the system itself generates noise, such as thermal noise. Considering that the external interference is eliminated, the resolution of the system is limited only by its own components. Op-amps, resistors and other electronic components have noise sources associated. A good circuit design considers these factors.

2.2.7.1 Noise Types

There are 3 major noise types: thermal noise; shot noise; and flicker noise.

Thermal noise is present in every conductive material, above 0K , and is a product of the randomly moving charges. It is common sense that in order for a current to flow, a voltage potential should be applied to the conductive material. However, it may seem strange that, for example, a resistor has a non-zero instantaneous current value, even when a voltage is not present. Since electrical current is defined as the rate of charge, then the movement of charged particles due to temperature alone can result in an electrical current. However, the average current is zero, and the noise power spectral density is uniform, which is given by:

$$P_{\mathrm{n}} = kTB, \tag{2.27}$$

where k is the Boltzmann's constant, T is the absolute temperature (in Kelvin) and B is the noise bandwidth. The noise in a resistor can be modeled by a Thevenin or Norton equivalent circuit. The noise voltage source, e_{nv}, and current noise source ,e_{ni}, are obtained from Equation 2.27, and are given by:

$$\begin{cases} e_{\mathrm{nv}} = \sqrt{4kTRB} \\ e_{\mathrm{ni}} = \sqrt{\frac{4kTB}{R}} \end{cases}, \tag{2.28}$$

where R is the real part of the impedance of the conductive material. The latter equation proves that the reactive part of the impedance does not contribute with noise, however, the ESR of a capacitor contributes to the real part of the impedance, for example. In Figure 2.16, the equivalent resistor model including noise, is presented.

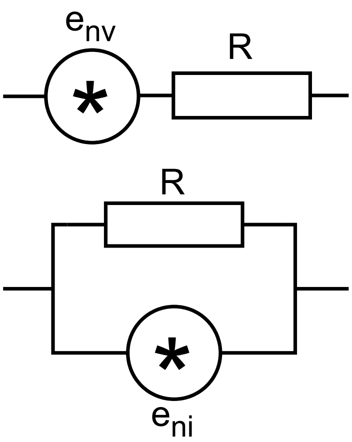

Figure 2.16: Resistor noise model.

Apart from thermal noise, flicker noise is also present in electronic circuits and devices. Due to its Power Spectral Density (PSD), flicker noise is also denominated by a $\frac{1}{f}$ noise and is mostly due to the impurities and imperfections of semiconductor devices, due to the charge redistribution and recombination in the surfaces of the materials. Moreover, as the name implies, its PSD is dominant for low frequencies and increases to infinity as frequency tends to zero. Thus, the noise in a specific frequency band, starting in $\mathrm{f_l}$ and ending in $\mathrm{f_h}$, is given by:

$$N_{\mathrm{f}} = A \ln \frac{f_{\mathrm{h}}}{f_{\mathrm{l}}}, \tag{2.29}$$

where $\mathrm{N_f}$ is the noise power (in Watt), $\mathrm{f_h}$ and $\mathrm{f_l}$ are the upper and lower frequency bounds, and A is a constant (in Watt).

It is also interesting to note that some resistor technologies feature significant flicker noise, in addition to the thermal noise. For example, wire-wound resistors have very little flicker noise, but film resistors and carbon-composed resistors feature high flicker noise, due to the multi-material composition.

The current flow through a semiconductor material is characterized by randomness. This behavior can be seen as noise, and is typically denominated as shot noise, whose RMS current value is given by:

$$I_{\mathrm{sh}} = \sqrt{2qIB}, \tag{2.30}$$

where $\mathrm{I_{sh}}$ is the RMS current shot noise, q is the charge of the electron, I is the DC current, and B is the noise bandwidth. Typically, shot noise is prominent in potential barriers, such as PN-junctions, due to the change in conducting media. So, in a normal conductor, shot noise does not exist.

Unlike thermal noise, which is temperature dependent, and flicker noise, whose PSD decreases with frequency, shot noise is commonly dominant for high frequencies and low temperatures. In Figure 2.17, the power spectral density of flicker noise and shot noise is shown. It can be seen that, at a frequency f_i, the PSD of flicker noise equal the PSD of shot noise. For frequencies lower than f_i, flicker noise is dominant, while the opposite is true for shot noise.

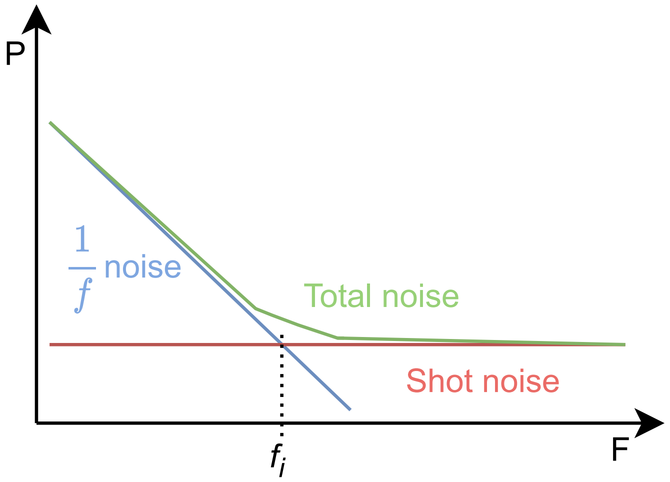

Figure 2.17: Noise spectral density (flicker noise and shot noise).

2.2.8 Filters

Filtering has become a ubiquitous process in signal processing, and is a process in which unwanted features from a given signal are removed or attenuated. For example, filtering is used to remove high frequency noise in numerous slow-moving biological signals, such as those from an electrocardiogram, while the low frequency information is kept unaltered.

The implementation of filters can be made in two forms [68]: analog; or digital. In the analog domain, filters can be implemented using passive components, such as resistors, capacitors, and inductors, in simple configurations, such as an RC, LC, or RL circuits, or active components, such as Op-amps. Furthermore, active analog filters provide advantages over a completely passive implementation, such as amplification and lower output-impedance.

On the other hand, digital filters can be implemented using digital circuit blocks, such as in dedicated DSP processors and FPGAs, or in software, using the filter transfer function. Digital implementations have become more practical, cheaper, more flexible, and more capable, in most applications. For that, two categories of digital filters exist: Infinite Impulse Response (IIR); and Finite Impulse Response (FIR).

Regarding the frequency response of a filter, the simpler topologies are the low-pass filter and the high-pass filter. An ideal low-pass filter is characterized by zero attenuation in the pass-band, and infinite attenuation in the stop-band, which correspond to the bands of frequencies that are below and above the intended cut-off point, respectively. Conversely, an ideal high-pass filter has the exact opposite frequency response. By combining low-pass and high-pass filters, band-pass and band-stop filters can be obtained. Additionally, more selective filters can be derived, such as notch-filters.

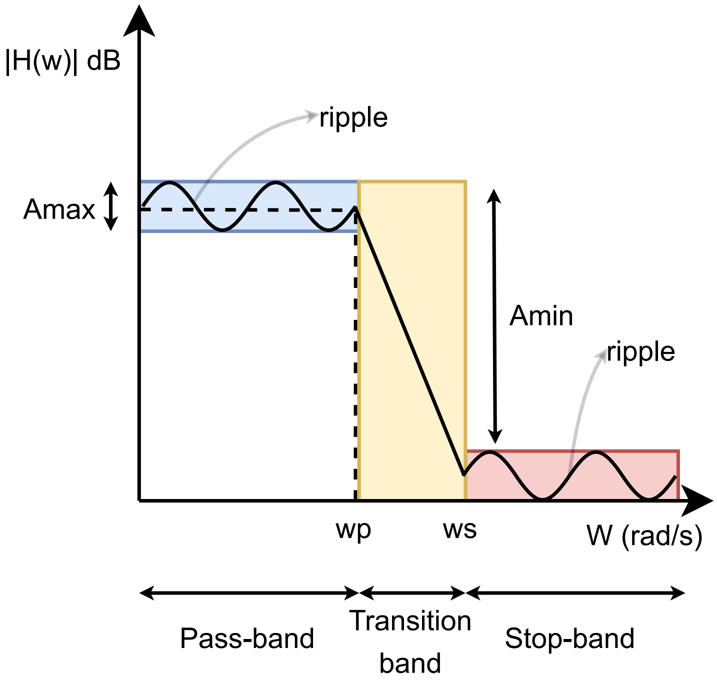

Figure 2.18: Generic low-pass filter frequency response. The ideal filter frequency response is represented in dashed lines.

To accurately characterize a filter, parameters such as, the cut-off frequency w_c, attenuation-rate, ripple, and filter order n, exists. The cut-off frequency defines the frequency at which the attenuation of the filter becomes out of the error band, which is commonly equivalent to the -3 dB level, for some filters. The attenuation of a filter quantifies the attenuation of the output signal as a function of frequency. Ripple describes a variation of the attenuation of the filter, either in the pass-band, or in the stop-band. In Figure 2.18, the frequency response of a generic low-pass filter is shown.

The order of the filter is directly related to the number of poles of the transfer function. Since each pole provides a 20 dB/decade attenuation, a higher order filter results in a higher steepness of the transition between the pass-band and stop-band regions.

2.2.8.1 Standard Filter Approximations

A number of different filter transfer functions are commonly used, each one having a unique frequency response behavior, as well as specific characteristics, such as linear phase response, or high attenuation rate for a given filter order.

One of the most used filter design approximations is the Butterworth filter [69], which is characterized by a monotonic frequency response and an attenuation proportional to n20 dB/decade, while providing a relatively large transition between the pass-band and stop-band. The transfer function of the Butterworth filter is given by:

$$|H(jw)| = \frac{1}{\sqrt{1 + \varepsilon^2 \left(\frac{w}{w_\text{c}}\right)^{2n}}}, \tag{2.31}$$

where w_c is the cut-off frequency (rad/s), n is the filter order, and ε is given by:

$$\varepsilon = \sqrt{10^{\frac{A_\text{max}}{10}} - 1}, \tag{2.32}$$

where A_max is the maximum attenuation in the pass-band region. The order of the filter can be obtained by an iterative process, by considering a specification for the minimum attenuation in the stop-band region, A_min, in which n is incremented in integer steps, so that $A(w_\text{s}) \geq A_\text{min}$ is met. For that:

$$10 \log_{10}\left(1 + \varepsilon^2 \left(\frac{w}{w_\text{c}}\right)^{2n}\right) \geq A_\text{min}. \tag{2.33}$$

Comparatively, the Chebyshev filter [69] features a sharper transition between the pass-band and stop-band, for the same filter order. However, this comes at the expense of ripple in the pass-band. The number of ripples in the pass-band region is equal to the filter order. Apart from this, the stop-band is monotonic, which means that it does not feature ripple. The transfer function of the Chebyshev filter is given by:

$$|H(jw)| = \frac{1}{\sqrt{1 + \varepsilon^2 \text{C}_\text{n}{}^2 \left(\frac{w}{w_\text{c}}\right)^{2n}}}, \tag{2.34}$$

where:

$$\begin{cases} C_0 = 1 \\ C_1 = \Omega \\ C_2 = 2\Omega^2 - 1 \\ C_3 = 4\Omega^3 - 3\Omega \\ C_\text{n} = 2\Omega C_\text{n-1}(\Omega) - C_\text{n-2}(\Omega) \end{cases}, \tag{2.35}$$

and $\Omega = \frac{w}{w_\text{p}}$. Considering the transfer function of the filter, the attenuation provided is $6(n-1)$ greater than the Butterworth filter. Furthermore, a variation of the Chebyshev approximation exists, the inverse Chebyshev [69], where the ripple appears in the stop-band, rather than in the pass-band, which could be beneficial in some applications. The inverse Chebyshev filter can be obtained from the regular Chebyshev filter by subtracting the filter response from unity and inverting the frequency values.

The elliptical filter approximation [69] is capable of providing a faster transition between the pass-band and stop-band than the previous ones. However, the downside is ripple in both the pass-band and stop-band, due to the addition of zeros in the transfer function. As with the Chebyshev filter, the poles of the transfer function are placed in an ellipse, which results in a similar time response, which often includes ringing. On the other hand, Bessel filters provide the most accurate time response, due to their linear phase response.

2.2.8.2 Digital IIR Filters

An IIR filter is recursive by nature, and its associated difference equation is a function of the current input signal, as well as the past input and output signals, as suggested by:

$$y\left(n\right)=\sum_{k=0}^{q}b_{\mathrm{k}}x\left(n-k\right)-\sum_{k=1}^{p}a_{\mathrm{k}}y\left(n-k\right), \tag{2.36}$$

where x and y are the input and output of the filter, respectively, $\mathrm{a_k}$ and $\mathrm{b_k}$ are coefficients, and p and k are the number of poles and zeros, respectively.

From the definition of an IIR filter, it is possible to observe that the poles affect the output variable. Thus, to ensure the stability of the filter, the poles should be within the unit circle. On the other hand, the zeros do not affect stability. When an impulse is applied to the filter, its output is infinite, hence the name. However, due to their nature, the implementation of such filter does not require much computational power, which is a clear advantage considering a microcontroller-based implementation.

The most common IIR filter design technique is based on the design of an analog prototype filter. In this stage, the filter approximation is chosen, as well as the filter order, cut-off frequency, and other parameters. Then, the digital filter is obtained via a discretization of the analog filter. For that, different processes can be used, such as the bilinear transformation. More specifically, the discretization of the analog filter can be described as:

$$H_{\mathrm{a}}(s)\longrightarrow H_{\mathrm{d}}(z), \tag{2.37}$$

where $\mathrm{H_a}$ and $\mathrm{H_d}$ correspond to the transfer function of the analog and digital filters, respectively. The bilinear transformation is used to convert the left s-domain semi-plane to the z-domain unity circle, which is mathematically described by:

$$H_{\mathrm{d}}\left(z\right)=H_{\mathrm{d}}\left(s=\frac{2}{T}\frac{1-z^{-1}}{1+z^{-1}}\right). \tag{2.38}$$

However, the mapping between the analog and digital frequencies is not linear, and their relation is given by:

$$w_{\mathrm{d}}=\frac{2}{T}\arctan\left(\frac{w_{\mathrm{a}}T}{2}\right). \tag{2.39}$$

.

Thus, to eliminate the frequency warping created by the bilinear transformation, a preliminary pre-warping transformation is required. This way, to obtain a correct mapping of the frequencies of the digital filter, the bilinear transformation with pre-warping is applied, which is given by:

$$H_{\mathrm{d}}\left(z\right) = H_{\mathrm{d}}\left(s = \frac{1}{\tan\left(\frac{w_{\mathrm{d}}T}{2}\right)}\frac{1-z^{-1}}{1+z^{-1}}\right). \tag{2.40}$$

Alternatively, the pre-warping process can be made before the bilinear transformation, in which case, Equation 2.38 is used. After this process, the transfer function of the digital filter, $H_{\mathrm{d}}(z)$ is obtained, whose difference equation can be derived and used for a software implementation.

2.2.8.3 Digital FIR Filters

Unlike IIR filters, FIR filters are non-recursive, meaning that there is no feedback from the output to the input of the filter, as given by:

$$y\left(n\right) = \sum_{k=0}^{M} b_{\mathrm{k}} x\left(n-k\right), \tag{2.41}$$

where M is the length of the filter. In addition, by analyzing the filter transfer function, it is possible to observe the lack of poles. The latter property of FIR filters guarantee stability, which is a clear advantage over an IIR filter. Another major advantage over an IIR filter is the linear phase response. As the name implies, the impulse response of an FIR filter is finite, which is also a consequence of the non-feedback architecture.

To design an FIR filter, the ideal filter transfer function is obtained. For example, an ideal low-pass filter transfer function is given by:

$$H_{lp}(w) = \begin{cases} 1 & \text{if } |w| \leq w_c \\ 0 & \text{if } otherwise \end{cases}. \tag{2.42}$$

The impulse response of such ideal filter is obtained by calculating the inverse discrete-time Fourier transform, and is given by:

$$h_d\left[n\right] = \frac{1}{2\pi}\int_{-\pi}^{+\pi} H_{lp}(w)e^{jwn}dw = \frac{sin\left(\pi n\right)}{\pi n}, \tag{2.43}$$

however, the impulse response is infinite and non-causal. Thus, the impulse response of the ideal filter has to be truncated. A better approach than truncation is based on the windowing method, where a window function is used. Window functions are finite in time, thus by multiplying the impulse response of the filter by a window function, a finite impulse response filter is obtained, as given by:

$$h_w(n) = w(n)\,h(n)\,. \tag{2.44}$$

Different window functions can be used to satisfy the requirements of the specific filter. The frequency response of the resulting filter can be obtained by the convolution of the window function and the ideal filter frequency response. The window function is directly related to the response of the filter, and the most commonly used are the rectangular, Bartlett, Hanning, Hamming and Blackman. The different characteristics of each window function are summarized in Table 2.2.

Window Function	Main Lobe Width	Minimum Stop-band Attenuation
Rectangular	$\frac{4\pi}{M+1}$	21 dB
Bartlett	$\frac{8\pi}{M}$	25 dB
Hanning	$\frac{8\pi}{M}$	44 dB
Hamming	$\frac{8\pi}{M}$	53 dB
Blackman	$\frac{12\pi}{M}$	74 dB

Table 2.2: Characteristics of different window functions. M represents the number of coefficients of the FIR filter.

The selection of the window function is based on the required stop-band attenuation. With the main lobe width of the selected window function, the required filter length, M can be calculated. The filter order is $N = M + 1$. At this point, the coefficients of the window and the ideal filter can be calculated using software such as Matlab, or Python, which considerably decreases the complexity of the design. The result of the windowing method is a usable FIR filter.

3

INNOVATIVE IONOGEL SENSORS

In this section, the ionogel sensor, briefly presented in subsection 2.1.2, is studied, including its construction, working principle, and sensing capabilities. Moreover, a detailed characterization of the sensor, based on multiple frequency response acquisitions, is made in two steps: the response of the sensor to RH; and the response of the sensor to different analytes.

Firstly, an array of sensors with different formulations is experimentally tested, under different RH conditions and without interaction with analyte. This study focuses on the impact of the RH level in the sensor impedance. For the second part, the array of sensors is tested with multiple analytes, while the RH is constant. In this case, the focus is placed on the impact of the different analytes in the frequency response. Thus, by applying the superposition theorem, a multi-variable characterization of the sensors as a function of analyte, sensor formulation and RH level, is obtained.

In addition, an equivalent electrical circuit model of the sensors is obtained, which is mandatory for the optimization of the AFE circuit, and enables a deeper understanding of the physical, chemical, and electrical processes involved in the sensor's operation.

3.1 Working Principle

As presented in subsection 2.1.2, a class of ionogel sensors, developed by the Biomolecular Engineering Laboratory, features interesting electrical properties, which originate from the presence of IL in the material. Such properties are modulated in the presence of VOC, or VOC mixtures, *e.g.* the impedance of the sensor changes when an interaction with an analyte occurs. An ionogel sensor is shown in Figure 3.1.

The construction of the ionogel sensor is based on a IDE structure, whose electrodes are coated in gold. A thin film of ionogel material acts as the sensitive element [70] and is spread on the electrodes. This configuration enables greater contact area between the sensing film and each electrode. When VOC molecules adsorb to the ionogel its conductivity changes, resulting in an impedance variation of the sensor.

Due to the capacitive nature of the IDE structure, an AC signal applied to the electrodes

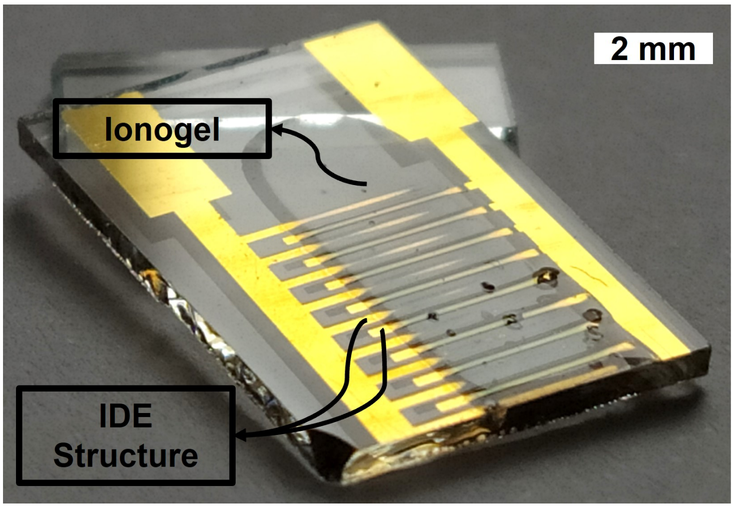

Figure 3.1: Ionogel sensor.

is required to measure the impedance of the sensor [14, 71]. Such AC signal creates an alternating electrical field which penetrates the sensing material, creating a displacement current through it. The properties of the AC signal are closely related to the sensitivity of the ionogel material to VOC, as well as to RH. Typically, the potential applied to the sensor is a sub-1V sinusoidal wave, to avoid electrolysis. For example, in the case of the Electrical E-nose V2, described in subsubsection 2.1.4.1, the sensor drive signal is a 100mV 2 kHz sine-wave.

One characteristic of the ionogel sensors is the negative impact of environmental conditions, such as the RH. Variations in RH result in variations of the water content of the sensor, culminating in a variation of the conductivity of the material. Thus, the impedance of the sensor is changed. However, this impedance variation superimposes the impedance change due to the response of the sensor to an analyte, which impacts the accuracy of the sensor [20, 21].

One strategy to control the influence of RH in the sensors signal is to rationally tune the composition of the sensing material [15]. Alternatively, an optimization can be made by characterizing the sensor's properties under different RH conditions and using that information to compensate for the parasitic signal. Another alternative is to optimize the sensor drive signal properties, such as frequency, to change its operating point, and thus, manipulate its sensitivity to RH.

3.2 The Impact of Relative Humidity in the Ionogel Sensor

3.2.1 Sensor Formulations

In this work, 8 different ionogels were studied, each one with a distinct formulation, as presented in Table 3.1. Sensor #1 to sensor #6 are composed by gelatin, IL and water. The IL is one of the 1-alkyl-3-methylimidazolium chloride family ($C_n$mimCl). Sensor #7 is composed of gelatin, the IL 1-butyl-3-methylimidazolium, and water. Finally, Sensor #8 is composed by a tripeptide, the IL choline phosphate, and water.

Sensor index	Ionic liquid name	No. of carbons in the IL alkyl chain
1	C_2mimCl	2
2	C_4mimCl	4
3	C_6mimCl	6
4	C_8mimCl	8
5	C_{10}mimCl	10
6	C_{12}mimCl	12
7	C_4mimDCA	4
8	Choline Phosphate	—

Table 3.1: Sensor formulations used.

3.2.2 Experimental Setup

The goal of this experiment is to expose the 8 different ionogel sensor formulations to multiple RH levels. A frequency response acquisition is made for each sensor and RH level combination. To obtain a reasonable resolution, a total of 9 discrete RH levels were considered, between 0% and 80%. In addition, a range of frequencies between 10 Hz and 100 MHz is targeted. The temperature is stabilized at 22 ± 1°C.

Sensors from 3 distinct production batches were tested, in 3 different days, in the course of a month, a week after their manufacturing. Duplicates of the same sensor formulation were used, for redundancy purposes. Thus, a total of 48 individual sensors were produced and tested. To avoid hysteresis, for each test run, consisting of the testing of 8 formulations for a RH sweep, two parts are considered: in the first part, the RH level is varied from 0% to 80%; in the second part, the RH level is varied from 80% to 0%.

Since each of the 48 sensors is tested for 9 discrete RH levels, and each test run consists of 2 parts, a total of 864 individual frequency response acquisitions were made. As a matter of fact, the total time required to perform the entirety of the experiment is superior to 24 hours. The experimental setup used for this experiment is presented in Figure 3.2, and photos are shown in Figure 3.3.

The goal of the setup was to generate a controlled humidity atmosphere inside the sensor's chamber. For that, a nitrogen bottle is connected to two Mass-Flow Controllers (MFCs). The MFCs enable control over the flow of nitrogen between two paths: dry path; and wet path.

The dry path consists of 100% nitrogen, which is at 0% RH. For the other path, the controlled nitrogen flow stream is used to bubble distilled water inside a flask. This bubbling process generates a humid headspace inside the flask, which is proportional to the flow of nitrogen, and can vary from 0% RH to 100% RH, in ideal conditions.

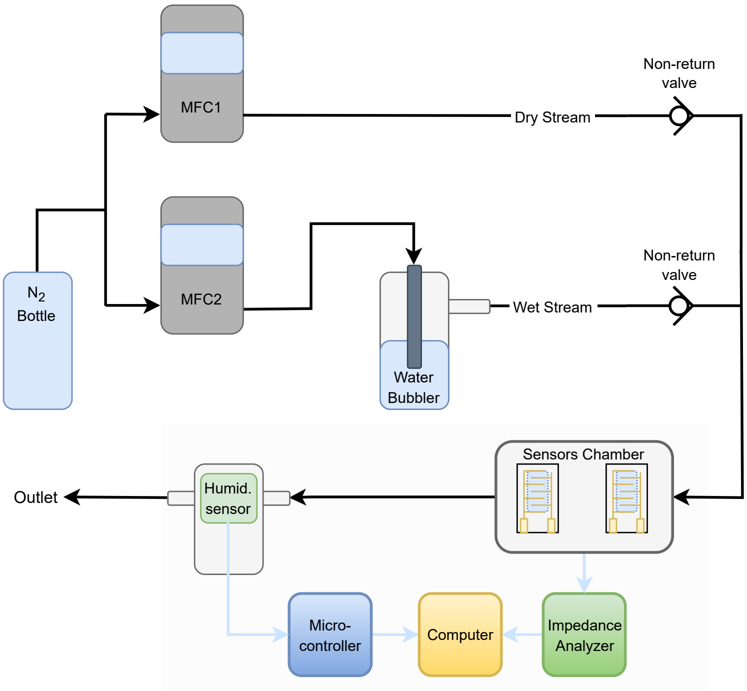

Figure 3.2: Simplified diagram of experimental setup.

After flowing through a non-return valve, the two flows, or streams, are combined and channelized to the sensor chamber. In the chamber, a total of 12 sensors are placed, which are exposed to the resulting atmosphere.

At the outlet of the chamber, a humidity sensor (HTU21D-F [72]) is used to measure the RH, which is connected to an Arduino DUE microcontroller [45]. Moreover, the MFCs are controlled via USB, and the entire system is controlled via a custom Python software.

The Python software receives information of the RH sensor and adjusts the individual MFCs' flow-rate to match the RH in the chamber to the target RH level. This target can either be set by the user, or the entire RH sweep is made automatically. In Figure 3.4, the flow-rates of the top (dry path) and bottom (wet path) MFCs as a function of the RH level created, are presented.

To obtain an RH level below 30%, the dry MFC flow-rate is set constant, while the wet MFC flow-rate is increased. For higher RH levels, the wet MFC flow-rate is set constant and the dry MFC flow-rate is decreased. It is important to note that this procedure may change depending on the ambient RH level.

For the frequency response acquisition, a calibrated impedance analyzer is used (Digilent Analog Discovery 2 [73]). However, this analyzer features a single input, and since there are 12 sensors in the chamber, a relay system is used to connect each sensor to the device, at a time. The control of the relays is made with the Python software and can either be automatic of manually done by the user.

Thus, this setup can automatically control the RH level, perform a frequency response acquisition for a given sensor, and store the resulting data. Furthermore, to process and

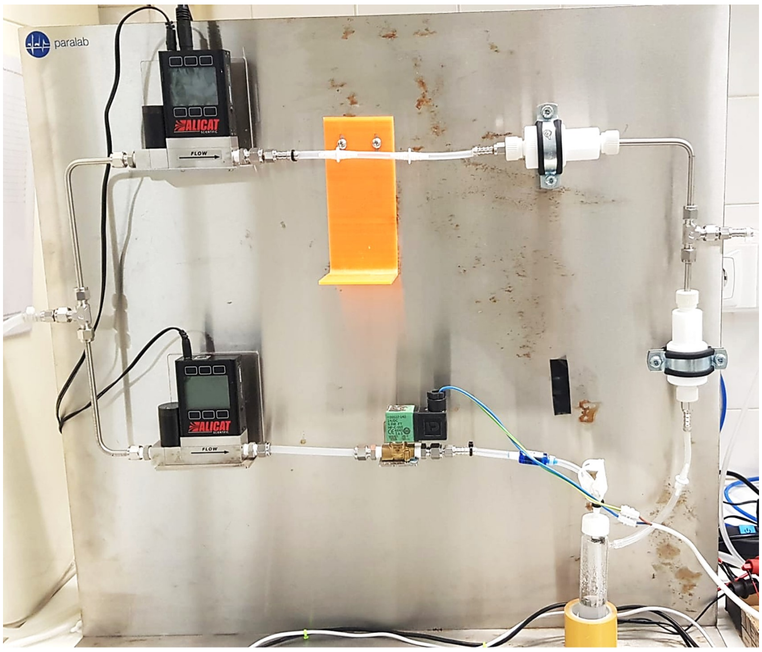

(a) MFCs, valves and water bubbler.

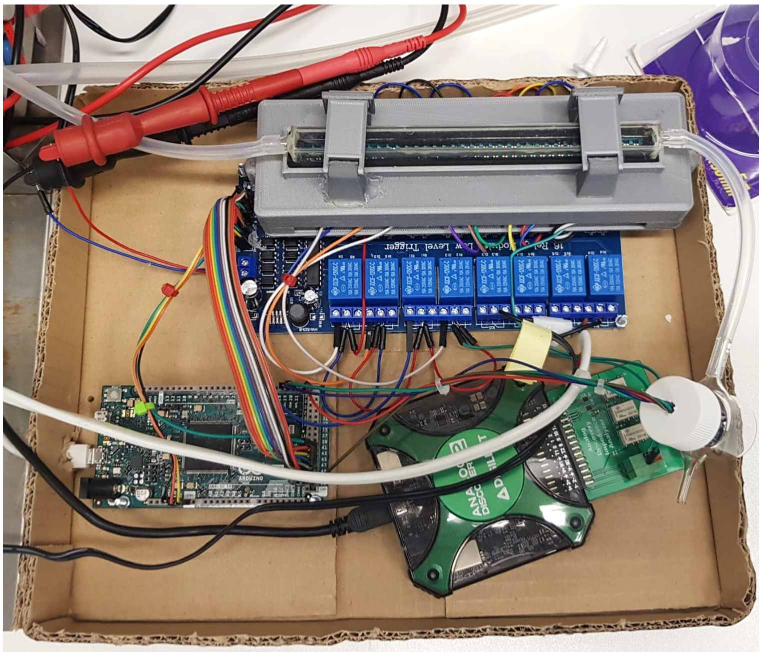

(b) Sensor chamber, relay circuit, RH sensor, microcontroller and impedance analyzer.

Figure 3.3: Experimental setup used in RH tests.

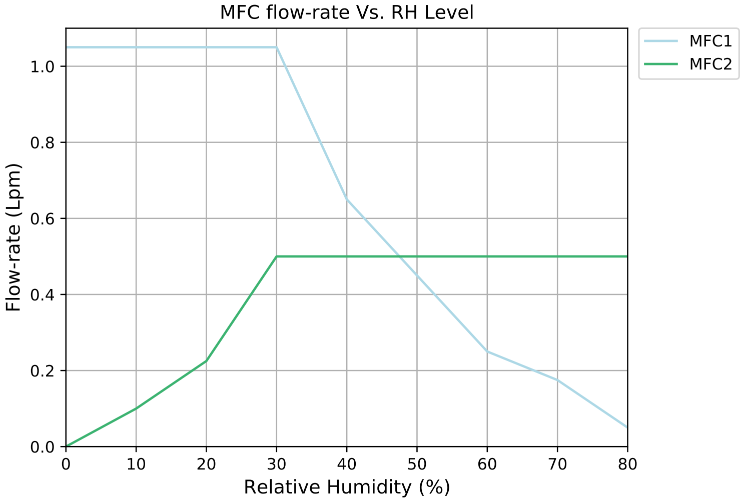

Figure 3.4: MFC flow-rate as a function of generated RH level.

visualize the data, another Python software was created. This software performs noise reduction on the signals and creates different plots, which can be the frequency response as a function of RH, or others such as the impact of the RH for a specific sensor, at a given frequency.

3.2.3 Frequency Response as a Function of RH

Considering the experimental setup and procedure described previously, after the 864 individual acquisitions were obtained, a custom Python software was used to process the data.

Firstly, for a given RH level and sensor formulation, the averages of the signals from the multiple test runs were made, corresponding to 6 frequency response acquisitions. This way, each sensor formulation has a frequency response curve, for a given RH level. To simplify the document, the plots not shown in this subsection are presented in Figure A.1 to Figure A.4. The frequency response of sensor #1, as a function of RH is presented in Figure 3.5.

This sensor formulation presents a low-frequency impedance between 10 kΩ and 20 kΩ , for the complete RH range. As the frequency increases, the impedance decreases. However, a stable plateau is observed for frequencies between 10 kHz and 1 MHz, where the impedance is highly dependent on the RH level. More specifically, the impedance varies between 50 Ω and 2 kΩ .

The phase response reveals useful information. It is possible to conclude that there is a low frequency pole since the phase tends to a value close to -90° for frequencies lower than 10 Hz. Then, the effect of a zero can be observed, between 100 Hz and 10 kHz since the phase increases to 0°. The frequency of the zero is directly proportional to the RH level, meaning that increasing the RH increases the frequency of the zero.

At a frequency of 100 kHz, and independently of the RH level, the phase has a value

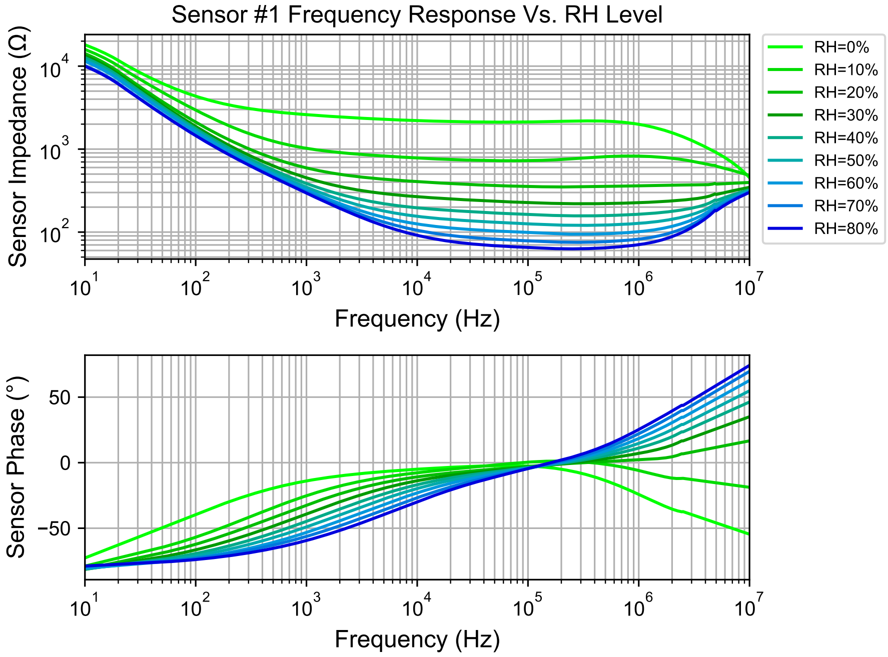

Figure 3.5: Frequency response of sensor #1 as a function of RH.

of 0°. At this frequency the sensor can be approximated by a resistor. For frequencies higher than 100 kHz and depending on the RH level, the effect of a pole or a zero can be observed. More specifically, for RH levels under 20% a pole exists, however this pole turns into a zero for RH levels equal or greater than 20%. This fact can also be observed in the amplitude plot. In Figure 3.6 the frequency response of sensor #6 is presented.

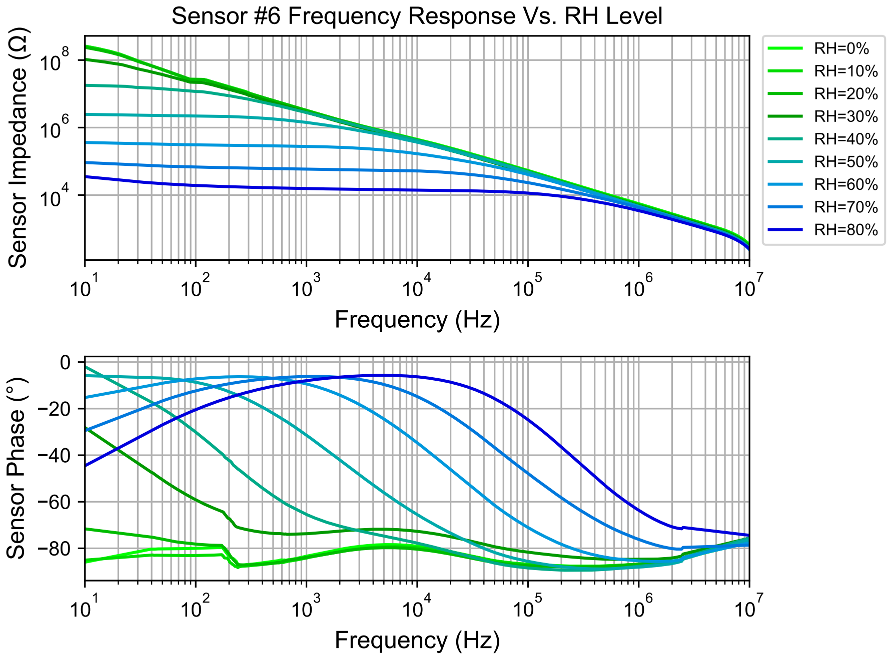

Figure 3.6: Frequency response of sensor #6 as a function of RH.

By increasing the number of carbons of the IL cation molecule, *i.e.* going from sensor #1 to sensor #6, it is possible to observe that the overall impedance level increases. For example, sensor #2 presents an impedance of 70 kΩ at a frequency of 10 Hz and an RH of 0%, while sensor #4 presents an impedance of 2 MΩ and sensor #6 presents an impedance greater than 100 MΩ in the same conditions.

Apart from the low frequency impedance being 4 orders of magnitude higher than that of sensor #1, sensor #6 presents an exponential relation between the impedance and the RH level. More specifically, decreasing the RH linearly creates an exponential increase in impedance.

The phase response shows that increasing the RH level creates a shift of the frequencies of poles and zeros to higher frequencies. Unlike sensor #2, there is not a single frequency at which the phase is 0°. However, considering a broad frequency range between 10 Hz and 10 kHz, the phase approaches a value near -5°, where the sensor could also be approximated by a resistor.

Considering Table 3.1, it is interesting to compare the impact of RH in sensor #2 and sensor #7, since their formulation only differs in the anions of the IL, which are $[Cl]^-$ and $[DCA]^-$, respectively. The frequency response plots of these two sensors are presented in Figure 3.7 and Figure 3.8.

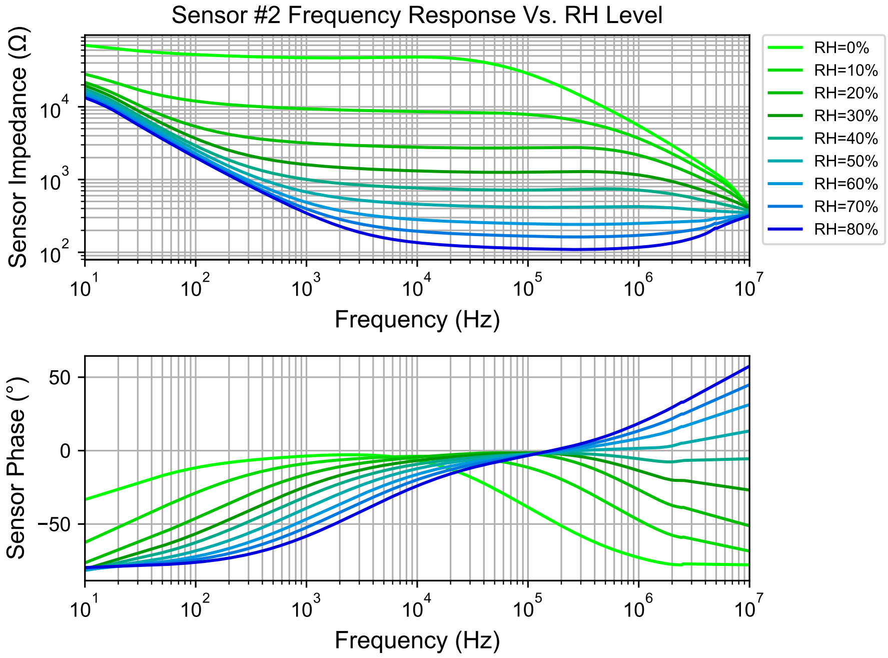

Figure 3.7: Frequency response of sensor #2 as a function of RH.

By inspection, it is clear that the two previously mentioned sensors present considerably different responses to RH. More specifically, for low frequencies, sensor #7 presents little impedance dependence on RH, which means that for these frequencies, the sensor is approximately immune to RH. Similarly to sensor #1, there is a frequency range between 10 kHz and 1 MHz where the impedance remains constant and is considerably dependent

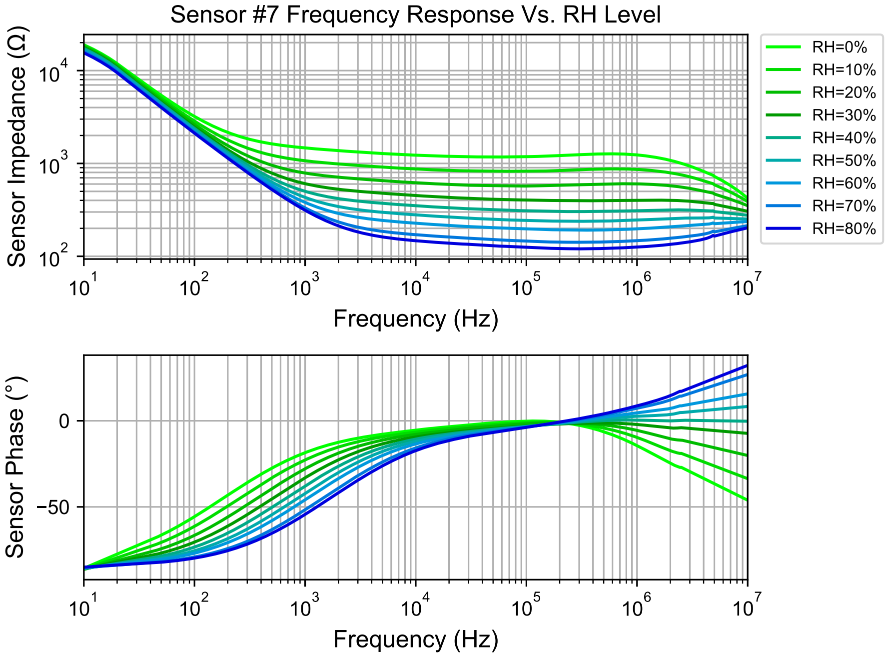

Figure 3.8: Frequency response of sensor #7 as a function of RH.

on RH. In this region, the sensor has an impedance between 150 Ω and 1.5 kΩ , for a RH of 80% and 0%, respectively. Also, for RH levels greater than 20%, a pole turns into a zero, and the phase has a value close to 0° at 100 kHz.

Even though the impedance of sensor #2 for lower RH levels is considerably higher, for RH levels greater than 20%, the two sensors present an equivalent impedance response. However, sensor #2 is notably more dependent on RH level. The phase response is quite similar, however for sensor #2 it is more dependent on RH level. Thus, it is correct to conclude that sensor #7 is less sensitive to RH than sensor #2, which goes accordingly to the conclusion presented by Esteves *et al.* in [15].

3.2.4 Equivalent Electrical Circuit Model

Considering the results previously mentioned, an equivalent electrical circuit model of the ionogel sensor was created [71, 74] and is shown in Figure 3.9.

The model presented describes an equivalent frequency response to that presented by the ionogel sensor. The circuit is constituted by the parallel of two impedances, one of which is a pure capacitance, and the other the series of two capacitances and a resistance. Apart from R_{sensor}, which describes the effective resistance of the ionogel material, the other components describe the parasitics of the sensor construction, such as the capacitance of the IDE structure and the capacitance between the ionogel material and the electrodes.

In Figure 3.9b, the leakage current that flows across the sensor is also modeled, which has an impact on the low frequency response of the sensor. Considering the simplified model, depicted in Figure 3.9a, the impedance of the sensor is given by:

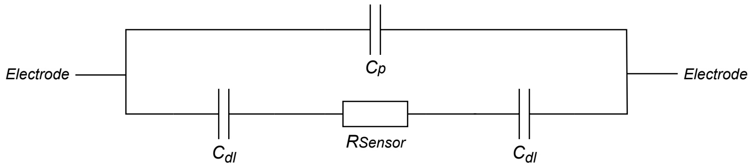

(a) Simplified model.

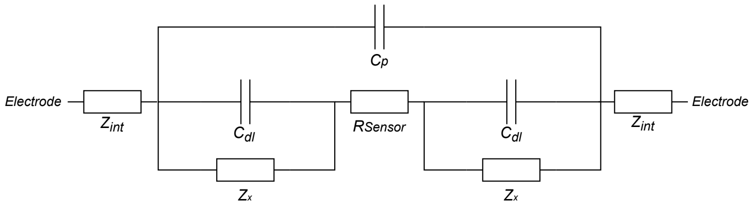

(b) Model including leakage.

Figure 3.9: Equivalent electrical circuit model of the ionogel sensor. C_{dl} represents the double-layer capacitance, R_{sensor} is the effective resistance of the sensing material, C_p represents the inter-electrode capacitance, Z_x represents the leakage across the sensor, and Z_{int} the impedance of the interface between the sensor and the measurement device.

$$Z(s) = \frac{s(R_{\text{sensor}}C_{\text{dl}}) + 1}{s^2(R_{\text{sensor}}C_{\text{p}}C_{\text{dl}}) + s(C_{\text{p}} + C_{\text{dl}})}. \tag{3.1}$$

From this equation, it can be concluded that the circuit has one zero and two poles. The zero is obtained at a frequency given by:

$$w_{\text{z}} = \frac{1}{R_{\text{sensor}}C_{\text{dl}}}[rad/s]. \tag{3.2}$$

One of the poles is a zero-frequency pole, and the non-zero-frequency pole is obtained at a frequency given by:

$$w_{\text{p}} = \frac{C_{\text{p}} + C_{\text{dl}}}{R_{\text{sensor}}C_{\text{dl}}C_{\text{p}}}[rad/s]. \tag{3.3}$$

Considering the behavior of the poles and zeros described in subsection 3.2.3, it is true that there is a very-low frequency pole, a zero, whose frequency is higher than the first pole, and a high-frequency pole. From the model, it is possible to confirm the existence of a zero-frequency pole, which corroborates the results. Also, there is a zero and another pole, at higher frequencies.

For high frequencies, the impedance of inter-electrode capacitance, C_p, decreases, which shunts the signal across the two electrodes. This is described by the pole in the frequency response, which occurs at high frequencies. On the other hand, the series of C_{dl} and R_{sensor} creates a zero in the frequency response. Thus, it is possible to estimate the relation between the values of C_{dl} and C_p. For that, 3.3 can be approximated by

$$w_{\text{p}} \approx \frac{1}{R_{\text{sensor}}}\frac{1}{C_{\text{eq}}}[rad/s], \tag{3.4}$$

where C_{eq} represents the equivalent series of capacitors C_p and C_{dl}, and is given by:

$$C_{\mathrm{eq}} = \frac{C_{\mathrm{dl}} C_{\mathrm{p}}}{C_{\mathrm{p}} + C_{\mathrm{dl}}}. \tag{3.5}$$

Assuming that $C_{\mathrm{dl}} \gg C_{\mathrm{p}}$, then $C_{\mathrm{eq}} \approx C_{\mathrm{p}}$. This way, the relation between $\mathrm{w_p}$ and $\mathrm{w_z}$, is approximately given by:

$$\frac{w_{\mathrm{z}}}{w_{\mathrm{p}}} \approx \frac{C_{\mathrm{p}}}{C_{\mathrm{dl}}}. \tag{3.6}$$

Since it is known that $w_{\mathrm{p}} > w_{\mathrm{z}}$, then it can be concluded that $\mathrm{C_{dl}} > C_{\mathrm{p}}$. This way, as the frequency increases from DC to tens of kHz, the impedance of $\mathrm{C_{dl}}$ decreases. Thus, the impedance of the sensor can be approximated by $\mathrm{R_{sensor}}$, which means that at a particular frequency, where the impedances of $\mathrm{C_{dl}}$ and $\mathrm{C_p}$ are low and high, respectively, the parasitics of the sensor construction do not contribute to the sensor response to RH. In these conditions, the phase should have a value close to 0°.

Considering the model presented in Figure 3.9b, the impedance of the sensor is given by:

$$Z(s) = \frac{Z1}{1 + sC_{\mathrm{p}}Z1} + 2Z_{\mathrm{int}}, \tag{3.7}$$

where:

$$Z1(s) = \frac{2Z_{\mathrm{x}}}{sZ_{\mathrm{x}}C_{\mathrm{dl}} + 1} + R_{\mathrm{sensor}}. \tag{3.8}$$

3.2.5 Model Fitting

To assess the quality of the equivalent electrical circuit model, the mathematical description presented in subsection 3.2.4 was used to create a software model. A curve fitting Python library was used to create a fitting for the 8 sensor formulations, for an RH range between 20% and 80%, and for frequencies between 10 Hz and 1 MHz.

The curve fitting enabled the calculation of the $\mathrm{R_{sensor}}$, $\mathrm{C_{dl}}$ and $\mathrm{C_p}$ parameters. It was possible to observe that the values of $\mathrm{C_{dl}}$, for a given formulation, remained relatively constant and independent on the RH level. On the other hand, the values of $\mathrm{C_p}$ varied according to the RH level. In Table 3.2, the maximum and minimum values of $\mathrm{R_{sensor}}$, the average of $\mathrm{C_{dl}}$, and the maximum value of $\mathrm{C_p}$, in the considered RH range, are presented for each sensor formulation.

From the previous table, it is possible to conclude that, considering all sensor formulations, the values for $\mathrm{C_{dl}}$ range between 750nF and 3μF, while the values for $\mathrm{C_p}$ typically are under 250pF. It is also important to note that, in the case of sensor #6, the software was not able to provide accurate values, and for sensor #1 and sensor #2, the values for $\mathrm{C_p}$ are given for a maximum RH level of 50%.

In Figure 3.10, the model fittings for sensor #4 and sensor #7 are presented. It is possible to see that the fittings are a considerably accurate representation of the sensors, for the

Sensor formulation	$\mathbf{R_{sensor,min}}$	$\mathbf{R_{sensor,max}}$	$\mathbf{C_{dl,avg}}$	$\mathbf{C_{p,max}}$
1	170 Ω	480 Ω	1.4μF	2nF
2	120 Ω	1.3 kΩ	970nF	135pF
3	230 Ω	3.8 kΩ	1.2μF	100pF
4	550 Ω	50 kΩ	2.8μF	100pF
5	580 Ω	160 kΩ	3μF	52pF
6	10 kΩ	—	—	39pF
7	83 Ω	326 Ω	1.3μF	240pF
8	460 kΩ	1.92 MΩ	780nF	430pF

Table 3.2: Equivalent circuit model parameters.

different RH levels, even though the frequency responses are considerably different. This result proves that the proposed model is a good representation of the sensors. However, the fitting for some sensors, such as sensor #1 and sensor #2, for RH values greater than 50% present significant error.

3.2.6 Effective Ionogel Sensor Resistance as a Function of RH

As previously mentioned, the sensitive element of the ionogel sensor, R_{sensor}, is resistive. In addition, at a given frequency, the impedances of the parasitic capacitances can be neglected, in which case the impedance of the sensor is approximated by R_{sensor}. This way, the impact of the RH can more directly be studied. However, in many cases, there is not a unique frequency where this is possible. For that, Table 3.3 contains the frequency or frequencies where the phase nears 0°.

Sensor Formulation	Lowest frequency	Highest frequency
1	—	100 kHz
2	20 kHz	100 kHz
3	10 kHz	100 kHz
4	1 kHz	50 kHz
5	200 Hz	20 kHz
6	100 Hz	2 kHz
7	—	100 kHz
8	1 kHz	100 kHz

Table 3.3: Frequencies where the phase has a value close to 0°.

It is possible to conclude that a frequency range between 100 Hz and 100 kHz is necessary to measure the effective resistance of the ionogel material, for the group of ionogel sensors studied. From the various frequencies, the 100 kHz is the most effective frequency to isolate the R_{sensor} parameter, for the majority of the formulations. In Figure 3.11, the approximate resistance of the sensing material as a function of RH, for one of the frequencies presented in Table 3.3, is shown.

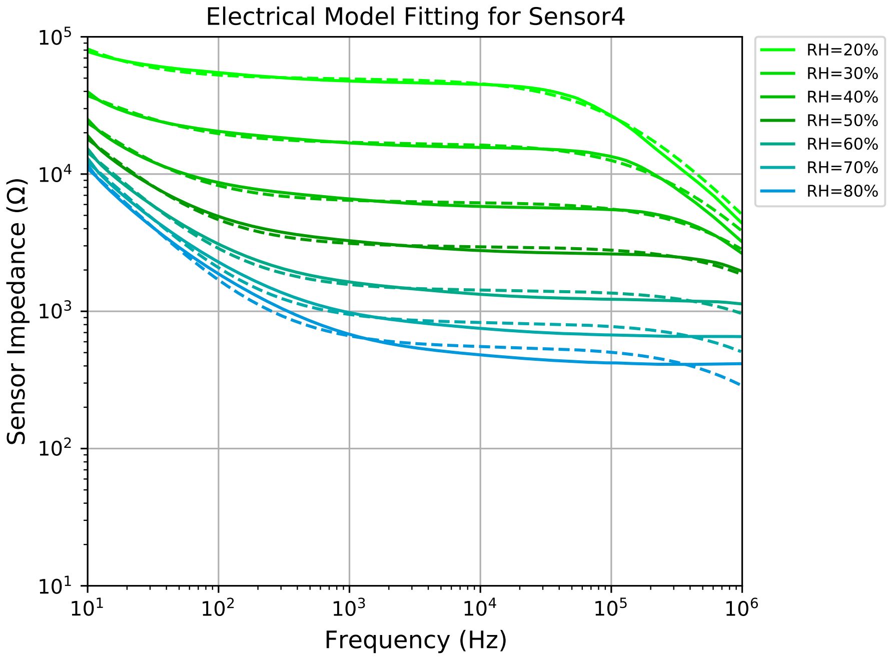

(a) Curve fitting for sensor #4.

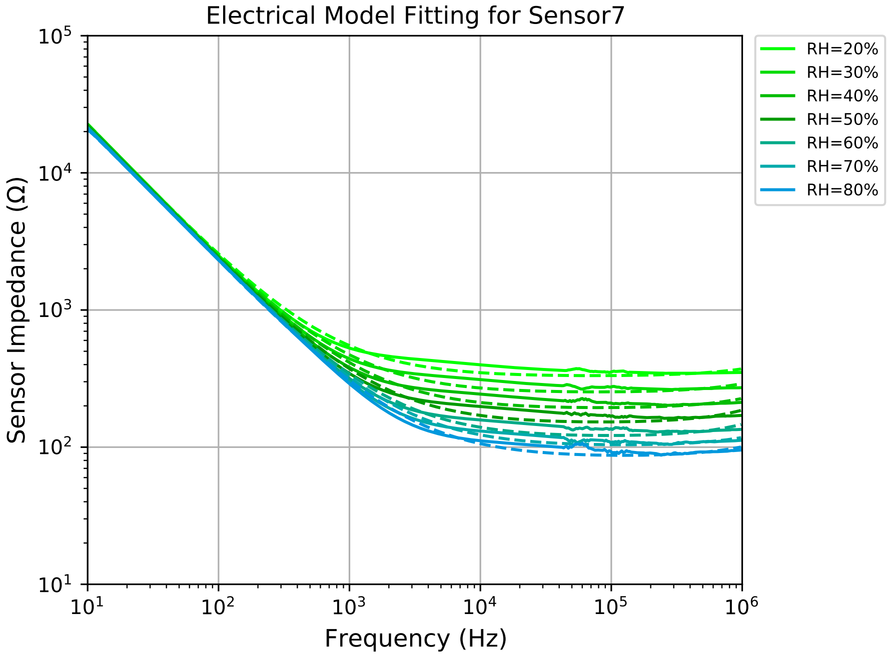

(b) Curve fitting for sensor #7.

Figure 3.10: Curve fittings obtained for sensor #4 (a) and sensor #7 (b). The acquired signals are represented using dashed lines, and the fittings are represented using solid lines.

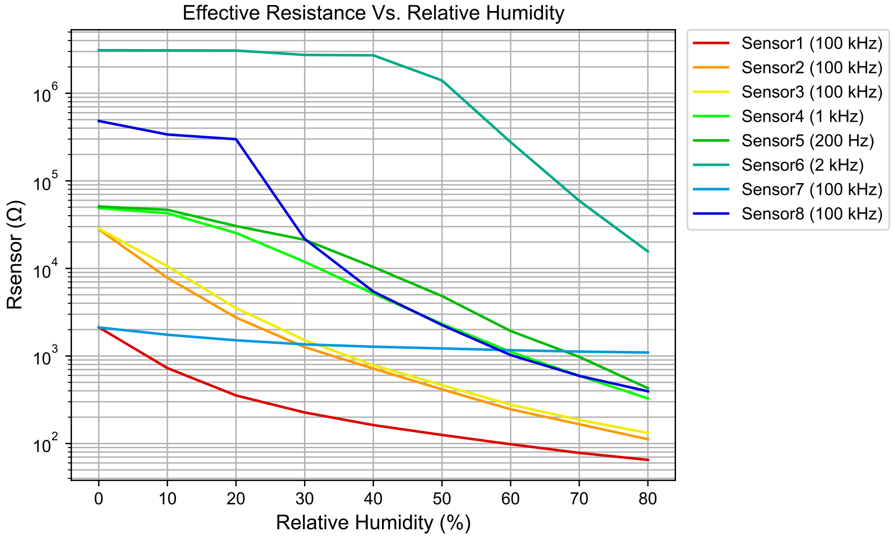

Figure 3.11: Approximate sensor resistance as a function of RH.

By inspecting Figure 3.11, the following conclusions can be obtained:

- Sensor #7 presents the least dependence on RH level. More specifically, for a RH range between 0% and 80%, the impedance ranges from 2115 Ω to 1095 Ω. On the other hand, sensor #8 is the most sensitive to RH, particularly for a RH range between 20% and 40%.

- The difference of the anion in the composition of sensor #2 and sensor #7, from $[Cl]^-$ to $[DCA]^-$, is apparent, as expected. This can be concluded by comparing the curves of sensor #2 and sensor #7. More specifically, the anion $[DCA]^-$ gives the sensor more immunity to RH.

- The results for sensor #1 to sensor #3 are similar in shape, and it is possible to observe that increasing the number of carbon atoms in the sensor formulation leads to an overall increase in impedance.

- Sensor #2 and sensor #3 present a highly similar response to RH, whose impedance drops from 28 kΩ to 130 Ω. Even though these two sensors only differ in two carbon atoms, from sensor #1 to sensor #2 and from sensor #3 to sensor #4 the impedance increases considerably more.

- The impedance of sensor #6, for a RH range between 0% and 40%, remains constant and approximately equal to 300 kΩ . However, for higher RH levels, the impedance decreases exponentially, and has a value close to 16 kΩ at a RH level of 80%. This result proves that this formulation is highly-hydrophilic, and its response to RH is considerably non-linear.

- Considering all the formulations except sensor #6, and an RH sweep between 20% and 80%, the impedance varies between 65 Ω and 300 kΩ , and the necessary frequency range is between 100 Hz and 100 kHz. If sensor #8 is also excluded, then the maximum impedance is limited at 50 kΩ .

3.2.7 Sensor Impedance as a Function of RH for a Frequency of 2kHz

In previous E-nose versions, the sensor drive frequency was fixed at 2 kHz. Due to this fact, it is important to study how the impedance of the sensor is affected by RH. For that, in Figure 3.12, the impedance of the various sensor formulations, as a function of RH, is presented.

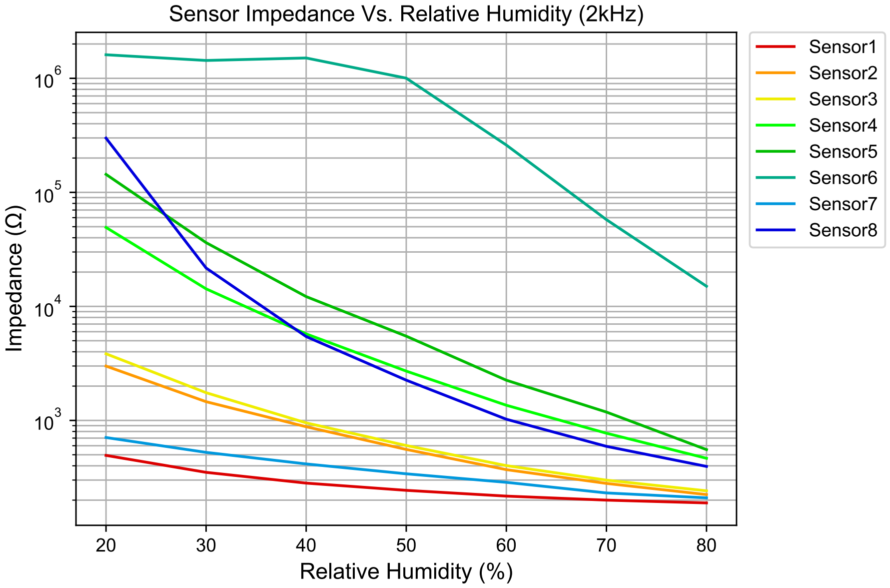

Figure 3.12: Sensor impedance as a function of RH, for a frequency of 2 kHz.

It can be concluded that the impedance ranges from 200 Ω to 1.5 MΩ , in an RH range between 20% and 80%. However, if sensor #6 is not considered, then the maximum impedance is approximately 200 kΩ .

3.3 The Response of the Ionogel Sensor to VOCs

3.3.1 Experimental Setup

To study the frequency response of the different sensor formulations to distinct analytes, or VOCs, a different experimental setup from the one presented in subsection 3.2.2, was used, and is shown in Figure 3.13.

In this setup, an automated delivery system was implemented, whose goal is to, alternately, deliver the VOC to the sensor detection chamber, and expose the sensors to ambient air. This alternate behaviour can be described by two phases, which are exposure and recovery, respectively.

VOC index	VOC name
1	Acetone
2	Ethanol
3	Acetonitrile
4	Ethyl Acetate
5	Hexane
6	Toluene
7	Dichloromethane

Table 3.4: List of VOCs used in the experiment.

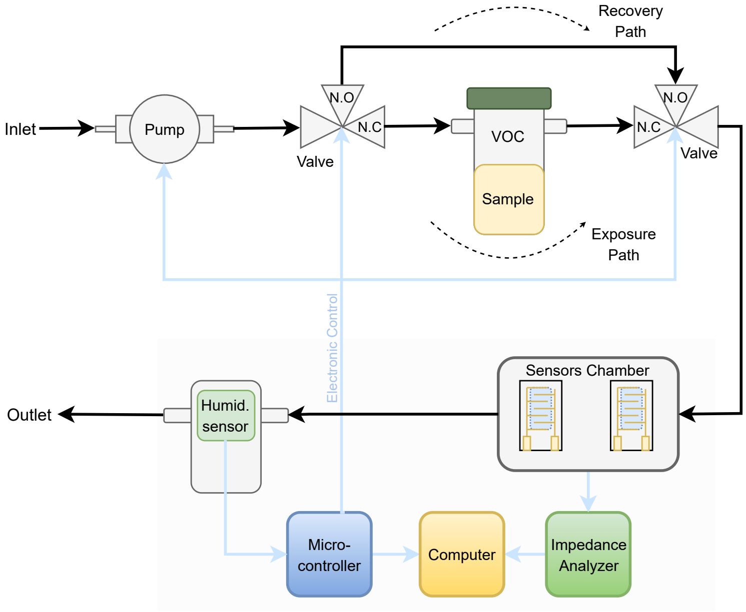

Figure 3.13: Simplified diagram of experimental setup used for the VOC experiments.

The eight sensor formulations presented in Table 3.1, and 7 distinct VOCs, presented in Table 3.4, were used. Three test runs were conducted, in different days, and using sensors from distinct production batches, which culminates in a total of 54 distinct sensors. Duplicates of each sensor were used, for redundancy.

For each test run, each individual sensor was, firstly, exposed to ambient air, which corresponds to a recovery phase. A frequency response acquisition is made, which sets the baseline for the sensor. Then, automatically after the recovery frequency response acquisition, the sensor is exposed to a given VOC, and another frequency response acquisition is made, which corresponds to the exposure phase. Thus, for each sensor/VOC combination, there are two acquisitions, each corresponding to a different phase, and the difference between the two responses corresponds to the sensor response to the particular VOC.

For the complete test run, the latter procedure was repeated for all the 16 sensors, corresponding to duplicates from each formulation. This method was reproduced for each VOC, which culminates in 756 individual acquisitions. The RH level remained approximately constant throughout the experiment, with a maximum variation of ±0.5%, and the sample was heated to a temperature of 37°C.

3.3.2 Frequency Response as a Function of VOC

As previously mentioned, two acquisitions were made for each sensor/VOC combination: recovery acquisition; and exposure acquisition.

The recovery acquisition sets the baseline frequency response, which corresponds to the normal and stable state of the sensor, at ambient air. To observe the impedance change of the sensor due to the response to a given VOC, the exposure acquisition is subtracted from the recovery acquisition.

In Figure 3.14, the recovery and exposure acquisitions for acetone are presented. It is possible to observe a variation between the exposure and recovery responses, which means that the interaction of this VOC with the different formulations culminate in an impedance change, or a response. In addition, the magnitude of the response is not equal for all formulations, as well as the response to a particular frequency.

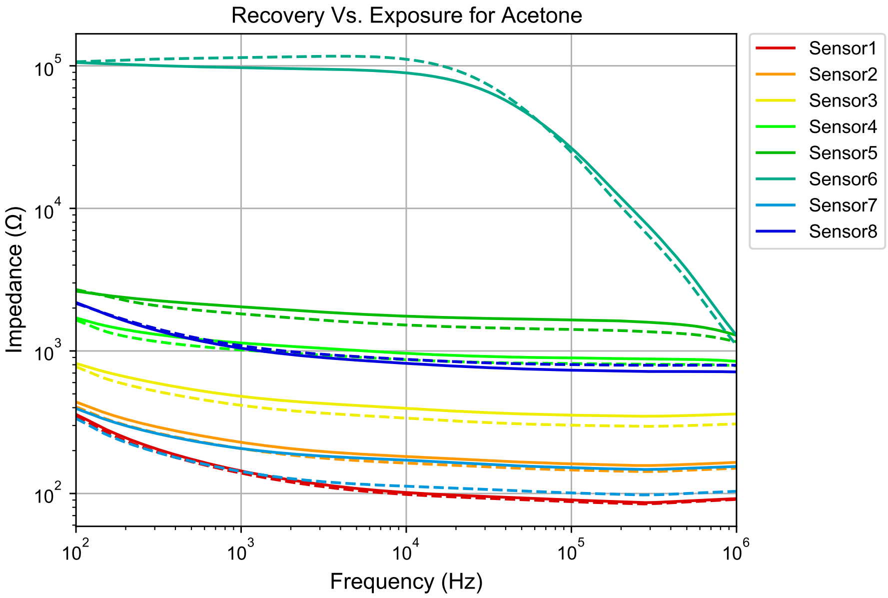

Figure 3.14: Frequency response of sensors to acetone. Dashed lines are used to represent the exposure phase acquisitions.

In Figure 3.15, the recovery and exposure acquisitions for ethanol are presented. This VOC provokes a considerably high response, for all sensor formulations, which is larger for sensor #6. In the case of this sensor, in the exposure acquisition, the impedance for low frequencies drops from the baseline, however, at approximately 200 kHz, the opposite is true.

To observe the impedance variation more accurately between the two phases, in Figure 3.16 the relative impedance variation, which is the difference between the impedance

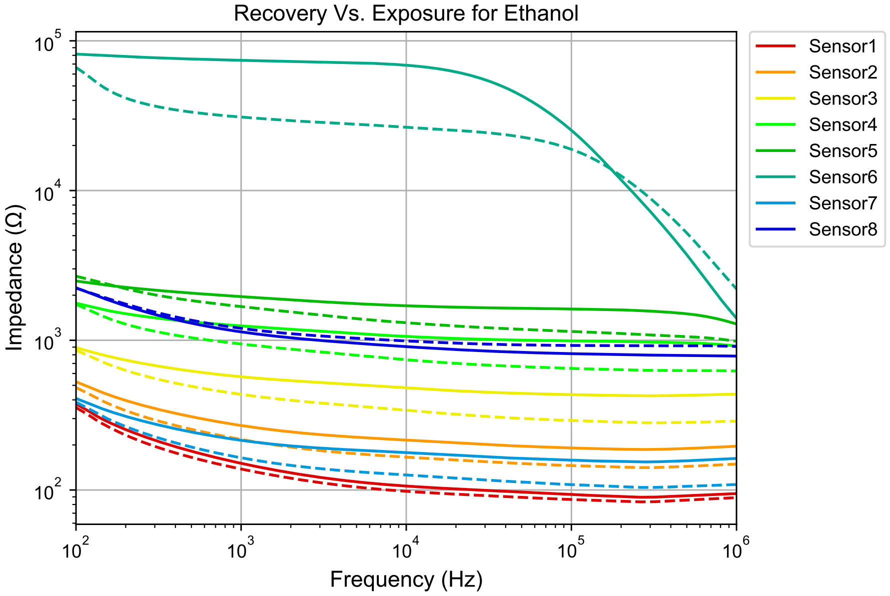

Figure 3.15: Frequency response of sensors to ethanol. Dashed lines are used to represent the exposure phase acquisitions.

of the sensor in the exposure and recovery acquisitions, is presented for acetone. It is possible to observe that for the majority of the sensor formulations, the impedance variation is negative, which means that the impedance decreases when the interaction with the VOC occurs. However, for sensor #5, sensor #7 and sensor #8, the frequency behavior is different.

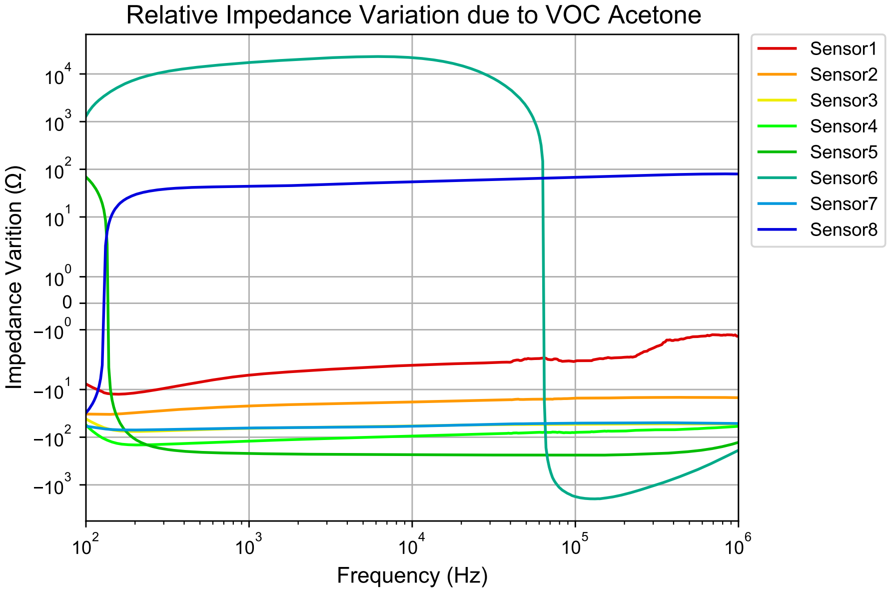

Figure 3.16: Impedance variation between recovery and exposure phases, for acetone.

More specifically, for sensor #5, the impedance variation is positive for frequencies under 100 Hz and remains approximately constant and equal to a negative value of 300 Ω .

For sensor #7, the opposite behavior to sensor #5 is observed. For sensor #6, the impedance variation is positive and has a maximum value of 20 kΩ , for frequencies under 60 kHz, above which the impedance variation rapidly decreases to a minimum negative value of 1 kΩ .

Likewise, in Figure 3.17, the difference between the exposure and recovery acquisitions is presented, for ethanol. As suggested by Figure 3.15, the magnitude of the impedance variation is greater for sensor #6, and the impedance decreases in the exposure phase, which is reinforced by a negative 42 kΩ variation, for frequencies under 200 kHz. Then, the impedance variation increases to a positive value of approximately 1 kΩ . Comparatively, it can be concluded that for some sensors the exposure to different VOCs can either lead to an increase or decrease in impedance.

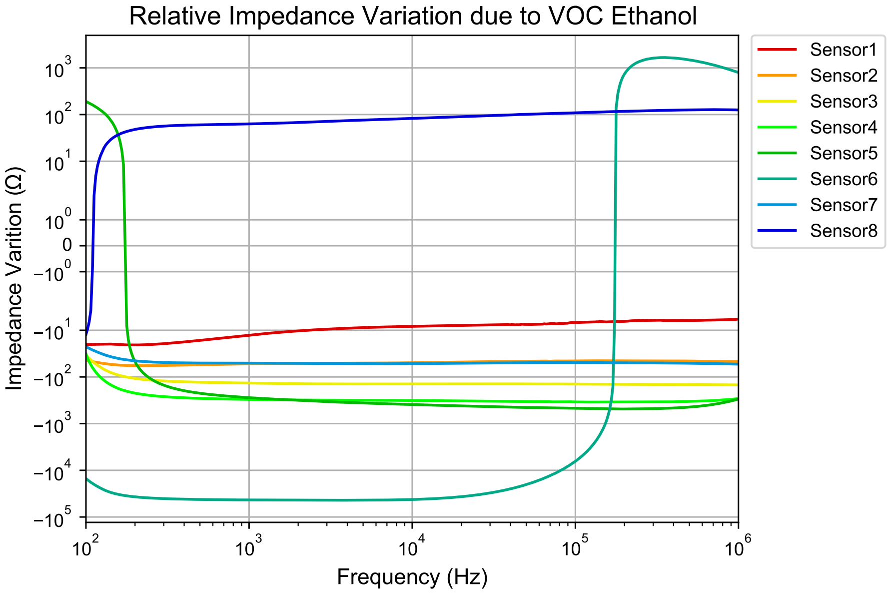

Figure 3.17: Impedance variation between recovery and exposure phases, for ethanol.

The affinity of a given sensor to a certain VOC can be estimated by calculating the relative response between the exposure and recovery acquisitions, as given by:

$$Z_{\text{relative}}(\%) = \frac{|Z_{\text{exposure}} - Z_{\text{recovery}}|}{Z_{\text{recovery}}} \times 100, \tag{3.9}$$

where Z_{exposure} and Z_{recovery} represent the impedance of the sensor in the exposure and recovery phases, respectively.

From the group of VOCs considered, it was possible to observe that the sensors present less affinity to toluene and hexane, and higher affinity to ethanol and acetonitrile [15]. This conclusion is supported by Figure 3.18, where the difference between the exposure and recovery acquisitions is presented, for hexane.

The impedance variation for sensor #1 and sensor #7 due to the interaction with hexane, is approximately constant and equal to a negative value of 10 Ω . Sensor #8 presents a

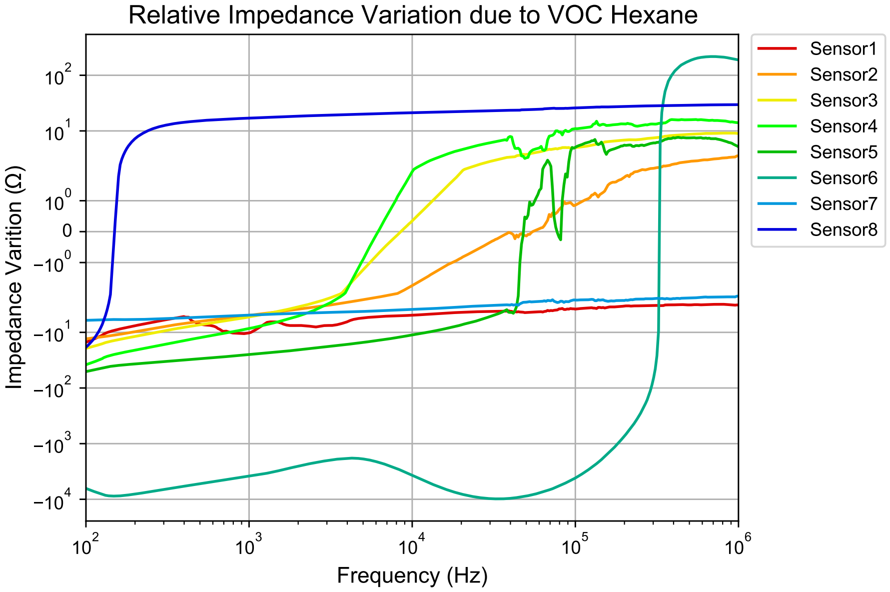

Figure 3.18: Impedance variation between recovery and exposure phases, for hexane.

negative impedance variation for frequencies below 150 Hz, above which the variation becomes approximately constant and equal to positive 10 Ω . For the remaining sensors, the variation is negative, up to a range of frequencies between 4 kHz and 40 kHz. Then, the impedance variation increases to a positive value close to 10 Ω . Lastly, for sensor #6, the impedance variation remains close to a negative value of 10 kΩ , up to approximately 300 kHz.

Regarding the affinity of the sensors to toluene, similar conclusions can be obtained by inspecting Figure 3.19. For this VOC, the impedance variations are, mostly, frequency-independent, and inferior to 10 Ω , apart from sensor #6. The latter sensor presents an interesting behavior, since its impedance variation is negative for frequencies below 600 Hz, and above 70 kHz, with an absolute value between 10 Ω and 2 kΩ . However, inside the mentioned frequency range, the impedance variation is positive and has a maximum value of approximately 1 kΩ .

It is possible to conclude that some sensors have, in fact, frequency-dependent variations to certain VOCs, such as sensor #5, sensor #6 and sensor #8. To further confirm this statement, in Figure 3.20, the impedance variation of sensor #6, as a function of VOC is presented.

From the previous figure, it is clear that for VOCs such as dichloromethane and toluene, the variation between exposure and recovery phases, presents negative values for frequencies below 600 Hz, and positive values for frequencies higher than 100 kHz. In addition, a similar behavior is observed for acetone, however the negative values are not shown for low frequencies. On the other hand, for the remaining VOCs, an approximately opposite behavior is observed. Similarly, sensor #8 presents a shift in the impedance variation, for frequencies below 300 Hz, as shown in Figure 3.21.

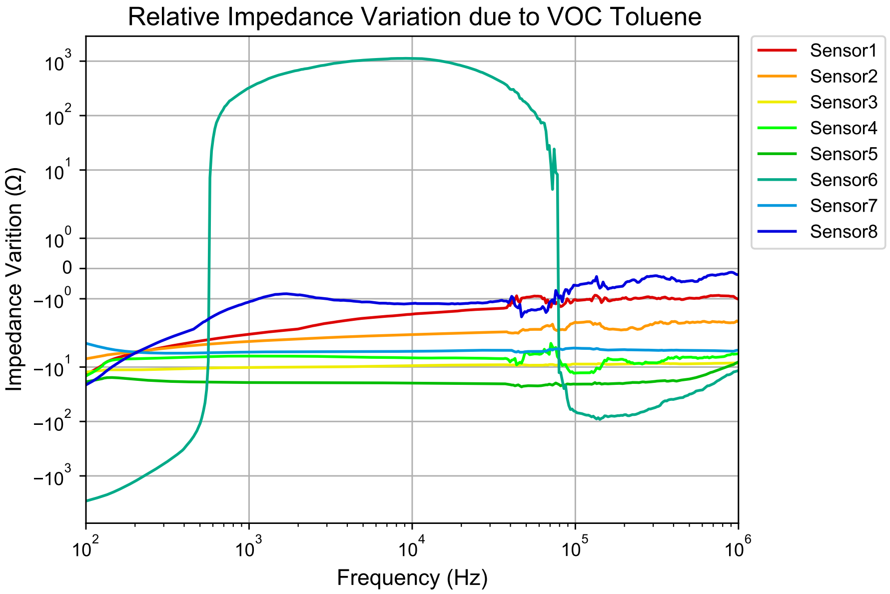

Figure 3.19: Impedance variation between recovery and exposure phases, for toluene.

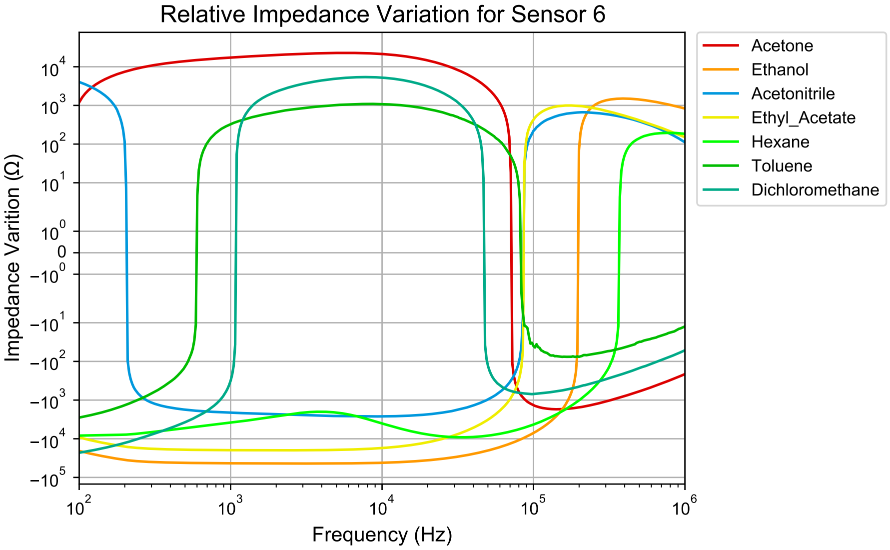

Figure 3.20: Impedance variation for sensor #6, as a function of VOC.

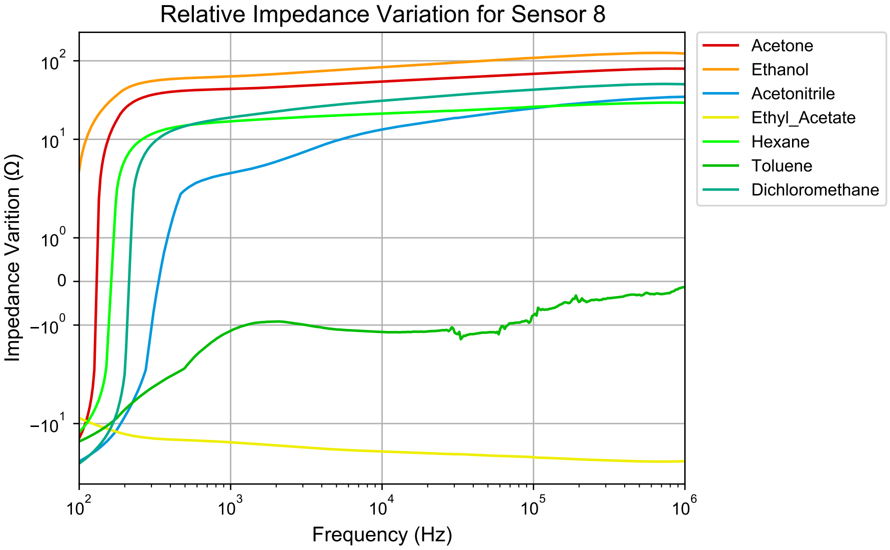

Figure 3.21: Impedance variation for sensor #8, as a function of VOC.

From Figure A.5 to Figure A.10, the impedance variations for the remaining sensor formulations, as a function of VOC, are presented.

3.3.3 Overall Sensor Affinity to VOC

Considering the previous results, it is possible to estimate the approximate affinity between a given sensor formulation and a VOC. For that, 7 distinct frequencies between 100 Hz and 100 kHz, were studied, where interesting and meaningful behavior was observed: 100 Hz; 200 Hz; 1 kHz; 2 kHz; 10 kHz; 50 kHz; and 100 kHz.

This way, the estimated affinity for a frequency of 100 Hz, is presented in Figure 3.22. It is possible to conclude that, at 100 Hz, the responses of the group of sensors are considerably low, achieving a maximum value of 16.9%. At this frequency, sensor #6 presents higher values of relative response than the remaining sensors.

At a frequency of 200 Hz, higher levels of affinity are achieved, for ethanol and acetonitrile, and for sensor #6, in particular, as shown in Figure 3.23. At higher frequencies, the overall affinity between the various sensor formulations and the different VOCs increases, as shown in Figure 3.24. In this case, the relative responses for ethanol and acetonitrile, achieve a maximum of 47.3%, for sensor #6. Apart from this, the affinity is considerably high for sensor #3, sensor #4 and sensor #7.

Lastly, at a frequency of 100 kHz, it is clear that the overall affinity is greater for ethanol, as shown in Figure 3.25. More specifically, the affinity between sensor #3 and ethanol, and sensor #7 and acetonitrile, is approximately 40%. The affinities for the remaining frequencies are presented from Figure A.11 to Figure A.14.

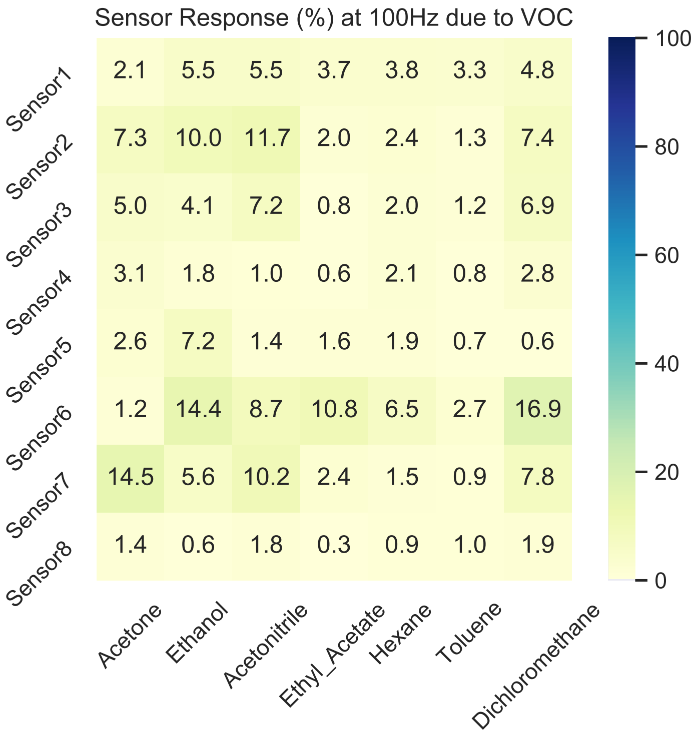

	Acetone	Ethanol	Acetonitrile	Ethyl_Acetate	Hexane	Toluene	Dichloromethane
Sensor1	2.1	5.5	5.5	3.7	3.8	3.3	4.8
Sensor2	7.3	10.0	11.7	2.0	2.4	1.3	7.4
Sensor3	5.0	4.1	7.2	0.8	2.0	1.2	6.9
Sensor4	3.1	1.8	1.0	0.6	2.1	0.8	2.8
Sensor5	2.6	7.2	1.4	1.6	1.9	0.7	0.6
Sensor6	1.2	14.4	8.7	10.8	6.5	2.7	16.9
Sensor7	14.5	5.6	10.2	2.4	1.5	0.9	7.8
Sensor8	1.4	0.6	1.8	0.3	0.9	1.0	1.9

Figure 3.22: Affinity between the different sensor formulations and VOCs, at a frequency of 100 Hz.

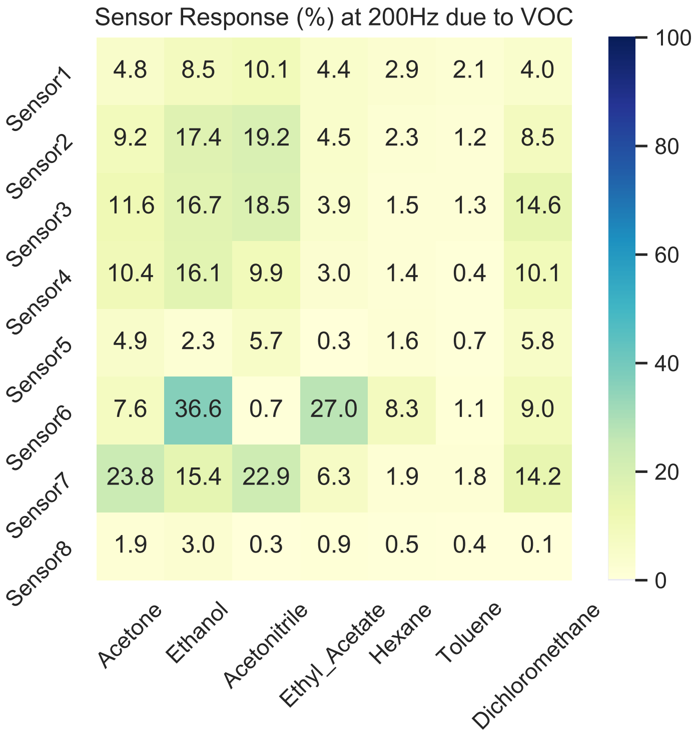

	Acetone	Ethanol	Acetonitrile	Ethyl_Acetate	Hexane	Toluene	Dichloromethane
Sensor1	4.8	8.5	10.1	4.4	2.9	2.1	4.0
Sensor2	9.2	17.4	19.2	4.5	2.3	1.2	8.5
Sensor3	11.6	16.7	18.5	3.9	1.5	1.3	14.6
Sensor4	10.4	16.1	9.9	3.0	1.4	0.4	10.1
Sensor5	4.9	2.3	5.7	0.3	1.6	0.7	5.8
Sensor6	7.6	36.6	0.7	27.0	8.3	1.1	9.0
Sensor7	23.8	15.4	22.9	6.3	1.9	1.8	14.2
Sensor8	1.9	3.0	0.3	0.9	0.5	0.4	0.1

Figure 3.23: Affinity between the different sensor formulations and VOCs, at a frequency of 200 Hz.

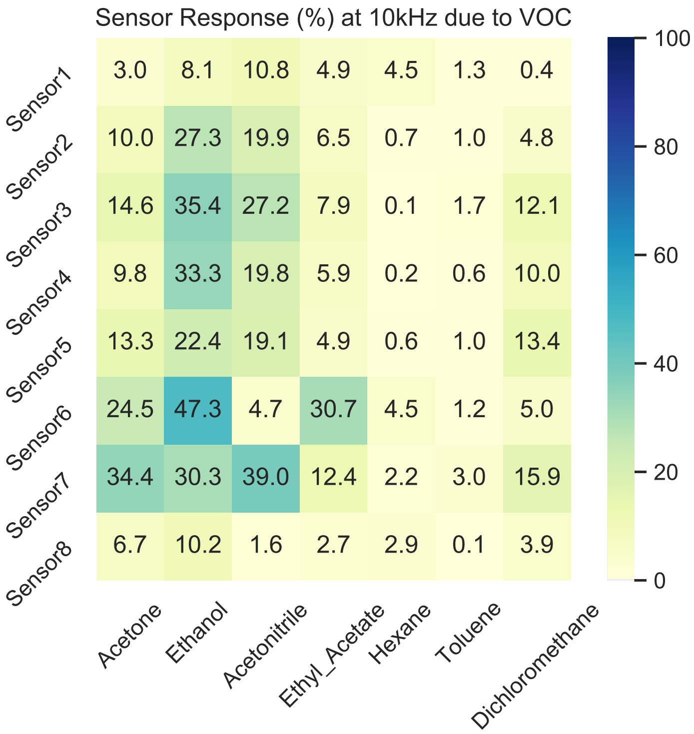

Figure 3.24: Affinity between the different sensor formulations and VOCs, at a frequency of 10 kHz.

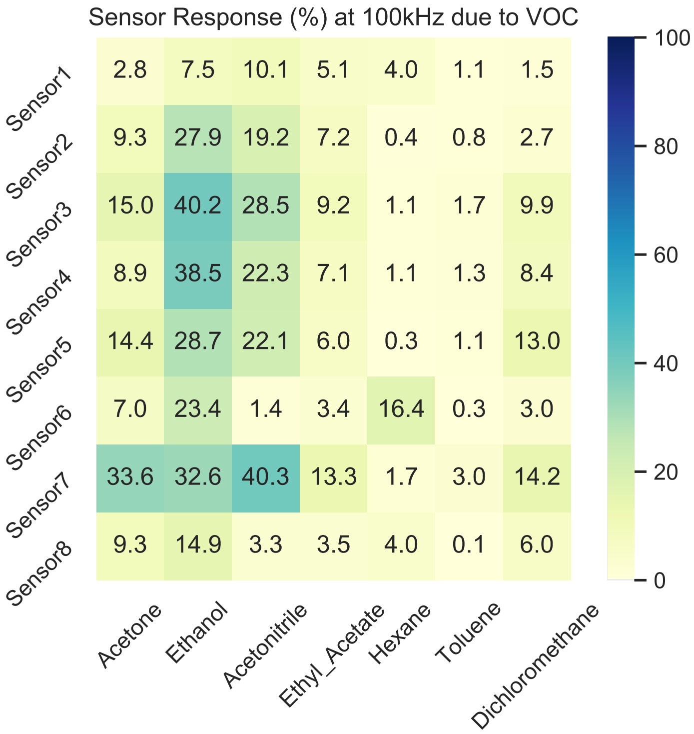

Figure 3.25: Affinity between the different sensor formulations and VOCs, at a frequency of 100 kHz.

3.4 Conclusions

Considering the experiments and results presented in the previous sections, the following items summarize the most relevant conclusions:

- The various sensor formulations presented considerably distinct responses to stimuli, such as a variation in RH levels and exposure to different analytes.
- Regarding the response of the sensors to the RH level, it was observed that the number of carbons in the sensor formulation is directly proportional to the affinity to water, which is a negative aspect. More specifically, sensor #6 presented a highly-hydrophilic behavior, since its impedance varied as much as 4 orders of magnitude, in an exponential manner, and reached tens of MΩ , for a linear sweep in RH level from 0% to 80%.
- On the other hand, sensor #7 presented the least dependence on RH level. For the considered RH sweep, the impedance varied approximately 1 kΩ , in contrast to 30 kΩ for sensor #2. In addition, the slight difference in chemical composition between the latter sensors was noticeable, and corroborated previous studies [15].
- Considering only the impact of RH level, the sensors presented an impedance between 65 Ω and 2 MΩ , for a frequency range between 100Hz and 100kHz. However, with the exception of sensor #6, the maximum impedance of the group of sensors is 300 kΩ .
- Considering the response of the sensors to different VOCs, it was possible to observe that the responses of some sensors present meaningful frequency-related behavior. More specifically, sensor #5, sensor #6, and sensor #8, presented interesting responses to different VOCs, which not only depend on VOC, but also on frequency.
- For sensor #6, the exposure to VOCs such as, acetonitrile and toluene, created a negative impedance variation, for frequencies below 600 Hz and above 100 kHz, and a positive impedance variation inside the given frequency range. However, an almost opposite behavior was observed for the remaining VOCs, while for acetone, the impedance variation is positive up to 100 kHz, above which becomes negative.
- The affinity of the sensors to the VOCs considered is proportional to frequency, while the maximum occurred for a frequency of 10 kHz, for sensor #6 and ethanol, with a value of 47.3%. Considerable affinity levels were observed for ethanol and acetonitrile, while the sensors presented an overall low-affinity to toluene and hexane. The most responsive sensors to the VOCs are sensor #3, sensor #4, sensor #6 and sensor #7.
- Considering an RH level of 50% and a frequency range between 100 Hz and 100 kHz, the minimum and maximum impedance of the group of sensors are 50 Ω and 200

kΩ , respectively. However, the maximum impedance greatly increases for lower RH levels, due to sensor #6. Thus, for the design of the AFE circuit, a minimum of 50% RH level for sensor #6 operation is established.

4

ELECTRICAL E-NOSE V3 SYSTEM DESIGN

In this chapter, the design of the Electrical E-nose V3, in a system perspective, is presented, which includes a hardware and a software part.

In the hardware part, the design of two variations of an AFE circuit is presented. For the first variation, the design of an AFE circuit that is fully-integrated in a PSoC 5LP, is presented. The SoC implementation enables greater flexibility, simplicity, and practicality since the entire circuit can easily be reconfigured without the need of redesigning a circuit board. This AFE circuit will be denominated AFE #1. For the second variation, the design of an optimized AFE circuit is presented, which is capable of measuring impedances in multiple frequencies, and will be referred to as AFE #2. Such AFE circuit is partially implemented in the PSoC5 LP, however, to achieve greater accuracy and precision, an external circuit to the PSoC 5LP is implemented.

The AFE circuit is intended to be implemented in a PCB, denominated main PCB. This PCB also implements a power control circuit, consisting of an array of relays that are used to control the E-nose delivery system. Moreover, a secondary PCB is used to route signals from a connector adapter to which the sensor's electrically connect to and is designed to be fitted into the main PCB.

In addition, the design of the electronics module, which contains the main and secondary PCBs, is presented, alongside the design of custom 3D-printed parts, using CAD software. More specifically, the design of the sensor's chamber, a custom sample heating device and other accessories is shown.

Moreover, the firmware developed for the control and signal acquisition of the E-nose is discussed, which runs in the ARM Cortex-M3 processor integrated in the PSoC 5LP. A Python software responsible for data logging and real-time plotting, intended to run in a computer, is presented. Furthermore, a digital filter was designed to reduce noise in the acquired signals, which is implemented in the latter Python software.

4.1 Fully PSoC-Integrated AFE Circuit Design

The AFE #1 circuit is fully implemented using the PSoC 5LP resources, requiring no external off-chip active components or ICs. Such implementation is focused on flexibility, simplicity and ease of implementation. In Figure A.17 the schematic of the complete circuit, in the PSoC Creator, is presented. In this section, the design of such circuit is presented, in detail.

4.1.1 Specifications and Architecture

The most important specifications for the design of the AFE #1 circuit are presented in Table 4.1.

Parameter	**Specification**
Nr. Channels	12
Effective Resolution	>12-bit
Sampling Rate (all channels)	10 Hz
Accuracy	>90%
$Z_{\text{sensor,min}}$	200 Ω
$Z_{\text{sensor,max}}$	200 kΩ
$F_{\text{sensor drive}}$	2 kHz

Table 4.1: AFE #1 circuit specifications.

Considering the specifications, the AFE #1 circuit should be capable to generate a sensor drive signal, whose frequency can be adjusted, to measure the effective resistance of the ionogel sensing material more directly, as described in subsection 3.2.6. For that, the PSoC 5LP programmable DAC offers a signal resolution of 8-bit, whose frequency, amplitude, and phase can be easily manipulated by configuring the DAC lookup tables. However, for the AFE #1, the sensor drive frequency is fixed at 2 kHz.

The sensor drive signal is applied to a common bus, to which one of the electrodes of each of the 12 sensors is connected to. The other electrode of each sensor is connected to one of the inputs of an analog multiplexer. For that, the configurable GPIO matrix of the PSoC 5LP is used, which is configured to have 12 analog inputs and a common analog output, resulting in a 12:1 multiplexer. Moreover, the control of the multiplexer is made via software.

The output of the multiplexer is connected to the amplifier, which is a programmable-gain TIA. This amplifier is implemented using a switched-capacitor circuit, in the PSoC 5LP, and offers 8 distinct trans-impedance gains. The programmable gain is useful to maximize the input dynamic range of the ADC, for the entire input impedance measurement range, and is controlled via software.

The multiplexer and amplifier implement a time-sharing mechanism, in which the amplifier is shared amongst all the 12 sensor channels, by connecting a given sensor to the amplifier for a given period of time. This way, the circuit becomes simpler and more efficient.

The output of the amplifier is fed into an ADC. As described in subsection 2.2.2, the PSoC 5LP offers a 12-bit 1 MHz SAR ADC, and an 8-bit to 20-bit ΣΔ ADC. For the AFE #1, the ΣΔ ADC is chosen, and it is configured for a resolution of 16-bit, resulting in a sampling frequency of 48 kHz.

The peak amplitude of the sampled AC signal is modulated by the impedance of the sensor, which is used to calculate its impedance. To obtain the amplitude of the AC signal, a peak detector circuit is implemented. The software implementation of the detector results in a higher SNR, since an hardware implementation contributes with noise, which ultimately increases the total system noise.

Considering the description of the AFE #1 circuit, its simplified circuit block diagram is presented in Figure 4.1.

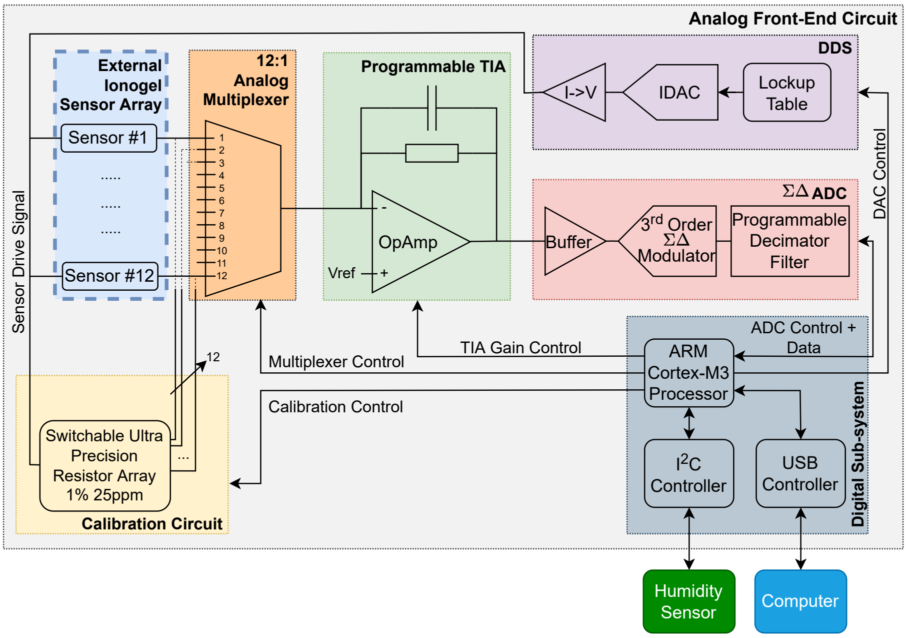

Figure 4.1: Simplified circuit block diagram of AFE #1.

4.1.2 Configurable Direct Digital Synthesizer

For the sensor drive signal generation, a configurable Direct Digital Synthesizer (DDS) was implemented. Such DDS is composed of a lookup table, a current DAC (IDAC), and a current-to-voltage converter.

The lookup table is used to configure the frequency of the sensor drive signal and can easily be manipulated in software. The PSoC Creator provides an intuitive GUI and comprehensive set of software functions that simplify the configuration of the DAC, as presented in Figure 4.2b. For the AFE #1, the frequency is fixed at 2 kHz, since this is the frequency used in previous E-nose versions and is within the 100 Hz to 100 kHz range. Thus, the DDS was configured to generate a 2 kHz sine-wave with an amplitude of 100mV.

Since the output of the IDAC is a current signal, the current-to-voltage converter attached to the IDAC was used to output a voltage signal, which varies from 0V to 1.2V. Considering the 8-bit resolution and a dynamic range of 1.2V, the step resolution of the DDS is 4mV. Thus, the 100mV amplitude output signal is composed of 50 steps, which is sufficient for this application.

To remove unwanted high-frequency content of the generated signal, an additional active low-pass filter can be implemented. In addition, this circuit results in a higher sensor driving capability. For that, the PSoC 5LP offers an Op-amp, which can be configured as an inverting amplifier, as shown in Figure 4.2a. A low-pass filter is formed by R2 and C2, whose cut-off frequency is given by:

$$F_{\text{LowPass}} = \frac{1}{2\pi R2C2}, \tag{4.1}$$

where C2 and R2 are set to 2.2nF and 10 kΩ , respectively, resulting in a cut-off frequency of approximately 7 kHz.

Since the AFE operates at a 5V single supply, the reference voltage is 2.5V. However, the generated signal has an average voltage of 510mV. Thus, a high-pass filter is made with C1 and R1, and the cut-off frequency is given by:

$$F_{\text{HighPass}} = \frac{1}{2\pi R1C1}, \tag{4.2}$$

where C1 and R1 are set to 100nF and 10 kΩ , respectively, resulting in a cut-off frequency of 159 Hz. This way, the average voltage at the output of the filter is 2.5V, which is set by the reference voltage at the non-inverting terminal. The DC gain of the circuit is approximately given by:

$$Gain_{\text{DC}} = -\frac{R2}{R1}, \tag{4.3}$$

which according to the values of R1 and R2 is unity.

4.1.3 Switchable GPIO Matrix

The implementation of an analog multiplexer in the PSoC 5LP is straightforward, by using the routing engine in the PSoC Creator IDE [57]. However, the selection of input and output pins of the analog multiplexer requires a careful understanding of the internal analog routing buses of the PSoC 5LP, otherwise unexpected signal crosstalk, excessive leakage and high on-resistance problems can occur.

The GPIOs of the PSoC 5LP can be configured to be either digital or analog, and the silicon is also divided in analog and digital sections. In Figure 4.3 a simplified diagram of the internal analog and digital structure is shown.

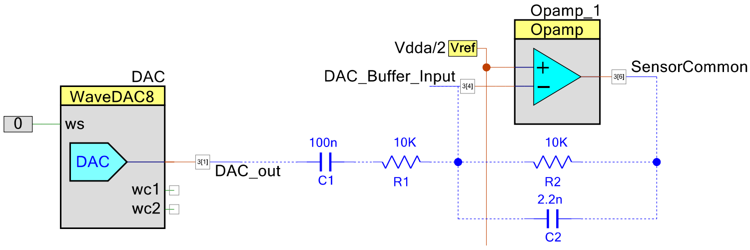

(a) DDS complete circuit schematic.

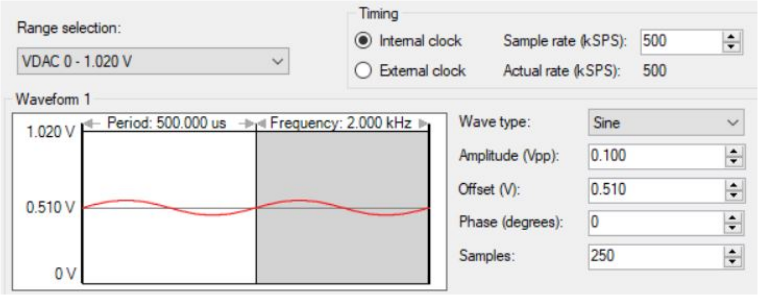

Range selection:
VDAC 0 - 1.020 V

Timing
● Internal clock Sample rate (kSPS): 500
○ External clock Actual rate (kSPS): 500

Waveform 1

Wave type: Sine
Amplitude (Vpp): 0.100
Offset (V): 0.510
Phase (degrees): 0
Samples: 250

(b) DAC configurations used in the PSoC Creator.

Figure 4.2: DDS implementation using the PSoC Creator. All passive components are externally implemented (represented in blue).

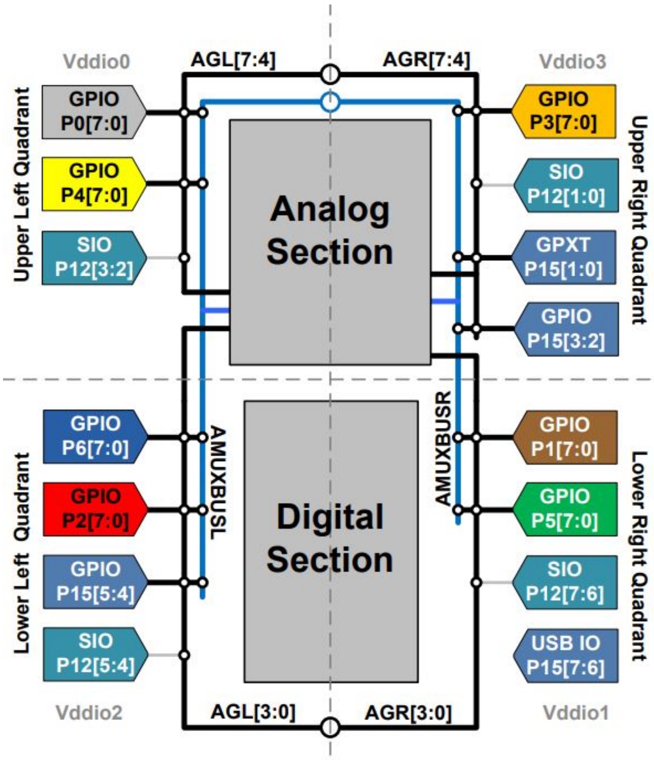

Figure 4.3: Simplified diagram of the analog buses of the PSoC 5LP ([75]).

The chip can be divided into 4 quadrants, which are associated with an analog global and analog multiplexer buses. The latter can be connected to the majority of GPIOs, while the analog globals connect a specific set of ports and GPIOs. The analog multiplexer bus provides a total of 18 different analog paths between GPIOs and analog blocks, and there are an additional 20 low impedance analog-dedicated paths.

For the connection itself, there are different kinds of switches, featuring resistances from 200 Ω to 700 Ω . The selection of a given GPIO for an analog signal may require the usage of multiple switches, which can be of different impedance. Thus, the on-resistance of distinct multiplexer channels can be different and is considerably dependent on the routing resources used.

In addition, specific analog blocks, such as Op-amps, have dedicated GPIO pins and analog busses assigned, which further constrains the routing of the signals on the multiplexer. To facilitate the routing, the manufacturer recommends using ports P0, P3 and P4, when possible, to obtain the best analog performance. Table 4.2 contains the GPIOs used for the implementation of the analog multiplexer.

Channel	**GPIO**
0	P0.6
1	P15.2
2	P2.7
3	P3.3
4	P15.5
5	P2.3
6	P1.7
7	P1.6
8	P15.3
9	P2.0
10	P0.0
11	P0.1
Output	P3.6

Table 4.2: Analog multiplexer GPIO pins.

4.1.4 Programmable-Gain TIA

As described in section 3.1, the drive signal applied to the sensor generates an electrical current. Thus, the impedance of the sensor can be calculated by measuring this current. For that, a TIA outputs a voltage that is proportional to the input current. In Figure 4.4 the analog multiplexer and TIA are presented.

The PSoC 5LP offers a programmable-gain TIA, whose trans-impedance gain can be software configured in 8 discrete values, ranging from 20 kΩ to 1 MΩ . Additionally, 3 different compensation capacitors can be configured, ranging from 1.3pF to 4.6pF.

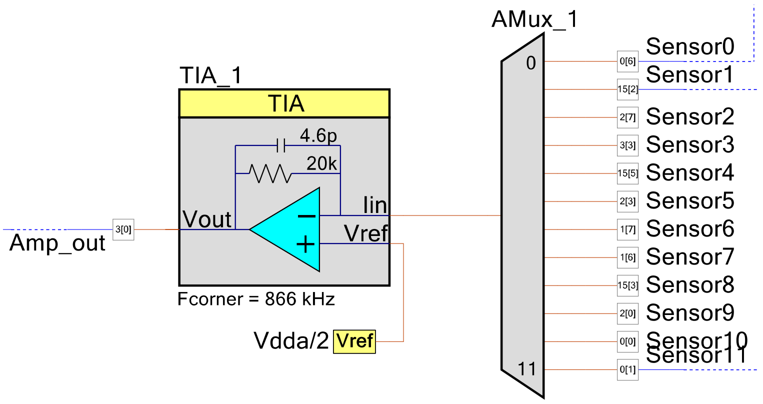

Figure 4.4: Analog multiplexer and TIA circuit schematic.

Moreover, 4 distinct power modes are available, which are useful for power critical applications.

Regarding the DC performance of the TIA, the values of the feedback resistor have a tolerance between -25% and 30% of their nominal value, which is considerable. Additionally, the input offset voltage has a nominal value of ± 3.5mV, and a maximum of ± 10mV. The datasheet does not provide figures for other parameters, such as input impedance, open-loop gain, CMRR, PSRR, and output voltage-swing, which constrains the design of the circuit.

The closed-loop bandwidth of the amplifier is dependent on the power mode, compensation capacitor, feedback resistance, and the amplifier GBW, and is given by:

$$B_{\text{closed-loop}} = \frac{1}{\sqrt{(2\pi RfCf)^2 + \frac{1}{GBW^2}}}, \tag{4.4}$$

where Rf and Cf are the feedback resistor and capacitor, respectively, and

$$GBW = \begin{cases} 200\text{ kHz, if minimum power} \\ 400\text{ kHz, if low power} \\ 600\text{ kHz, if medium power} \\ 1\text{ MHz, if high power} \end{cases}. \tag{4.5}$$

In Figure 4.5, the noise characteristic of the TIA is presented. In Table 4.3, the summary of the TIA specifications are presented. In this case, the power mode was set to *high power*, since it results in the highest Op-amp bandwidth of 1 MHz, enabling the use of the larger compensation capacitor, 4.6pF. This way, quiescent current consumption, Id_{max}, is close to 1.1mA.

Considering that the absolute value of the impedance values, Z_{sensor}, can vary from 200 Ω to 200 kΩ , then the current for a given sensor i, $I_{\text{sensor}}[i]$, is calculated by:

$$I_{\text{sensor}}[i] = \frac{V_{\text{osc}}}{Z_{\text{sensor}}[i]}, \tag{4.6}$$

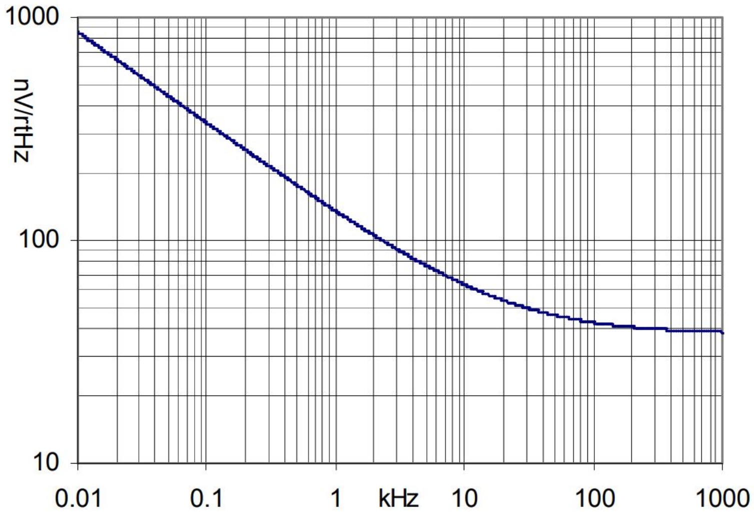

Figure 4.5: TIA noise figure ([76]).

Parameter	Specification
Rf_{min}	20 kΩ
Rf_{max}	1 MΩ
N. of Rf settings	8
Rf tolerance	-25% to 35%
Cf_{min}	1.3pF
Cf_{max}	4.6pF
Id_{min} (5V) (minimum power)	650μA
Id_{max} (5V) (maximum power)	1.1mA
Voffset	± 3.5mV
$B_{closed\ loop,max}$ (Cf_{max}, Rf_{min}, high power)	866 kHz
$B_{closed\ loop,min}$ (Cf_{max}, Rf_{max}, high power)	35 kHz
e_{nf} (10 Hz)	850nV/$\sqrt{Hz}$
e_{nBB} (100 kHz)	40nV/$\sqrt{Hz}$

Table 4.3: TIA specifications.

where V_{osc} is the amplitude of the sensor drive signal, and Z_{sensor}[i] is the impedance of a given sensor i. This way, the maximum and minimum sensor currents are obtained by Equation 4.6 where $Z_{sensor,min}$=200 Ω and $Z_{sensor,max}$=200 kΩ, resulting in $I_{sensor,max}$=500μA and $I_{sensor,max}$=500nA, respectively. Considering that each channel is associated with a sensor i, the ideal output voltage of the TIA is calculated by:

$$V_{\text{out}}[i] = V_{\text{ref}} - I_{\text{sensor}}[i]R_{\text{f}}[i], \tag{4.7}$$

where V_{ref} is the reference voltage of the circuit, I_{sensor}[i] is the sensor current of a given sensor, and R_f[i] is the feedback resistance configured for a particular channel.

However, the on-resistance of each multiplexer channel appears in series with the impedance of the sensor, and its value may change from channel to channel, depending on the routing configuration. Moreover, the input offset voltage of the Op-amp is affected by the non-inverting gain, which is unity, and affects the common-mode voltage. Thus, the output voltage of the TIA is given by:

$$V_{\text{out}}[i] = V_{\text{ref}} + V_{\text{off}} - \frac{Vosc \times R_{\text{f}}[i]}{Z_{\text{sensor}}[i] + R_{\text{on}}[i]}, \tag{4.8}$$

where $R_{\text{on}}[i]$ is the on-resistance of a given multiplexer channel i, and V_{off} is the Op-amp input offset voltage.

Considering that the output voltage swing of the TIA is between 250mV and 4.75V, and that the ADC has an equal input dynamic range, to comply with $V_{\text{out,max}}$ = 4.75 V, and considering the minimum feedback resistance, $R_{\text{f,min}}$, of 20 kΩ , then the minimum sensor impedance, $Z_{\text{sensor,min}}$, that can be measured is given by:

$$Z_{\text{sensor,min}} = \frac{V_{\text{osc}} R_{\text{f,min}}}{V_{\text{out,max}}}, \tag{4.9}$$

and as a value of $Z_{\text{sensor,min}}$ = 420 Ω . However, considering that $R_{\text{on}} = R_{\text{on,max}}$ = 700 Ω , theoretically, $Z_{\text{sensor,min}}$ = 0 Ω . In practice, this means that it is possible to lower $Z_{\text{sensor,min}}$, but the limitation factor becomes the sensor current. The $R_{\text{f,max}}$ value required to comply with $V_{\text{out,min}}$ = 250mV, while $Z_{\text{sensor}} = Z_{\text{sensor,max}}$=200 kΩ , is given by:

$$R_{\text{f,max}} = \frac{(Z_{\text{sensor,max}} + R_{\text{on,max}}) V_{\text{out,min}}}{V_{\text{osc}}}, \tag{4.10}$$

and as a value of $R_{\text{f,max}}$ = 500 kΩ . Thus, it is possible to conclude that a strategy to dynamically control the trans-impedance gain for each sensor is mandatory. Also, the requirement for the $R_{\text{f,max}}$ can be accomplished with the second highest value of R_{f} = 500 kΩ , which results in a closed-loop bandwidth of 69 kHz.

The RH level sets the baseline impedance level of a given sensor. However, when the sensor is exposed to a given VOC, its impedance varies. Thus, the minimum and maximum impedance levels of the sensor, regarding this dynamic behavior, have to be considered in the design of the AFE circuit. For that, in Figure A.15, the dynamic impedance variation, in Ω , that occurs when the various sensors are exposed to the different VOCs, is presented.

It is possible to observe that the dynamic impedance variation can be as low as a 1 Ω , or as large as 44 kΩ . Thus, the AFE circuit needs to have a precision level of mΩ , to be able to measure such low impedance variations. On the other hand, sensor #6 requires a lower precision level, but a higher dynamic-range.

Due to lack of information in the TIA datasheet, and considerably high tolerances for some specifications, a more detailed circuit design and simulations are not possible. Because of this, to assess the stability of the circuit, a physical test of it was conducted. In addition, the selection of the different R_{f} values associated with different trans-impedance gain levels, is made in the calibration procedure, presented in subsection 4.1.6.

Considering the available data in the TIA datasheet, it is possible to estimate the approximate total noise of the circuit, and its equivalent SNR. For that, the TIA configuration that provides the highest trans-impedance gain, where $R_f = 1\ M\Omega$, and lowest closed-loop bandwidth, B = 35 kHz, was initially considered. The approximate thermal noise voltage, E_{nr}, due to the feedback resistor is given by:

$$E_{\mathrm{nr}} = \sqrt{4kT \times R_{\mathrm{f}} \times NBW}, \tag{4.11}$$

where NBW is the noise bandwidth, given by:

$$NBW = B\frac{\pi}{2}. \tag{4.12}$$

The calculated resistor thermal noise voltage is, approximately, 30.2μVrms. The flicker noise voltage, E_{nf}, of the Op-amp is calculated by:

$$E_{\mathrm{nf}} = e_{\mathrm{fnorm}}\sqrt{\ln\frac{NBW}{fl}}, \tag{4.13}$$

where

$$e_{\mathrm{fnorm}} = e_{\mathrm{fl}}\sqrt{fl}, \tag{4.14}$$

where $e_{\mathrm{fl}} = 850nV/\sqrt{Hz}$ is the noise spectral density at the lowest frequency, $fl = 10Hz$. The calculated noise voltage due to the Op-amp flicker noise is 7.9μVrms. The broadband noise voltage of the Op-amp is calculated by:

$$E_{\mathrm{nBB}} = e_{\mathrm{nBB}}\sqrt{NBW}, \tag{4.15}$$

where $e_{\mathrm{nBB}} = 40nV/\sqrt{Hz}$ is the broadband noise spectral density. The calculated noise voltage due to the Op-amp broadband noise is 9.4μVrms. Due to the lack of data regarding the current noise spectral density, the approximate total Op-amp noise voltage, E_{nop}, is calculated by the root sum of squares (RSS), as given by:

$$E_{\mathrm{nOp}} = \sqrt{E_{\mathrm{nf}}^2 + E_{\mathrm{nBB}}^2}, \tag{4.16}$$

and has a value of 12.3μVrms. This way, the approximate total circuit noise voltage, E_{nTotal}, is also calculated by the RSS, as given by:

$$E_{\mathrm{nTotal}} = \sqrt{E_{\mathrm{nOp}}^2 + E_{\mathrm{nr}}^2}, \tag{4.17}$$

and has a value of 32.6μVrms, where the dominant noise source is the thermal noise of the feedback resistor. The equivalent SNR is given by:

$$SNR = 20\log_{10}\frac{1}{E_{\mathrm{nTotal}}}, \tag{4.18}$$

and has a value of 89.7 dB, which according to Equation 2.24, is equivalent to an effective resolution of 14.6-bit. Applying the same procedure for lowest trans-impedance gain, $R_f = 20\ k\Omega$, and highest closed-loop bandwidth, B = 866 kHz, the ENOB is 13.9-bit.

Thus, the required ADC resolution is between 13-bit and 15-bit. However, it is important to consider that this result suffers from numerous approximations and simplifications, which results in an over-estimation of the effective resolution of the circuit.

4.1.5 Configurable ΣΔ ADC

For the signal acquisition, the ΣΔ ADC of the PSoC 5LP is chosen since it offers multiple levels of configuration. This ADC is composed of 3 main sections: an input buffer, with configurable gain and configurable single-ended of differential input; a 3^{rd} modulator; and a programmable 4-stage decimator filter.

Oversampling is used to spread the quantization noise, over a larger bandwidth. An internal low-pass filter attenuates the noise outside the signal bandwidth. This way, the ΣΔ ADC is capable of up to 20-bit resolution at 10 Hz sampling rate. For this application, since the AFE #1 uses a fixed frequency of 2 kHz, the maximum resolution is chosen in order to obtain a sampling frequency greater or equal than the Nyquist rate, which is 4 kHz. For that, a resolution of 16-bit results in a sampling frequency, $f_{sampling}$, of 48 kHz.

Four conversion modes are available: single-sample; multi-sample; continuous; and turbo. In the multi-sample mode, the converter takes consecutive samples and resets the modulator between them, while in turbo mode the same occurs, but it is optimized for resolutions greater than 16-bit. For the AFE #1, the continuous mode was used, which corresponds to the typical ΣΔ operation. Even though the datasheet specifies that this mode should not be used in multiplexed systems, the firmware implementation guarantees minimal leakage between channels.

For the reference voltage of the ADC, multiple choices are available, which can be either internal voltage references, or external voltage references. For this application, the internal 2.5V voltage reference of the PSoC 5LP is used. This reference is based on a curvature compensated voltage bandgap circuit and utilizes a resistive divider to provide different voltages.

The PSoC 5LP integrated reference voltage is capable of a maximum temperature drift of 30 ppm/°C, an absolute accuracy of ± 1%, and is independent of the supply voltage, which maximizes the performance of the ADC. Optionally, the reference voltage can be bypassed with an external capacitor to reduce the reference noise and improve the effective resolution of the ADC. For a 16-bit resolution a capacitance between 100nF and 1μF is recommended, which can be connected to pins P0.3 or P3.2.

The input impedance of the ADC buffer is 10 MΩ , and its gain can be configured from 1 to 8, however a trade-off between gain and bandwidth exists. In addition, the input range can also be configured from 0V to 5V, or from 0V to multiples of the reference voltage. Moreover, it is possible to bypass the buffer circuit. For this application, the input buffer was configured for unity-gain, single-ended input, input range from 0V to 5V, and rail-to-rail operation from 100mV to 4.75V. This way, the LSB voltage is calculated by Equation 2.19, and has a value of 76.3μV.

To prevent aliasing, a first-order active low-pass filter is implemented at the input of the ADC, using the input buffer of the ADC, whose cut-off frequency is set to, approximately, $0.5 f_{\text{sampling}} \approx$24 kHz. The schematic of the filter is presented in Figure 4.6a.

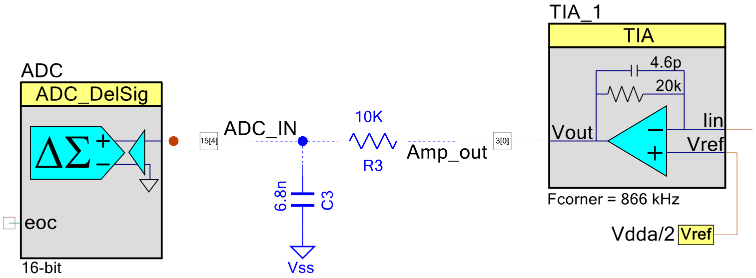

(a) ΣΔ ADC and active low-pass anti-aliasing filter.

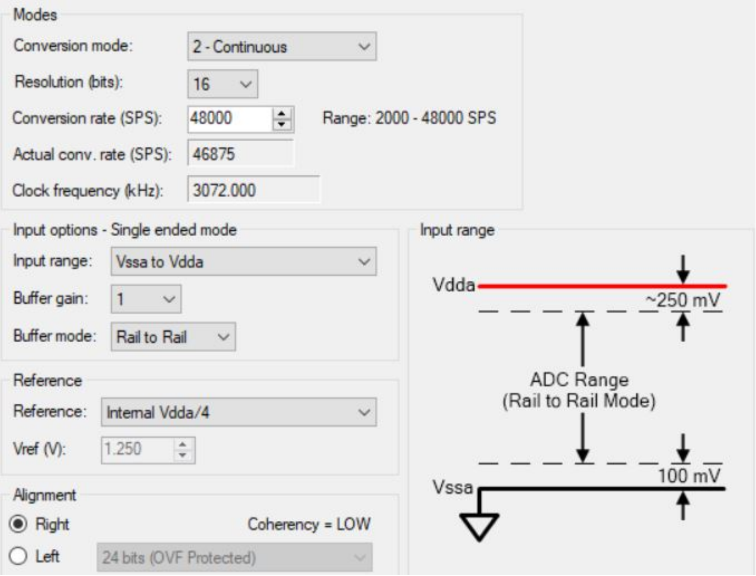
Modes

Conversion mode: 2 - Continuous

Resolution (bits): 16

Conversion rate (SPS): 48000 Range: 2000 - 48000 SPS

Actual conv. rate (SPS): 46875

Clock frequency (kHz): 3072.000

Input options - Single ended mode

Input range: Vssa to Vdda

Buffer gain: 1

Buffer mode: Rail to Rail

Reference

Reference: Internal Vdda/4

Vref (V): 1.250

Alignment

● Right Coherency = LOW

○ Left 24 bits (OVF Protected)

(b) ΣΔ ADC configurations used.

Figure 4.6: Anti-aliasing filter implementation and ΣΔ ADC configurations.

The cut-off frequency of the low-pass filter is given by:

$$F_{\text{anti-aliasing}} = \frac{1}{2\pi R3C3}, \tag{4.19}$$

where R3=1 kΩ and C3=6.8nF. In Table 4.4 the most relevant specifications for the ΣΔ ADC are presented. In Figure 4.7 the noise and non-linear characteristics of the PSoC 5LP ΣΔ ADC are presented.

4.1.6 Calibration

Due to the high component tolerances presented in Table 4.3, and considerable non-ideal specifications, such as input offset voltage and multiplexer on-resistance, a detailed calibration of the AFE circuit is required.

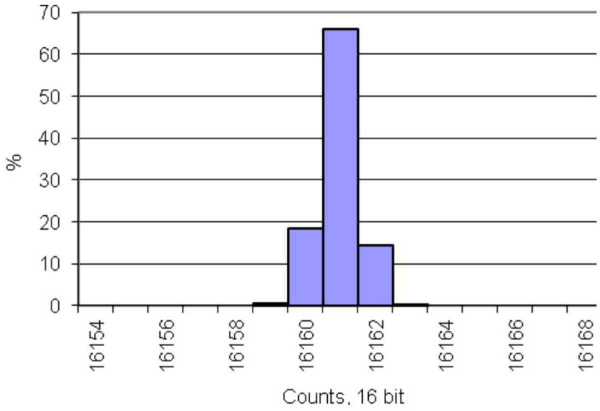

(a) Noise histogram.

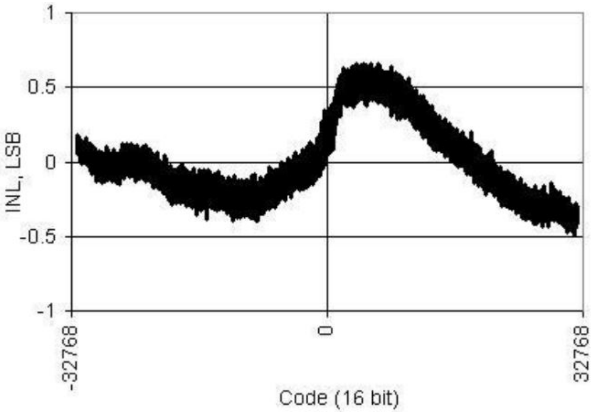

(b) INL as a function of digital code.

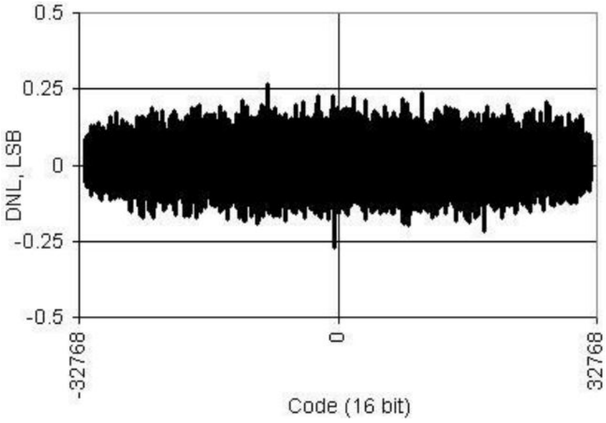

(c) DNL as a function of digital code.

Figure 4.7: PSoC 5LP ΣΔ ADC noise and non-linear characteristics ([77]).

Parameter	Specification
Gain error	± 0.4%
Input offset voltage	± 200μV
PSRR	90 dB
CMRR	85 dB
INL	± 2 LSB
DNL	± 1 LSB
THD	0.0032%
SINAD	81 dB
Current consumption	1.5mA

Table 4.4: ΣΔ ADC specifications.

The calibration procedure is performed once, is not related to the system auto-calibration, and its goal is to find a relation between the measured ADC voltage and the absolute value of the impedance of the sensor, Z_{sensor}. This is required due to the large tolerances of the PSoC 5LP component parameters, which vary from device to device. For that, an external circuit consisting of a switchable array of 16 1% 25 ppm resistors, ranging from 200 Ω to 200 kΩ , was created.

For the calibration procedure, each of the precision resistors is connected to one of the 12 channels of the AFE circuit, at a time, which models a perfect ionogel sensor, with a known resistance. Then, the measured voltage for each resistor, and the resistor value, are used to obtain a calibration curve, which presents a mathematical relation between a given sensor impedance and the measured voltage. This procedure is done for each channel, and for all of the 8 trans-impedance gain levels.

At the end of the calibration procedure, the selection of the different trans-impedance gains is made, to maximize the available ADC input dynamic range, thus optimizing the precision level of the AFE circuit. In Figure 4.8, the measured voltage for the given resistance range, as a function of the selected trans-impedance gains is presented, for one of the 12 channels.

In the latter figure, the calibration curves presented correspond to 3 different trans-impedance gains, which are sufficient to cover an impedance measurement range between 200 Ω and 200 kΩ . It can be observed that the relation between the measured voltage and equivalent sensor resistance is considerably non-linear. In addition, for voltages higher than 3.5V, a significant non-linear behavior is found, thus the maximum voltage is limited at 3.5V. From this data, the most appropriate calibration function is given by:

$$Z_{\text{measured}} = A \times V_{\text{measured}}{}^{B}, \tag{4.20}$$

where Z_{measured} and V_{measured} correspond to the measured impedance and voltage, respectively, and A and B are functions of the TIA gain and multiplexer channel.

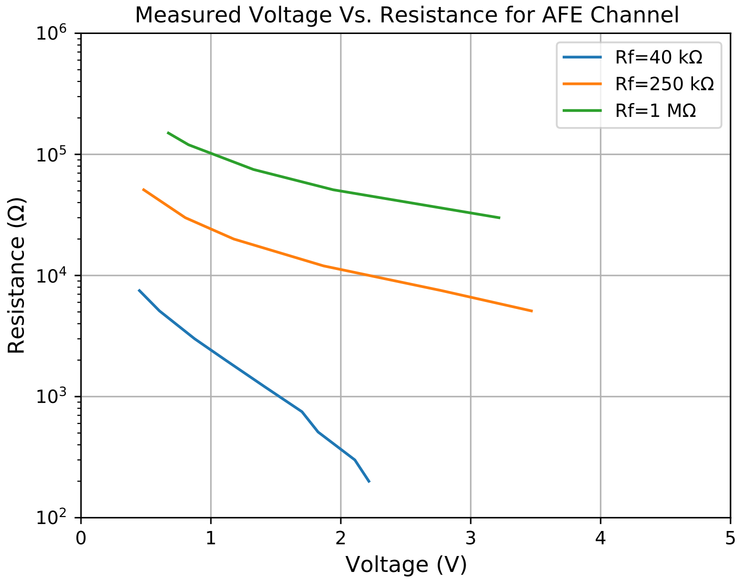

Figure 4.8: Calibration curves for the AFE #1 circuit.

In subsection 4.1.8, an automatic gain adjustment algorithm is presented, which is used to dynamically configure the appropriate trans-impedance gain for the required range. This way, the AFE automatically selects the appropriate trans-impedance gain, that guarantees the best accuracy and precision for the required sensor impedance range. Thus, the output variable is in unit of Ω and corresponds to the calibrated sensor impedance, which is independent of the circuit parameters, such as trans-impedance gain and TIA output voltage.

4.1.7 Digital Subsystem

The digital subsystem, presented in Figure 4.1, is composed of 3 main parts: an ARM Cortex-M3 processor; and I2C controller; and an USB controller.

The ARM processor integrated in the PSoC 5LP is at the core of the device. It controls all the configurable analog and digital circuit blocks and runs the necessary firmware for the AFE circuit operation. In the case of AFE #1, the processor controls the multiplexer channel selection, the trans-impedance gain of the TIA, the ADC acquisition, the sensor drive signal generated by the DAC, and communicates with an I2C controller which collects data from an external RH sensor, and with an USB controller, that is used for communication with a computer.

An I2C controller is available to use, as a configurable macro-cell in the PSoC Creator. Four modes of operation are available, such as master, slave, multi-master, or multi-master-slave. The data rate can be configured from 50 kbps to 1000 kbps. By default, the implementation of the device is made in software, however it is possible for the implementation to be made in hardware, by using the universal digital blocks available in the PSoC 5LP. To connect to an external device, two pins are necessary, which can be any of the GPIOs, or a specific set of pins on P12.0, P12.1, P12.4 or P12.5.

For this application, an external temperature and RH sensor (HTU21D-F [72]) is used to measure the RH inside the sensor detection chamber. Thus, the I2C interface of the sensor is used to establish a connection with the I2C controller, while the sensor works as a slave device, and the I2C controller works as a master device.

The data rate was set to 50 kbps, which is enough for the application and results in good stability. The implementation of the controller was made using the universal digital blocks, which frees up the processor. The pins used for SDA and SCL are the P12.5 and P12.4, respectively. Moreover, the 5.6 kΩ internal pull-up resistors of the PSoC 5LP were used, by configuring the SCL and SDA pin drive modes to resistive pull-up, as presented in Figure 4.9.

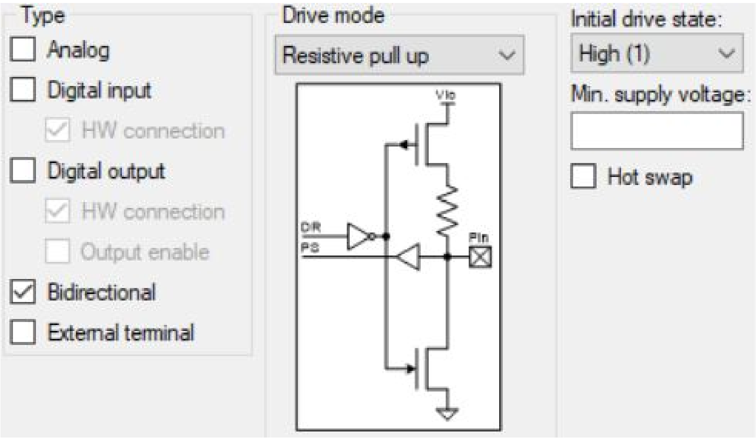
Type
☐ Analog
☐ Digital input
☑ HW connection
☐ Digital output
☑ HW connection
☐ Output enable
☑ Bidirectional
☐ External terminal

Drive mode: Resistive pull up

Initial drive state: High (1)

Min. supply voltage:

☐ Hot swap

Figure 4.9: I2C pin configuration [57].

The USB controller used is available on the PSoC Creator as a full-speed USB macro-cell (USBFS), which can also be configured by the designer. The standard configurations were used, and the system clocks were configured as presented in Figure 4.10.

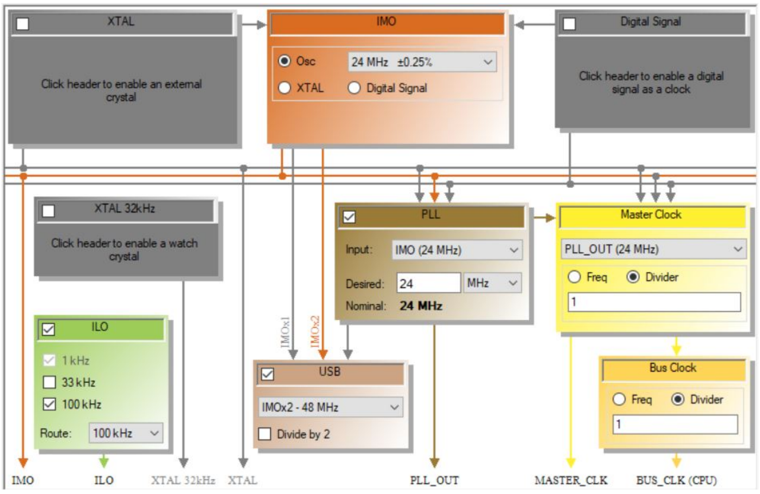
☐ XTAL
Click header to enable an external crystal

IMO
● Osc: 24 MHz ±0.25%
○ XTAL
○ Digital Signal

☐ Digital Signal
Click header to enable a digital signal as a clock

☐ XTAL 32kHz
Click header to enable a watch crystal

☑ PLL
Input: IMO (24 MHz)
Desired: 24 MHz
Nominal: 24 MHz

Master Clock
PLL_OUT (24 MHz)
○ Freq ● Divider
1

☑ ILO
☑ 1 kHz
☐ 33 kHz
☑ 100 kHz
Route: 100 kHz

☑ USB
IMOx2 - 48 MHz
☐ Divide by 2

Bus Clock
○ Freq ● Divider
1

Figure 4.10: USB and system clock configurations [57].

In addition to the main digital subsystem, a timer was implemented, whose goal is to synchronize the different hardware components, and set the timing for the signal acquisition. A timer macro-cell is available in the PSoC Creator, and features a clock input, and two outputs, one of which is activated via interrupts. Additionally, the counter can operate with 8-bit, 16-bit, 24-bit or 32-bit resolution, depending on its implementation being in software or a hardware. The GUI enables an efficient and easy configuration of the timer.

A clock signal with a frequency of 24 MHz is connected to the clock input of the timer. The resolution was set to 16-bit and the period parameter was set to 24000 cycles, which generates a high signal at the output of the timer every 1ms. In Figure 4.11 the configurations of the timer are presented.

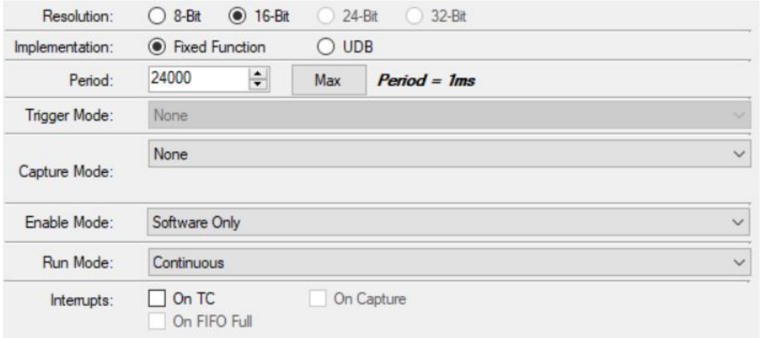
Resolution: ○ 8-Bit ● 16-Bit ○ 24-Bit ○ 32-Bit
Implementation: ● Fixed Function ○ UDB
Period: 24000 Max *Period = 1ms*
Trigger Mode: None
Capture Mode: None
Enable Mode: Software Only
Run Mode: Continuous
Interrupts: ☐ On TC ☐ On Capture ☐ On FIFO Full

Figure 4.11: Timer configurations [57].

4.1.8 Firmware

For the control of the entire AFE circuit, the PSoC 5LP offers an ARM Cortex-M3 processor, which was used to implement the firmware of the Electrical E-nose V3. The firmware is responsible to send low-level commands to the various circuit blocks, such as the selection of feedback resistor of the TIA, digital sample acquisition from the ADC, and multiplexer channel selection.

In addition to the control perspective, a peak-detector algorithm is used to calculate the peak voltage of the sampled sensor signals, at the output of the TIA. As previously mentioned, this firmware implementation results in a simpler hardware circuit and reduced system noise.

A block of code implemented in the main function runs continuously and is responsible for the higher-level control of the device. More specifically, this main function implements a command line between the Python software, running in the computer, and the E-nose, which is used to initialize and end an experiment, send the experiment configurations from the PC to the E-nose, and request individual sensor readings.

After receiving the appropriate commands, the E-nose enters in normal operation mode. In this mode, the E-nose acquires signals from all the AFE channels, followed by the acquisition of temperature and RH data from an external temperature and RH sensor. After the acquisition of all the data elements, a USB data transmission occurs to the computer. Lastly, the data buffers are cleared, and this procedure is repeated until the end of the E-nose experiment. Considering the latter description of the main function, the signal acquisition of the AFE channels can be described by the flow-chart shown in Figure 4.12.

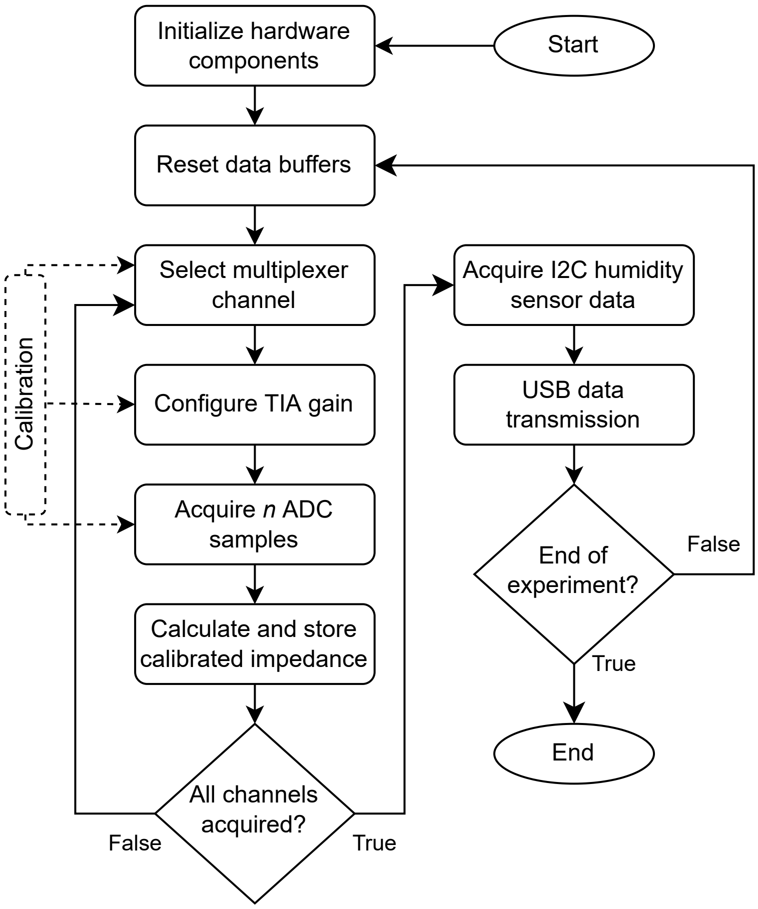

Figure 4.12: AFE operation algorithm flow-chart.

For the control and operation of the AFE circuit, the hardware components are initialized, using predefined software functions provided by the individual PSoC 5LP circuit block datasheets. Then, the data buffers required to store the individual sensor ADC samples are initialized.

After the initialization process, the algorithm enters in a loop, which is broken by a timeout signal indicative of the end of the experiment. This timeout signal is generated by the timer circuit described in subsection 4.1.7. For the acquisition of the signals, the multiplexer is configured to select the first AFE channel, to which a sensor is connected to.

Consecutively, the appropriate trans-impedance gain of the TIA is configured, following the procedure described in subsection 4.1.6. After the stabilization of the TIA output voltage, a number of ADC samples, $N_{samples}$, are acquired and stored in the data buffers. The number of samples required to acquire a complete sine-wave, which is modulated by the sensor response to the stimuli, is calculated by:

$$N_{\text{samples}} = \frac{T_{\text{signal}}}{T_{\text{sampling}}} = \frac{F_{\text{sampling}}}{F_{\text{signal}}}, \tag{4.21}$$

where F_{sampling} is the sampling frequency of the ADC (44 kHz), and F_{signal} is the signal frequency (2 kHz). Thus, a minimum $N_{\text{samples}} = 22$ samples are required to acquire a single 2 kHz sine-wave. However, considering that the peak voltage can be affected by noise and offset, to obtain a reasonable accuracy, multiple sine-wave cycles are acquired, whose peak voltages are averaged. The overall sampling rate, SR, corresponding to the acquisition of all 12 AFE channels, is calculated by:

$$SR = \frac{F_{\text{sampling}}}{N_{\text{channels}} N_{\text{samples}}}, \tag{4.22}$$

where N_{sensors} is the number of AFE channels (12). Thus, considering that N_{samples} is a base 2 number, $N_{\text{samples}} = 64$ corresponds to 3 sine-wave cycles, which results in an $SR = 57$ Hz but lower accuracy, while $N_{\text{samples}} = 256$ corresponds to 10 sine-wave cycles, and results in an $SR = 14$ Hz but higher accuracy. Considering the SR requirement of 10 Hz, presented in Table 4.1, $N_{\text{samples}} = 256$ was chosen.

After the acquisition of all AFE channels, the peak-detector algorithm calculates the peak voltages of each AFE channel, corresponding to each sensor, and the calibrated impedance measurement is stored in a buffer. Afterwards, the temperature and RH data are acquired and stored in the buffer. The complete data buffer contains 14 entries, which correspond to the impedance measurements of each channel, temperature and RH measurements, and is then sent to the computer via USB, for further processing and plotting. This algorithm runs continuously until the end of the experiment, after which the E-nose is reset. Additionally, the multiplexer channel selection, TIA feedback resistance selection, and individual ADC sample acquisition, can be individually performed in the calibration procedure.

In Figure 4.13, the flow-chart of the peak-detector algorithm is presented. As previously mentioned, the peak-detector is used to obtain the peak amplitude of the sensor signal, which is proportional to its impedance. The algorithm can calculate both the positive and negative peaks of the signal. For that, in $mode = 1$ the positive peak is calculated, while in $mode = 0$ the negative peak is calculated, which are stored in the maximum and minimum variables, respectively.

To apply the peak-detector algorithm, the data buffer containing the sampled sensor signal is divided into 4 auxiliary buffers, each one having 64 samples. Then, the peak-detector algorithm is applied to this each auxiliary buffer, and its positive and negative voltage peaks are obtained. This division ensures that in each data buffer there is, at least, two positive and negative peaks.

The positive and negative peaks are stored in additional buffers, $\text{Maximum}_{\text{buffer}}$, and $\text{Minimum}_{\text{buffer}}$, respectively. Then, the peak voltage of the signal, V_{peak}, that is used to calculate the calibrated impedance value of a given sensor, is calculated by:

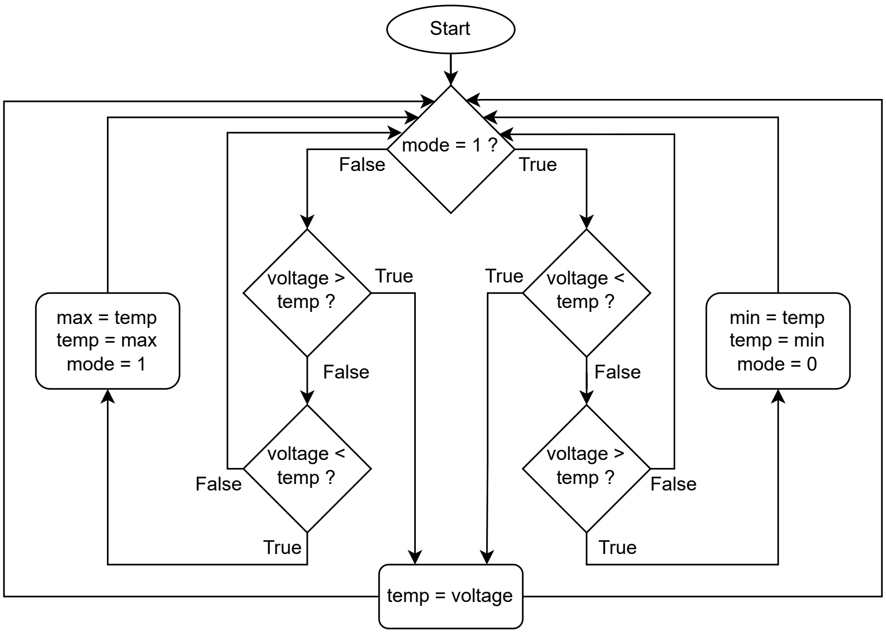

Figure 4.13: Peak-detector algorithm flow-chart. The variables $voltage$ and $temp$ correspond to consecutive samples of the signal, while min and max correspond to the minimum and maximum peak voltages.

$$V_{\text{peak}} = \frac{\sum Maximum_{\text{buffer}} + \sum |Minimum_{\text{buffer}}|}{N_{\text{peaks}}}, \tag{4.23}$$

where $\mathrm{N}_{\text{peaks}}$ is the number of peaks acquired.

4.2 Optimized AFE Circuit

The flexibility and reconfigurability of the fully-PSoC integrated AFE circuit, presented in section 4.1, come at the expense of accuracy and precision. The accuracy of the AFE #1 circuit decreases considerably for sensor impedances lower than 200 Ω , and the circuit operates at a fixed frequency of 2 kHz, which is a limiting factor since the sensitivity of the sensors depends on the driving frequency, as presented in subsection 3.3.3.

As such, in this section, the design of an optimized AFE circuit that can be more accurate and precise than the AFE #1 circuit and can drive the sensors in a wider frequency range, is presented, and is denominated AFE #2 circuit.

4.2.1 Optimizations and Specifications

To optimize the AFE #1 circuit, the error sources that contribute to its limited accuracy are studied. The main source of inaccuracy is related to the analog multiplexer high on-resistance and mismatch between channels, as well as considerable off-state leakage currents.

The high on-resistance of the multiplexer impacts the accuracy of the measurement of low impedance sensors, particularly bellow 500 Ω . In addition, the on-resistance of each of the 12 analog channels varies considerably. Furthermore, a relatively low off-resistance of the multiplexer switches results in a leakage current that flows into the amplifier and is summed with the current of the active sensor channel, which culminates in a voltage error.

Apart from the errors generated by the analog multiplexer, the switched capacitor-based programmable-gain TIA integrated into the PSoC 5LP contributes with additional errors. One example of such errors is the tolerance of the trans-impedance gain, which can be as much as 35%, resulting in gain and bandwidth errors. In addition, the noise performance of such TIA is moderate and could be improved.

To correct the latter errors, a detailed calibration of each AFE channel was done, as presented in subsection 4.1.6, however, it proved not to be completely effective. A more effective solution is to implement the analog multiplexer with discrete components external to the PSoC 5LP. This way, a dedicated analog multiplexer IC can be chosen to yield a higher accuracy level.

Likewise, for the AFE #2 circuit, a more accurate and precise amplifier circuit is externally implemented to the PSoC 5LP. For that, a similar amplifier circuit topology was chosen, which is based on a programmable-gain TIA. As in the AFE #1 circuit, a way to control the trans-impedance gain is mandatory to maximize the use of the ADC input dynamic range, which maximizes the precision level of the circuit. Also, such amplifier circuit is designed to operate in a frequency range between 100 Hz and 100 kHz, which corresponds to the range of frequencies relevant to the group of sensors.

The specifications for the AFE #2 circuit are presented in Table 4.5.

Parameter	Specification
$Z_{\text{sensor,min}}$	$200\ \Omega \leq (\geq 50\ \Omega)$
$F_{\text{drive,min}}$	100 Hz
$F_{\text{drive,max}}$	100 kHz
Effective Resolution	12-bit

Table 4.5: AFE #2 circuit specifications

4.2.2 Circuit Architecture

As previously mentioned, the AFE #2 circuit topology is similar to the AFE #1 circuit. More specifically, both AFE circuits feature a configurable DDS, a 12:1 analog multiplexer, and a programmable-gain TIA whose output is connected to the input of an ADC. The most relevant differences regarding the AFE #2 circuit are:

- Instead of generating a 100mV amplitude sine-wave signal with a frequency of 2 kHz, the DDS generates a sinusoidal frequency sweep between 100 Hz and 100 kHz, with an amplitude of 100mV, consisting of 7 different frequencies (100 Hz; 200 Hz; 1 kHz; 2 kHz; 10 kHz; 50 kHz; and 100 kHz), which were identified as relevant in subsection 3.3.3.

- The 12-channel analog multiplexer is implemented using multiple 4-channel analog multiplexer ICs, external to the PSoC 5LP. Such multiplexer ICs feature low on-resistance and accurate channel-to-channel matching.
- The TIA is implemented using a precision Op-amp with multiple configurable feedback resistor and compensation capacitor networks. For that, another analog multiplexer is used in the feedback network of the Op-amp, which can be controlled by the PSoC 5LP GPIOs.
- Due to the high frequency specification of 100 kHz, the SAR ADC is used to sample the output voltage of the amplifier, which is capable of a sampling rate of 1 MHz at a resolution of 12-bit, as presented in subsection 2.2.2.
- The circuit is powered using an external 3.3V voltage regulator.

Considering the specifications for the AFE #2 circuit, its simplified circuit block diagram is presented in Figure 4.14.

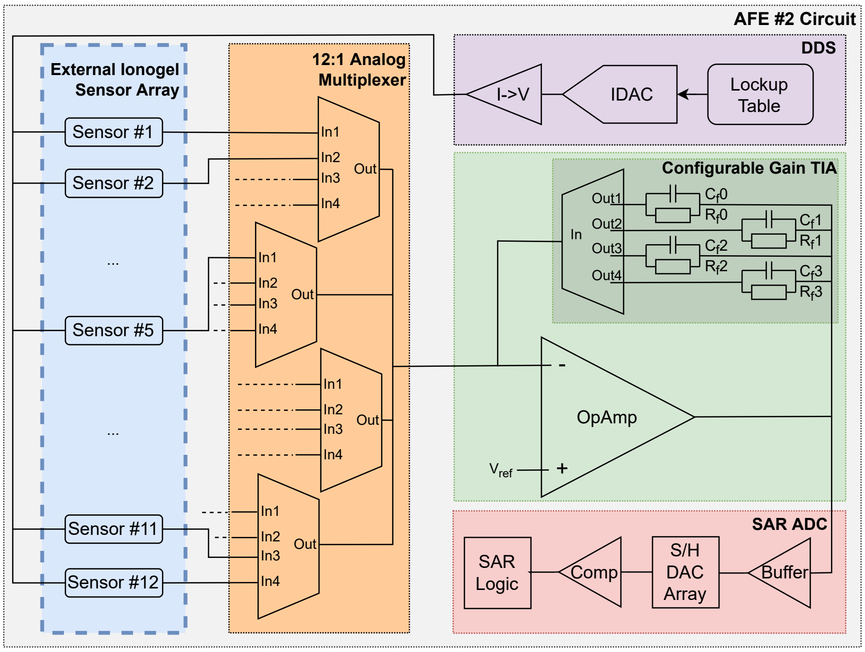

Figure 4.14: AFE #2 simplified circuit block diagram. Digital sub-system and calibration circuit not shown.

4.2.3 Multi-Channel Analog Multiplexer Design

The implementation of the analog multiplexer can be made with multiple analog multiplexer ICs. Due to the need of 12 channels, three 4-channel analog multiplexer ICs are used, whose outputs are connected to a common bus.

To choose the most appropriate multiplexer IC, the values of on-resistance, leakage current, switching time, capacitance and other parameters are calculated to yield an error inferior 5%. If such error is linear with frequency, current, input voltage, and is similar between the 12 different channels, then a simple calibration procedure can be implemented to improve the overall accuracy of the circuit.

Considering that the on-resistance of the multiplexer can be modeled as a resistor, R_{on}, in series with the impedance of the sensor, the error due to the on-resistance of the multiplexer switch is calculated by:

$$Error_{\text{Ron}}(\%) = \frac{R_{\text{on,max}}}{|Z_{\text{sensor}}| + R_{\text{on,max}}} * 100, \tag{4.24}$$

where $|Z_{\text{sensor}}|$ is the absolute value of the impedance of the sensor, and $R_{\text{on,max}}$ is the maximum on-resistance of the switch, which is dependent on the input voltage. It is possible to conclude that the error due to the on-resistance of the multiplexer increases as the impedance of the sensor decreases. Considering the specification of $Z_{\text{sensor}} = 50\ \Omega$, presented in Table 4.5, the error as a function of the multiplexer on-resistance is presented in Table 4.6.

R_{on}	Error
50 mΩ	0.1 %
250 mΩ	0.5 %
500 mΩ	1 %
1 Ω	2 %
2.5 Ω	5 %
5 Ω	10 %

Table 4.6: Error due to multiplexer on-resistance.

Thus, for this application, the maximum multiplexer on-resistance should be inferior to 2.5 Ω . The error due to the mismatch between channels, is calculated by:

$$Error_{\text{channels}}(\%) = \frac{\Delta R_{\text{on,channel}}}{R_{\text{on}}} * 100, \tag{4.25}$$

where $\Delta R_{\text{on,channel}}$ corresponds to the on-resistance matching between channels. In addition, the error due to the leakage current of the off-state multiplexer switches can be calculated by:

$$Error_{\text{Leakage}}(\%) = \frac{I_{\text{leakage,switch}} N_{\text{switches,off}} R_{\text{f}}}{V_{\text{drive}}} * 100, \tag{4.26}$$

where $I_{\text{leakage,switch}}$ is the leakage current that flows through an open multiplexer switch, $N_{\text{switches,off}}$ is the total number of open switches (11), R_f is the feedback resistance in the Op-amp feedback loop, and V_{drive} is the amplitude of the drive signal (100mV). Considering the worst-case scenario and assuming $R_f = 200\ \text{k}\Omega$, Table 4.7 contains the error due to the leakage current of a multiplexer switch.

$I_{\text{leakage,switch}}$	Error
5 pA	0.01 %
45 pA	0.1 %
91 pA	0.2 %
227 pA	0.5 %
455 pA	1 %

Table 4.7: Error due to multiplexer leakage current.

In addition to the DC errors that are inherent to multiplexers, AC errors are also important. As presented in subsection 2.2.5, the parasitic capacitance of the multiplexer switches and their on-resistance can limit the bandwidth of the circuit. Furthermore, the capacitance of the control pins can also affect the switching time.

Considering the calculated switch specifications, the TMUX1112 [78], from Texas Instruments, is appropriate for the application, and its characteristics are summarized in Table 4.8. This way, the maximum error introduced by the multiplexer is 5.5%, which is mostly due to the on-resistance, and the maximum mismatch between channels is 6.5%, which is acceptable. In addition, the multiplexer fulfils the requirements for switching time, operating voltage, and bandwidth.

Parameter	Specification
On-resistance	2 Ω
On-resistance flatness	850 mΩ
On-resistance matching between channels	130 mΩ
Leakage Current	5 pA
On-capacitance	17 pF
Bandwidth	300 MHz
Switching Time	83 MHz
Number of Channels	4
Supply Voltage	5V

Table 4.8: TMUX1122 specifications.

4.2.4 Programmable-Gain TIA Design

4.2.4.1 Trans-impedance Gain Configurations

As presented in Figure 4.14, the optimized AFE circuit features a TIA, which is based on an Op-amp circuit. To achieve the specifications presented in Table 4.5, the trans-impedance gain of the amplifier is reconfigured, to yield optimal precision in an impedance measurement range between 50 Ω and 200 kΩ . For that, an analog multiplexer is connected in the feedback loop of the amplifier. Different value resistors are connected to each of the multiplexer inputs. This way, by controlling the active multiplexer channel, the trans-impedance gain of the amplifier can be adjusted.

For the AFE #2 circuit, the supply voltage is generated by a 3.3V low-dropout voltage regulator. However, such regulators have a typical regulation accuracy of ±5%. Considering the use of a rail-to-rail Op-amp, the maximum output voltage of the amplifier is considered to be 3.1V. Moreover, the sensor impedance together with the TIA can be mathematically modeled as a voltage amplifier, whose output voltage is given by:

$$V_{\text{out}} = -\frac{R_{\text{f}}}{|Z_{\text{sensor}}|} V_{\text{drive}}. \tag{4.27}$$

This way, the maximum voltage gain of the amplifier, in absolute value, Gain_{max}, is given by:

$$Gain_{\text{max}} = \frac{Vout_{\text{max}} - V_{\text{ref}}}{V_{\text{drive}}}, \tag{4.28}$$

and has a value of 14.5 V/V, considering that V_{ref} = 1.65V. The minimum voltage gain, Gain_{min}, can be chosen to yield a minimum precision level, however, in this case Gain_{min} = 2 V/V. The lowest trans-impedance gain setting, $x = 0$, required for measuring the $Z_{\text{sensor,min}}$ = 50 Ω , is given by:

$$R_{\text{f}}[x = 0] = |Z_{\text{sensor,min}}| * Gain_{\text{max}}, \tag{4.29}$$

where R_{f} represents the trans-impedance gain. The maximum sensor impedance that can be measured with the latter trans-impedance gain, while complying with the minimum voltage gain requirement is given by:

$$|Z_{\text{sensor,max}}| = \frac{R_{\text{f}}[x = 0]}{Gain_{\text{min}}}. \tag{4.30}$$

Considering the previous equations, the minimum trans-impedance gain is 725 Ω , and the maximum sensor impedance that can be measured with the latter trans-impedance gain is 363 Ω . Thus, to measure impedances greater than 363 Ω , another trans-impedance gain value is required, $x = 1$. To ensure a smooth transition between the trans-impedance gain settings, an overlap of 5% was established. Thus, the minimum impedance that can be measured with the trans-impedance gain setting $x = 1$, is given by:

$$|Z_{\text{sensor,min}}[x=1]| = |Z_{\text{sensor,max}}[x=0]|\,(1 - overlap)\,, \tag{4.31}$$

and has a value of 344 Ω . Applying the latter procedure results in a total of 4 trans-impedance gain settings required to cover the entire impedance measurement range. The multiple trans-impedance gain settings are summarized in Table 4.9. However, for $x = 3$, it is not possible to comply with the minimum voltage gain requirement for $|Z_{\text{sensor,max}}|$ = 200 kΩ . This limitation could be solved by adding another trans-impedance gain setting, however, considering the physical implementation of the circuit, this approach would result in the use of two 4-channel multiplexers, which is not ideal. Thus, the circuit is designed to operate with a single 4-channel multiplexer, resulting in 4 distinct trans-impedance gain settings.

x	**$\mid Z_{\text{sensor,min}} \mid$**	**$\mid Z_{\text{sensor,max}} \mid$**	**R_f**
0	50 Ω	363 Ω	725 Ω
1	344 Ω	2.5 kΩ	5 kΩ
2	2.38 kΩ	17.2 kΩ	34.5 kΩ
3	16.4 kΩ	119 kΩ	238 kΩ

Table 4.9: Trans-impedance gain settings.

4.2.4.2 Errors Inherent to Op-amp

As presented in subsubsection 2.2.4.5, there are multiple sources of error in Op-amp circuits. For this application, the most relevant error sources are the input offset voltage, Vos, and the input bias currents, Ibias. Due to the specification of the maximum sensor drive frequency, $F_{\text{drive,max}}$ = 100 kHz, the error due to finite open-loop gain is also considered. In addition, for the implementation of such circuit, 0.1% tolerance resistors with low temperature coefficients are recommended.

Considering an Op-amp with infinite open-loop gain, and the non-ideal channel selection multiplexer, the error voltage due to the Op-amp input offset voltage, is given by:

$$Verror_{\text{vos}} = V_{\text{os}}\left(1 + \frac{R_{\text{f}}}{|Z_{\text{sensor}}| + R_{\text{on}}}\right), \tag{4.32}$$

and is equivalent to an output voltage error percentage given by:

$$Error_{\text{Vos}}(\%) = \frac{V_{\text{os}}}{V_{\text{os}} + V_{\text{drive}}} * 100. \tag{4.33}$$

Table 4.10 contains the error due to the Op-amp input offset voltage.

The error due to the Op-amp input bias currents is given by:

$$Verror_{\text{Ibias}} = -Ibias_{\text{neg}}R_{\text{f}} + Ibias_{\text{pos}}R_{\text{pos}}\left(1 + \frac{R_{\text{f}}}{|Z_{\text{sensor}}| + R_{\text{on}}}\right), \tag{4.34}$$

V_{os}	**Error**
1 μV	0.001 %
10 μV	0.01 %
50 μV	0.05 %
100 μV	0.1 %
500 μV	0.5 %
1 mV	1 %

Table 4.10: Error due to op-amp input offset voltage.

where $Ibias_{\text{neg}}$ and $Ibias_{\text{pos}}$ are the input bias currents of the inverting and non-inverting input terminals of the Op-amp, respectively, and $\mathrm{R_{pos}}$ is the resistance seen by the Op-amp non-inverting terminal. It can be seen that, these errors are dependent on the impedance of the sensor, which is variable. However, considering that $R_{\text{pos}} \approx 0$, the error due to the Op-amp input bias currents is approximately given by:

$$Verror_{\text{Ibias}} \approx -Ibias_{\text{neg}} R_{\text{f}}, \tag{4.35}$$

and can be approximated as a DC error. Thus, considering the errors due to the multiplexer circuit, the output voltage of the TIA is given by:

$$V_{\text{out}} = Vref - R_{\text{f}} \left(I_{\text{sensor}} + I_{\text{leakage,mux}} + Ibias_{\text{neg}} \right) + Verror_{\text{vos}}, \tag{4.36}$$

where:

- $I_{\text{sensor}} = \frac{V_{\text{drive}}}{|Z_{\text{sensor}}| + R_{\text{on}}}$
- $I_{\text{leakage,mux}} \approx I_{\text{leakage,switch}} N_{\text{switches,off}}$

This way, the output voltage of the TIA can be decomposed in a DC part, which is independent on the sensor impedance, and an AC part, which is dependent on the sensor impedance. The DC component is given by:

$$V_{\text{out,DC}} = Vref - R_{\text{f}} \left(Ibias_{\text{neg}} + I_{\text{leakage,mux}} \right) + V_{\text{os}}, \tag{4.37}$$

and the AC component is given by:

$$V_{\text{out,AC}} = -\frac{R_{\text{f}}}{|Z_{\text{sensor}}| + R_{\text{on}}} V_{\text{drive}}. \tag{4.38}$$

The DC component of the TIA output voltage can vary slightly around the reference voltage, due to the leakage and bias currents, however it does not present an error since the calculation of the sensor impedance is independent of the average value of the TIA output voltage. This way, the impedance of the sensor can be calculated by:

$$|Z_{\text{sensor}}| = R_{\text{f}} \frac{|V_{\text{os}} - V_{\text{drive}}|}{V_{\text{out,AC}}} - R_{\text{on}}. \tag{4.39}$$

However, the latter expression becomes inaccurate as the open-loop gain of the Op-amp decreases with frequency. This error can be described as:

$$Error_{\mathrm{Gain}}(\%) = \frac{1}{A\beta} * 100, \tag{4.40}$$

where A is the frequency dependent open-loop gain of the Op-amp, and β is the feedback attenuation factor. Thus, considering the theory presented in subsubsection 2.2.4.2, the output voltage of the amplifier is given by:

$$V_{\mathrm{out,AC}} = -\frac{AR_{\mathrm{f}}}{R_{\mathrm{f}} + A\left(|Z_{\mathrm{sensor}}| + R_{\mathrm{on}}\right)} V_{\mathrm{drive}}, \tag{4.41}$$

and the impedance of the sensor is calculated by:

$$|Z_{\mathrm{sensor}}| = R_{\mathrm{f}}\left[\left|\frac{V_{\mathrm{drive}}}{V_{\mathrm{out,AC}}}\right| - \frac{1}{A}\right] - R_{\mathrm{on}}. \tag{4.42}$$

Open-loop Gain	Error
100 dB	0.015 %
90 dB	0.05 %
80 dB	0.15 %
60 dB	1.5 %
50 dB	5 %

Table 4.11: Error due to op-amp limited open-loop gain.

In Table 4.11 the error due to limited open-loop gain at high frequencies, for a closed-loop gain of $Gain_{\mathrm{max}} = 14.5$ V/V, is presented. Considering the requirements, the OPA2320 [79], from Texas Instruments, is adequate for the application. The most relevant characteristics of such Op-amp are summarized in Table 4.12.

Considering the specifications of the Op-amp presented in Table 4.12, as well as the specifications of the multiplexer presented in Table 4.8, the maximum error of the circuit occurs for the measurement of low impedance sensors, and as a value of 3.8% at a frequency of 100 Hz, and increases to 8.9% at a frequency of 100 kHz, due to the finite Op-amp open-loop gain. Considering the remaining Op-amp error sources presented in subsubsection 2.2.4.5, such as CMRR and PSRR, the maximum error is inferior to 10%, at 100 kHz.

However, the majority of the error can be compensated in software, by calculating the impedance of the sensor with Equation 4.42. This way, the remaining error is due to temperature drifts and mismatch between the multiplexer channels, which has a maximum value of 1.6%. Furthermore, an auto-calibration procedure can be implemented to further reduce the 1.6% error, culminating in a high accuracy AFE circuit.

Parameter	**Specification**
Input Offset Voltage (max)	150 μV
Input Bias Current (max)	0.9 pA
Input Bias Current Offset (max)	0.9 pA
Input Capacitance (differential + common)	9 pF
Open-loop Gain (DC)	132 dB
Open-loop Gain (100 kHz)	48 dB
Gain-Bandwidth Product (typical)	20 MHz
Voltage Swing from Rails (maximum)	35 mV
Input Noise Voltage Density (1 kHz)	8.5 nV/$\sqrt{Hz}$
Input Noise Current Density (1 kHz)	0.6 fA/$\sqrt{Hz}$

Table 4.12: OPA320 specifications.

4.2.4.3 Amplifier Bandwidth and Stability

TIAs can easily become unstable for high trans-impedance gain levels and large capacitive inputs. Thus, to ensure the correct operation of the TIA, a stability analysis is mandatory. The stability of the amplifier can be accomplished by correctly sizing the feedback capacitors, C_f, of the different trans-impedance gain configurations. For that, the minimum feedback capacitance that ensures the stability of the TIA circuit is given by:

$$C_\text{f,min} = \sqrt{\frac{C_\text{in}}{2\pi R_\text{f} GBW}}, \tag{4.43}$$

where:

$$C_\text{in} = C_\text{mux1} + C_\text{mux2} + C_\text{sensor} + C_\text{op-amp} + C_\text{PCB}, \tag{4.44}$$

where C_mux1 and C_mux2 is the capacitance of the multiplexer at the input and in the feedback network of the Op-amp, respectively, C_sensor is the capacitance of the sensor, $\text{C}_\text{op-amp}$ is the total capacitance of the Op-amp input, and C_PCB is the parasitic capacitance of the PCB. The values for C_mux1 and C_mux2 are obtained by:

$$C_\text{mux} = C_\text{on} N_\text{on} + C_\text{off} N_\text{off}, \tag{4.45}$$

where C_{on} and C_{off} correspond to the capacitance of an active and non-active multiplexer switch, and N_{on} and N_{off} correspond to the number of active and non-active multiplexer switches. Considering the values presented in the multiplexer datasheet, C_{mux1} = 204 pF, and C_{mux2} = 268 pF. The value of C_{PCB} was considered to be 10 pF.

Considering the values of feedback resistance, R_f, presented in Table 4.9, the minimum feedback capacitance, C_f, required to ensure stability for the highest trans-impedance gain, is 4.2 pF, while for the minimum trans-impedance gain, the value required is 76 pF.

To maximize the SNR of the circuit, the closed-loop bandwidth was limited to approximately 300 kHz, to obtain minimal attenuation at the maximum frequency of 100 kHz. In addition, considering the standard values for resistors and capacitors, in Table 4.13, the final values for the circuit components, and resulting closed-loop bandwidth, are presented.

x	R_f	C_f	$B_{closed\text{-}loop}$	$\lvert Z_{sensor,min} \rvert$	$\lvert Z_{sensor,max} \rvert$
0	750 Ω	680 pF	312 kHz	50 Ω	375 Ω
1	4.99 kΩ	100 pF	319 kHz	350 Ω	2.5 kΩ
2	33.2 kΩ	15 pF	319 kHz	2.4 kΩ	16.6 kΩ
3	221 kΩ	5.6 pF	129 kHz	15.7 kΩ	200 kΩ

Table 4.13: Final AFE #2 circuit component values.

It is possible to observe that for the highest trans-impedance gain configuration, $x = 3$, the bandwidth is limited to 129 kHz, in order to guarantee stability, due to the relatively large capacitance of the sensor, C_{sensor} = 250 pF. However, this results in an attenuation of approximately 2dB, at 100 kHz.

4.2.5 Simulation

In this subsection, the AFE #2 circuit was simulated, in order to assess its AC and noise performance. For that, the circuit was simulated using a dedicated Texas Instruments simulation software, TINA-TI [80]. The macro-cells of the OPA2320 and TMUX1122 were used, to obtain a realistic simulation.

4.2.5.1 Stability Analysis

To assess the stability of the AFE #2 circuit, its AC transfer characteristic was obtained using the TINA-TI simulation software. Two bode-plots were obtained, corresponding to the lowest and highest trans-impedance gain configurations, $x = 0$ and $x = 3$, respectively. From the bode-plots, the PM was obtained, which is an indicator of the circuit stability. In Figure 4.15, the bode-plot obtained for $x = 0$ is presented.

From the bode-plot it is possible to observe a voltage gain of 23.5 dB, equivalent to 14.5 V/V, which is constant up to a frequency of 100 kHz. The -3dB frequency is at 255 kHz, which is close to the value calculated in the design process. In addition, the calculated

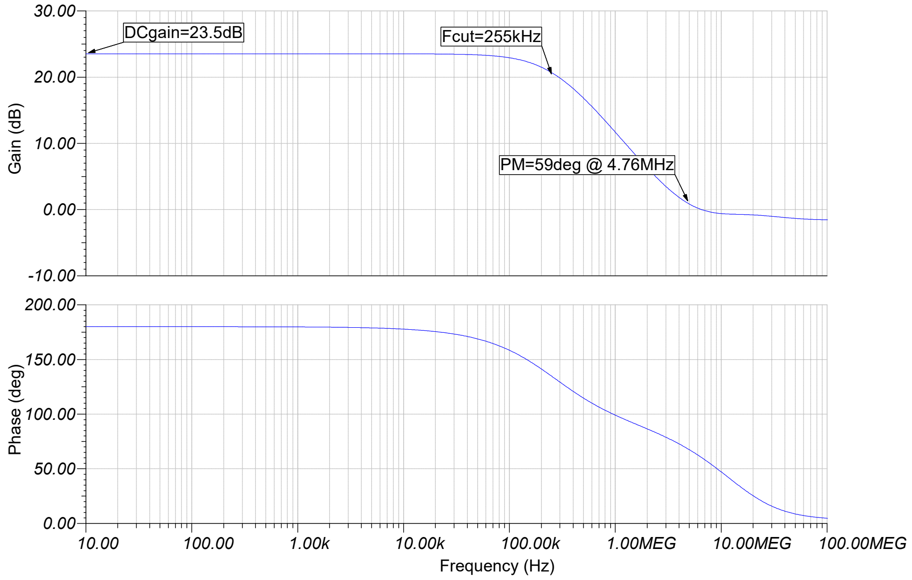

Figure 4.15: Bode-plot of AFE #2 circuit configured for the lowest trans-impedance gain, $x = 0$. Graph obtained in [80].

PM is 59°, which is indicative of a stable circuit, and was measured at a frequency of 4.76 MHz. In Figure 4.16, the bode-plot obtained for $x = 3$ is presented.

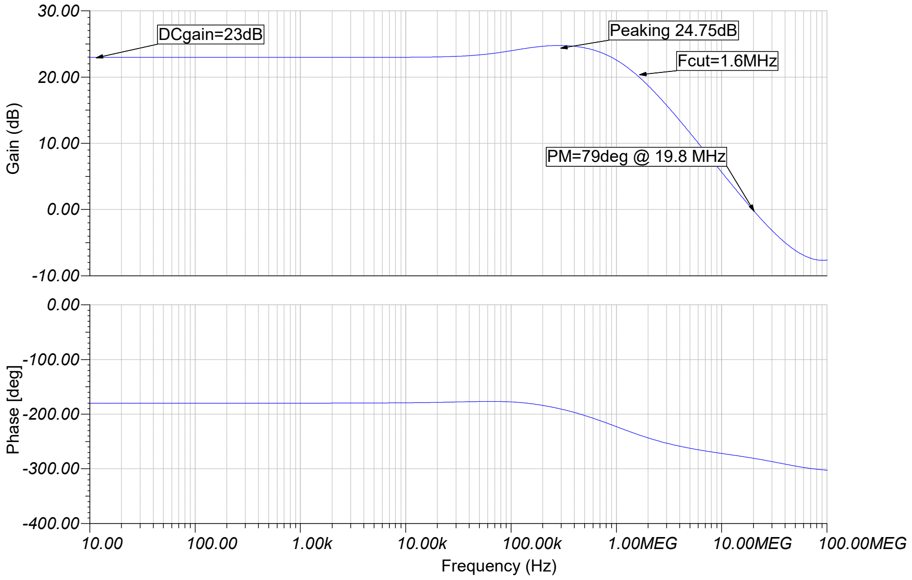

Figure 4.16: Bode-plot of AFE #2 circuit configured for the highest trans-impedance gain, $x = 3$. Graph obtained in [80].

From the bode-plot is possible to observe a voltage gain of 23 dB, however the gain curve presents a peak of 24.75 dB, at a frequency of 300 kHz, which indicates that the feedback compensation capacitor, C_f, should be increased to compensate for the parasitic capacitance at the input of the Op-amp. However, this phenomenon has no considerable impact on the circuit. In addition, this results in an extension of the bandwidth of the circuit, increasing the -3dB frequency to 1.6 MHz.

In the latter case, the PM has a value of 79°, which proves the stability of the circuit. However, considering the physical implementation of the AFE #2 circuit, it is recommended that the feedback compensation capacitor, C_f, is tuned to achieve minimal gain peaking. Considering the results, it can be concluded that the circuit is stable.

4.2.5.2 Noise Analysis

The circuit was configured for the highest trans-impedance gain, $x = 3$, which results in a poorer noise performance, than for lower trans-impedance gain configurations. This way, the results are obtained for the worst-case scenario. The total circuit noise referred to the output was calculated, and the result is presented in Figure 4.17.

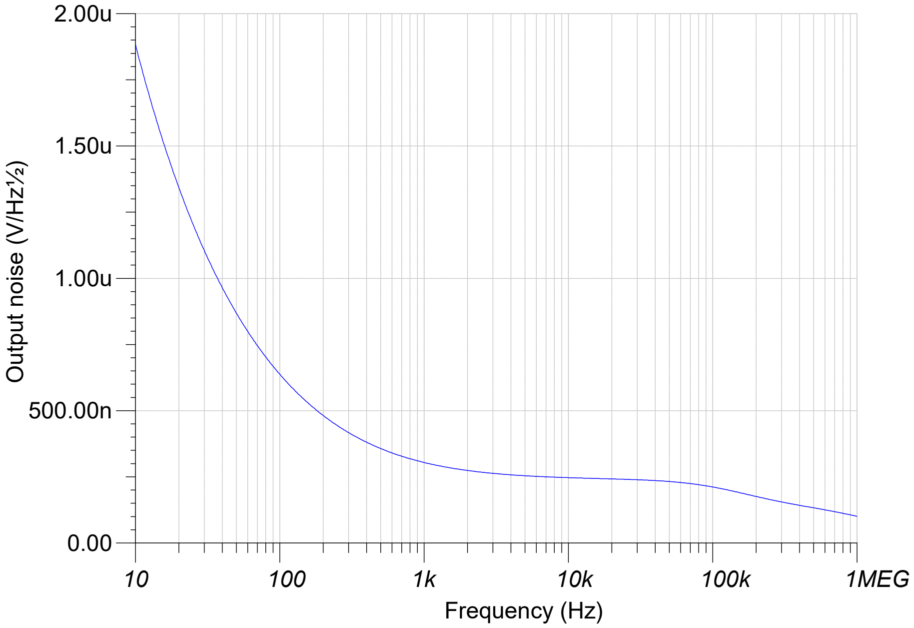

Figure 4.17: AFE #2 total output-referred noise spectral density. Graph obtained in [80].

It is possible to observe that the output voltage noise spectral density of the AFE #2 circuit decreases as the frequency increases. At the beginning of the frequency band of interest, 100 Hz, the output voltage noise spectral density is approximately 640 nV/$\sqrt{Hz}$. For a frequency range between 1 kHz and 100 kHz, the output voltage noise spectral density decreases from 300 nV/$\sqrt{Hz}$ to 210 nV/$\sqrt{Hz}$. For frequencies greater than 100 kHz, the output voltage noise spectral density decreases considerably, as expected, due to the limited signal bandwidth.

Likewise, the SNR of the circuit was obtained using the simulation software. The results are presented in Figure 4.18. In Table 4.14, the values of SNR and ENOB of the AFE #2 circuit are presented for 4 frequencies inside the band of interest. It is possible to observe that at a frequency of 100 Hz, the SNR of the circuit has a maximum value of 97.8 dB, which is equivalent to an ENOB of 16-bit. At 100 kHz, the SNR decreases to 82.5 dB, which is equivalent to an ENOB slightly above 13-bit. Using the same procedure for the noise analysis as in subsection 4.1.4, similar ENOB results are obtained.

Considering the lowest trans-impedance gain configuration, $x = 0$, the minimum and maximum SNR values are 89 dB and 100 dB, respectively, resulting in an ENOB between 14.5-bit and 16.3-bit.

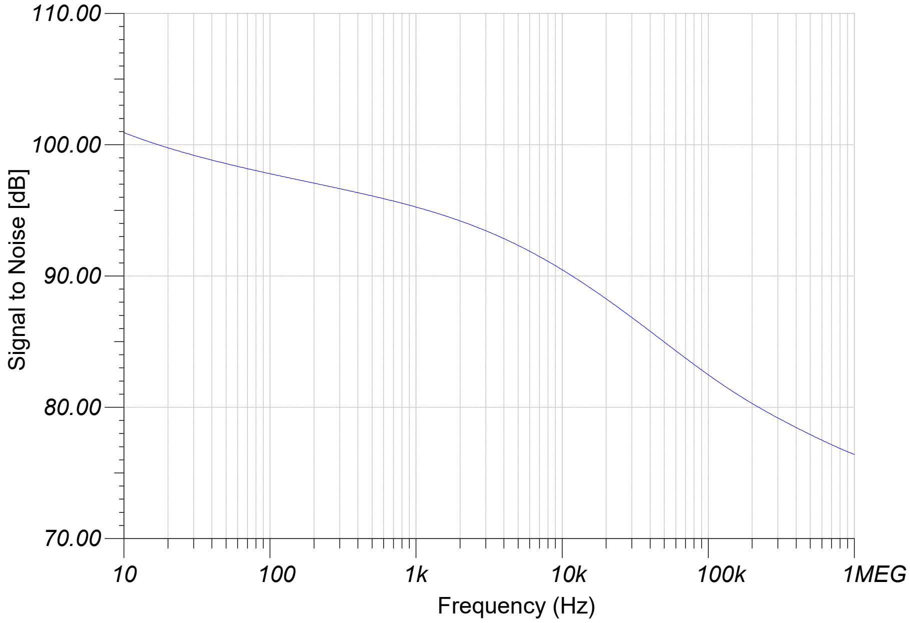

Figure 4.18: AFE #2 SNR simulation obtained in TINA-T I[80].

Frequency	SNR	ENOB
100 Hz	97.8 dB	16.0-bit
1 kHz	95.2 dB	15.5-bit
10 kHz	90.5 dB	14.7-bit
100 kHz	82.5 dB	13.4-bit

Table 4.14: AFE #2 SNR inside the frequency band of interest.

To maximize the precision of the AFE #2 circuit, a ADC with a resolution between 13-bit and 16-bit, is required. In practical terms, due the highest signal frequency of 100 kHz, the PSoC 5LP ΣΔ ADC is not suitable, since it has a limited sampling frequency of 56 kHz, at a resolution of 13-bit. On the other hand, the PSoC 5LP SAR ADC provides a resolution of 12-bit, at a sampling rate of 667 kHz, which is adequate for the application.

However, a strategy of using both ADCs could be implemented, in a way that the ΣΔ ADC is used to sample signals with a resolution of 16-bit, up to a frequency of 10 kHz, while the SAR ADC is used to sample signals with a resolution of 12-bit, up to a frequency of 100 kHz. This could be accomplished by connecting both ADC inputs to the output of the amplifier and controlling them using software. However, this results in a more complex circuit, which does not present a considerable improvement in the final impedance measurement precision, for the application. Thus, the sampling is done using the SAR ADC, resulting in an effective signal resolution of 12-bit and 667 kHz sampling rate.

4.3 Delivery System Design

As presented in Figure 2.2, at the core of the delivery system of the E-nose is the sample, which contains the VOC, or VOCs, in its saturated headspace. In typical E-nose operation, two cycles exist: exposure; and recovery.

In these two cycles, the sensors are exposed to the saturated headspace of the sample, after which they are exposed to clean ambient air, removing the VOC particles from the sensor detection chamber and resets the sensors to their baseline state. In addition to the latter two phases, a retention phase can be implemented, in which the gaseous sample is trapped inside the sensor detection chamber, promoting the interaction between the two.

To implement this cyclic behavior, an automated system is required. The delivery system is composed of a single, or a set, of pumps and valves, which can be electrically controlled. For example, in the case of the Optical E-nose V4, described in subsubsection 2.1.4.2, the delivery system implements all 3 phases, which makes it more complex, and ultimately increases the wasted parasitic volume of the tubing system, diluting the gas sample.

In addition, a sample heating device is implemented, whose goal is to heat the sample in the flask to a temperature of 37 °C . Even though there are plenty of commercial heaters for the application, the majority tends to be considerably big, heavy, and power-hungry. In addition, typical heaters for this application require a water bath, which increases the complexity of the system. Thus, the design and implementation of a custom sample heating device is presented in subsection 4.3.5.

4.3.1 Positive-Pressure Delivery System

In Figure 4.19, a simplified diagram of the Electrical E-nose V3 delivery system #1, is presented. The delivery system #1 is a positive-pressure system, which means that a pump continuously forces air into the system. This air can be routed between two paths: exposure path; or recovery path. To select the route that the air takes, a set of 2 valves divert the flow between a common inlet and two outlets.

The normally-open (N.O) port is used for the recovery path, and the normally-closed (N.C) port is used for the exposure path. This way, when power is not applied to the system, the inlet and outlet of the sample-flask are closed by the valves, which is mandatory to prevent the VOC flowing thru the system inadvertently.

In the exposure phase the valves are energized, which leads to a unimpeded path between the common port and the N.C port. This way, the air forced by the pump pushes the saturated headspace of the sample, containing the analyte, out of the sample-flask into the sensor detection chamber, where the interaction with the sensors occurs. After

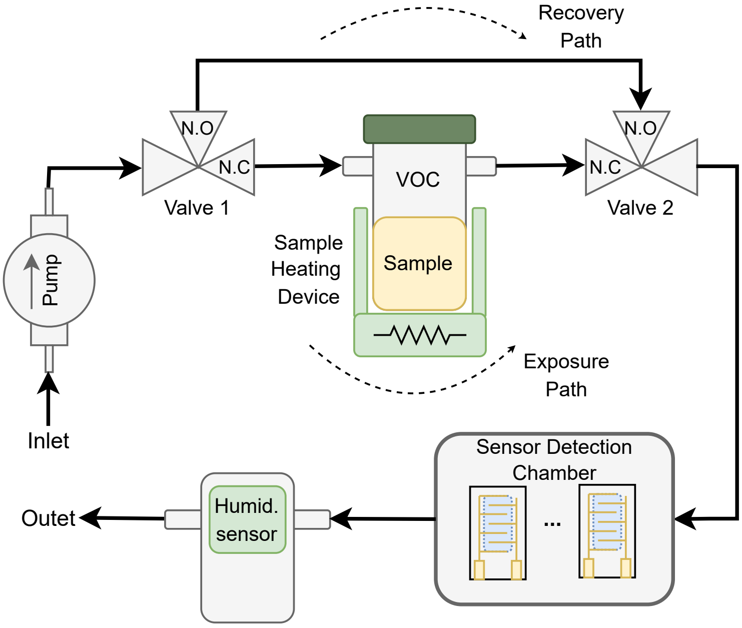

Figure 4.19: Simplified diagram of delivery system #1.

the exposure phase, the power for the valves is turned off, and the common inlet of each is connected to the N.O port. Thus, the air forced by the pump bypasses the sample-flask, which is sealed, and is routed to the sensor detection chamber, trough valve #2.

4.3.2 Negative-Pressure Delivery System

In Figure 4.20, a simplified diagram of the Electrical E-nose V3 delivery system #2, is presented. The goal of this variation is to be more compact, minimize the wasted volume in tubing and to reduce the VOC travel distance between the sample-flask and the detection chamber. In addition, this delivery system setup is targeted to low VOC concentrations, where the experiments consist in a single exposure and recovery phase.

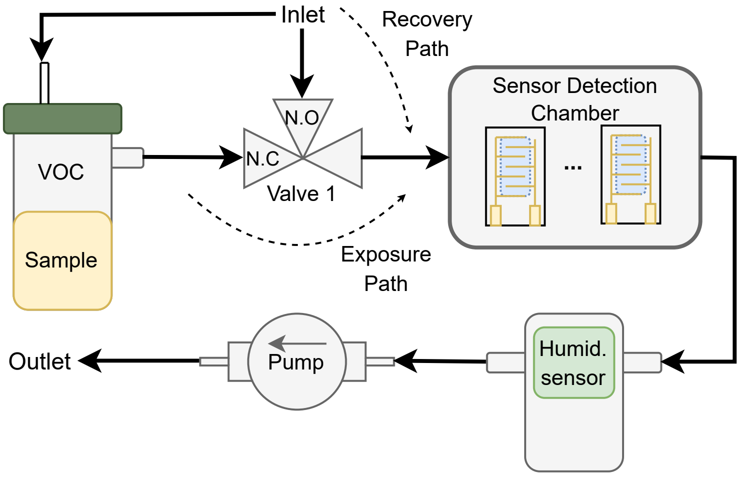

Figure 4.20: Simplified diagram of delivery system #2.

Contrary to the delivery system #1, this variation is based on a negative-pressure differential between the input and output, which means that a vacuum is created. In the delivery system #2, the pump is placed at the output of the system, with the outlet of the pump being the outlet of the system. When the pump is energized, a negative pressure develops across the sensor detection chamber. Depending on the state of the valve, either the VOC or clean ambient air is forced into the detection chamber, due to the vacuum.

In the exposure phase, the valve is energized, so that the outlet of the sample-flask is connected to the inlet of the detection chamber. Moreover, a small orifice is made in the lid of the sample-flask, and is kept open, which is mandatory for the vacuum to develop, since a typical inlet port is excessively big, and does not trap the VOC inside the flask if open. On the recovery phase, the power to the valve is removed, and ambient air is forced into the sensor detection chamber due to the vacuum.

This variation of the delivery system has the advantages of being more compact and less complex since it requires one valve less than the delivery system #1. In addition, due to the need of less components, the parasitic wasted volume in tubing is greatly reduced. However, this variation has some disadvantages such as, not including a sample heating device, and that it can be more unreliable, since any small leak in the system leads to a great loss in vacuum pressure.

4.3.3 Mass-Flow Controller-based Delivery System

In addition to the two previous variations of the delivery system, the Electrical E-nose V3 was also designed to operate with an MFC-based delivery system, denominated delivery system #3. These devices have been previously used in the sensor characterization experiments depicted in subsection 3.2.2.

Contrary to delivery system #1 and delivery system #2, the MFC-based delivery system is already assembled in an up-right panel, depicted in Figure 3.3a. As previously mentioned, the MFCs are controlled via USB. Thus, this delivery system #3 only requires the control of a single solenoid valve.

4.3.4 Delivery System Power Control Circuit

As previously mentioned, for the operation of both delivery system variations, a way to control the power to the pump and valve(s) is required. For the Electrical E-nose V3, a D3K micropump from TCS Micropumps [81] is used, and the valves are the NR1-3-12 from Clippard [82]. The most relevant specifications for the pump and valves are presented in Table 4.15.

To only turn on the pump during an experiment, a power signal is required. Since the valves operate in equal manner, a single power signal is required for the operation of both. In addition, since the sample heating device has its own thermostat, it does not require a controllable power signal, rather a simple power connection.

	Pump	**Valves**
Manufacturer	TCS Micropumps	Clippard
Model	D3K	NR1-3-12
Supply Voltage (V)	3 to 6	12
Supply Current (mA)	50 to 350	100
Input Power (W)	0.3 to 2.1	1.2
Maximum Capacity (L/m)	3.6	6
Material	PC and ABS polymer	PTFE

Table 4.15: Pump and valve specifications.

Thus, the delivery system power control circuit has to provide two distinct power signals, capable of carrying the necessary power to the devices, and provide continuous power to the thermostat of the sample heating device. This is also true for the delivery system #2.

Considering the power levels required, a decision of using an external 12V power supply was made. Also, due to the inductive properties of the electric motor of the pump and solenoid of the valves, a galvanic isolation between the delivery system power control circuit and the AFE circuit is mandatory, to prevent considerable voltage spikes that interfere with the sensitive analog signals and can damage the sensitive mixed-signal circuit.

This way, the power control circuit is implemented with relays, which provide a simple and effective way to switch power to the delivery system loads. Alternatively, an equivalent circuit could be implemented with MOSFETs to reduce the circuit size and power consumption, however, for this application the relay circuit does not present a significant constrain. To enable further expansions of the system, a circuit consisting of 4 relays was implemented.

In Figure 4.21, the schematic for a single relay circuit, is presented. Thus, the delivery system power control circuit is constituted by 4 replicas of the latter circuit, as shown in Figure A.20.

Miniature 12V relays were used, which feature two independent switches, rated at a maximum of 3A each. To increase the current capacity of the circuit, the two switches were connected in parallel, resulting in a maximum switching current of 6A, which is far superior to the intended operating current. The power to the load, that is switched by the relay circuit, comes from an external 12V 36W medical-grade switching power supply.

The relay coil is rated at 150 mW, which is equivalent to a coil current of 12.5mA. To control the relay, one terminal of the coil is connected to the 12V power supply rail, and the other terminal is switched to ground with an opto-isolator, which features an NPN photo-transistor on the load side. To turn on the photo-transistor, and thus control the relay, the Light-Emitting Diode (LED) in the input side of the opto-isolator is controlled by a digital pin of the PSoC 5LP, whose signal is labeled as R1_CTR.

Moreover, it is important to note that two distinct and isolated ground potentials

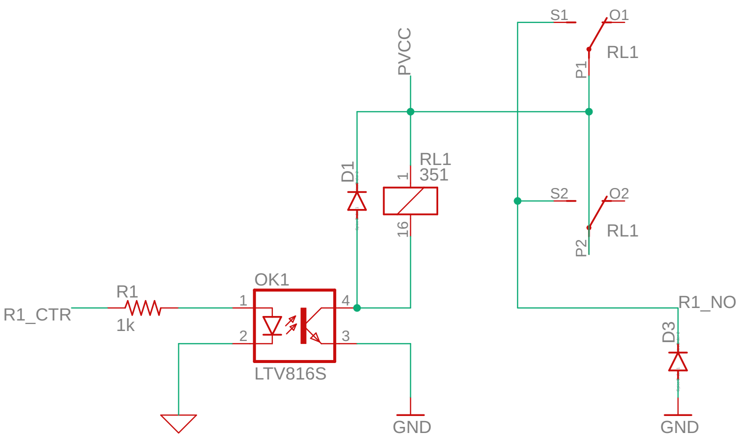

Figure 4.21: Schematic for a single relay circuit with optical isolation.

exist: AFE ground, which corresponds to the USB ground; and power supply ground, corresponding to the external power supply. This way, the galvanic isolation between the high-power circuit and the AFE circuit is guaranteed, due to the optical-isolation and separate ground signals.

Due to the inductive properties of the relay coil, and according to Lenz's law, when the relay is de-energized, a back Electromotive Force (EMF) is generated, which leads to a current with opposite polarity. Because the circuit is open, and the current has no low impedance path to ground, a high-voltage spike is created, which can damage the circuit. To prevent such voltage spike, a flywheel diode is placed in parallel with the relay coil, which becomes a conductive path for the back EMF generated current. Likewise, due to the inductive properties of the delivery system loads, another flywheel diode is added at the output of the relay switch, which is labeled as R1_NO.

As presented in Table 4.15, the pump is rated at a maximum of 6V, however the supply rail is 12V. To comply with the pump requirements, an additional voltage regulator circuit was implemented. This circuit can be bypassed, to enable the use of a 12V pump, if necessary.

4.3.5 Sample Heating Device

As previously mentioned, a custom sample heating device was designed to fulfil the size and power requirements of the system. Furthermore, this system does not require a water bath, which not only is easier to use, but also the eliminates problems related to water spillage.

A resistive heater was implemented, through the use of multiple ceramic power resistors, which can be closely placed alongside the perimeter and base of the sample-flask. It was observed that 20W to 30W of heating power was enough to quickly reach a temperature of 37°C. For that, four 33 Ω 5W resistors were placed around the flask and another on the bottom, which were connected in parallel, resulting in a net resistance of 6.6 Ω and a total maximum power dissipation of 25W. Thus, considering a power supply voltage of 12V, the current for the heater device is approximately 1.8A, which is appropriate for the circuit and power supply used.

A commercial thermostat module was used to control the temperature, which is composed of a temperature sensor, a relay circuit, and an LCD screen with push-buttons, that enable the E-nose user to manually set the target temperature of the sample. The resistor array is switched by the thermostat relay circuit, and the temperature sensor is attached to one of the resistors.

4.4 Electronics Module Design

4.4.1 Architecture

For the implementation of the electronics of the Electrical E-nose V3, presented in section 4.1 and section 4.3, an electronics module was created. This module consists of two PCBs, that were designed using Eagle [83].

One of the PCBs, the main PCB, implements the AFE circuit, the delivery system power control circuit, and provides all the necessary connections, such as a power supply input, an external temperature and RH sensor port, an USB port, and controlled power outputs for the delivery system loads. Furthermore, the main PCB features a dedicated expansion port that can be used to connect an additional PCB, which implements the optimized AFE circuit presented in section 4.2.

The other PCB, denominated adapter PCB, is used to route the sensitive analog signals from the sensors to the AFE in the main PCB. More specifically, this PCB is designed to fit a 72-pin card-edge connector [84], to which the electrodes of the 12 sensors in the sensor detection chamber electrically connect to.

Considering the sensitive nature of the sensor analog signals, and the precision requirements for the AFE circuit, electromagnetic shielding for the PCBs is mandatory. For that, a number of Electromagnetic Interference (EMI)-resistance and Electromagnetic Compatibility (EMC) compliant aluminum enclosures are available on the market, and provide a stable, reliable, and sturdy housing for the PCBs, as well as protection against mechanical damage.

The company Hammond Manufacturing provides various models of extruded aluminum enclosures, which are designed to fit standard EuroCard-sized PCBs. For example, the 1457-EMI series [85] provides the required electromagnetic shielding, and the PCBs can be fitted by sliding it into dedicated slots. In addition, the aluminum enclosure can easily be machined or drilled to accommodate connectors.

As previously mentioned, the sensors are electrically connected to a 72-pin card-edge connector, which is placed inside the sensor detection chamber. Since each sensor requires an individual and a common connection, a total of 13 connections are required for the sensor detection chamber. The approach taken by the designers of the Electrical E-nose V2, presented in subsubsection 2.1.4.1, was to use individual wires to connect the sensor detection chamber to the AFE circuit. However, this leads to interference and noise in the sensitive analog signals, due to the length required and lack of shielding.

To solve the latter problem, a decision to reduce the length of the connection between the sensor detection chamber and the AFE circuit was made and consists of implementing an adapter PCB to the sensor chamber, to which the card-edge connector directly connects to. This way, the 13 signals are routed in this adapter PCB, which features and additional 2 connectors, that are used to pass the signals to the AFE circuit, in the main PCB. Thus, by using the adapter PCB in the sensor detection chamber, and directly connecting it to the main PCB, the length of the connection is minimized, and no wiring is required.

In addition, the PCB ground-planes provide shielding to the signals, which further helps to prevent noise and interference. Also, this arrangement is also used to mechanically stabilize the sensor detection chamber, by attaching it to the enclosure of the main PCB. This way, the sensor detection chamber is part of the electronics module.

After the decision of integrating the sensor detection chamber into the electronics module, some decisions regarding the remaining E-nose system wiring were made. More specifically, shielded cables terminated with mini-DIN connectors were chosen for the connections with the external temperature and RH sensor, which provide a reliable mechanical interface and protection against noise and interference. In addition, a 2.1mm DC jack was used as the power input connector. Lastly, the PSoC 5LP offers a micro-USB connector, which was used for the connection with a computer.

4.4.2 Printed Circuit Board Design

As previously mentioned, the electronics of the Electrical E-nose V3 are implemented in two PCBs: main PCB; and adapter PCB.

4.4.2.1 Main PCB

The main PCB was designed with the PSoC 5LP at its core, which integrates the AFE #1 circuit. In addition, the main PCB features a dedicated expansion port for the AFE #2 circuit PCB since a choice to implement it on a separate PCB was made. This design decision provides some advantages, such as, easier revision of the AFE #2 circuit, flexibility to change the design without the need of redesigning the entire main PCB, and a more efficient assembly since soldering problems in one PCB do not affect the other.

Considering the AFE #1 circuit part, a few external passive components are required, which are presented in Figure A.17. For the implementation of the delivery system power control circuit, as mentioned in subsection 4.3.4, the circuit presented in Figure 4.21 is replicated 4 times. Due to the galvanic isolation requirements, the latter circuit is implemented in a separate part of the main PCB. Thus, the main PCB can be divided in two independent parts: low-power section; and high-power section.

In Figure 4.22, the main PCB design is presented, and in Figure A.18 the same PCB design is presented in a higher scale. A 4-layer circuit-board stack-up was chosen since it provides more flexibility at a reasonably low-cost. The top-layer, shown in red, is used to route the majority of signals, including the signals between the PSoC 5LP and one of the expansion headers for the AFE #2 circuit. In addition, the top-layer was also used to route the majority of the power traces in the high-power section.

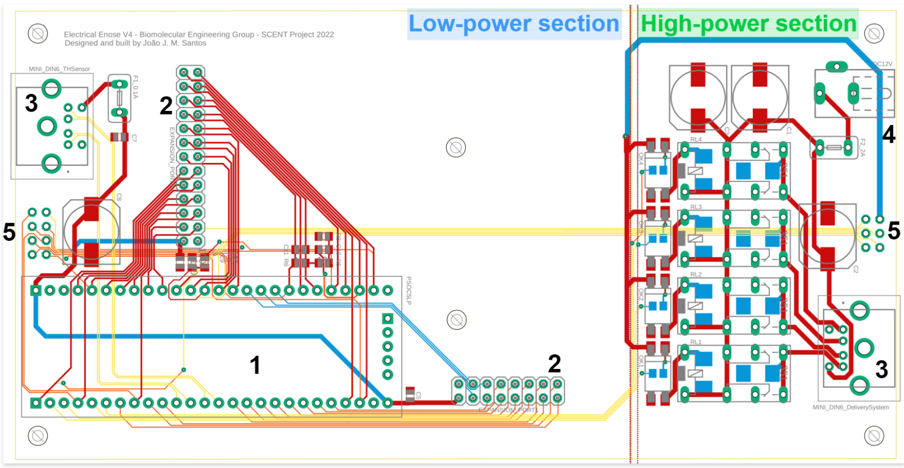

Figure 4.22: Main PCB design. Labels: 1-PSoC 5LP; 2-expansion ports; 3-mini DIN connectors; 4-DC power input; 5-connectors for sensor detection chamber adapter PCB.

The bottom-layer, shown in blue, is primarily used to route the 5V supply-rail in the low-power section. The two inner-layers are shown in yellow and orange and are mostly used to route the sensitive analog signals, and digital signals to the second expansion port, respectively.

To avoid cross-talk and interference in the sensitive analog signals, which are fed into the main PCB by two connectors at each end, these traces were routed as far away as possible from the high-speed digital signal traces. In addition, when this is not possible, *i.e.* there is a high-speed digital signal in an adjacent layer, the two traces are routed at an angle of 90° , which significantly reduces the coupling between the fields.

Each of the 4-layers in the low-power section has a ground-plane, which provides a low impedance path for ground currents, as well as some degree of electromagnetic shielding for the inner layers, where the sensitive analog signals are routed. For the high-power section, a ground-plane is created in the top-layer and in the bottom-layer, which provides a low impedance return path for the relatively high-currents.

Even though the main PCB features few components, due to the PSoC 5LP integration, all the passive components, such as diodes, resistors, and capacitors, are implemented using 0805 Surface Mount Device (SMD) packages, with the exception of bigger electrolytic capacitors, which come in an aluminum can. In addition, the opto-isolators are also implemented in SMD technology. Due to the lack of availability, the relays chosen are of thru-hole technology. Moreover, to provide a better mechanical stability and reliability, all the connectors are thru-hole, since this technology provides more contact area between the component and the PCB, and the solder is typically stronger. More specifically, aluminum-enclosed miniature DIN-6 connectors were used, which present a good relation between small footprint and strength.

To provide a stable 5V supply-rail, three bypass capacitors were connected to it, which are a 10nF 0805 ceramic capacitor, a 100nF 0805 ceramic capacitor, and a 100μF electrolytic capacitor. Each capacitor has a resonant frequency, which is dependent on its capacitance, equivalent series resistance and equivalent series inductance, where the impedance of the capacitor reaches a minimum value and starts to increase for higher-frequencies. Thus, a single capacitor only effectively covers a relatively small frequency range. This way, the impedance curves of the three capacitors are overlapped, which results in overall lower impedance for a larger frequency range. Thus, the larger capacitor provides filtering for lower frequencies, while the smaller capacitors filter higher frequency ripple.

On the other hand, for the high-power section, 3 330μF electrolytic capacitors were used to provide energy storage for the delivery system loads. Since the maximum load current can reach 2.4A, the impedance of the traces can significantly impact the power delivery, leading to a decrease in efficiency. This way, the capacitor's ability to quickly discharge is used to supply the required inrush current when the load is switched. Thus, by placing the capacitor as close as possible to the output connector, the effective length that the current has to travel is reduced.

To select the required trace width for high-power traces, the Saturn PCB Design calculator [86] was used. Considering a typical current of 1.8A and a maximum of 2.4A, a PCB thickness of 1.55mm, and a maximum track length of 100mm, the closest standard trace width required is 1 mm. This way, the current that results in a maximum temperature rise of the PCB trace to 20° C, is 3.2A, and the trace impedance is inferior to 50 mΩ . In addition, no vias were used, and the necessary layer changes were made using the component pads.

4.4.2.2 Adapter PCB

The adapter PCB design has the purpose of accommodating a 72-pin card-edge connector, to which the sensors electrically connect to. Such connector has a length of 166mm, a width of 13mm and features 72 thru-hole pins, spaced at 3.96mm pitch. In Figure 4.23, the design of the adapter PCB is presented.

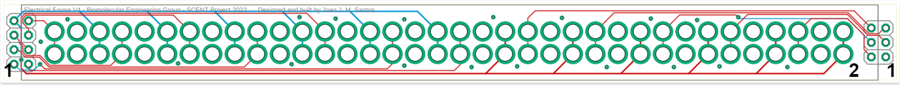

Figure 4.23: Adapter PCB design. Labels: 1-sensor signal connectors; 2-card-edge connector footprint.

Due to its simplicity, the adapter PCB is a 2-layer board. The two layers, shown in red and blue, are used to route the signals from the card-edge connector to the two connectors at each end, which are used to pass the signals to the AFE circuit, in the main PCB. These connectors are 2.54mm male straight headers, which are intended to fit into the female header receptacles in the main PCB, placed in its underside. This way, both PCBs are electrically and mechanically connected, as presented in Figure 4.24.

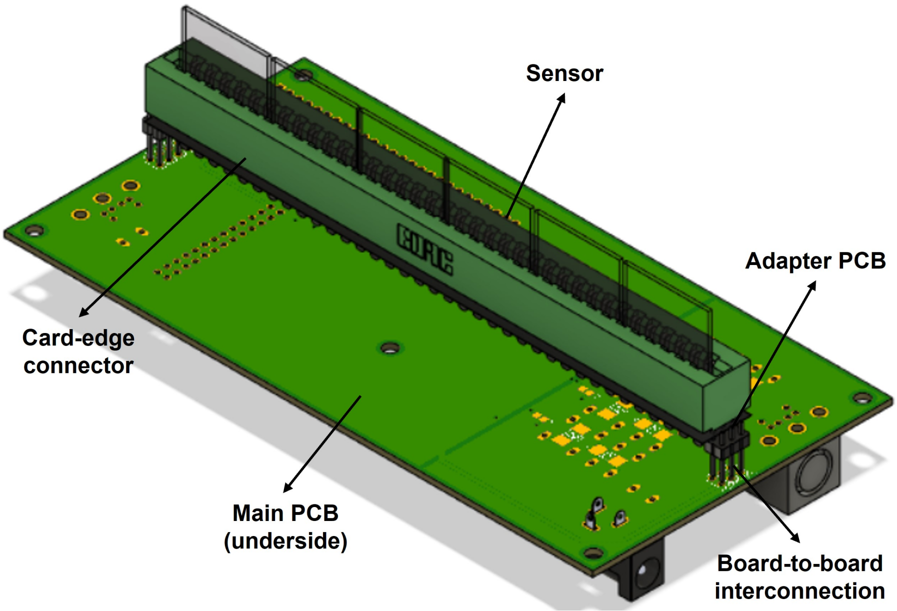

Figure 4.24: Complete PCB assembly design.

4.4.3 3D CAD Model

For the design and implementation of the electronics module, 3D CAD models were created, using Fusion 360 [87]. Together with the PCB design files, made using Eagle [83], the 3D models of the PCBs were imported into Fusion 360 [87], where the whole electronic module was designed. In Figure 4.25, a CAD design of the complete electronics module is presented.

The CAD model for the aluminum enclosure, shown in black, was obtained from the manufacturer, which enables an accurate and precise design, and helps to inspect the compatibility between the PCB design and the targeted enclosure. For example, this methodology was used to accurately place holes in the enclosure side-panels for the connectors. In Figure 4.26, the sensor detection chamber assembly is highlighted, which was custom designed for the Electrical E-nose V3.

The sensor detection chamber is composed of 4 mains parts: the sensors; a glass chamber, inside which the VOC interact with the sensors; the card-edge connector and adapter PCB assembly, which are used to electrically connect to the sensors; and an outer 3D-printable shell, which accommodates the latter components and provides a simple way to seal the glass chamber and provides a mechanical connection to the enclosure.

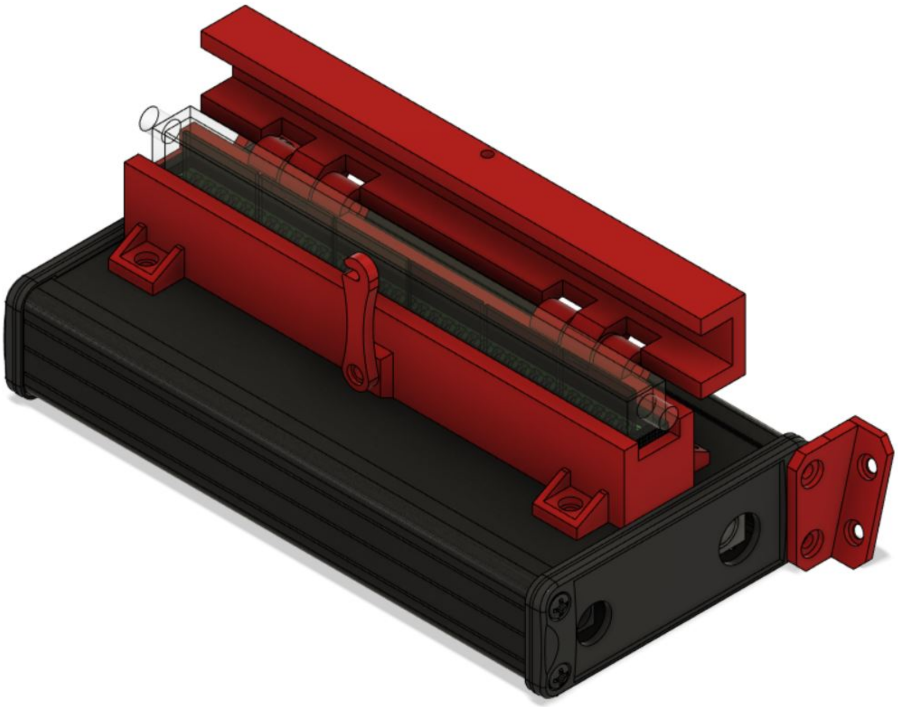

Figure 4.25: CAD model of electronics module. The enclosure is shown in black, and the sensor detection chamber in orange.

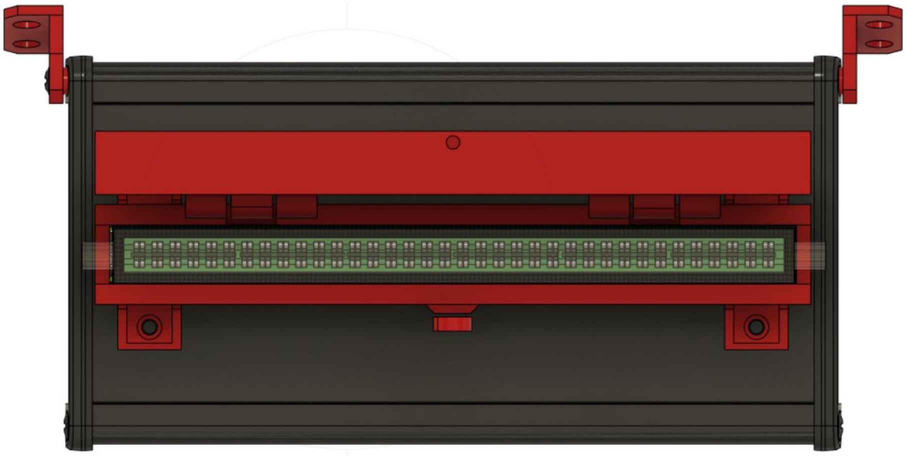

Figure 4.26: Top view of the sensor detection chamber CAD model, shown in the open position.

4.5 Software

The software of the Electrical E-nose V3 was developed in Python. This software is intended to run in a computer, which is connected to the E-nose via USB and is responsible for the communication with the E-nose, as well as storing the data generated in the experiments and plotting it in real-time. In addition, a digital filter is implemented using Python, which removes unwanted frequency components of the sensor signals.

The Python software is divided into 3 parts, corresponding to 3 different scripts: the main script, which is responsible for the communication with the E-nose and to store the experiment data; the plotting script, which is responsible to plot the acquired data, in real-time; and the GUI script, which provides a means for the E-nose user to configure the device for a given experiment.

4.5.1 Data Acquisition and Communication

The main Python script, responsible for the data acquisition and communication with the E-nose, starts by establishing a serial communication channel with the PSoC 5LP. For that, the serial Python library is used, and the serial port is configured for a baud-rate of 115200 bps.

After the successful configuration of the serial communication channel, a number of commands are sent to the E-nose, which are used to configure it for the experiment. In Table 4.16, the list of commands is presented.

Firstly, a reset command is sent, after which the E-nose serial number is requested. The E-nose serial number is required for data tracking purposes, and because the different E-nose variations require a different group of commands. After receiving the E-nose serial number, the duration of the delivery system phases (recovery, exposure, and optionally retention) and total experiment duration are sent to the E-nose. In addition, the E-nose features a pre-experiment recovery phase, whose duration can be configured by the user, and is referred to as the clean-up phase. This procedure is used to remove any unwanted VOC particles from the sensor detection chamber before the start of the experiment.

Consecutively, the operation mode command configures the E-nose for normal operation or calibration mode. Then, the delivery system power control system is configured. For that, the states of the four power outputs, controlled by the relay circuit, are defined for each delivery system phase. For example, the command *G*011 is used to activate the output port #0 during the exposure phase, while the command *G*200 is used to remove power from output port #2 during the recovery phase. After all the configuration commands are sent, the command *A* is sent to the E-nose, which closes the command line and starts the experiment.

After the configuration process, the Python software enters a loop, which can only be interrupted by one of two conditions: the communication channel is blocked or has been closed; or the E-nose has sent an experiment end command. To assess the state of the

Command	**Function**	**Description**
A	Send ready signal	Starts the E-nose experiment
B	Reset	Resets all data buffers and configurations
Cxxx	Send recovery phase duration (s)	Configure the recovery phase time of the experiment, to a maximum of 999s
Dxxx	Send exposure phase duration (s)	Configure the exposure phase time of the experiment, to a maximum of 999s
Exxxx	Send total experiment duration (s)	Configure the total duration of the experiment, to a maximum of 9999s
Gxyz	Send delivery system configurations	x - output port (0 to 3) y - delivery phase (0 - exposure; 1 - recovery; 2 - retention) z - output state (0 - off; 1 - on)
Hxxx	Send clean-up time (s)	Configure the pre-experiment sensor chamber auto-cleaning time (similar to a recovery phase)
Jxxx	Send retention phase duration (s)	Configure the retention phase time of the experiment. Valid for E-nose with serial number 2
K	Request E-nose serial number	The E-nose sends the serial number (1 or 2)
Mx	Send operation mode	1 - Normal operation 2 - Calibration mode
W	Send wake-up notification	Sent periodically to check if the channel is not blocked

Table 4.16: Serial commands for E-nose configuration

communication channel, the command *W* is sent periodically to the E-nose, which should reply with an acknowledge signal within 1s. Otherwise, the E-nose stops the experiment and resets itself, and the Python software issues an exception to the E-nose user.

During the experiment, the E-nose sends a data buffer which contains the impedance readings of the 12 sensors, the temperature measurement, the RH measurement, and the current delivery system phase. In the Python script, the impedance measurements are stored in a circular buffer, for each sensor. This buffer feds a simple outlier-rejection filter, which rejects samples whose distance from the median value is greater than 3 standard deviations, resulting in a smoother and more consistent signal. Such outliers result from random voltage spikes in the output of the TIA, which may originate from the multiplexer switching, or during the configuration of the TIA feedback resistor.

For each data packet, the filtered data is converted into a string, which is written in two text files: the temporary file; and the experiment data file. The temporary file has a maximum of 10 lines, is used by the plotting script, and is deleted in the end of the experiment. The data file can be divided into two parts: the header, which contains the experiment configurations; and the experiment data. For the latter part, each data packet corresponds to a row, which contains 17 columns, separated by empty spaces. The first column contains the time value, in seconds, the second column corresponds to the delivery system phase, and the 12 adjacent columns correspond to the impedance measurements of the sensors, starting from sensor 1 and ending in sensor 12. The three last columns correspond to the temperature and RH measurements, and the effective processing time of the data packet, which can be used in the post-processing stage for troubleshooting.

4.5.2 Real-Time Data Plotting

During an experiment, the data acquired by the E-nose is stored in the computer, which can be plotted and manipulated after the experiment has ended. However, to provide an instantaneous analysis and interpretation of the data, a plotting software was developed, which plots the recorded data for each sensor in the computer screen.

For that, the *qtgraph* Python library was used. The plotting window was configured for 15 distinct plots, including: 12 sensor impedance plots, which present the impedance measurements of each sensor; a temperature plot, presenting the temperature inside the sensor detection chamber; an RH plot, presenting the RH inside the sensor detection chamber; and a delivery phase plot, which indicates the delivery system phase as a function of time. In Figure A.16, a plotting window example is presented, which corresponds to an experiment done with the Electrical E-nose V3.

To plot the data, the temporary data files generated throughout the experiment are read and the information is segmented and stored in data buffers. At a given rate, the data in each buffer is plotted, the x-axis is automatically panned to present the data within a time frame of a minute, and the y-axis is automatically adjusted to maximize the plotting area. During the experiment, the E-nose user can interact with each plot by applying zoom in a specific section, apply filters to the signal, or calculate the FFT of the signal.

4.5.3 Graphical User Interface

To facilitate the configuration of the Electrical E-nose V3, a GUI was developed, and is presented in Figure 4.27. Such GUI is based on the work developed by [23] and is adapted to the Electrical E-nose V3.

The GUI enables the user to easily control the E-nose, as well as configuring it for an experiment. The GUI is composed of 5 main frames, and 2 buttons. In the *Films ID* frame, 12 text boxes enable the user to insert the formulation, or name, of the sensor in each sensor detection chamber position. In the *Session Configuration* frame, the user can insert the duration for each delivery system phase and total experiment time. In the *Sample Specifications* frame, the user can insert the sample name, quantity, and temperature. In the remaining frames, the user can insert its name, or identification, the goal of the experiment

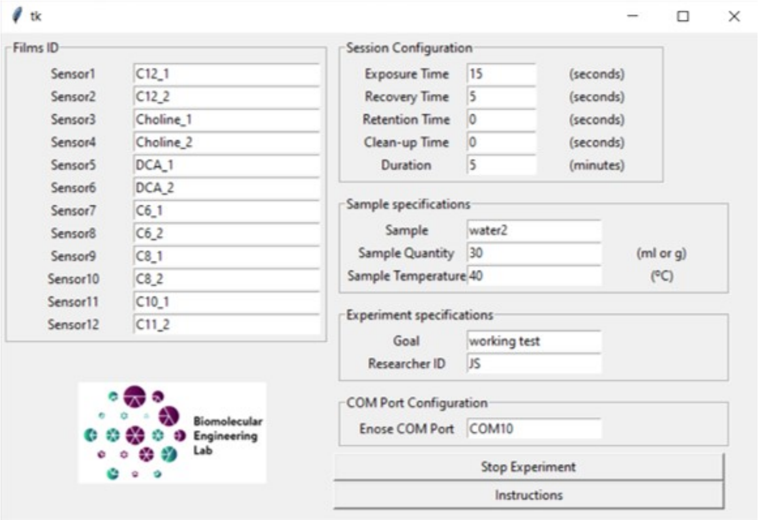

Films ID
Sensor1 C12_1
Sensor2 C12_2
Sensor3 Choline_1
Sensor4 Choline_2
Sensor5 DCA_1
Sensor6 DCA_2
Sensor7 C6_1
Sensor8 C6_2
Sensor9 C8_1
Sensor10 C8_2
Sensor11 C10_1
Sensor12 C11_2

Session Configuration
Exposure Time 15 (seconds)
Recovery Time 5 (seconds)
Retention Time 0 (seconds)
Clean-up Time 0 (seconds)
Duration 5 (minutes)

Sample specifications
Sample water2
Sample Quantity 30 (ml or g)
Sample Temperature 40 (ºC)

Experiment specifications
Goal working test
Researcher ID JS

COM Port Configuration
Enose COM Port COM10

Figure 4.27: GUI developed for the Electrical E-nose V3.

and configure the COM port. To start, or stop, an experiment, the *Start Experiment / Stop Experiment* button can be used. Additionally, the *Instructions* button opens a PDF file containing detailed instructions on how to use the device, as well as troubleshooting advice.

The GUI is based on the *tkinter* Python library and is the main process of the entire Python software. When the *Start Experiment* button is pressed, the configurations inserted by the user are stored in a text file, and a thread is created, in which the data acquisition and communication software runs. This latter software reads the configuration file and configures the E-nose, as presented in subsection 4.5.1. When the experiment is initialized, another thread is created, corresponding to the real-time plotting software.

4.5.4 Digital Filter Design

As is typical with most measurements of real-world phenomena, the acquired signals often require some form of filtering. In the case of the signals acquired by the Electrical E-nose V3 during an experiment, the useful information corresponds to a low frequency signal, which is typically in the range of 1 Hz to 5 Hz, while unwanted high frequency content exists up to 100 Hz. Thus, a low-pass filter can be used to remove the high frequency noise.

The frequency range of interest is dependent on the delivery system configurations, such as the duration of the exposure and recovery phases, as well as the response time of the sensors to a given VOC. Due to this, it is unpractical to choose a single cut-off frequency, since it may not be adequate for the signals acquired in different experiments. In addition, due to compatibility reasons with already implemented signal processing software, it is important that the signals are in their raw and unfiltered form.

A Python software implementation for the filter was chosen over an implementation in the PSoC 5LP. This choice enables an easier manipulation of the filter parameters, such as the cutoff frequency, filter type, and filter order, as well as providing the raw sensor signals, which are required for the post-processing stage. The PSoC 5LP implementation would be more computationally-efficient, but also less flexible and more complex.

This way, in the normal E-nose operation, the raw impedance data acquired is sent to the computer, where it is stored. The digital filter receives the raw sensor signals, and the filtered signals of each sensor are presented in the computer screen, during the experiment. Moreover, the filtered signals can also be stored in the computer, alongside the raw sensor signals.

Since the filter will be operating during an E-nose experiment, low-latency is required. Due to this reason, an IIR filter is chosen, due to its simplicity comparatively with a FIR filter. The theory behind FIR and IIR filters, as well as a comparison between the two topologies, is presented in subsection 2.2.8. For the design of the filter, the *scipy* Python library was used.

Typically, the design of a filter is based on certain specifications, such as the maximum attenuation in the pass-band and minimum attenuation in the stop-band. However, for this design the order of the digital low-pass filter was set to 4, and the cut-off frequency was set to 1 Hz, which are adequate for the majority of the signals acquired by the E-nose. However, the latter configurations can easily be adapted to a more specific case.

To select the most appropriate filter approximation, the frequency response of each is presented in Figure 4.28. Two different types of Chebyshev filter are considered: type-1, which has ripple in the pass-band region; and type-2, or inverse Chebyshev, which has no pass-band ripple, but has ripple in the stop-band. In this case, the maximum ripple in the pass-band region was set to 0.01 dB and the maximum attenuation in the stop-band was set to 20 dB.

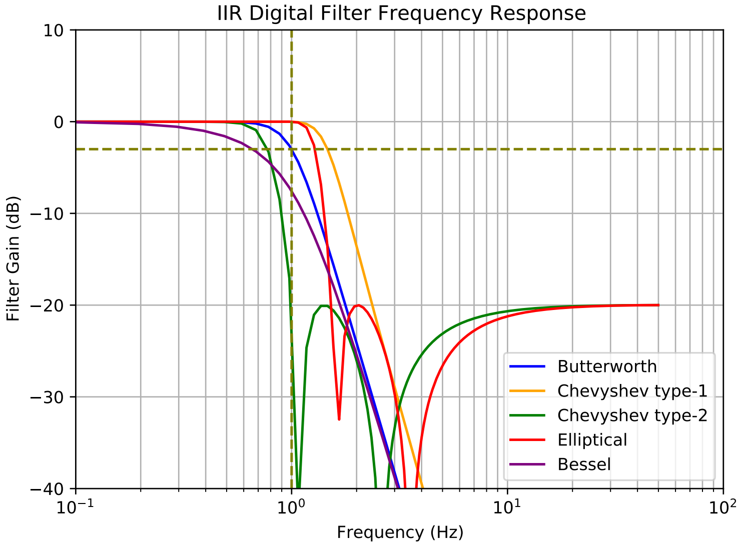

Figure 4.28: Frequency response of different filter approximations. The dashed lines represent the -3 dB value at the cut-off frequency.

By analyzing the frequency response of the different filter approximations, it is possible to conclude that the Butterworth filter provides a 3 dB attenuation at the cut-off frequency of 1 Hz, while the Bessel approximation has a considerable attenuation in the pass-band region. On the other hand, the elliptical filter provides the steeper roll-off, at the cost of some ripple in the stop-band region. The type-2 Chebyshev approximation provides similar roll-off characteristics, but a higher attenuation in the pass-band region. The type-1 Chebyshev features a smaller roll-off than the elliptical filter, however no ripple is observed in the stop-band region, and little is observed in the pass-band region.

The step response of the considered filter approximations is presented in Figure 4.29. With the exception of the Bessel approximation, a considerable overshoot is observed, which may be problematic and undesirable since it results in a higher settling time. In contrast, the Bessel approximation has no overshoot, however it has a slower response.

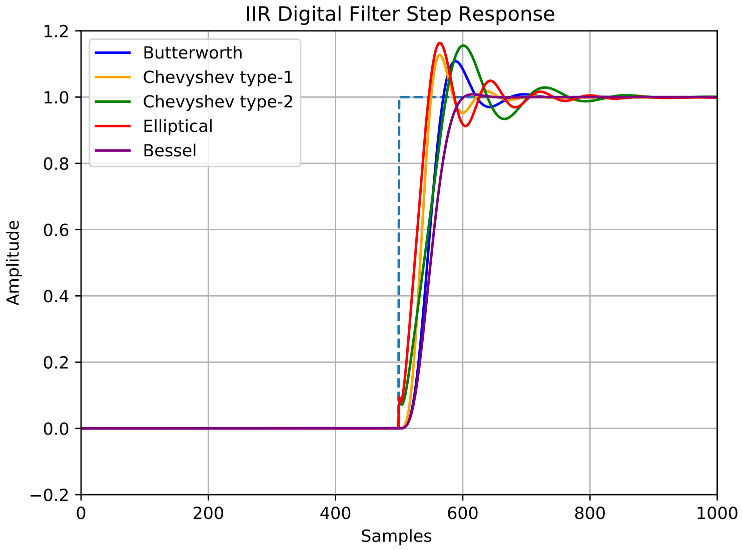

Figure 4.29: Step response of different filter approximations. In blue, the input step signal is represented.

To assess the effectiveness of each filter approximation, a unfiltered signal previously acquired by the E-nose was used as an input signal. The filtered signals are presented in Figure 4.30. It is possible to conclude that the elliptical and type-1 Chebyshev approximations have the fastest response, resulting in less delay, and retain more high frequency content than the other approximations. By comparison, the type-2 Chebyshev approximation has a slower response than the type-1 variant, but less high frequency content. In addition, the Butterworth and Bessel approximations provide a smoother signal, however the delay is considerable.

In Figure 4.31, a comparison between the filtered signals from different filter approximations, for a different input signal, is presented. As expected, the Bessel approximation provides a more accurate signal, at the cost of some attenuation and delay. By comparison, the Butterworth filter features less attenuation, but also some overshoot. The type-2

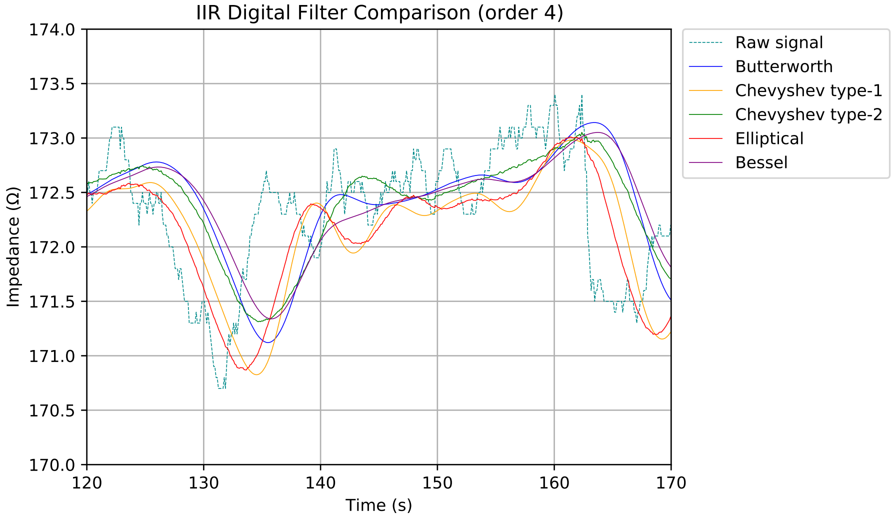

Figure 4.30: E-nose signal filtered by different filter approximations (example 1).

Chebyshev approximation features considerable overshoot and slow response, which is similar to that of the Bessel filter. The type-1 Chebyshev features minimal overshoot, minimal delay, and fast response, which are positive features. The elliptical filter provides a similar response but with a higher overshoot.

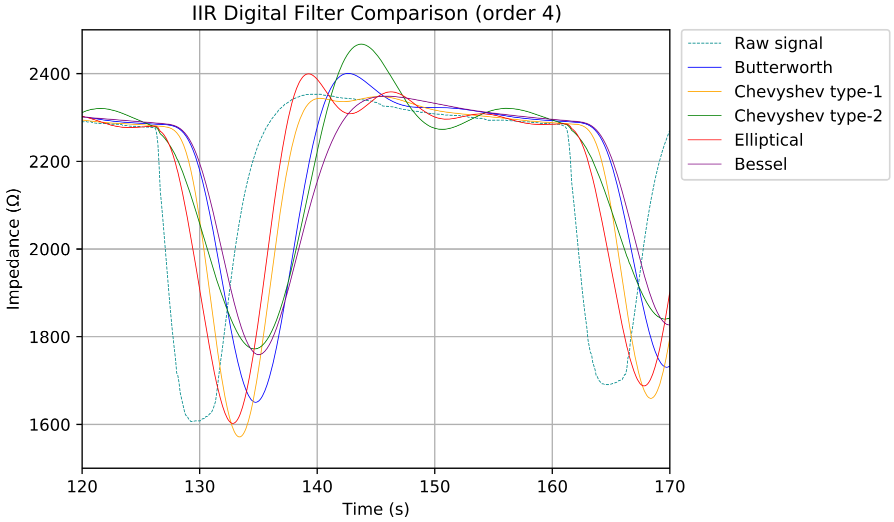

Figure 4.31: E-nose signal filtered by different filter approximations (example 2).

From these results, the most appropriate filter approximations are the Butterworth and type-1 Chebyshev, while the Bessel approximation can be considered due to its overdamped step response. In Figure 4.32, a more direct comparison between the Butterworth, type-1 Chebyshev and Bessel filter approximations is presented.

In example 1, the Butterworth approximation provides the best trade-off between response time and high frequency filtering, while the Bessel filter features a slower response, and the type-1 Chebyshev has more high frequency content. In example 2, the most appropriate filter approximation is the type-1 Chebyshev, providing the fastest and more accurate step response, without overshoot. Thus, as previously mentioned, the most appropriate filter depends on the signal, however, the Butterworth approximation is more effective in the majority of the cases.

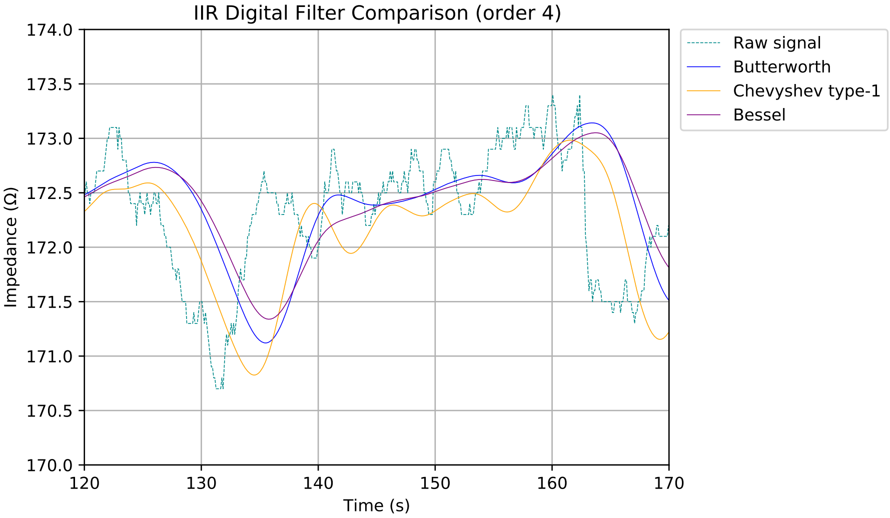

(a) Example 1.

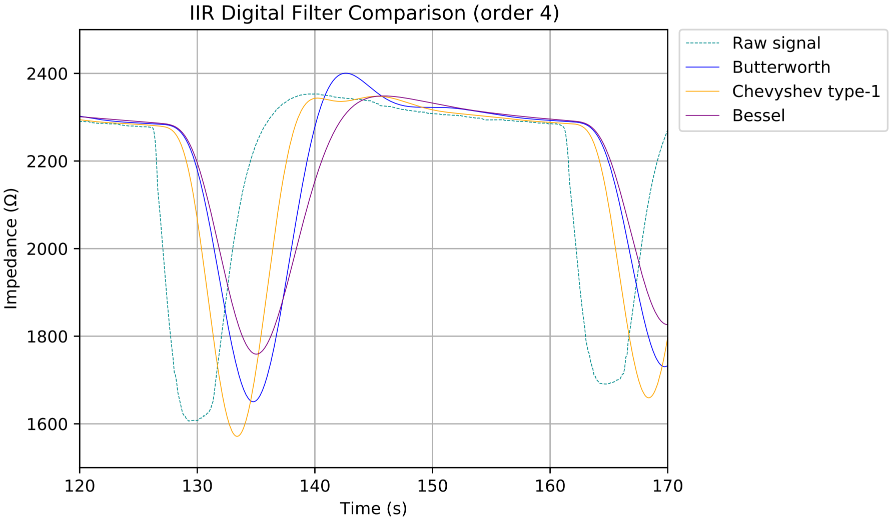

(b) Example 2.

Figure 4.32: Comparison between the filtered signals from the Butterworth, Bessel and type-1 Chebyshev filter approximations.

5

IMPLEMENTATION AND TEST OF THE ELECTRICAL E-NOSE V3

In this chapter, the implementation and test of the Electrical E-nose V3 is presented. The implementation is based on the design presented in chapter 4, and includes the physical assembly of the complete device, as well as its most relevant components.

After the implementation of the device, the AFE circuit is tested and validated, and its accuracy is measured. Then, the E-nose is experimentally tested in laboratory, during a period of 90 days. Data acquired from various real-world experiments is presented, and the performance of the device is analyzed and discussed.

5.1 E-nose Implementation

5.1.1 Electronics Module Implementation

After the design process, the electronics module presented in section 4.4, was implemented. For that, the implementation of the PCBs and the 3D models of the sensor detection chamber are required. The PCB design files were sent to a PCB manufacturer, for production. In addition, the bill-of-materials was used to order the required components for the implementation of the device. After receiving the manufactured PCBs and respective components, the two PCBs were hand-soldered, one at a time, using a soldering station. After the soldering process, the completely assembled main PCB, adapter PCB, and electronics module assembly are shown in Figure 5.1.

Considering the 3D CAD model presented in subsection 4.4.3, some of the sensor detection chamber parts were 3D-printed, and the aluminum enclosure was drilled and prepared for the PCB assembly.

5.1.2 Complete Implementation

As mentioned in section 4.3, a total of 3 delivery system variations were designed. Thus, in this subsection, 3 distinct implementations are presented.

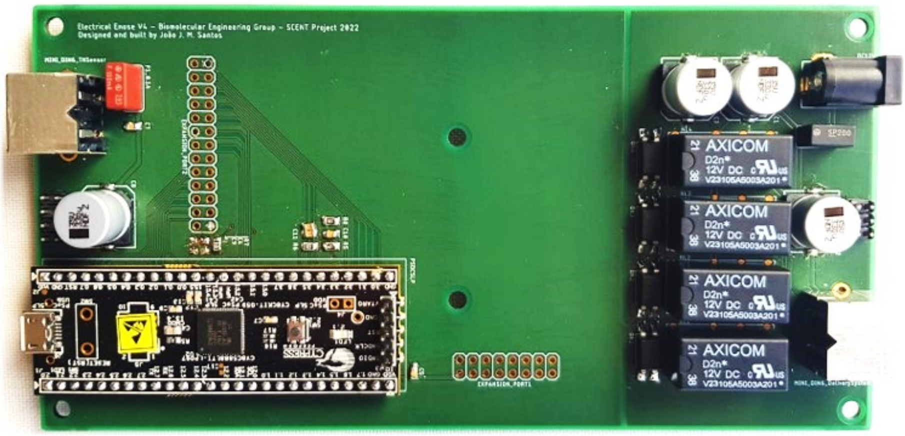

(a) Main PCB viewed from the top side.

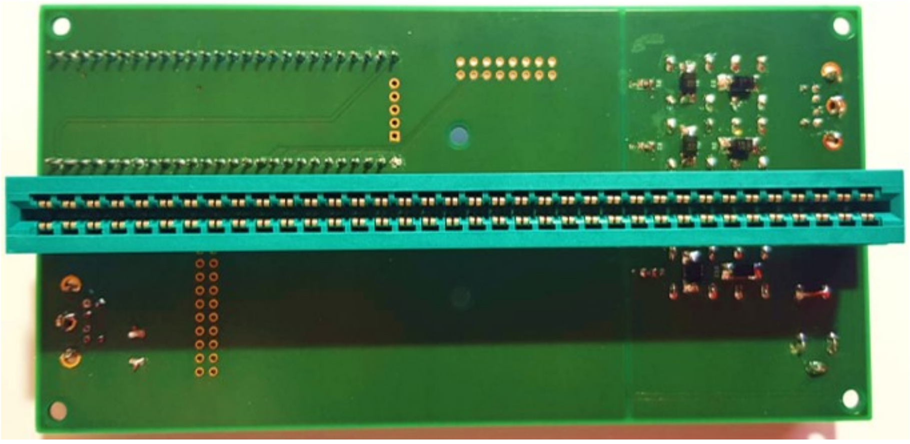

(b) Main PCB and sensor connector adapter (card-edge connector) viewed from the underside.

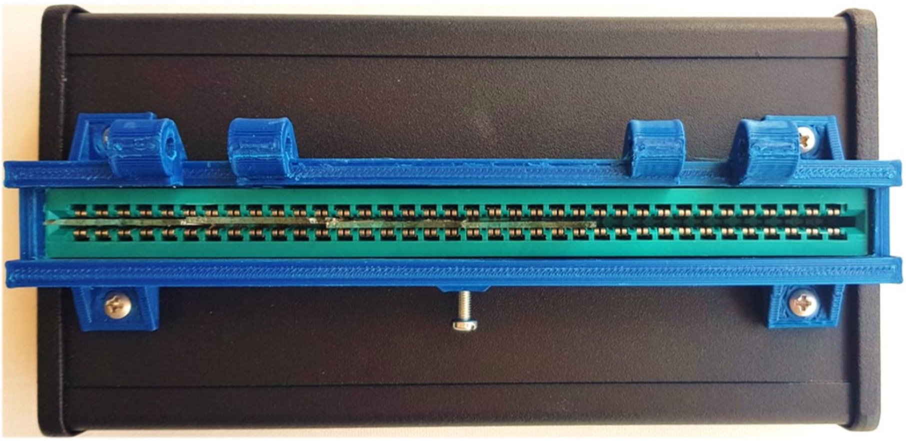

(c) First prototype of electronics module assembly.

Figure 5.1: Complete electronics module assembly.

The implementation of the delivery system is what defines the size and footprint of the E-nose device, since it has to be functional, easy to use and as small as possible. However, for the Electrical E-nose V3, there is no strict requirement regarding the maximum size of the device, but an efficient footprint is mandatory.

Considering previous works developed for the Optical E-nose V4, as presented in subsubsection 2.1.4.2, this E-nose version follows a similar implementation, regarding the use of a portable hardcase. Moreover, due to a higher level of optimization, it is possible to use a smaller 7L hardcase, which is equivalent to the size of a common laptop (37cm x 25cm).

5.1.2.1 Electrical E-nose V3 Implementation #1

In Figure 5.2, the complete implementation of the Electrical E-nose V3 with the positive-pressure delivery system, denominated Electrical E-nose V3.1, is presented.

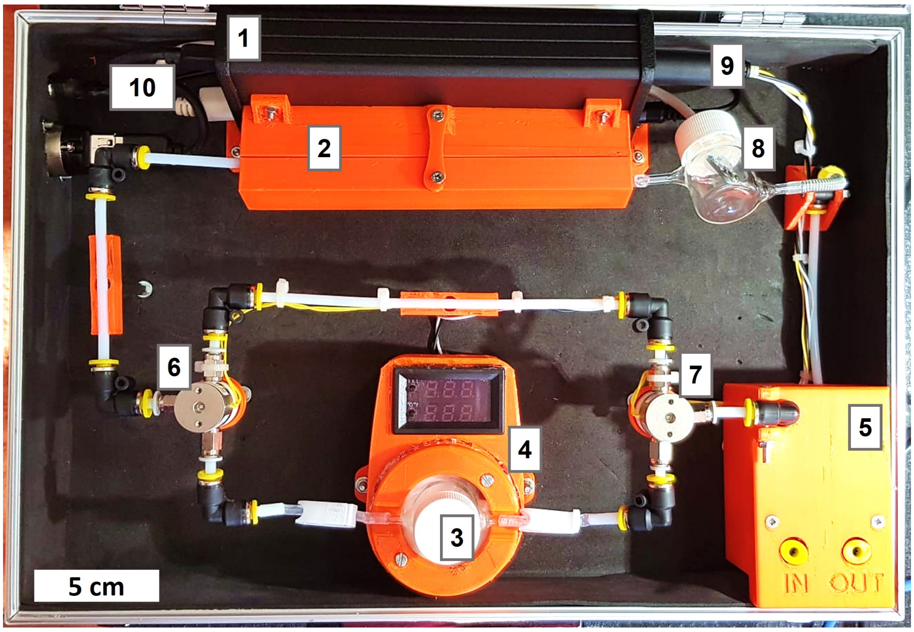

Figure 5.2: Electrical E-nose V3 implemented with positive-pressure delivery system. Labels: 1-electronics module; 2-sensor detection chamber; 3-sample flask; 4-sample heating device; 5-pump housing, inlet and outlet of the system; 6-valve #1; 7-valve #2; 8-RH sensor; 9-delivery system power outputs; 10-USB and power connectors.

For the implementation of the delivery system, 4mm PTFE tubing was used, which is resistant to chemical reactions with the various VOCs. In addition to the PTFE tubing, silicone tubing was also used for increased flexibility and connection with the glass chamber. Push-quick connectors are used to connect different tubing sections and provide a simple way of connecting and disconnecting various sample flasks, throughout an experiment.

The inlet and outlet of the system feature push-quick connectors, that enables the user to perform a quick connection with external components, such as an exhaust tube or a nitrogen feed. The pump, and associated tubing, is hidden under a 3D-printed enclosure, which has the purpose of securing it to the hardcase, as well as providing a better visual presentation. The 3D CAD model of such assembly was designed using Fusion 360 [87] and is presented in Figure 5.3a.

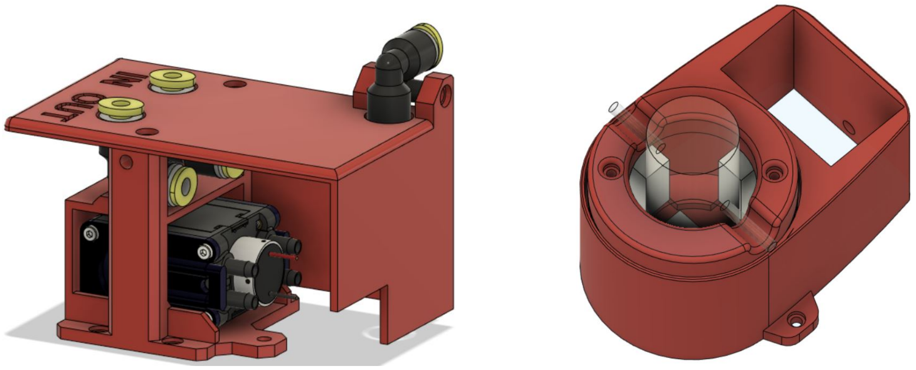

(a) Pump housing assembly.

(b) Sample heating device.

Figure 5.3: Additional 3D CAD models.

As described in subsection 4.3.1, the pump feeds air into valve #1, where two paths are created: recovery path, on the top; and the exposure path, on the bottom. The recovery path is a simple bypass tube between valve #1 and valve #2. On the exposure path, the outlet of valve #1 is connected to the sample flask, which is placed inside the sample heating device. Then, the output of the flask is connected to one inlet of valve #2, whose outlet is connected to the sensor detection chamber with PTFE and silicone tubing. At the output of the sensor detection chamber, another flask contains a temperature and RH sensor, whose output is connected to the outlet of the system.

Apart from the pump housing, and sensor detection chamber, there are some other 3D-printed components, such as the sample heating device, whose 3D CAD model is shown in Figure 5.3b. The sample heating device is composed of an array of ceramic power resistors, which transfer the heat to the sample flask. In Figure 5.2, it is possible to observe a screen in the sample heating device, which is a programmable thermostat. This device is screwed to the bottom of the hardcase, and also provides a way to secure the sample flask in place.

Due to the viscous nature of the ionogel sensors, it is mandatory that they are used on a horizontal orientation, since a vertical position would lead to permanent damage, or malfunction of the sensors. For that, the electronics module was attached to the bottom of the hardcase with a 3D-printed adapter, which provides an inclination of 75° , which is also comfortable for the E-nose user to work with.

5.1.2.2 Electrical E-nose V3 Implementation #2

In Figure 5.4, the complete implementation of the Electrical E-nose V3 with the negative-pressure delivery system, denominated Electrical E-nose V3.2, is presented.

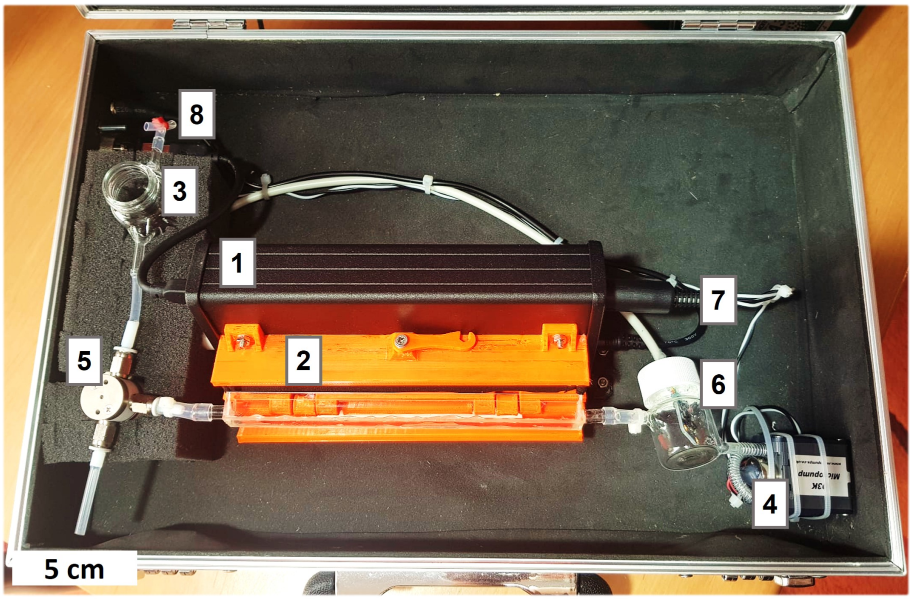

Figure 5.4: Electrical E-nose V3 implemented with negative-pressure delivery system. Labels: 1-electronics module; 2-sensor detection chamber; 3-sample flask; 4-pump; 5-valve #1; 6-RH sensor; 7-delivery system power outputs; 8-USB and power connectors.

As presented in Figure 4.20, the goal of this variation is to reduce path length between the sample flask and sensor detection chamber. For that, the pump creates a vacuum, which depending on the state of the valve, can force the VOC in the saturated headspace of the sample flask, or ambient air, into the sensor detection chamber.

In this case, 3mm silicon tubing was used, which minimizes the wasted volume in the exposure path to approximately 1 mL, including the valve. The total sensor detection chamber volume is 25 mL, which leads to an overall volumetric efficiency of 96%. On the other hand, the recovery path is simply a silicon tube open at the end.

Due to the need of being an easily reconfigurable implementation, apart from the electronics module, the components were not attached to the hardcase. A foam block was used to secure the sample flask and the valve. The pump was secured with zip-ties. In addition, no push-quick fittings were used.

Apart from being a more efficient and simpler delivery system, there are some disadvantages to this implementation. The most relevant is the necessity of vacuum-tight sealing, since any air leak considerably decreases the pressure differential across the chamber, thus the VOC is not pushed into the detection chamber. The greatest source of leak is the card-edge connector, represented in Figure 5.1, to which to sensors are connected. More specifically, this connector features minuscule orifices between the plastic and soldering pads, thus the underside of the sensor detection chamber was completely sealed with a special gel, which successfully seals all the leaks. In addition, due to the exposure path length optimization, this variation does not provide heating for the sample flask, thus an external heating device has to be used when sample heating is required.

5.1.2.3 Electrical E-nose V3 Implementation #3

Apart from the two previous variations, a third Electrical E-nose V3 which is designed to operate with an MFC-based delivery system, denominated Electrical E-nose V3.3, was implemented, and is shown in Figure 5.5.

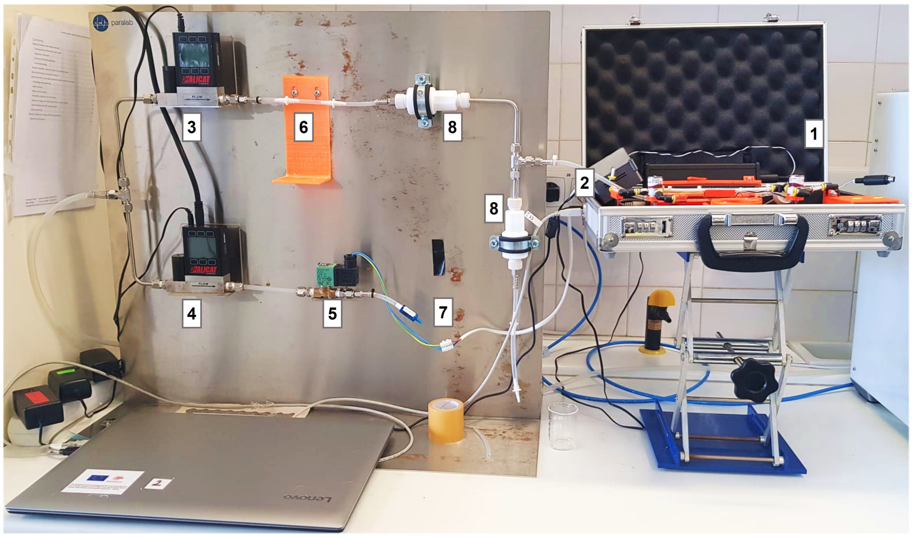

Figure 5.5: Electrical E-nose V3 implemented with MFC-based delivery system. Labels: 1-Electrical E-nose V3.1; 2-adapter relay circuit; 3-MFC #1; 4-MFC #2; 5-solenoid valve; 6-sample flask #1 (not shown); 7-sample flask #2 (not shown); 8-non-return valves.

This E-nose variation is based on the Electrical E-nose V3.1, which uses the positive-pressure delivery system. However, the MFCs and valves presented in the panel are used in the place of those presented in subsubsection 5.1.2.1, while both systems share the sensor detection chamber and RH sensor.

However, since the solenoid valve in the panel is rated at a nominal 24V voltage, an adapter relay circuit is used. This circuit is composed of a relay, which is controlled by the delivery system control circuit of the electronics module, and the 24V from an external power supply is switched by the relay contacts. This way, compatibility between the delivery systems is guaranteed, by simple connecting this adapter relay circuit in the place of the connector which is used in the Electrical E-nose V3.1.

5.2 E-nose Test and Validation

5.2.1 AFE Circuit Test

To assess the correct working of the Electrical E-nose V3, its AFE #1 circuit was tested. For that, a digital oscilloscope was used to measure the signals of the AFE circuit, as presented in Figure 5.6.

Considering the AFE circuit, depicted in Figure A.17, the sensor drive signal, at the output of the DDS, is presented in channel 1 of the oscilloscope, shown in yellow. It is

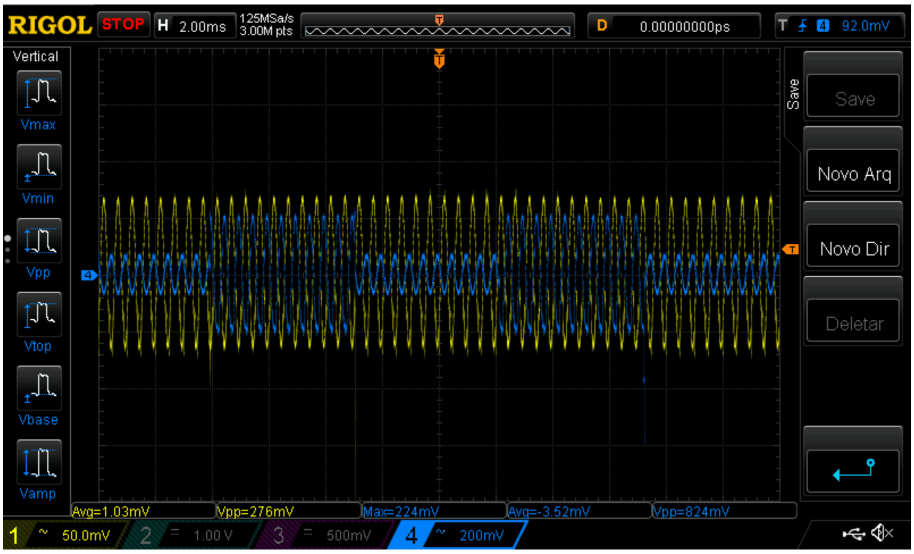

Figure 5.6: AFE circuit signals measured with a digital oscilloscope. Channel 1 is shown in yellow and channel 4 is shown in blue. Both channels are AC coupled.

possible to observe a 2 kHz sine-wave signal, with an amplitude close to 100mV. Due to the low resolution of the digital oscilloscope, the amplitude of the signal appears distorted, however it is possible to conclude that the DDS is working as expected.

Moreover, the output voltage of the TIA is presented in channel 4, which corresponds to the amplified signals of 4 different sensors, in this case. It is possible to differentiate the signals from the 4 distinct sensors, by analyzing the different amplitudes of the blue signal, which varies every 10 sine-wave cycles. Thus, each 10 consecutive cycles, or every 5ms, a different sensor is connected to the TIA. This way, it can be concluded that the TIA and the multiplexer are working as intended.

To measure the accuracy of the AFE circuit, 16 different precision 1% resistors ranging from 200 Ω to 150 kΩ were connected to each of the AFE channels, at a time, which model a ionogel sensor with a known and stable impedance level. This way, the average accuracy of all channels, as a function of the equivalent sensor impedance, is presented in Figure 5.7.

It was possible to observe that the accuracy for lower impedances has an average value of 87%, however it can be as low as 82%. This can be explained by the relatively large tolerance of the analog multiplexer on-resistance, as discussed in subsection 2.2.5. More specifically, since the on-resistance of the multiplexer appears in series with the sensor impedance, the error increases as the sensor impedance decreases.

In addition, the accuracy decreases for an impedance measurement range between 2 kΩ and 4 kΩ . This is mostly due to the change in trans-impedance gain level. For higher impedance levels, the accuracy increases to a maximum of 98% and has a value of 97% for an impedance of 200 kΩ .

Thus, for an impedance measurement range between 300 Ω and 200 kΩ , the AFE circuit is capable of an average accuracy greater than 90%. Furthermore, for the majority of the impedance measurement range, the average accuracy is greater than 95%. This way,

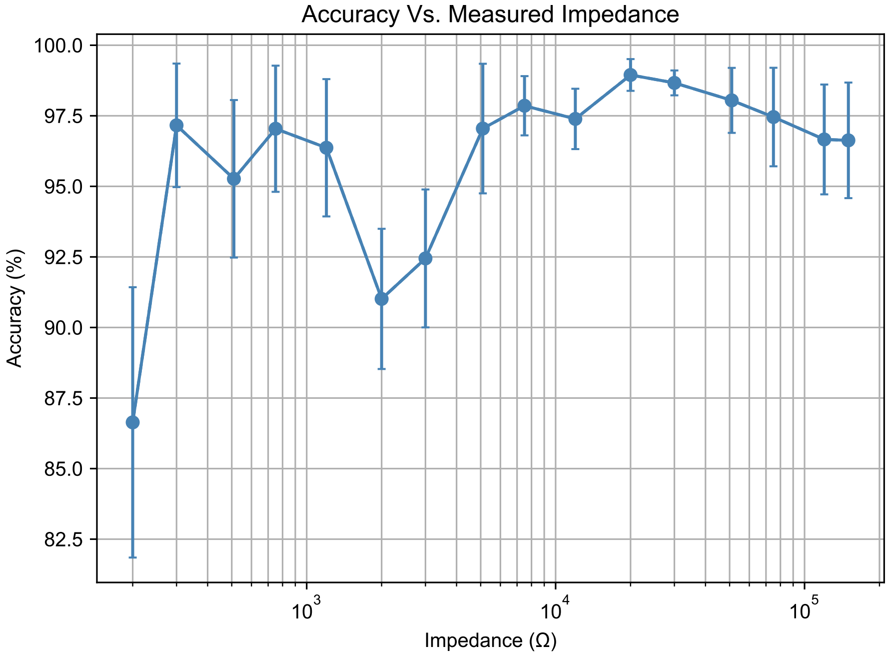

Figure 5.7: AFE circuit accuracy as a function of equivalent sensor impedance.

the developed AFE circuit met the design specifications presented in Table 4.1.

5.2.2 Typical E-nose Operation Test

After the validation of the AFE circuit, the complete system was tested. For that, the 3 variations of the Electrical E-nose V3 were subjected to numerous experimental activities and trials, performed by the Biomolecular Engineering Laboratory, during a period of 90 days. The various experimental tests differed in the sample used and included the exposure to some of the VOCs presented in Table 3.4, as well as VOCs generated by bacteria.

In Figure 5.8a, the response of sensor formulation #1 to toluene is presented. For redundancy purposes, two replicas of the same sensor were tested, which were placed in positions 3 and 4 of the sensor detection chamber. In addition, the filtered impedance signal is superimposed to the raw E-nose impedance measurement, which enables the assessment of the effectiveness of the digital filter presented in subsection 2.2.8.

From the results presented in section 3.3, the expected impedance variation of sensor #1 due to the exposure to toluene, at a frequency of 2 kHz, is approximately 2 Ω , as presented in Figure A.15. From Figure 5.8a, the sensor in position #3 presents an average impedance of approximately 173 Ω , with a variation of ± 1 Ω , and the sensor in position #4 presents an average impedance of approximately 178 Ω , with a variation of ± 1 Ω .

In relative terms, such impedance variations are inferior to 1.2%, which demonstrates a considerable signal resolution. Moreover, it is possible to observe that during the exposure phase the impedance of the sensors decreases, which is expected according to Figure 3.19.

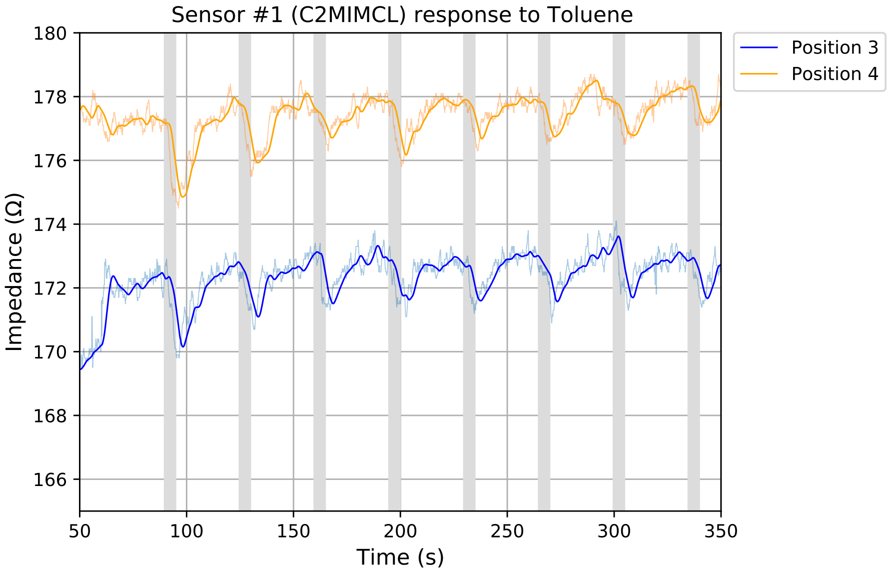

(a) Response to toluene.

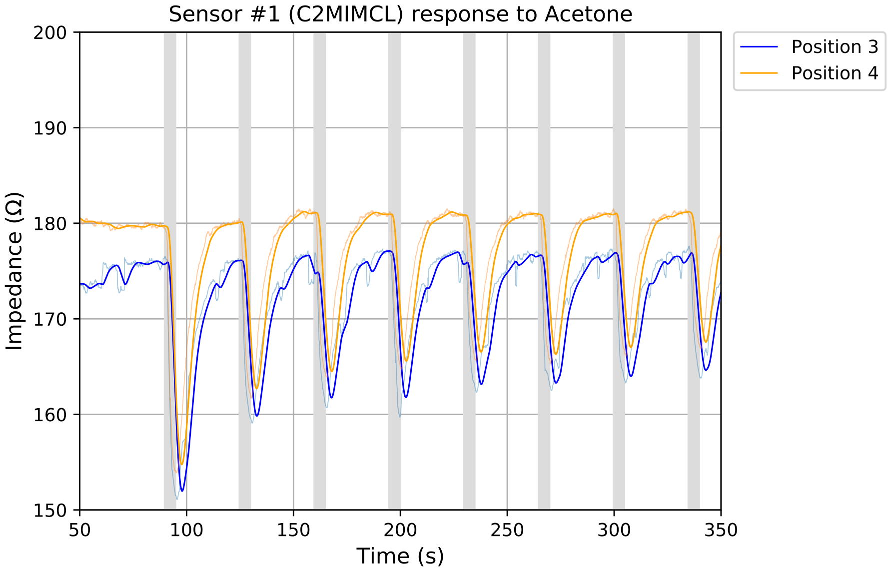

(b) Response to acetone.

Figure 5.8: Impedance of sensor #1 in response to the exposure to VOC, in duplicates, measured with the Electrical E-nose V3. The filtered signal corresponds to the thicker trace. The exposure phase is highlighted in grey.

In Figure 5.8b, the response of the same sensors to acetone is presented. Comparatively, the response of the sensors to this VOC is greater, as expected. In this case, the average impedance of the sensors is approximately equal to the previous case, however the variation is approximately ± 15 Ω .

In Figure 5.9, the response of sensor formulation #4 to acetonitrile and ethanol is presented. It is possible to observe that the sensor in position #10 is more responsive than its replica in position #9. In the case of the response to acetonitrile, presented in Figure 5.9a, a more pronounced baseline impedance shift is observed, which is due to a higher differential in RH level between the beginning and end of the experiment. The impedance variations are ± 200 Ω and ± 300 Ω , for the sensor in positions #9 and #10, respectively. In the case of Figure 5.9b, the impedance variations are ± 175 Ω and ± 300 Ω , for the sensor in positions #9 and #10, respectively.

In Figure 5.10, the impedance response over time of sensors #1, #2, #3 and #7, due to the exposure to acetonitrile and ethanol is presented. The latter figure enables a side-by-side visual comparison between the response of the same sensors to a different VOC. Both acetonitrile and ethanol feature a strong interaction with the sensors presented, however the responses to ethanol are smaller, especially for sensor #7.

In Figure 5.11, the impedance response over time of sensor #4, due to the exposure to the different VOCs is presented. This way, it is possible to directly compare the affinity of this sensor formulation to the different VOCs. It is possible to conclude that sensor #4 presents a higher affinity to acetonitrile and ethanol, while the response to toluene is considerably small. These results are expected, as discussed in section 3.3 and presented in Figure A.15.

5.2.3 E-nose Performance Analysis

To assess the SNR of the signals acquired with the Electrical E-nose V3, a Python software was used. The Python software divides each signal into segments of 5 samples, corresponding to 500ms intervals. The average, minimum and maximum impedance value in each portion is calculated, which is used to calculate the average SNR of the signal.

After applying the latter procedure to the entirety of the signals, the maximum SNR obtained is 65 dB, which is equivalent to an ENOB of 10-bit and corresponds to the signal acquired for sensor #4 (position 10) with acetonitrile. Moreover, the average SNR of all signals is 48 dB, which is equivalent to an ENOB of 7-bit. Considering the digital low-pass filter, the maximum SNR increases to 85 dB, which is equivalent to an ENOB of 13-bit, and the average SNR of all signals is 68 dB, which is equivalent to an ENOB of 11-bit. Considering the results presented, it is possible to conclude that:

- The AFE circuit of the E-nose can measure impedance variations inferior to 2 Ω , enabling detailed data acquisition of weak interactions between a given sensor and VOC, such as the response of sensor #7 and ethanol presented in Figure 5.10a.

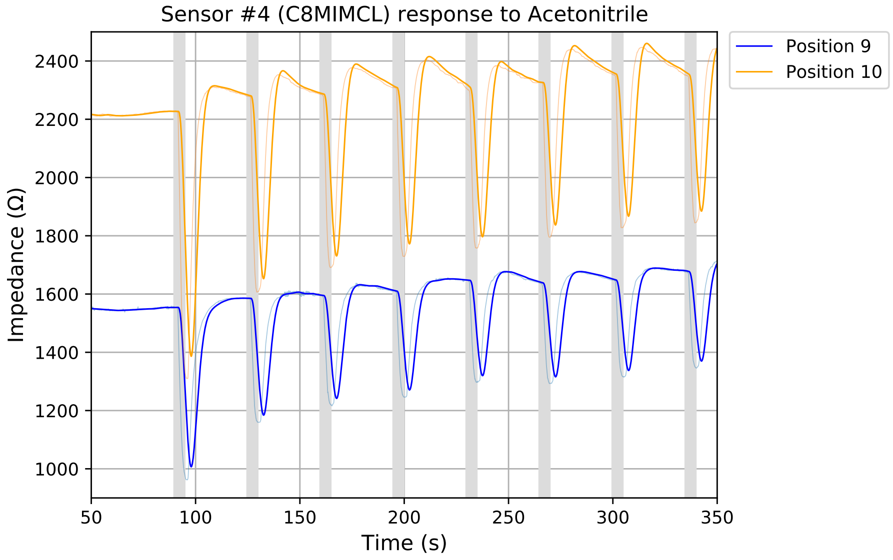

(a) Response to acetonitrile.

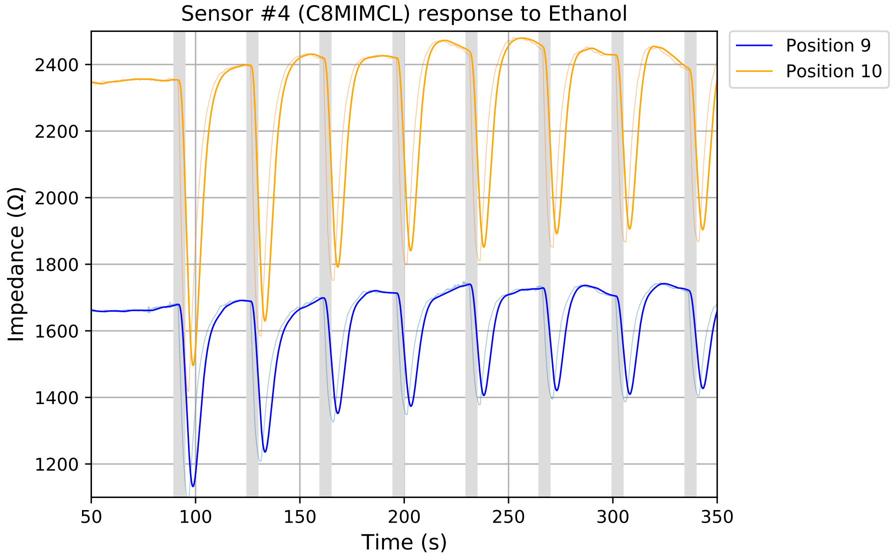

(b) Response to ethanol.

Figure 5.9: Impedance of sensor #4 in response to the exposure to VOC, in duplicates, measured with the Electrical E-nose V3.

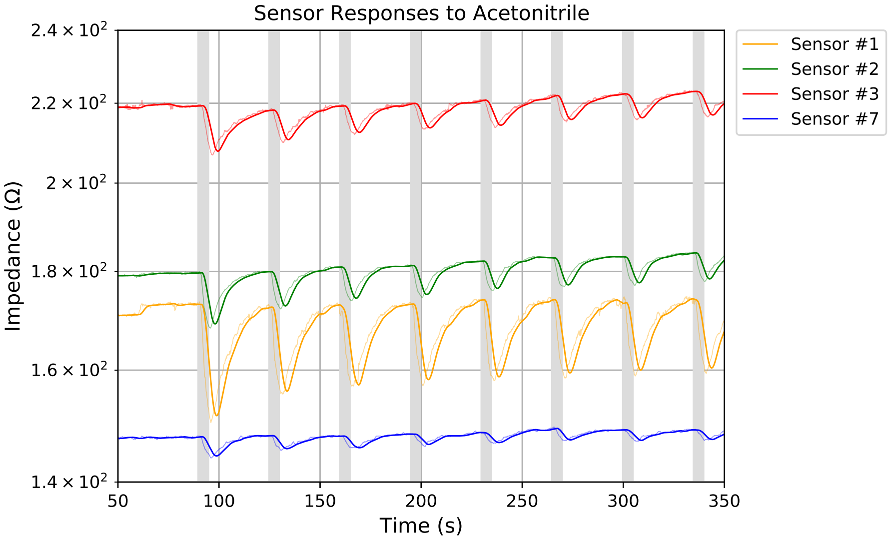

(a) Response of multiple sensors to acetonitrile.

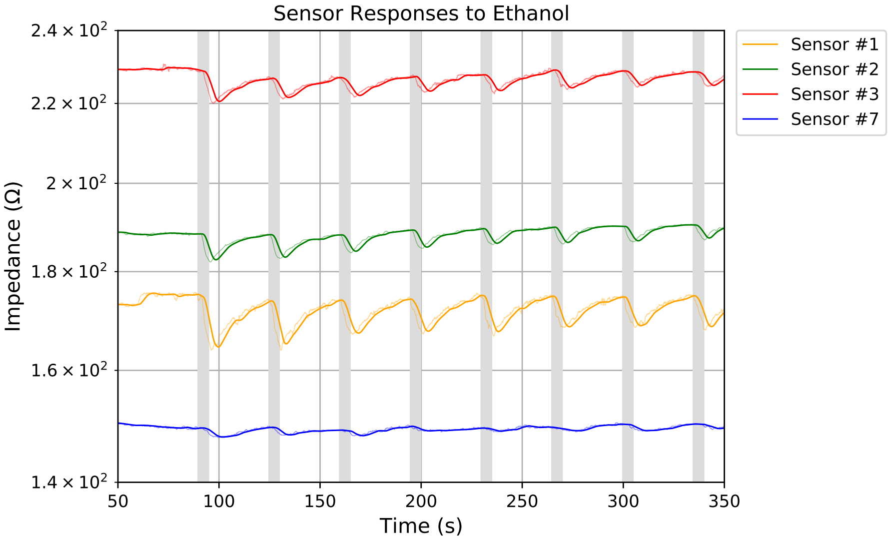

(b) Response of multiple sensors to ethanol.

Figure 5.10: Impedance of sensors #1,#2,#3 and #7 in response to the exposure to VOC, measured with the Electrical E-nose V3.

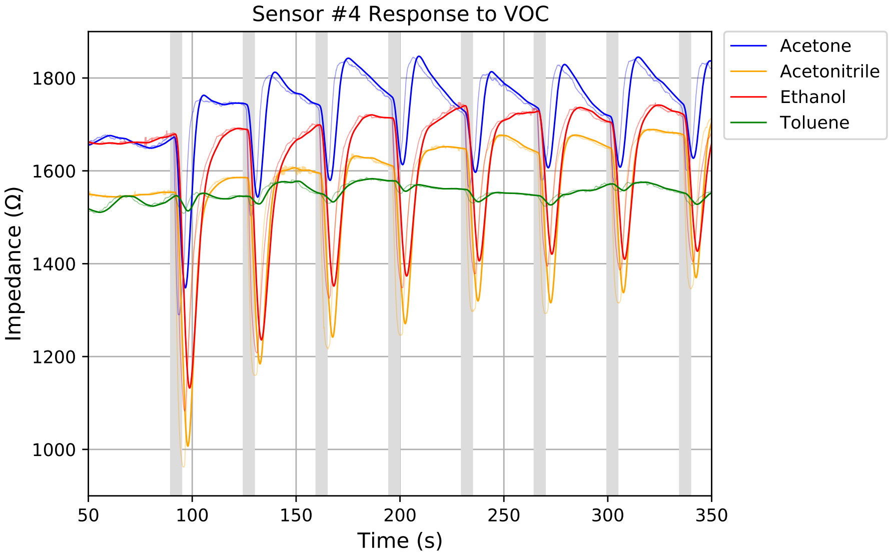

Figure 5.11: Impedance response over time of sensor #4 due to the exposure to different VOC.

- The AFE circuit is capable of measuring impedances up to 260 kΩ , however the SNR decreased considerably for impedances greater than 200 kΩ , which is the design specification for the maximum impedance value. On the other hand, the lowest impedance level measured was 140 Ω , which is under the specification for the minimum impedance measurable of 200 Ω . In the latter case, no SNR degradation was observed.

- In relative terms, the AFE circuit of the E-nose is able to measure variations as small as 1.2% and as high as 81%, which validates the effectiveness of the automatic trans-impedance gain adjustment mechanism, presented in section 4.1.

- Due to the high precision level of the E-nose AFE circuit, it is possible to quantify the differences between sensor duplicates, which are inherent to the sensor manufacturing process. This result enables a characterization of the sensor manufacturing process, which can be statistically relevant.

- The maximum recorded SNR of 65 dB implies an effective signal resolution greater than 10-bit. However, considering the implemented digital low-pass filter, the maximum SNR increased by 20 dB, resulting in an ENOB value close to 14-bit. Considering the theoretical 16-bit resolution, the AFE circuit presents a considerable noise performance and a good optimization level.

- Throughout the 90 days of laboratory implementation, it was possible to observe a high level of repeatability and consistency, regarding the quality of the acquired data, the performance of the delivery system, and device implementation, in general.

- The results are consistent with the expectations provided in previous chapters, mainly regarding the baseline impedance levels, and the dynamic impedance variation due to VOC. The correlation with the results obtained from a calibrated instrument suggests a good accuracy of the AFE circuit developed.

6

CONCLUSION

In this chapter, an overview of the work developed is presented.

The developments achieved are analyzed and compared with the initial goals, proposed in section 1.2. Moreover, the most relevant results obtained, as well as significant innovations in the context of the E-nose and ionogel sensor technology, are analyzed. Furthermore, higher level conclusions regarding the work developed are presented, as well as suggestions for future improvements, which are useful for the continuation of the work, and to enable advances in the E-nose technology, and in other sensing fields.

6.1 Overall Conclusions

As previously mentioned, this work was developed in the context of the Biomolecular Engineering Laboratory, who designed and built an innovate class of E-nose sensors, denominated ionogel sensors. In addition, the latter group also developed a custom E-nose device, that operates with the respective ionogel sensors, the *Electrical E-nose V2*.

The E-nose device required improvements, to increase the quality of the data acquired, and to maximize the sensitivity of the ionogel sensors, in different operating conditions. Such improvements are mandatory to achieve a higher sensing accuracy and precision levels. In addition, these improvements are fundamental to improve the sensing capabilities, flexibility, and versatility of the device, which help the group develop their research work.

Furthermore, it was known that the ionogel sensors response was dependent on the RH of the gaseous sample. However, a more detailed characterization of the impact of the RH in the impedance of the ionogel sensors, is mandatory to improve the sensing capabilities of the system. Thus, a total of 8 distinct ionogel sensor formulations, presented in Table 3.1, were subjected to numerous tests, which can be divided into two groups: the response of the sensors to RH, without the presence of analyte; and the response of the sensors to different analytes, or VOCs, with a known and constant RH level. This way, a multi-variable characterization of the ionogel sensors was obtained.

Regarding the response of the sensors to RH, without the presence of analyte, as shown in section 3.2, a total of 864 individual frequency response acquisitions were obtained, using a calibrated impedance analyzer. In this study, the sensors were exposed to 9 discrete RH values between 0% and 80%, while the temperature remained constant and equal to 22°C. The results showed that the impact of the RH varies significantly depending on the sensor formulation. For example, sensor #7 presented the least dependence on the RH level, with an impedance variation from 2 kΩ to 1 kΩ , for an RH between 0% and 80%. On the other hand, sensor #6 presented the highest impedance variation, from 300 kΩ to 16 kΩ , in the same RH conditions. In addition, this sensor presented a highly non-linear behaviour with RH. These results are supported by Figure 3.11.

In addition, it was possible to observe that the impact of the RH on each sensor formulation is considerably dependent on the frequency of the sensor drive signal, however the majority of the sensor formulations tested presented a lower dependence on the RH level at a frequency of 100 kHz. Furthermore, considering a frequency range between 100 Hz and 100 kHz, the impedance of the various sensor formulations, as a group, can vary between 65 Ω and 2 MΩ , in the considered RH range.

To study the sensors response to VOC, the 8 distinct ionogel sensor formulations were exposed to 7 different VOCs, which are listed in Table 3.4. The affinity between the various sensors and VOCs was studied, as a function of frequency. It was possible to observe that the sensitivity of a given sensor formulation to a certain VOC is highly dependent on the frequency of the sensor drive signal. More specifically, the affinity of the sensors to VOC generally increases as the frequency increases, and the maximum occurred for a frequency of 10 kHz, while at a frequency of 100 kHz the overall affinity of the group of sensors to the VOCs is greater. This fact proves that driving the sensors at a frequency of 100 kHz increases their sensitivity to analytes and decreases their dependence on RH, which are two positive outcomes.

Considering the characterization of the ionogel sensors, it was possible to establish the specifications for the design of the AFE circuit, such as an impedance measurement range between 65 Ω and 200 kΩ , and a drive frequency between 100 Hz and 100 kHz. Considering the goals, defined in section 1.2, an AFE circuit was designed. The design of such circuit was based in a PSoC device, and two variations of the circuit were created: AFE #1; and AFE #2.

The AFE #1 circuit is fully implemented in the PSoC 5LP, achieving a high level of integration, simplicity, flexibility, reconfigurability, and portability. This AFE circuit is rated for an impedance measurement range between 200 Ω and 200 kΩ , a resolution of 16-bit, and a fixed sensor drive frequency of 2 kHz. After the design process, the AFE #1 circuit was implemented alongside a sample delivery system, and a detection system. At this point, the complete device was denominated *Electrical E-nose V3*, as the improved version of the *Electrical E-nose V2*.

A total of 3 distinct *Electrical E-nose V3* implementations were created, each targeted for a different application. The differences between these implementations are related to the working principle of the sample delivery system. In the *Electrical E-nose V3.1*, a positive-pressure sample delivery system was implemented, which works by forcing clean air into the system, pushing the gaseous sample into the detection chamber, where the interaction with the ionogel sensors occurs. On the other hand, the *Electrical E-nose V3.2* was implemented with a negative-pressure sample delivery system, in which the gaseous sample is forced into the detection chamber due to a vacuum. This configuration is optimized for lower sample concentrations. Moreover, the *Electrical E-nose V3.3* enables the use of MFCs, as part of the sample delivery system, and is optimized for applications where control over the sample concentration is critical.

After the implementation phase, the *Electrical E-nose V3* was experimentally tested, during a period of 3 months, by the Biomolecular Engineering Laboratory. The data acquired from various experiments was examined, and the results were analyzed. It was concluded that the E-nose operated as expected, validating the entire system. At the AFE circuit level, the effective accuracy measured was between 82% and 99%, and the ENOB obtained has a maximum value of 14-bit. Furthermore, the AFE circuit enabled the measurement of relative impedance variations between 1.2%, corresponding to an absolute impedance variation of 2 Ω superimposed to a baseline impedance level of 170 Ω , and 81%, while the minimal sensor impedance measured was 140 Ω , and the maximum was 230 kΩ , which slightly exceed the design specifications.

Thus, a fully-operational E-nose device, specifically designed to maximize the performance of the innovative ionogel sensors, in different sensing conditions, was designed, implemented, tested, and validated. This way, the *Electrical E-nose V3* can, and will, be used by the Biomolecular Engineering Laboratory, to support their research work, mostly targeted to the medical field. In addition, the developed E-nose device, and the ionogel sensor characterization, may present considerable value and relevance to other artificial olfaction technologies and sensing applications.

6.2 Improvements and Future Work

Considering the results obtained for the AFE #1 circuit, and data regarding the performance of the *Electrical E-nose V3* in multiple real-world experiments, it was possible to conclude that the specifications for the design of an improved E-nose version were met. However, some improvement opportunities were found, mostly regarding the accuracy of the device. In addition, the AFE #1 circuit was not capable of driving the sensors at a frequency greater than 20 kHz. According to the ionogel sensor characterization, a sensor drive frequency of 100 kHz maximizes the overall performance of the sensors.

Considering the latter specifications, the AFE #2 circuit was designed. This AFE circuit was rated for a sensor drive frequency range between 100 Hz and 100 kHz, an expected accuracy greater than 98 % after calibration, an ENOB greater than 12-bit, and a sampling frequency of 667 kHz. However, due to limited time for the development of this work, the implementation of the AFE #2 circuit was not realized. This way, the implementation of the AFE #2 circuit in an E-nose device can be a starting point for the continuation of this work. Such implementation requires the design of an add-on PCB, which can be easily integrated into the main PCB, presented in subsubsection 4.4.2.1, as initially intended. In addition, it would be interesting to control the AFE #2 circuit DDS, to generate a frequency sweep between 100 Hz and 100 kHz, which enables the measurement of the impedance of the sensors in multiple frequencies, at once. Lastly, it would be interesting to create a more detailed mathematical model of the ionogel sensor, including temperature as a variable.

Bibliography

[1] J. M. Lourenço. *The NOVAthesis LaTeX Template User's Manual*. NOVA University Lisbon. 2021. URL: `https://github.com/joaomlourenco/novathesis/raw/master/template.pdf` (cit. on p. ii).

[2] A. Kannadan. "History of the Miasma Theory of Disease". In: *Essai* 16 (2018), p. 18 (cit. on p. 1).

[3] L. R. Bijland, M. K. Bomers, and Y. M. Smulders. "Smelling the diagnosis A review on the use of scent in diagnosing disease". In: *Netherlands Journal of Medicine* 71.6 (2013), pp. 300–307. ISSN: 03002977 (cit. on p. 1).

[4] D. B. Walker et al. "Naturalistic quantification of canine olfactory sensitivity". In: *Applied Animal Behaviour Science* 97.2-4 (2006-05), pp. 241–254. ISSN: 0168-1591. DOI: `10.1016/J.APPLANIM.2005.07.009` (cit. on p. 1).

[5] D. S. Hardin, W. Anderson, and J. Cattet. "Dogs Can Be Successfully Trained to Alert to Hypoglycemia Samples from Patients with Type 1 Diabetes". In: *Diabetes Therapy* 6.4 (2015-12), pp. 509–517. ISSN: 18696961. DOI: `10.1007/s13300-015-0135-x` (cit. on p. 1).

[6] C. M. Willis et al. "Volatile organic compounds as biomarkers of bladder cancer: Sensitivity and specificity using trained sniffer dogs". In: *Cancer Biomarkers* 8.3 (2010), pp. 145–153. ISSN: 15740153. DOI: `10.3233/CBM-2011-0208` (cit. on p. 1).

[7] M. Maurer et al. "Detection of bacteriuria by canine olfaction". In: *Open Forum Infectious Diseases* 3.2 (2016-04). ISSN: 23288957. DOI: `10.1093/ofid/ofw051` (cit. on p. 1).

[8] W. H. van Geffen et al. "The electronic nose: Emerging biomarkers in lung cancer diagnostics". In: *Breathe* 15.4 (2019-12), e135–e141. ISSN: 20734735. DOI: `10.1183/20734735.0309-2019` (cit. on p. 1).

[9] G. Santini et al. "Electronic Nose and Exhaled Breath NMR-based Metabolomics Applications in Airways Disease". In: *Current Topics in Medicinal Chemistry* 16.14 (2016), pp. 1610–1630. ISSN: 15680266. DOI: `10.2174/1568026616666151223113540` (cit. on p. 1).

[10] H. Tyagi et al. "Non-invasive detection and staging of colorectal cancer using a portable electronic nose". In: *Sensors* 21.16 (2021-08). ISSN: 14248220. DOI: `10.3390/s21165440` (cit. on p. 1).

[11] C. Baldini et al. "Electronic nose as a novel method for diagnosing cancer: A systematic review". In: *Biosensors* 10.8 (2020-08). ISSN: 20796374. DOI: `10.3390/bios10080084` (cit. on p. 2).

[12] R. van de Goor et al. "Training and Validating a Portable Electronic Nose for Lung Cancer Screening". In: *Journal of Thoracic Oncology* 13.5 (2018-05), pp. 676–681. ISSN: 1556-0864. DOI: `10.1016/J.JTHO.2018.01.024` (cit. on p. 2).

[13] C. Esteves et al. "Effect of film thickness in gelatin hybrid gels for artificial olfaction". In: *Materials Today Bio* 1 (2019-01), p. 100002. ISSN: 2590-0064. DOI: `10.1016/J.MTBIO.2019.100002` (cit. on p. 2).

[14] A. Hussain et al. "Tunable Gas Sensing Gels by Cooperative Assembly". In: *Advanced Functional Materials* 27.27 (2017-07), p. 1700803. ISSN: 1616-3028. DOI: `10.1002/ADFM.201700803` (cit. on pp. 2, 5, 6, 42).

[15] C. Esteves et al. "Tackling Humidity with Designer Ionic Liquid-Based Gas Sensing Soft Materials". In: *Advanced Materials* (2022). ISSN: 15214095. DOI: `10.1002/adma.202107205` (cit. on pp. 2, 5, 42, 49, 59, 65).

[16] J. Frazão et al. "Optical gas sensing with liquid crystal droplets and convolutional neural networks". In: *Sensors* 21.8 (2021-04). ISSN: 14248220. DOI: `10.3390/s21082854` (cit. on pp. 2, 5, 6).

[17] G. Santos et al. "An optimized e-nose for efficient volatile sensing and discrimination". In: *BIODEVICES 2019 - 12th International Conference on Biomedical Electronics and Devices, Proceedings; Part of 12th International Joint Conference on Biomedical Engineering Systems and Technologies, BIOSTEC 2019*. Prague, Czech Republic, 2019, pp. 36–46. ISBN: 9789897583537. DOI: `10.5220/0007390700360046` (cit. on pp. 2, 5).

[18] W. B. Gonçalves et al. "Ionogels based on a single ionic liquid for electronic nose application". In: *Chemosensors* 9.8 (2021-08). ISSN: 22279040. DOI: `10.3390/chemosensors9080201` (cit. on pp. 2, 5).

[19] W. Liu et al. "A highly sensitive and moisture-resistant gas sensor for diabetes diagnosis with Pt@In2O3 nanowires and a molecular sieve for protection". In: *NPG Asia Materials* 10.4 (2018-04), pp. 293–308. ISSN: 18844057. DOI: `10.1038/s41427-018-0029-2` (cit. on p. 2).

[20] S. K. Ayyala, J. A. Covington, and S. Mariani. "Humidity Dependence of Commercial Thick and Thin-Film MOX Gas Sensors under UV Illumination". In: *Engineering Proceedings 2021, Vol. 10, Page 10* 10.1 (2021-11), p. 10. ISSN: 2673-4591. DOI: `10.3390/ECSA-8-11246` (cit. on pp. 2, 42).

[21] P. Wei et al. “Impact Analysis of Temperature and Humidity Conditions on Electrochemical Sensor Response in Ambient Air Quality Monitoring”. In: *Sensors 2018, Vol. 18, Page 59* 18.2 (2018-01), p. 59. ISSN: 1424-8220. DOI: `10.3390/S18020059` (cit. on pp. 2, 42).

[22] A. C. Pádua et al. “Design and evolution of an opto-electronic device for VOCs detection”. In: *BIODEVICES 2018 - 11th International Conference on Biomedical Electronics and Devices, Proceedings; Part of 11th International Joint Conference on Biomedical Engineering Systems and Technologies, BIOSTEC 2018*. Vol. 1. Brazil, 2018, pp. 48–55. ISBN: 9789897582776. DOI: `10.5220/0006558100480055` (cit. on pp. 5, 7).

[23] A. C. Pádua. “Design and assembly of an opto-electronic device for artificial olfaction”. PhD thesis. FCT-NOVA, 2020-07. URL: `https://run.unl.pt/handle/10362/108950` (cit. on pp. 5, 7, 113).

[24] A. Sharma et al. “Sense of Smell: Structural, Functional, Mechanistic Advancements and Challenges in Human Olfactory Research”. In: *Current Neuropharmacology* 17.9 (2018), pp. 891–911. ISSN: 1570159X. DOI: `10.2174/1570159x17666181206095626` (cit. on p. 5).

[25] A. Madzharov et al. “The impact of coffee-like scent on expectations and performance”. In: *Journal of Environmental Psychology* 57 (2018-06), pp. 83–86. ISSN: 15229610. DOI: `10.1016/j.jenvp.2018.04.001` (cit. on p. 6).

[26] Brainline. *Interactive Brain - How Injury Can Affect the Brain | BrainLine*. 2022. URL: `https://www.brainline.org/tbi-basics/interactive-brain` (visited on 2022-07-05) (cit. on p. 6).

[27] Nyco Products Company. *The Simple Science of Smell | The Smell of Clean |*. 2020. URL: `https://www.nycoproducts.com/resources/blog/the-simple-science-of-smell-the-smell-of-clean/` (visited on 2022-07-05) (cit. on p. 6).

[28] J. Gutiérrez and M. C. Horrillo. “Advances in artificial olfaction: Sensors and applications”. In: *Talanta* 124 (2014-06), pp. 95–105. ISSN: 00399140. DOI: `10.1016/J.TALANTA.2014.02.016` (cit. on p. 6).

[29] S. E. Zohora, A. M. Khan, and N. Hundewale. “Chemical sensors employed in electronic noses: A review”. In: *Advances in Intelligent Systems and Computing* 178 (2013), pp. 177–184. ISSN: 21945365. DOI: `10.1007/978-3-642-31600-5_18/COVER/` (cit. on p. 6).

[30] C. Wang et al. “Metal Oxide Gas Sensors: Sensitivity and Influencing Factors”. In: *Sensors (Basel, Switzerland)* 10.3 (2010-03), p. 2088. ISSN: 14248220. DOI: `10.3390/S100302088` (cit. on p. 6).

[31] N. Boden et al. “Device applications of charge transport in discotic liquid crystals”. In: *Journal of Materials Chemistry* 9.9 (1999-01), pp. 2081–2086. ISSN: 1364-5501. DOI: `10.1039/A903005K` (cit. on p. 6).

[32] H. Bai and G. Shi. “Gas Sensors Based on Conducting Polymers”. In: *Sensors 2007, Vol. 7, Pages 267-307* 7.3 (2007-03), pp. 267–307. ISSN: 1424-8220. DOI: `10.3390/S7030267` (cit. on p. 6).

[33] L. O. Péres et al. “Conductive polymer gas sensor for quantitative detection of methanol in Brazilian sugar-cane spirit”. In: *Food Chemistry* 130.4 (2012-02), pp. 1105–1107. ISSN: 0308-8146. DOI: `10.1016/J.FOODCHEM.2011.08.014` (cit. on p. 6).

[34] J. R. Cordeiro et al. “Wood identification by a portable low-cost polymer-based electronic nose”. In: *RSC Advances* 6.111 (2016), pp. 109945–109949. ISSN: 20462069. DOI: `10.1039/C6RA22246C` (cit. on p. 6).

[35] H. M. Saraoğlu and B. Edin. “E-Nose system for anesthetic dose level detection using artificial neural network”. In: *Journal of medical systems* 31.6 (2007), pp. 475–482. ISSN: 0148-5598. DOI: `10.1007/S10916-007-9087-7` (cit. on p. 7).

[36] The eNose Company. *Research - The eNose Company*. 2022. URL: `https://www.enose-company.com/research/` (visited on 2022-08-15) (cit. on p. 7).

[37] Sensigent. *Cyranose Electronic Nose*. 2022. URL: `https://www.sensigent.com/products/cyranose.html` (visited on 2022-08-15) (cit. on p. 7).

[38] A. K. Pavlou et al. “Use of an electronic nose system for diagnoses of urinary tract infections”. In: *Biosensors and Bioelectronics* 17.10 (2002-10), pp. 893–899. ISSN: 09565663. DOI: `10.1016/S0956-5663(02)00078-7` (cit. on p. 7).

[39] X. Li. *Electronic Nose to Monitor the Freshness of Red Fish (Sebastes marinus) Stored in Ice and Modified Atmosphere Packaging (MAP)*. Tech. rep. Reykjavik, Iceland: Dalian Fisheries University, 2000 (cit. on p. 7).

[40] AIRSENSE Analytics. *Portable Electronic Nose | AIRSENSE Analytics*. 2019. URL: `https://airsense.com/en/products/portable-electronic-nose` (visited on 2022-08-15) (cit. on p. 7).

[41] FOODsniffer. *FOODsniffer*. 2022. URL: `http://www.myfoodsniffer.com/` (visited on 2022-08-15) (cit. on p. 7).

[42] W. Bourgeois and R. M. Stuetz. “Use of a chemical sensor array for detecting pollutants in domestic wastewater”. In: *Water Research* 36.18 (2002-11), pp. 4505–4512. ISSN: 00431354. DOI: `10.1016/S0043-1354(02)00183-5` (cit. on p. 7).

[43] J. P. Laboratory. *JPL Electronic Nose*. 2022. URL: `https://enose.jpl.nasa.gov/` (visited on 2022-08-15) (cit. on p. 7).

[44] R. T. Da Rocha, I. G. Gutz, and C. L. Do Lago. “A Low-Cost and High-Performance Conductivity Meter”. In: *Journal of Chemical Education* 74.5 (1997), pp. 572–574. ISSN: 00219584. DOI: `10.1021/ED074P572` (cit. on p. 8).

[45] Arduino.cc. *Arduino Due | Arduino Official Store*. 2022. URL: `https://store.arduino.cc/arduino-due` (visited on 2022-09-18) (cit. on pp. 8, 11, 44).

[46] J. Park and S. Mackay. *Practical Data Acquisition for Instrumentation and Control Systems*. Ed. by Elsevier. Newnes, 2003. ISBN: 978-0-7506-5796-9. DOI: `10.1016/b978-0-7506-5796-9.x5000-9` (cit. on pp. 11, 12).

[47] M. Usher and D.A. Keating. *Sensors and transducers*. 2nd ed. London: Red Globe Press London, 1996. DOI: `https://doi.org/10.1007/978-1-349-13345-1` (cit. on p. 11).

[48] Measurement Computing Corporation. *Data Acquisition Handbook | A Reference For DAQ And Analog & Digital Signal Conditioning*. 3rd ed. United States of America: Measurement Computing, 2012 (cit. on p. 12).

[49] Analog Devices. *High Performance Electrocardiogram (ECG) Signal Conditioning | Education | Analog Devices*. 2022. URL: `https://www.analog.com/en/education/education-library/articles/high-perf-electrocardiogram-signal-conditioning.html` (visited on 2022-02-10) (cit. on p. 12).

[50] P. Szakacs-Simon, S. A. Moraru, and F. Neukart. "Signal conditioning techniques for health monitoring devices". In: *2012 35th International Conference on Telecommunications and Signal Processing, TSP 2012 - Proceedings*. Prague, Czech Republic, 2012. DOI: `10.1109/TSP.2012.6256369` (cit. on p. 12).

[51] Analog Devices. *Chapter 20: Analog to Digital Conversion [Analog Devices Wiki]*. 2013. URL: `https://wiki.analog.com/university/courses/electronics/text/chapter-20` (visited on 2022-02-10) (cit. on pp. 13, 27).

[52] P. Narczyk and W. A. Pleskacz. "Analog Frontend for Reliable Human Body Temperature Measurement for IoT Devices". In: *Electronics 2022, Vol. 11, Page 434* 11.3 (2022-01), p. 434. ISSN: 2079-9292. DOI: `10.3390/ELECTRONICS11030434` (cit. on p. 13).

[53] F. Naaz and N. S. Grewal. "An SoC based wearable system for continuous Blood Pressure measurement". In: *2016 International Conference on Signal Processing and Communication, ICSC 2016*. Noida, India: Institute of Electrical and Electronics Engineers Inc., 2016, pp. 392–397. ISBN: 9781509026845. DOI: `10.1109/ICSPCOM.2016.7980612` (cit. on p. 13).

[54] S. Masui et al. "An ultra-low-power wireless transceiver SoC for medical applications". In: *2015 IEEE International Symposium on Radio-Frequency Integration Technology, RFIT 2015 - Proceedings*. Sendai, Japan: Institute of Electrical and Electronics Engineers Inc., 2016-01, pp. 1–3. ISBN: 9781467377942. DOI: `10.1109/RFIT.2015.7377867` (cit. on p. 13).

[55] Infineon Technologies. *PSoC ® 5LP: CY8C58LP Family Datasheet Programmable System-on-Chip (PSoC ®) General Description*. CY8C58LP datasheet. Rev. N. 2014. URL: `https://www.infineon.com/dgdl/Infineon-PSoC%7B%5C_%7D5LP%7B%5C_%7DCY8C58LP%7B%5C_%7DFamily%7B%5C_%7DDatasheet%7B%5C_%7DProgrammable%`

7B%5C_%7DSystem-on-Chip%7B%5C_%7D(PSoC%7B%5C_%7D)-DataSheet-v15%7B%5C_%7D00-EN.pdf?fileId=8ac78c8c7d0d8da4017d0ec547013ab9 (cit. on p. 14).

[56] A. Raj Kansal. "A Study on Programmable System on Chip". In: *IOSR journal of VLSI and Signal Processing* 4.5 (2014), pp. 31–37. ISSN: 23194197. DOI: 10.9790/4200-04513137 (cit. on p. 14).

[57] Infineon Technologies. *PSoC™ Creator - Infineon Technologies*. 2022. URL: https://www.infineon.com/cms/en/design-support/tools/sdk/psoc-software/psoc-creator/ (visited on 2022-09-24) (cit. on pp. 14, 70, 82, 83).

[58] Analog Devices. *ADUCM355 Precision Analog Microcontroller with Chemical Sensor Interface*. ADUCM355 datasheet. Rev. C. 2020. URL: https://www.analog.com/media/en/technical-documentation/data-sheets/ADuCM355.pdf (cit. on p. 15).

[59] H. Zumbahlen. "The Op Amp". In: *Linear Circuit Design Handbook*. Ed. by Hank Zumbahlen. Oxford, UK: Newnes/Elsevier, 2008. Chap. 1, pp. 1–82. ISBN: 978-0-7506-8703-4. DOI: 10.1016/b978-0-7506-8703-4.00001-8 (cit. on p. 16).

[60] J. A. Connelly and C. Motchenbacher. *Low-noise electronic system design*. United States of America: John Wiley & Sons, Ltd, 1993. ISBN: 0471577421 (cit. on pp. 16, 32).

[61] Texas Instruments. *Stability Analysis of Voltage- Feedback Op Including Compensation Techniques Application Report*. Tech. rep. Dallas, Texas: Texas Instruments, 2001. URL: www.ti.com/sc/docs/stdterms.htm (cit. on p. 16).

[62] ST Microelectronics. *Application note Operational amplifier stability compensation methods for capacitive loading applied to TS507*. Tech. rep. November. 2007, pp. 1–22. URL: Application%20note%20Operational%20amplifier%20stability%20compensation%20methods%20for%20capacitive%20loading%20applied%20to%20TS507 (cit. on p. 16).

[63] B. Carter and L. P. Huelsman. *Handbook Of Operational Amplifier Active RC Networks*. Ed. by Texas Instruments. Dallas, Texas: Texas Instruments, 2001, pp. 1–85. URL: https://www.ti.com/lit/an/sboa093a/sboa093a.pdf (cit. on p. 16).

[64] T. Green, P. Semig, and C. Wells. *Analog Engineer's Circuit Cookbook: Amplifiers*. Ed. by T. Green, P. Semig, and C. Wells. 2nd ed. Dallas, Texas: Texas Instruments, 2019, p. 278. URL: https://www.ti.com/seclit/eb/slyy137a/slyy137a.pdf (cit. on pp. 16, 27).

[65] W. Kester. *Analog switches and multiplexers*. Tech. rep. 2009. URL: https://www.analog.com/media/en/training-seminars/tutorials/mt-088.pdf (cit. on p. 26).

[66] H. Zumbahlen. "Fundamentals of Sampled Data Systems". In: *Linear Circuit Design Handbook*. Elsevier, 2008. Chap. 1, pp. 307–335. DOI: `10.1016/b978-0-7506-8703-4.00005-5`. URL: `https://www.sciencedirect.com/science/article/pii/B9780750687034000055?via%7B%5C%%7D3Dihub` (cit. on p. 27).

[67] P. Brokaw and J. Barrow. *Grounding for Low- and High-Frequency Circuits*. Tech. rep. 1989. URL: `https://www.analog.com/media/en/technical-documentation/application-notes/60011428695520149489604926984551317555846730208 28an%7B%5C_%7D345.pdf` (cit. on p. 33).

[68] H. Uhrmann, R. Kolm, and H. Zimmermann. "Analog Filters". In: *Analog Filters in Nanometer CMOS*. Berlin: Springer Berlin, Heidelberg, 2014. Chap. 8, pp. 3–11. ISBN: 978-3-642-38013-6. DOI: `10.1007/978-3-642-38013-6_2`. URL: `https://link.springer.com/chapter/10.1007/978-3-642-38013-6%7B%5C_%7D2` (cit. on p. 35).

[69] P. A. D. *Handbook of Formulas and Tables for Signal Processing*. 1st ed. Berlin: Springer Berlin, Heidelberg, 1999, p. 838. DOI: `10.1201/9781315219707`. URL: `https://link.springer.com/book/9783540648345` (cit. on pp. 36–38).

[70] N. Zoric et al. "Design and Simulations of Idc Sensor Using Comsol Multyphysics and Dielectric". In: *Buletinul Agir* 4 (2013), pp. 63–69 (cit. on p. 41).

[71] R. R. Khan and S. W. Kang. "Highly sensitive multi-channel IDC sensor array for low concentration taste detection". In: *Sensors (Switzerland)* 15.6 (2015-06), pp. 13201–13221. ISSN: 14248220. DOI: `10.3390/S150613201` (cit. on pp. 42, 49).

[72] MEAS. *HTU21D(F) Digital Relative Humidity sensor with Temperature output*. HTU21D(F) datasheet. Rev. A. 2013. URL: `https://cdn-shop.adafruit.com/datasheets/1899_HTU21D.pdf` (cit. on pp. 44, 82).

[73] Digilent. *USB Oscilloscope and Logic Analyzer - Digilent Analog Discovery 2*. Analog Discovery 2 datasheet. Rev. A. 2021. URL: `https://www.ni.com/pdf/manuals/AnalogDiscovery2NIDatasheet.pdf` (cit. on p. 44).

[74] I. S. Dos Santos-Neto et al. "Interdigitated Electrode for Electrical Characterization of Commercial Pseudo-Binary Biodiesel–Diesel Blends". In: *Sensors 2021, Vol. 21, Page 7288* 21.21 (2021-11), p. 7288. ISSN: 1424-8220. DOI: `10.3390/S21217288` (cit. on p. 49).

[75] Infineon Technologies. *AN58304 - PSoC® 3 and PSoC 5LP – Pin Selection for Analog Designs | Cypress Semiconductor*. Tech. rep. 2015. URL: `http://www.cypress.com/documentation/application-notes/an58304-psoc-3-and-psoc-5lp-pin-selection-analog-designs?source=search%7B%5C&%7Dkeywords=AN58304` (cit. on p. 71).

[76] Infineon Technologies. *Trans-Impedance Amplifier (TIA)*. PSoC® Creator™ Component Datasheet. Rev. 1.80. 2011. URL: https://www.infineon.com/dgdl/Infineon-Component%7B%5C_%7DTIA%7B%5C_%7DV1.80-Software%20Module%20Datasheets-v02%7B%5C_%7D00-EN.pdf?fileId=8ac78c8c7d0d8da4017d0e7e89831085 (cit. on p. 74).

[77] Infineon Technologies. *Delta Sigma Analog to Digital Converter (ADC_DelSig)*. PSoC® Creator™ Component Datasheet. Rev. 3.30. 2017. URL: https://www.infineon.com/dgdl/Infineon-Component_Delta_Sigma_ADC_(ADC_DelSig)_V3.30-Software+Module+Datasheets-v03_03-EN.pdf?fileId=8ac78c8c7d0d8da4017d0e7ce9430ebe&utm_source=cypress&utm_medium=referral&utm_campaign=202110_globe_en_all_integration-files (cit. on p. 79).

[78] Texas Instruments. *TMUX111x 5-V, Low-Leakage-Current, 1:1 (SPST), 4-Channel Precision Switches*. TMUX1112 Datasheet. Rev. B. 2019. URL: https://www.ti.com/lit/ds/symlink/tmux1112.pdf?ts=1664124335796&ref_url=https%253A%252F%252Fwww.ti.com%252Fproduct%252FTMUX1112 (cit. on p. 90).

[79] Texas Instruments. *Dual, precision, zero-crossover, 20-MHz, 0.9-pA Ib, RRIO, CMOS operational amplifier*. OPA2320 Datasheet. Rev. F. 2016. URL: https://www.ti.com/lit/ds/symlink/opa2320.pdf?ts=1664124523922&ref_url=https%253A%252F%252Fwww.ti.com%252Fproduct%252FOPA2320 (cit. on p. 94).

[80] Texas Instruments. *TINA-TI Simulation tool | TI.com*. 2022. URL: https://www.ti.com/tool/TINA-TI (visited on 2022-09-18) (cit. on pp. 96–99).

[81] TCS Micropumps. *D3K Series Miniature Diaphragm Gas/Air Pump*. D3K Datasheet. Rev. 1. 2022. URL: https://micropumps.co.uk/DATA/pdf/DS27%20-%20D3k%20Data%20Sheet%20rev%201.pdf (cit. on p. 102).

[82] Clippard. *NIV Series PTFE Media Isolation Valves*. NR1-3-12 Datasheet. Rev. 1. 2022. URL: https://www.clippard.com/downloads/PDF_Documents/Product%20Data%20Sheets/Clippard%20NIV%20Media%20Isolation%20Valves.pdf (cit. on p. 102).

[83] Autodesk. *EAGLE | PCB Design And Electrical Schematic Software | Autodesk*. 2022. URL: https://www.autodesk.com/products/eagle/overview (visited on 2022-09-24) (cit. on pp. 105, 109).

[84] EDAC. *Card Edge Connectors*. 305-072-500-201 Datasheet. Rev. 1. 2009. URL: https://files.edac.net/edac/content/305/305-072-500-201%20-%20EDAC%20Card%20Edge%20Connector.PDF (cit. on p. 105).

[85] Hammond Manufacturing. *Black Watertight Extruded Aluminum Enclosure*. 1457J1601BK Datasheet. Rev. 1. 2022. URL: https://www.hammfg.com/files/parts/pdf/1457J1601BK.pdf (cit. on p. 105).

[86] Saturn PCB Design. *Saturn PCB Toolkit - Saturn PCB Design | Saturn PCB Design*. 2020. URL: `https://saturnpcb.com/saturn-pcb-toolkit/` (visited on 2022-08-14) (cit. on p. 108).

[87] Autodesk. *Fusion 360 | Software CAD, CAM, CAE e PCB 3D | Autodesk*. 2022. URL: `https://www.autodesk.it/products/fusion-360/overview?term=1-YEAR%7B%5C&%7Dtab=subscription%7B%5C&%7Dplc=F360` (visited on 2022-09-24) (cit. on pp. 109, 122).

A

Appendix 1

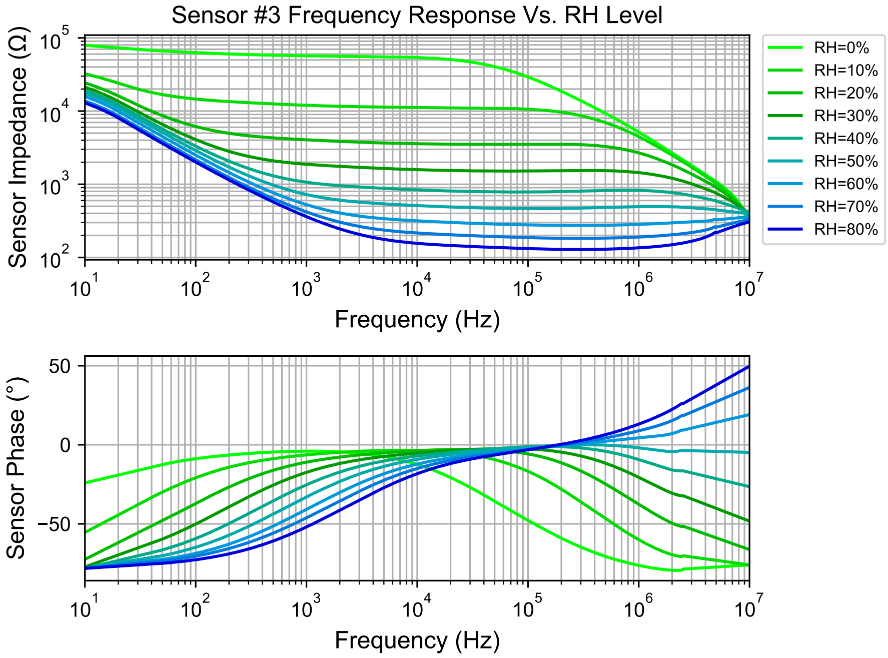

Figure A.1: Frequency response of sensor #3 as a function of RH.

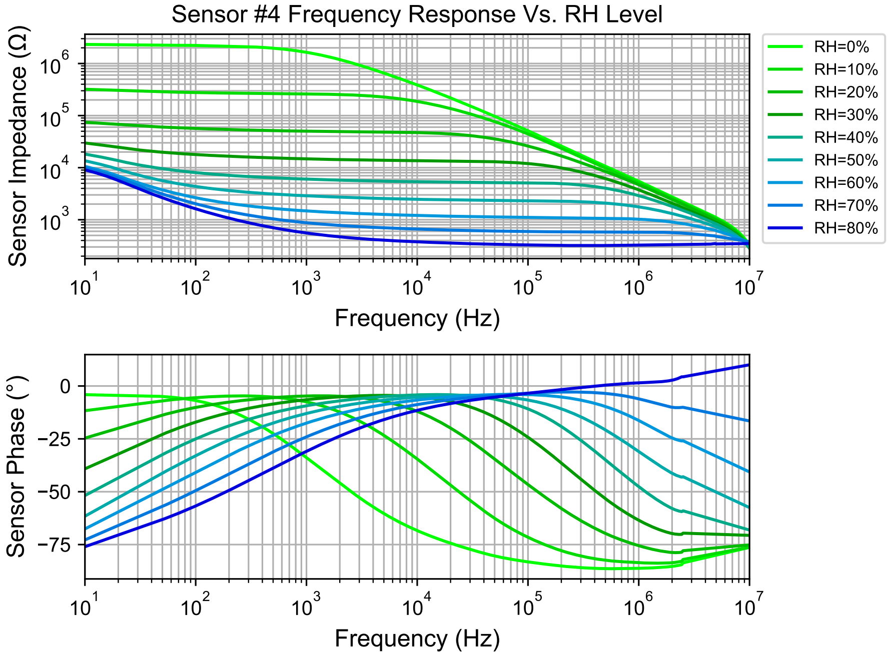

Figure A.2: Frequency response of sensor #4 as a function of RH.

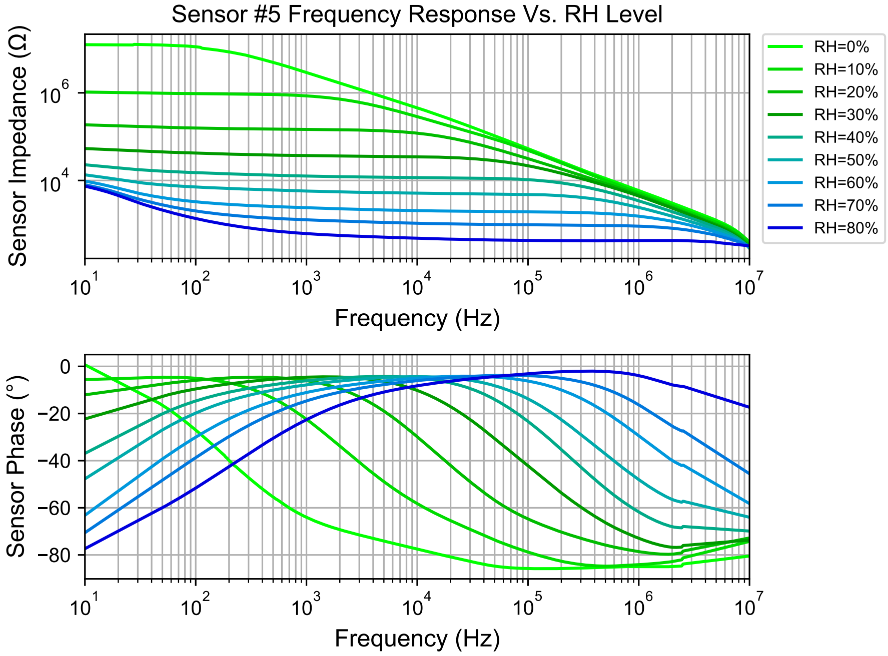

Figure A.3: Frequency response of sensor #5 as a function of RH.

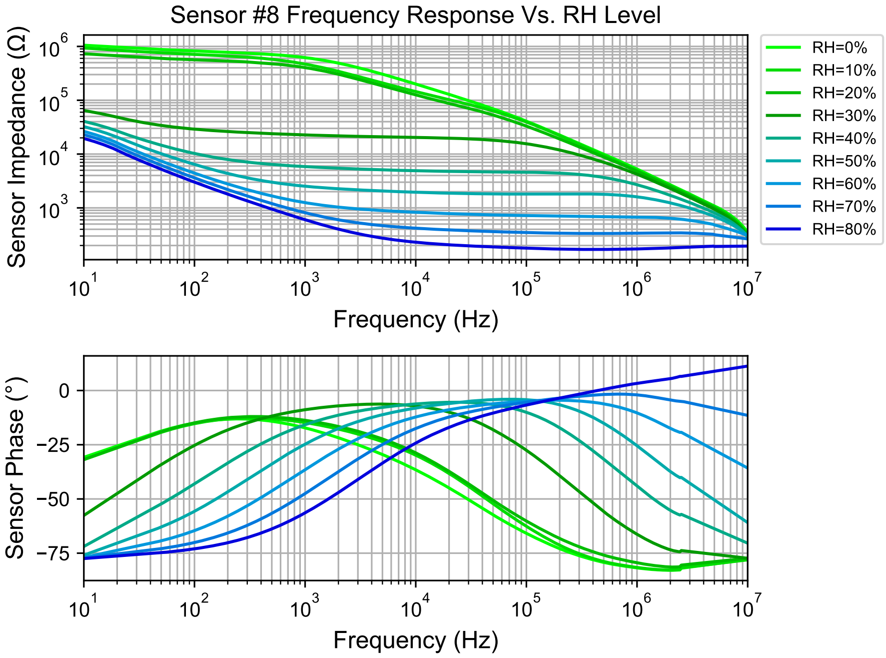

Figure A.4: Frequency response of sensor #8 as a function of RH.

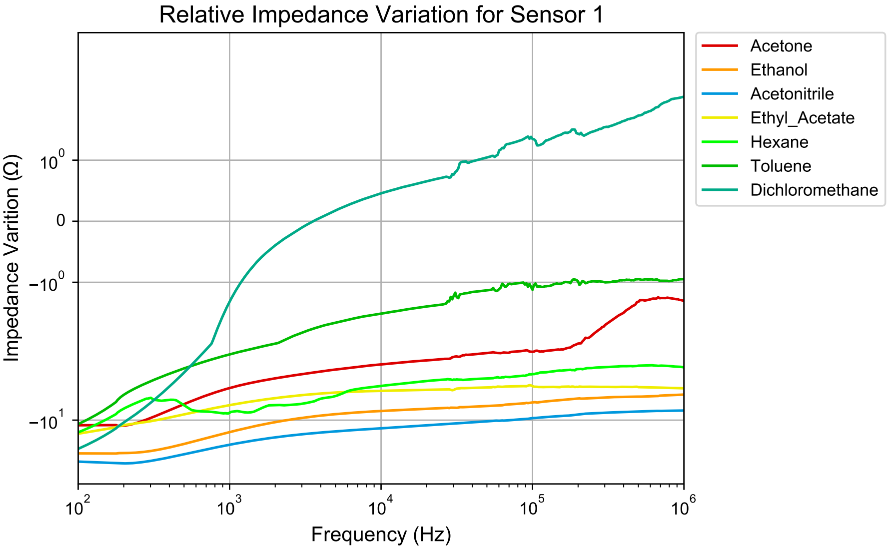

Figure A.5: Impedance variation for sensor #1, as a function of VOC.

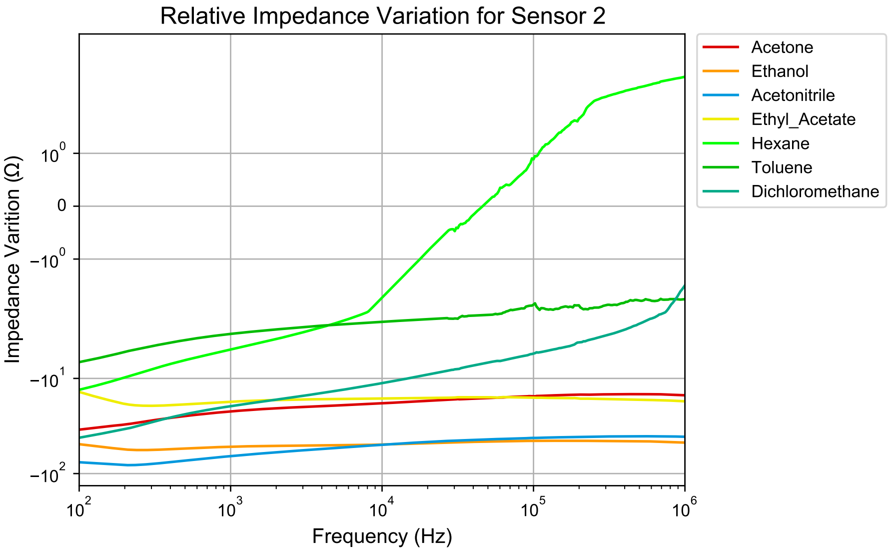

Figure A.6: Impedance variation for sensor #2, as a function of VOC.

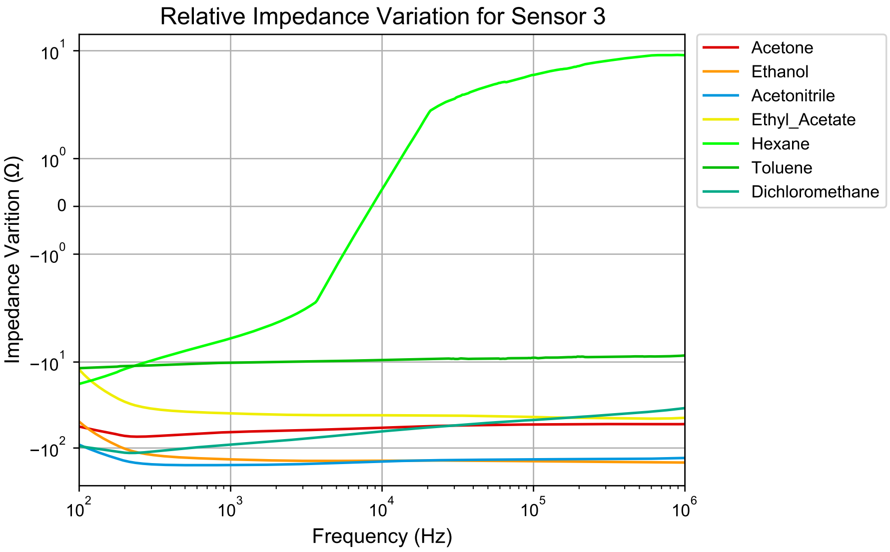

Figure A.7: Impedance variation for sensor #3, as a function of VOC.

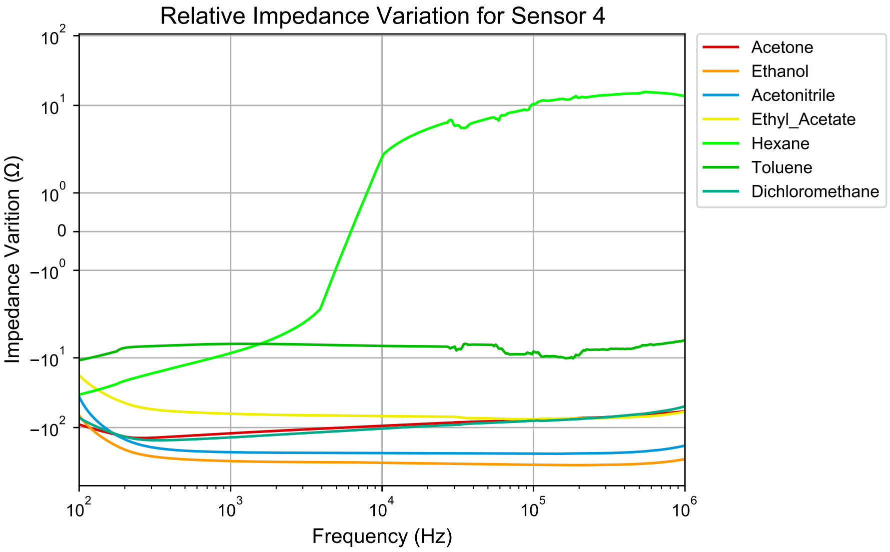

Figure A.8: Impedance variation for sensor #4, as a function of VOC.

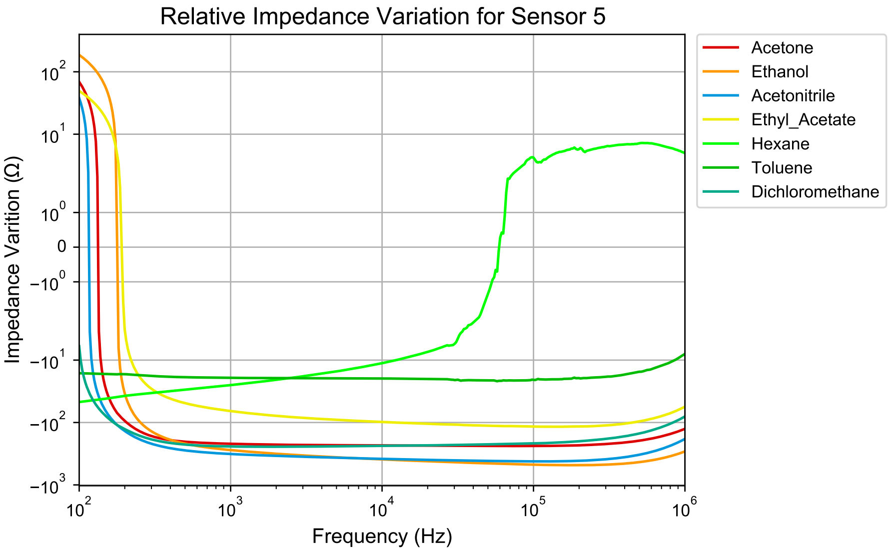

Figure A.9: Impedance variation for sensor #5, as a function of VOC.

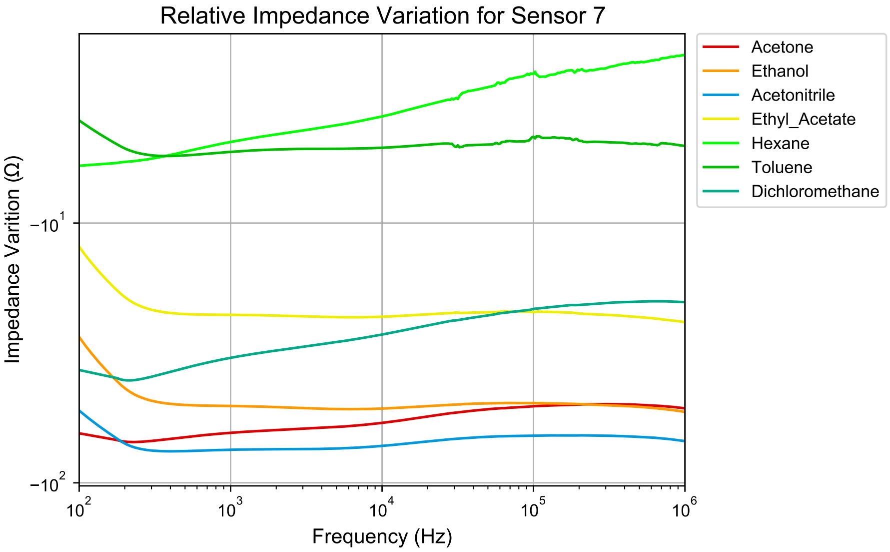

Figure A.10: Impedance variation for sensor #7, as a function of VOC.

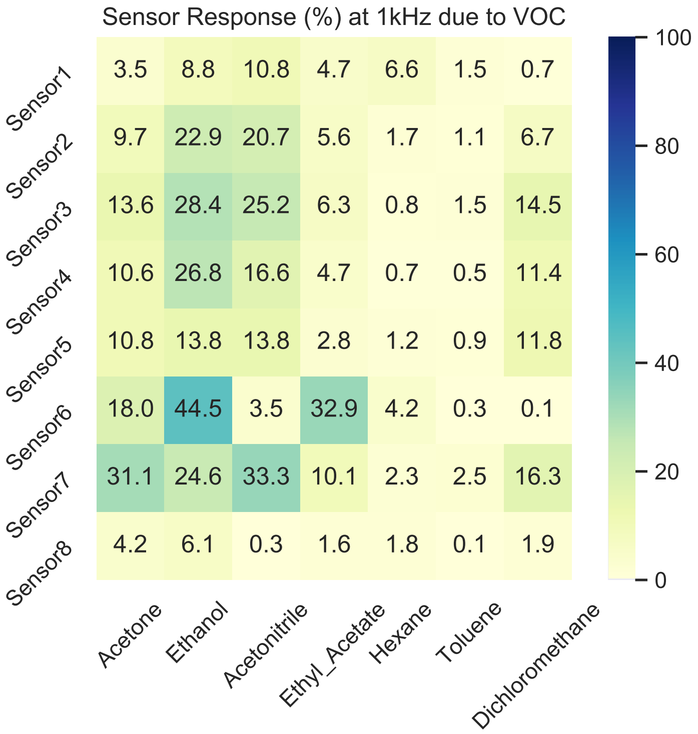

	Acetone	Ethanol	Acetonitrile	Ethyl_Acetate	Hexane	Toluene	Dichloromethane
Sensor1	3.5	8.8	10.8	4.7	6.6	1.5	0.7
Sensor2	9.7	22.9	20.7	5.6	1.7	1.1	6.7
Sensor3	13.6	28.4	25.2	6.3	0.8	1.5	14.5
Sensor4	10.6	26.8	16.6	4.7	0.7	0.5	11.4
Sensor5	10.8	13.8	13.8	2.8	1.2	0.9	11.8
Sensor6	18.0	44.5	3.5	32.9	4.2	0.3	0.1
Sensor7	31.1	24.6	33.3	10.1	2.3	2.5	16.3
Sensor8	4.2	6.1	0.3	1.6	1.8	0.1	1.9

Figure A.11: Affinity between the different sensor formulations and VOCs, at a frequency of 1 kHz.

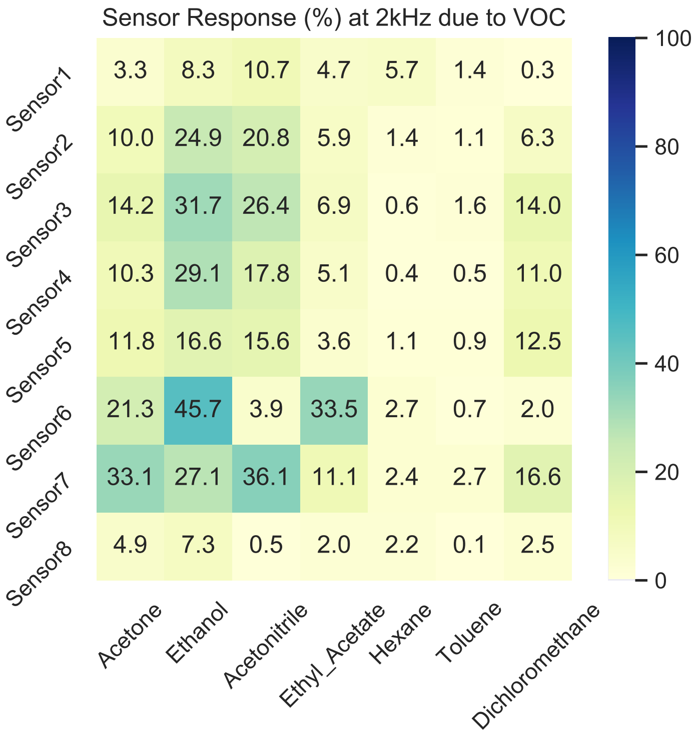

Figure A.12: Affinity between the different sensor formulations and VOCs, at a frequency of 2 kHz.

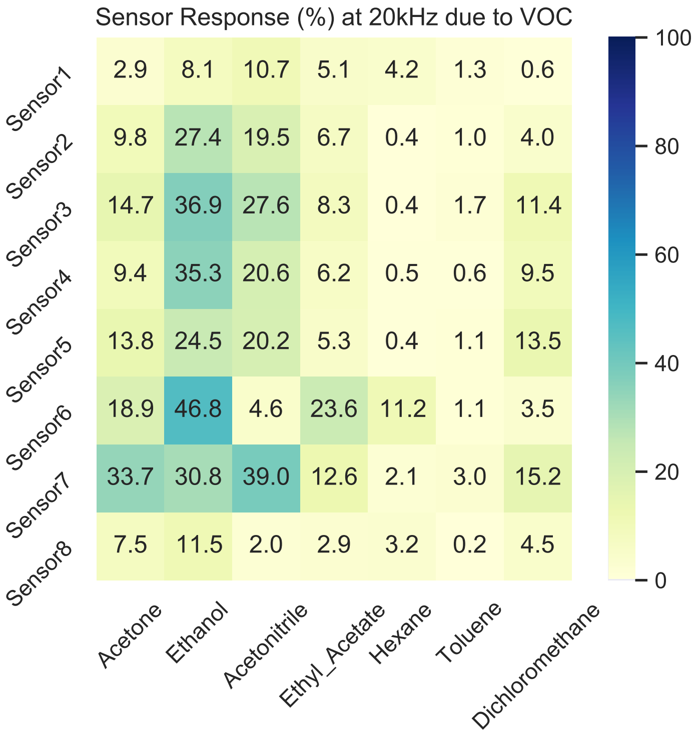

Figure A.13: Affinity between the different sensor formulations and VOCs, at a frequency of 20 kHz.

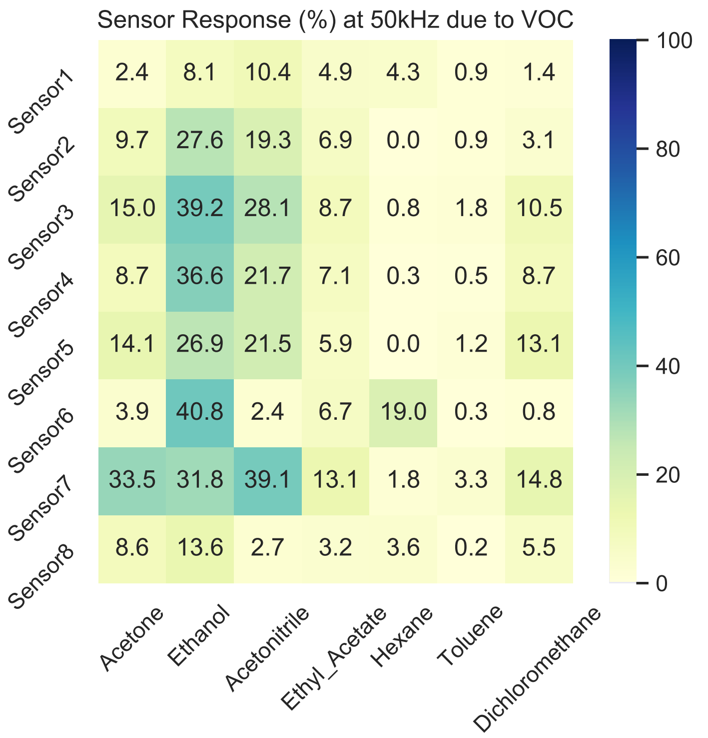

	Acetone	Ethanol	Acetonitrile	Ethyl_Acetate	Hexane	Toluene	Dichloromethane
Sensor1	2.4	8.1	10.4	4.9	4.3	0.9	1.4
Sensor2	9.7	27.6	19.3	6.9	0.0	0.9	3.1
Sensor3	15.0	39.2	28.1	8.7	0.8	1.8	10.5
Sensor4	8.7	36.6	21.7	7.1	0.3	0.5	8.7
Sensor5	14.1	26.9	21.5	5.9	0.0	1.2	13.1
Sensor6	3.9	40.8	2.4	6.7	19.0	0.3	0.8
Sensor7	33.5	31.8	39.1	13.1	1.8	3.3	14.8
Sensor8	8.6	13.6	2.7	3.2	3.6	0.2	5.5

Figure A.14: Affinity between the different sensor formulations and VOCs, at a frequency of 50 kHz.

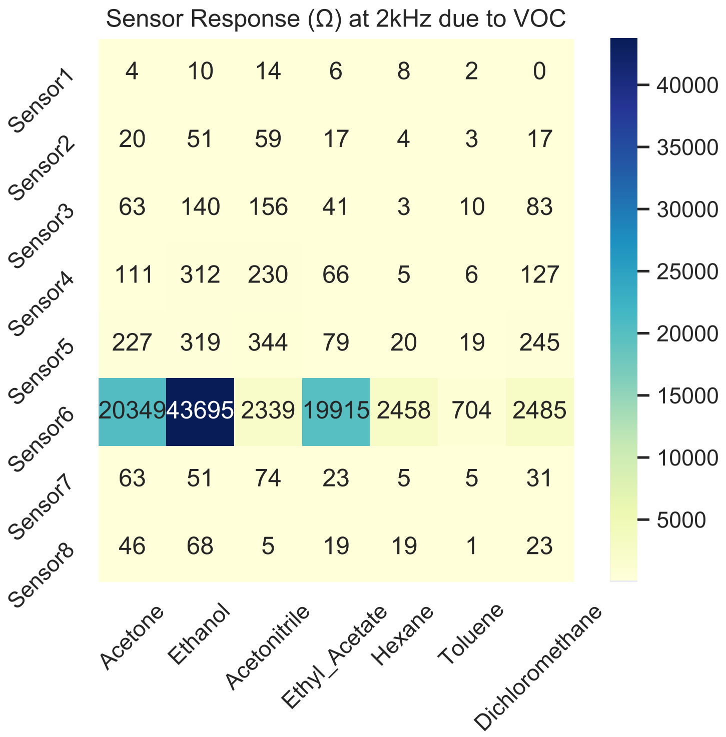

	Acetone	Ethanol	Acetonitrile	Ethyl_Acetate	Hexane	Toluene	Dichloromethane
Sensor1	4	10	14	6	8	2	0
Sensor2	20	51	59	17	4	3	17
Sensor3	63	140	156	41	3	10	83
Sensor4	111	312	230	66	5	6	127
Sensor5	227	319	344	79	20	19	245
Sensor6	20349	43695	2339	19915	2458	704	2485
Sensor7	63	51	74	23	5	5	31
Sensor8	46	68	5	19	19	1	23

Figure A.15: Impedance variation between recovery and exposure phases, for a frequency of 2 kHz.

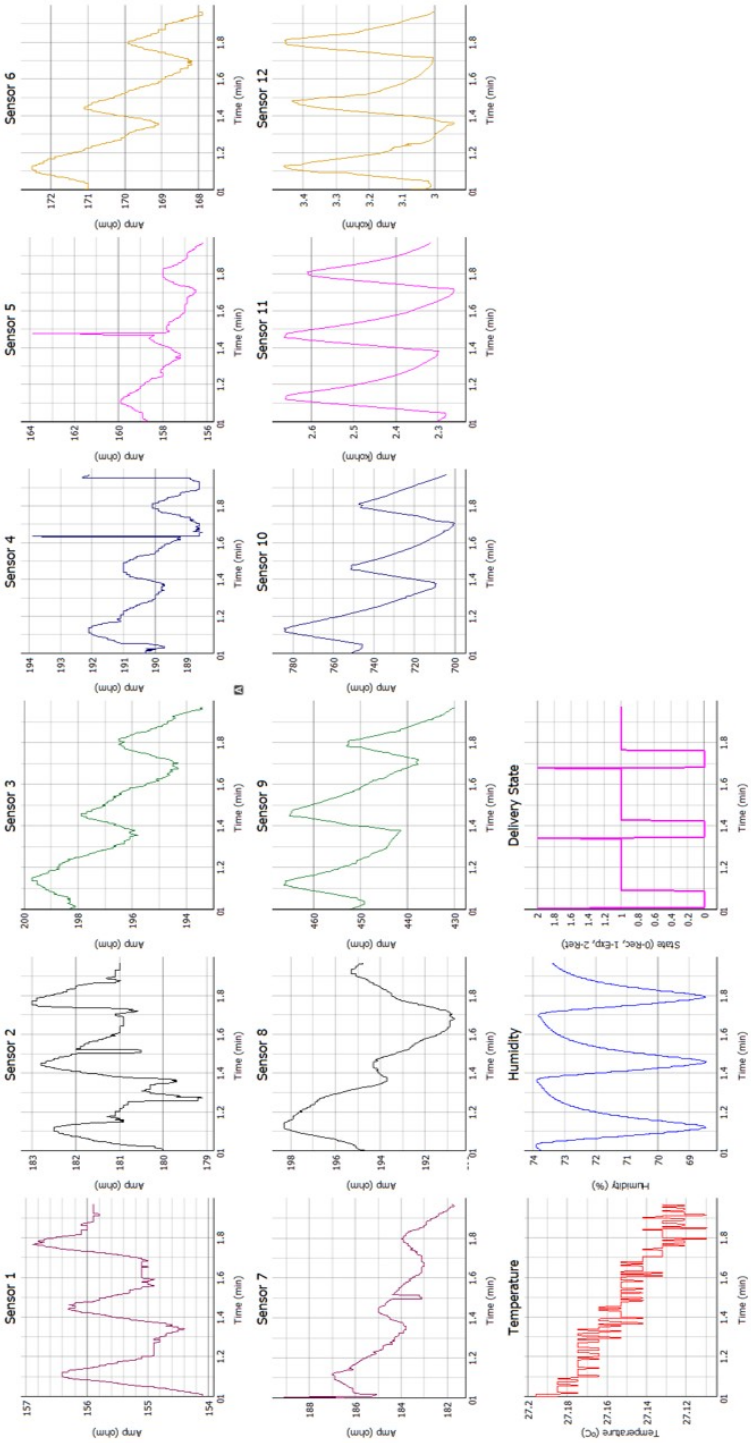

Figure A.16: Plotting window presenting real-time data collected by the e-nose. *Sensor*1 to *Sensor*12 correspond to the impedance measurements of the sensor array; *Temperature* and *Humidity* correspond to the data from the external temperature and RH sensor; and *Delivery State* corresponds to the delivery phase changes throughout the experiment.

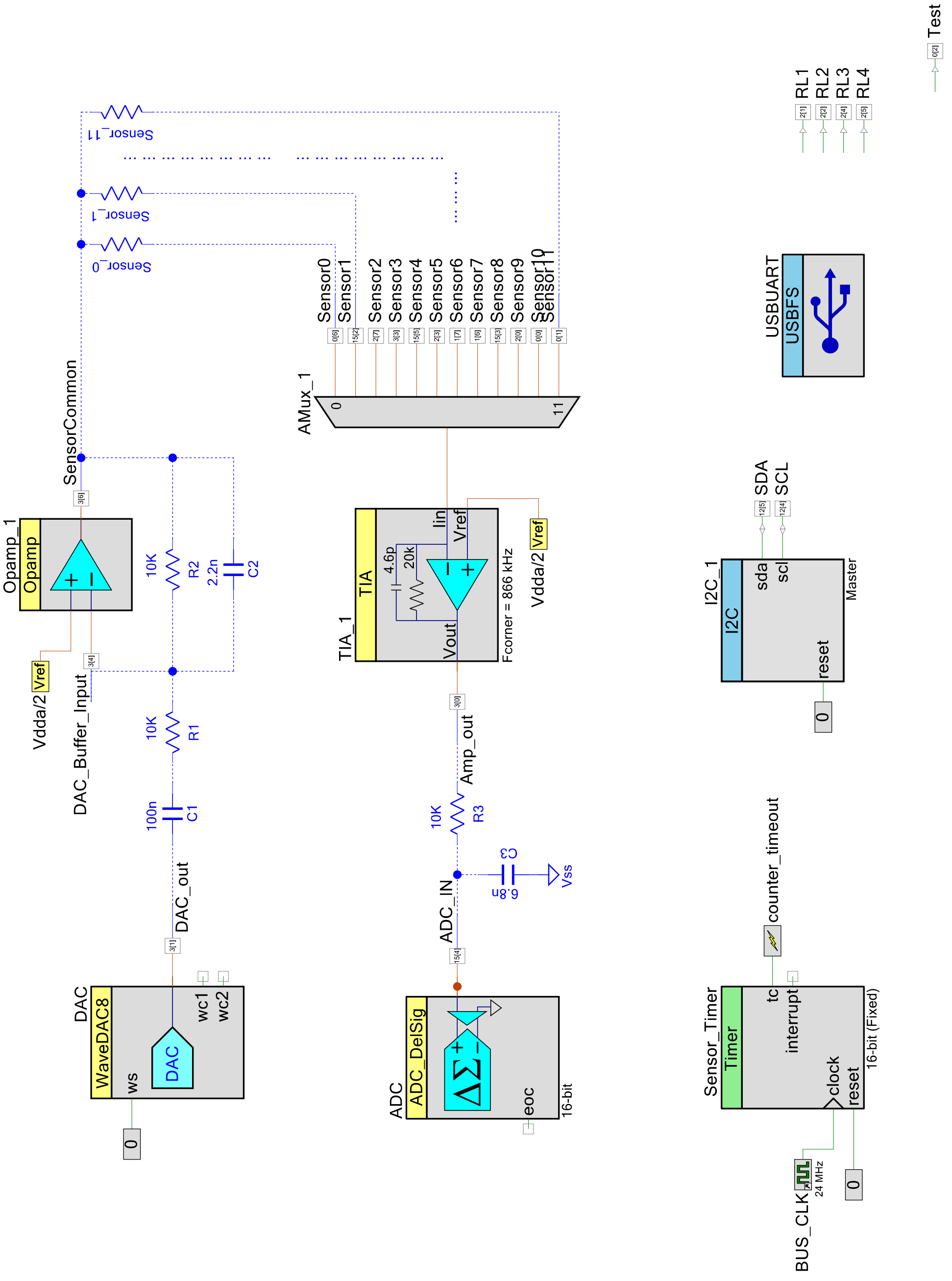

Figure A.17: Complete AFE#1 circuit schematic. All external components are shown in blue, including a resistive model of the sensors.

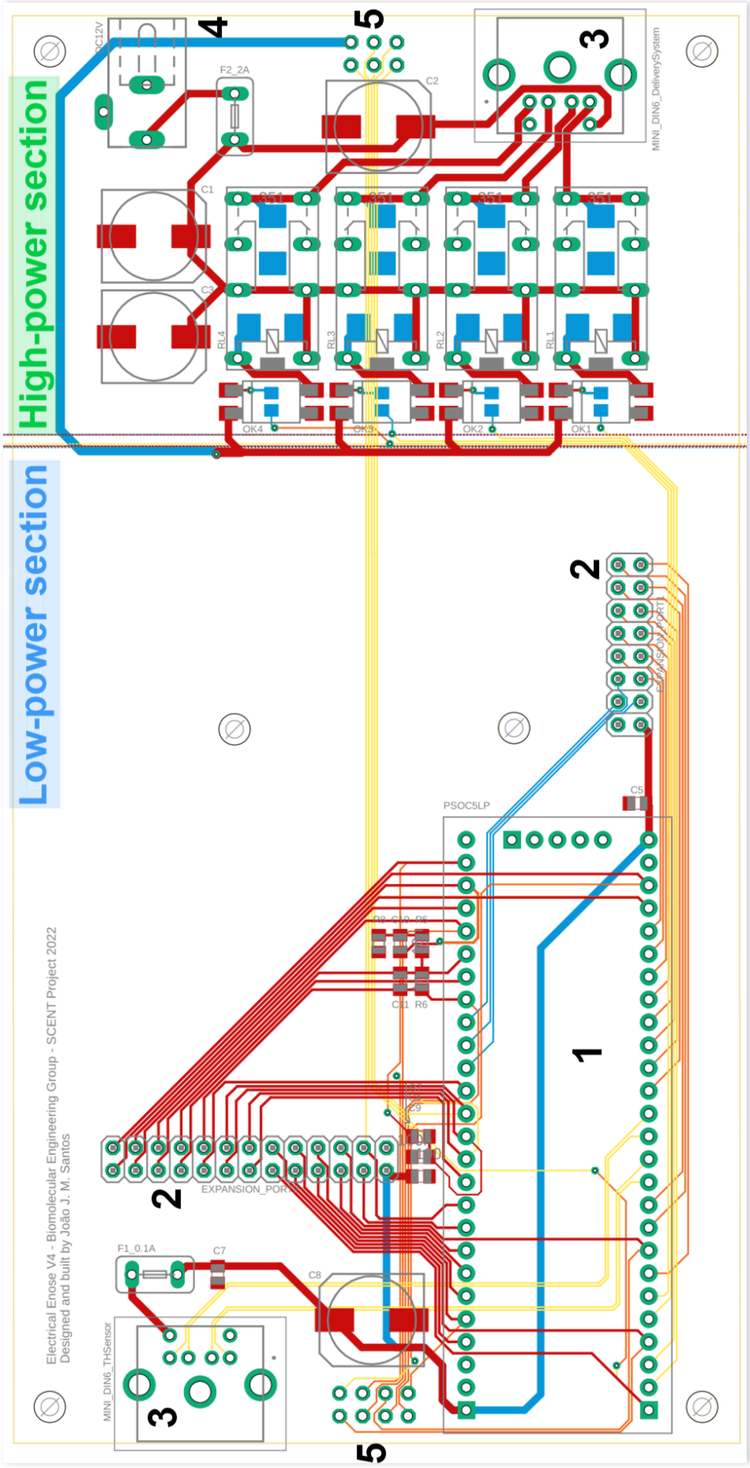

Figure A.18: Main PCB design. Labels: 1-PSoC 5LP; 2-expansion ports; 3-mini DIN connectors; 4-DC power input; 5-connectors for sensor detection chamber adapter PCB.

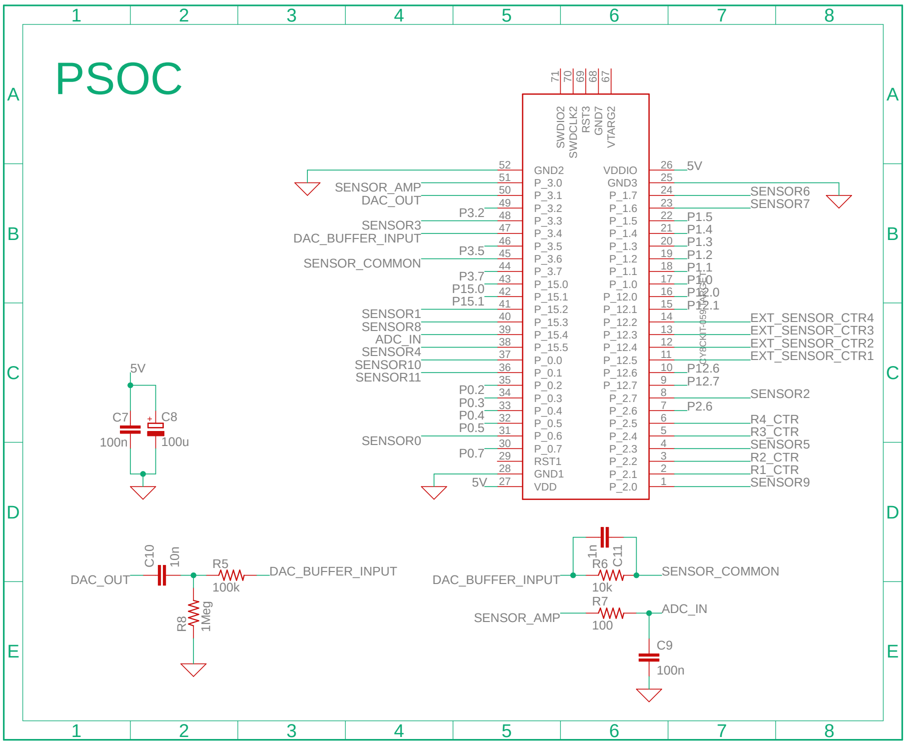

Figure A.19: AFE #1 circuit schematic sheet #1.

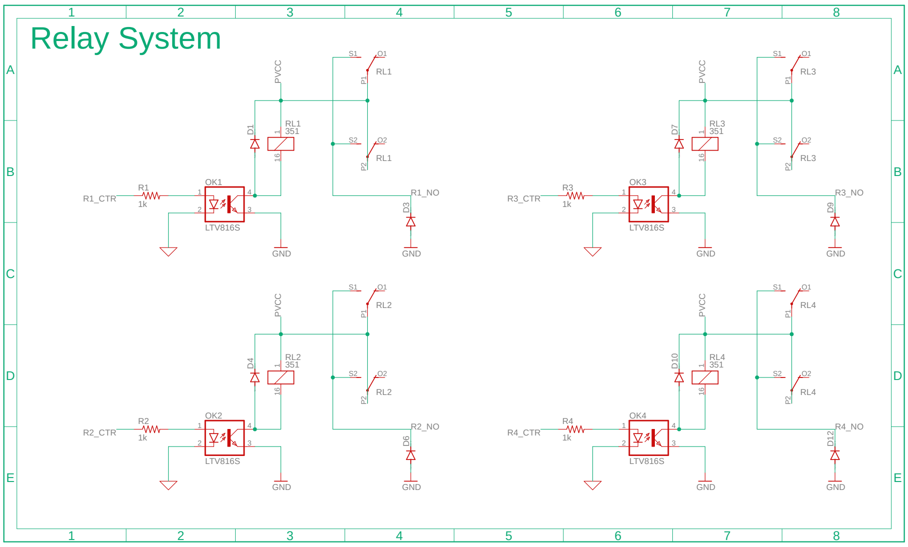

Figure A.20: AFE #1 circuit schematic sheet #2.

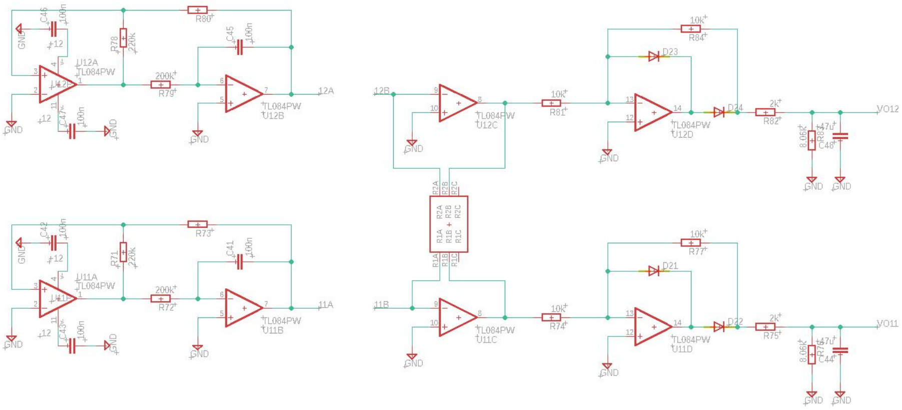

Figure A.21: Electrical E-nose V2 simplified circuit schematic.

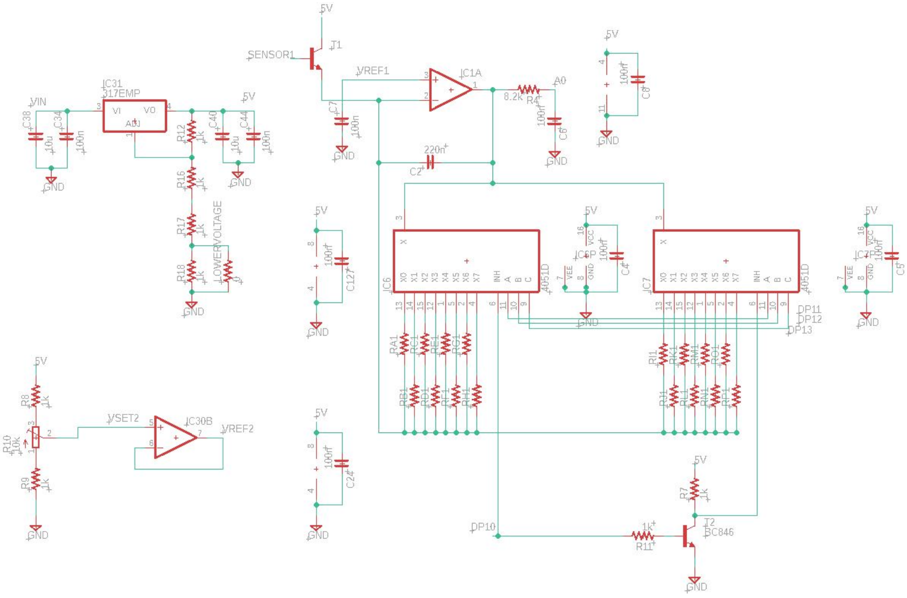

Figure A.22: Optical E-nose V4 simplified circuit schematic.

B

APPENDIX 2

An electrical model characterization of an electronic nose chemical sensor using a programmable system-on-a-chip based AFE

João J. M. Santos^{1,2,3}, Susana I. C. J. Palma^{2,3}, Carina Esteves^{2,3},
Hugo Gamboa^{4}, João Pedro Oliveira^{1,5}, Ana C. A. Roque^{2,3}

^{1}*Department of Electrical and Computer Engineering*
^{2}*Associate Laboratory i4HB – Institute for Health and Bioeconomy*
^{3}*UCIBIO – Applied Molecular Biosciences Unit, Department of Chemistry*
^{4}*LIBPhys - Laboratory for Instrumentation, Biomedical Engineering and Radiation Physics*
^{5}*Center for Technology and Systems (CTS) - UNINOVA*
NOVA School of Science and Technology, NOVA University of Lisbon, 2829-516 Caparica, Portugal
jj.santos@campus.fct.unl.pt, {jpao, h.gamboa, cecilia.roque, s.palma, ca.esteves}@fct.unl.pt

Abstract—**The diagnosis of many diseases involves invasive detection methods, which are both painful and stressing for patients. In the last decades, the ever-growing development in electronic nose (E-Nose) technology made them great candidates for non-invasive disease detection methods. Such devices mimic the human olfactory system through a set of sensors which produce signals that can be associated with diseases. Recently, a class of low-cost and innovative ionogel sensors, developed by our group demonstrated their full applicability in E-Nose systems, opening a new and promising approach to the field. However, the operation of such sensor needs a background calibration phase which relies on the correct characterization and parameterization of the corresponding electrical sensor model.**

This paper proposes a model characterization methodology based on a set of frequency responses acquisitions of the sensor, under several humidity conditions. To obtain a flexible acquisition tool capable of acquiring accurate results, an analog front-end (AFE) circuit to interface with the interdigitated electrode (IDE) sensors is presented. Such AFE circuit is fully implemented using a programmable system-on-a-chip (PSoC), helping to reduce system size and cost. Lastly, a comparison between the electrical model and data acquired with the proposed system is presented.

Index Terms—**Analog front-end, Programmable system-on-a-chip, Electronic nose, Ionogel sensor, Interdigitated electrode sensor.**

I. INTRODUCTION

Since the 5th century BC, olfaction was used as a disease detection method [1]. Studies have found that canine scent detection capability is, at least, 4 orders of magnitude more powerful than the human's [2], with great success at detecting numerous diseases. The technology boom and the curiosity for understanding the mammalian olfactory system, made possible the creation of a device that mimics the biological olfaction sense: the electronic nose (E-Nose) [3].

An E-Nose relies on the detection of volatile organic compounds (VOCs). To sense a sample, the E-Nose features an array of semi-selective gas sensors that produce response patterns to different VOCs, mimicking the human olfactory system [4]. Such sensors are typically found inside a detection chamber, where the interaction with the gaseous sample occurs. An acquisition system is responsible to obtain and convert electrical signals into digital information, which is, typically, fed into artificial intelligence or machine learning algorithms, for pattern recognition and odor classification.

The applications for E-Nose devices dramatically increased, ranging from agriculture [5] to food quality assessment [6], and, specially, medical and healthcare, in which a number of E-Nose devices targeted to detect different forms of diseases have been reported [7]–[9]. Depending on the application, E-Nose devices might employ different types and families of sensors, such as electrochemical, carbon nano-tube, optical and acoustic sensors. Our group, the Biomolecular Engineering Laboratory, developed sensors made from the combination of biopolymers and ionic liquids, known as ionogel sensors [10].

Due to the unique and innovative composition and construction of ionogel sensors, a background calibration and characterization phase is mandatory to understand the sensor's behavior under different ambient conditions. In this paper, an electrical model of such sensors is obtained from a set of frequency response acquisitions. In addition, a reconfigurable analog front-end (AFE) circuit dedicated to interface with a multi-sensor array, capable of acquiring accurate results, is presented.

This work was supported by funding from the European Research Council (ERC) under the EU Horizon 2020 research and innovation program (grant agreement No. SCENT-ERC-2014-STG-639123, 2014-2022) and also by national funds from Fundação para a Ciência e Tecnologia, I.P. (FCT) in the scope of the project UIDP/04378/2020 and UIDB/04378/2020 of the Research Unit on Applied Molecular Biosciences – UCIBIO and the project LA/P/0140/2020 of the Associate Laboratory Institute of Health and Bioenconomy – i4HB.

II. A NEW IONOGEL SENSOR FOR AN ELECTRONIC NOSE

A. *Sensor's Working Principle and Signal Generation*

A Ionogel sensor is formed by a mixture of gelatin and ionic liquid. Due to the presence of ionic liquid, the ionogels generate an electrical response to volatile analytes [10]. The construction of the ionogel sensors is based on an interdigitated electrode (IDE) structure, maximizing the contact area of the electrodes, which are coated in gold and deposited on a glass substrate. A thin film of ionogel material is then spread across the two electrodes, acting as the sensing element [11]. Fig. 1 shows the resulting sensor. When VOC molecules adsorb to the ionogel they cause alterations in its conductivity, which results in variations in the impedance of the sensor. When an AC signal is applied between the two electrodes, an alternating electrical field is created, which penetrates the ionogel material under test (MUT), reflecting a change in the impedance of the sensor [10], [12].

One of the major limitations of gas sensors is the negative impact of environmental conditions, such as the relative humidity (RH). In the normal E-nose operation, the sensors are cyclically exposed to gas samples, whose RH level is variable, resulting in a signal. However, this signal masks the sensor's response to analytes, reducing the accuracy of the E-nose. One strategy to control the influence of RH in the sensors signal is to rationally tune the composition of the sensing material [13]. Alternatively, an optimization can be made by characterizing the sensor's properties under different RH conditions, and improving the accuracy and precision of the AFE circuit.

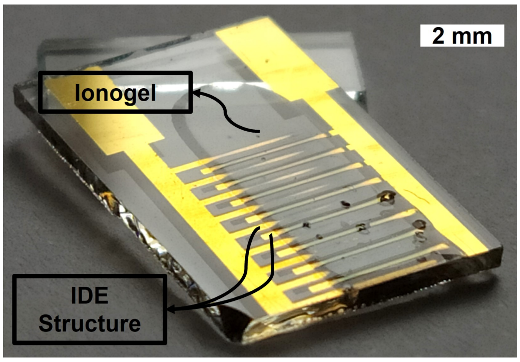

Fig. 1. Ionogel sensor.

B. *Frequency Response Test Setup*

To characterize the sensors and obtain a mathematical model, multiple frequency response acquisitions were experimentally obtained, for 9 distinct RH levels, and a fixed temperature of 22 ± 1ºC. A total of 3 experiment runs were conducted, in different days, and using distinct sensors from 3 production batches. Each experiment run was composed of two parts, in which the sensors were exposed to either an increasing or decreasing RH level. A total of 8 distinct sensor formulations were tested (sensor #1 to sensor #8), each tuned to a specific analyte, resulting in a sample size of 48 sensors and 864 individual tests.

Impedance measurements, for a range of frequencies between 10 Hz and 10 MHz, were obtained using a calibrated impedance analyzer (Digilent Analog Discovery 2) [14]. The distinct RH levels were created using the setup presented in Fig. 2, in which two mass flow controllers (MFCs) [15] were used to vary the flow of nitrogen between two paths, generating a dry and a wet stream, which are mixed inside the sensors chamber. The RH measurement was made with a dedicated sensor (HTU21D-F) [16], resulting in a RH measurement uncertainty of ± 1%.

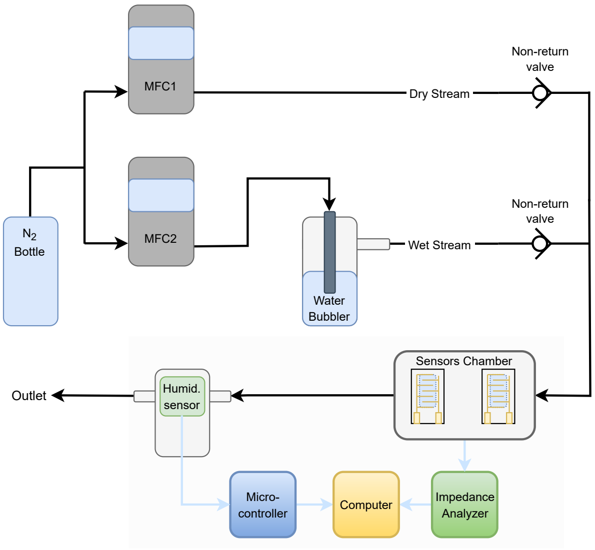

Fig. 2. Experimental setup used to obtain the frequency response of the sensors.

III. ELECTRICAL MODEL FROM FREQUENCY RESPONSE EXPERIMENTS

A. *Data Analysis*

In Fig. 3, the frequency response curves of sensor #1, for RH values between 0% and 80%, are presented. The sensor's impedance is in the order of tens of kΩ for low frequencies, however as frequency increases the impedance decreases, remaining relatively constant for a range of frequencies between 10 kHz and 1 MHz.

The RH level contribution to the sensor's impedance is considerable, particularly at frequencies greater than 10 kHz. This behavior is supported by the phase diagram, in which is clear that the RH level not only shifts the frequencies of poles and zeros of the sensor's frequency response, but also affects the overall impedance. More specifically, for frequencies between 200 kHz and 1 MHz, the impedance ranges from 50 Ω to 2 kΩ , for RH levels between 80% and 0%, respectively.

In Fig. 4, the frequency response curves of sensor #2, for RH values between 0% and 80%, are presented. Comparatively, the sensor #2 presents an impedance that is 4 orders of magnitude higher than sensor #1. The RH contribution is notorious, *i.e.* the impedance range from 30 kΩ to 300 MΩ , for low frequencies. Moreover, a linear decrease in RH level creates an exponential increase in impedance. The negative phase angles reveal a low frequency pole, however as the RH level increases, the effect of a zero can be observed. In addition, increasing the RH level shifts the dominant poles of the frequency responses to higher frequencies.

The impact of the RH in the sensor impedance can be directly measured at the frequency at which the sensor can be approximated by a resistor, which corresponds to a phase value of 0º. In Fig. 5, the approximate resistance of sensors #1 and #2 as a function of RH is presented. For example, for sensor #2, at a frequency of 10 kHz, the approximate resistance, R, remains constant and equal to 400 kΩ , for RH levels bellow 50%, and decreases exponentially as the RH level increases, as described by,

$$R \approx 10^8 * e^{-0.112*RH}. \tag{1}$$

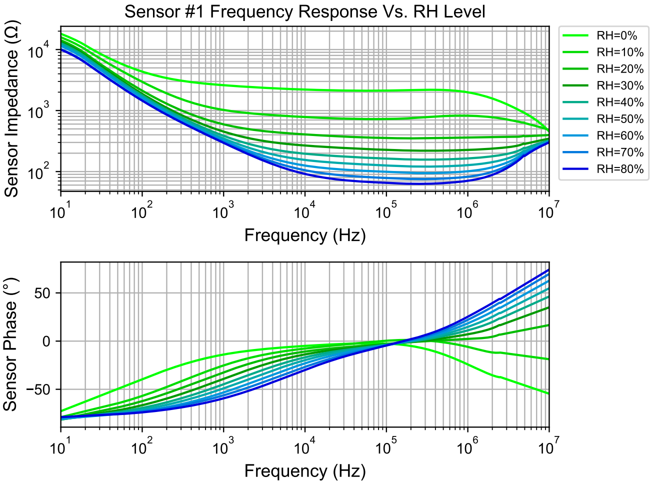

Fig. 3. Frequency response of sensor #1 for levels of RH between 0% and 80%.

B. Electrical Model

Considering the analysis of the frequency responses depicted in III-A, a possible electrical equivalent model for the sensors, that approximately describes a similar frequency behavior, is represented by the circuit represented in Fig. 6a. The circuit transfer function is given by,

$$Z(s) = \frac{s(R_{\text{sensor}}C_{\text{dl}}) + 1}{s^2(R_{\text{sensor}}C_{\text{p}}C_{\text{dl}}) + s(C_{\text{p}} + C_{\text{dl}})}, \tag{2}$$

where $\mathrm{C_{dl}}$ represents the double-layer capacitance, $\mathrm{R_{sensor}}$ the effective resistance of the sensing material, and $\mathrm{C_p}$ represents the inter-electrode capacitance.

The frequency of the zero is easily determined by

$$w_{\text{z}} = \frac{1}{R_{\text{sensor}}C_{\text{dl}}}[rad/s]. \tag{3}$$

A zero frequency pole exists and a higher frequency pole is obtained at

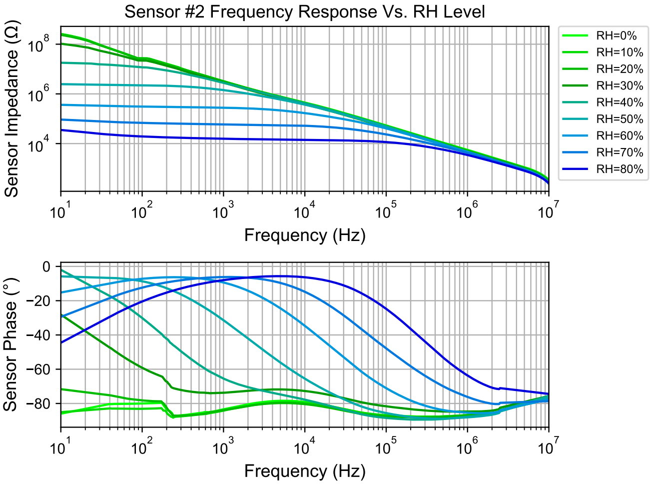

Fig. 4. Frequency response of sensor #2 for levels of RH between 0% and 80%.

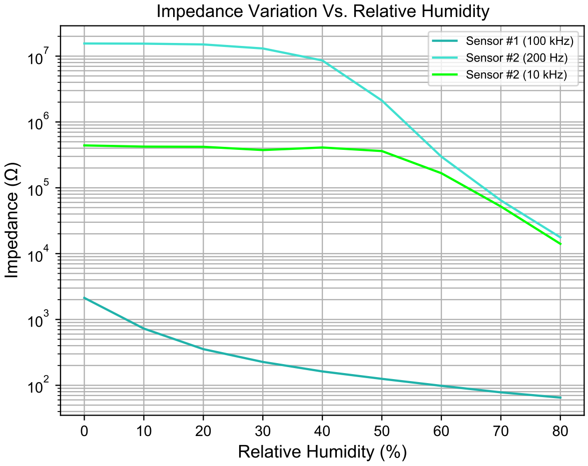

Fig. 5. Approximated resistance of sensor #1 and #2 as a function of RH.

$$w_{\text{p}} = \frac{C_{\text{p}} + C_{\text{dl}}}{R_{\text{sensor}}C_{\text{dl}}C_{\text{p}}}[rad/s]. \tag{4}$$

In essence, the equivalent electrical circuit of the sensor is composed of a parallel arrangement of two impedances, one of which is a pure capacitance, and the other a series combination of a resistance and two capacitors. From the model, it can be seen that for low frequencies, and assuming that $\mathrm{C_p}$ is much smaller than $\mathrm{C_{dl}}$, the impedance of the sensor can be approximated by the resistance of the MUT, $\mathrm{R_{sensor}}$. For higher frequencies, the sensing material's capacitance, $\mathrm{C_p}$, shunts the signal between the electrodes, decreasing the sensor impedance. In addition, the transfer function presents a pole at the origin, which goes accordingly to the information provided by the phase plot of Fig. 3 and Fig. 4.

Moreover, it is possible to determine that the frequency of the zero is smaller than the non-zero frequency pole. To

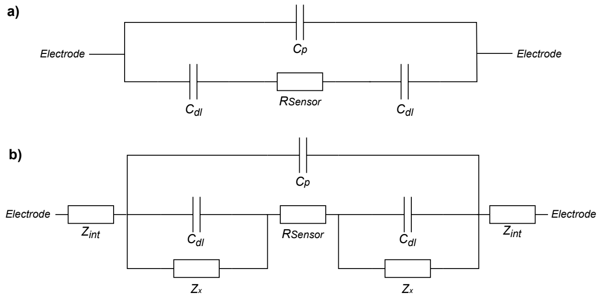

Fig. 6. a) Ideal IDE sensor electrical circuit model. b) Non-ideal IDE sensor electrical circuit model.

support this observation, equation 4 can be approximated by

$$w_{\text{p}} \approx \frac{1}{R_{\text{sensor}}}\frac{1}{C_{\text{eq}}}[rad/s], \tag{5}$$

where C_{eq} represents the equivalent series of capacitors C_{p} and C_{dl}.

Considering that C_{p} is much smaller than C_{dl}, the value of C_{eq} can be approximated by C_{p}. The ratio between the frequency of the zero and the non-zero frequency pole is approximately given by

$$\frac{w_{\text{z}}}{w_{\text{p}}} \approx \frac{C_{\text{p}}}{C_{\text{dl}}}, \tag{6}$$

which, according to the value assumption of C_{p} and C_{dl}, is smaller than unity, validating the observation.

A more realistic equivalent electrical circuit is represented in Fig. 6b, which accounts for the connection between the sensor and the measurement device, as well as the losses and imperfections of the double layer capacitance, Z_{x}, which appear in parallel with C_{dl}. The transfer function of this circuit is given by,

$$Z(s) = \frac{Z1}{1 + sC_{\text{p}}Z1} + 2Z_{\text{int}}, \tag{7}$$

where Z_{int} represents the impedance of the interface between the measurement device and the sensor, and

$$Z1(s) = \frac{2Z_{\text{x}}}{sZ_{\text{x}}C_{\text{dl}} + 1} + R_{\text{sensor}}. \tag{8}$$

The influence of the RH on the frequencies of poles and zeros can be calculated using (3) and (4), where the value of R_{sensor} is a function of RH, as described by (1), for the particular case of sensor #2.

To assess the quality of the model, Fig. 7 presents a comparison between the expected impedance from the model and the measured impedance. Considering a range of frequencies between 10 kHz and 200 kHz, both models fit the frequency response curves of distinct sensors, with a maximum relative error of 10%. However, the simplified model presents a higher error outside this frequency band.

The fitting presented proves the equivalent electrical model potential and value, as an important tool that can be used to compensate the RH impact on the ionogel sensors. In addition, the model enables a better understanding of the AFE circuit specifications required for accurate signal acquisition.

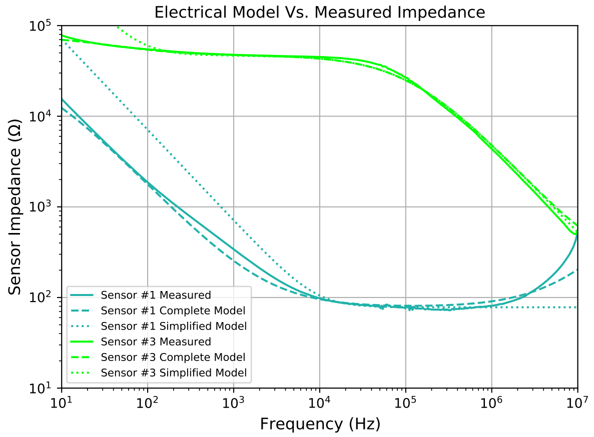

Fig. 7. Modeled impedance and measured impedance comparison.

IV. PROPOSED RECONFIGURABLE ANALOG FRONT-END FOR MULTI-SENSOR ARRAY BASED ELECTRONIC NOSE

A. Analog Front-End Building Blocks Description

Due to need of a reconfigurable, yet accurate, system, the proposed AFE circuit is fully implemented in a programmable-system-on-a-chip (PSoC) device (Cypress PSoC 5LP CY8C56LP) [17]. A simplified block diagram of the AFE circuit is presented in Fig. 8a.

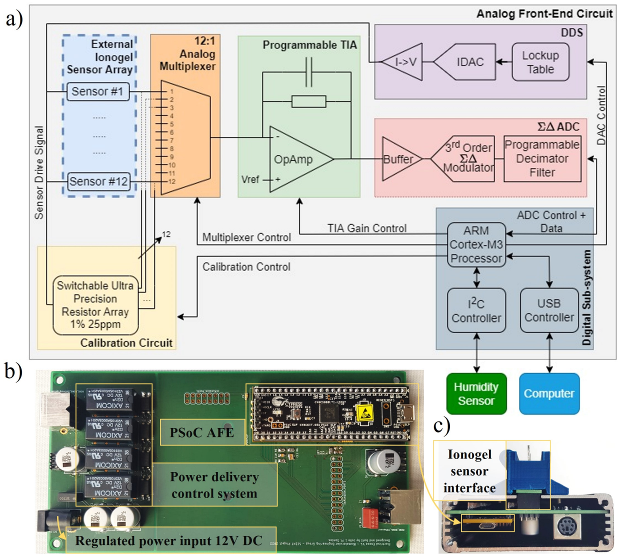

Fig. 8. a) Simplified block diagram of PSoC 5LP integrated AFE circuit. b) Printed circuit board of AFE circuit. c) Assembly of printed circuit board inside an enclosure.

This circuit topology offers a good balance between flexibility and accuracy, since it uses the internal building blocks available on the PSoC, such as a digital-to-analog converter

(DAC), an analog-to-digital converter (ADC), an analog multiplexer, and a programmable-gain trans-impedance amplifier (TIA), which can be easily reconfigured and dynamically adapted to each sensor. In addition, the PSoC's Cortex-M3 ARM processor was programmed to establish a bi-directional serial communication channel with a computer, in which a custom Python software presents data in real-time.

As previously described in II, an AC signal is required to drive the sensors. For that purpose, a direct digital synthesizer (DDS) was implemented. The PSoC offers a 8-bit current DAC, which can be coupled to a current to voltage converter and output a voltage signal. A sine-wave with an amplitude of 100 mV was generated. The frequency and waveform of the signal can easily be controlled by manipulating the lockup table attached to the DAC.

The AFE circuit was designed to work with an array of 12 individual ionogel sensors. For that, 12 general purpose input/output (GPIO) pins were multiplexed, to which the 12 ionogel sensors connect to. Furthermore, the switching is done in a circular way, where each sensor is selected for a given period of time, and is controlled by the firmware implemented in the ARM processor. However, one limitation of this topology is the high on-resistance of the multiplexer, which has been taken into account in the firmware design, namely involving a calibration step, as will be presented later on.

The PSoC offers two types of ADC: a Successive-Approximation Register (SAR) ADC; and a Delta-Sigma ADC. The SAR ADC is capable of a maximum sampling frequency of 1 MHz, at a resolution of 12-bit. The Delta-Sigma ADC is based on a 3rd order modulator and a programmable decimator filter, which enables resolutions from 8-bit to 20-bit. Considering that the frequencies necessary to the normal VOC-analysis operation are under 10 kHz, the Delta-Sigma ADC was chosen, due to its higher resolution. However, when the system requires a higher operational frequency, the AFE can easily be reconfigured to use the SAR ADC.

In addition, a programmable gain TIA, which is derived from a switched capacitor circuit, internal to the PSoC, was used to dynamically adjust the signal amplitude at the input of the ADC. The trans-impedance gain is controlled by the firmware, as will be presented later on. Some additional circuitry was implemented, mainly an inter-integrated circuit (I^2C) controller, that establish communication with an external temperature and humidity sensor, and a USB interface driver, which was used for communication with a computer.

B. Firmware

The firmware that controls the AFE circuit runs in the ARM Cortex-M3 processor of the PSoC, which was programmed in C language, using the PSoC Creator 4.4, which is the manufacturer recommended integrated development environment. The normal AFE operation follows an algorithm, whose flowchart is represented in Fig. 9.

Firstly, the hardware component parameters are initialized, such as the ADC resolution and DAC lockup table. Then, a loop ensures that signals from the 12 individual channels are acquired and stored in a buffer. The impedance calculation is based on the last calibration coefficients and the voltage readings stored in the buffer. The impedance measurements from each channel, as well as data from the external I^2C sensor, are transmitted to a computer, via USB, in which a custom Python software stores and presents the data.

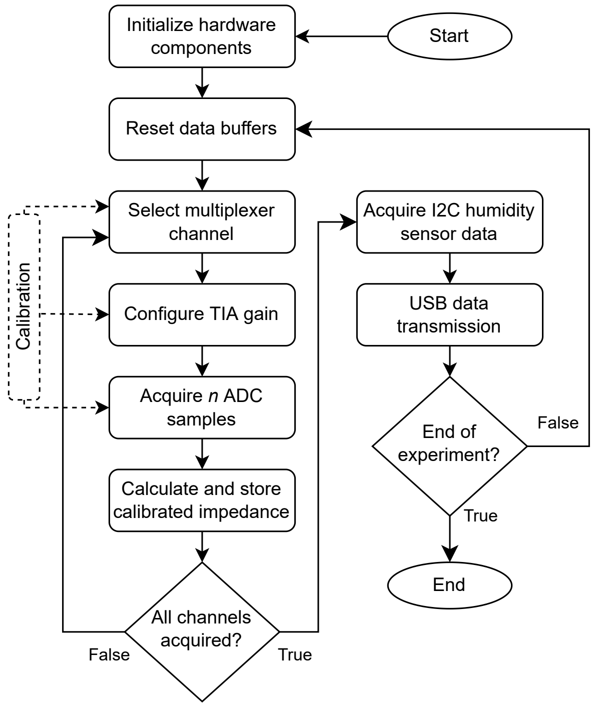

Fig. 9. Flowchart of the main algorithm that controls the AFE circuit.

To maximize the dynamic range of the AFE circuit, the gain of the TIA is dynamically adjusted, according to the voltage at its output. More specifically, 3 different trans-impedance gains are necessary to maintain the amplified signal voltage within a range that ensures an adequate SNR. The values of these gains and the respective measuring impedance range are presented in Table 1.

TABLE I
TRANS-IMPEDANCE AMPLIFIER GAIN SELECTION

TIA Gain	Minimum Impedance	Maximum Impedance
30 kΩ	200 Ω	4 kΩ
250 kΩ	4 kΩ	50 kΩ
500 kΩ	50 kΩ	200 kΩ

C. Calibration

The accuracy of the AFE circuit is affected by error, which originates from multiple sources. The greatest source of non-linearity is due to the on-resistance of the multiplexer, which is signal dependant. In addition, the mismatch between multiplexer channels is considerable, due to unequal routing paths in the PSoC internal switching matrix. Apart from this, the gain tolerance of the TIA can be as high as 35%, which is another source of error. Thus, a multi-channel calibration procedure is required.

The calibration of the AFE circuit is done using a similar algorithm to that presented in Fig. 9. However, a Python software running on a computer, controls the individual steps, using USB commands, such as the multiplexer channel selection, TIA gain configuration and ADC signal acquisition. A switchable matrix of 16 1% 25 ppm SMD resistors, ranging from 200 Ω to 150 kΩ , was implemented. Low resistance switches were used to connect the various resistors to each multiplexer input. Unlike the normal operation of the AFE, in calibration mode, the transmitted data corresponds to the peak-to-peak voltage at the output of the TIA.

The most appropriate fitting function that relates the impedance and voltage measured is described by

$$Z_{\text{measured}} = A \times V_{\text{measured}}{}^{B}, \tag{9}$$

where Z_{measured} and V_{measured} correspond to the measured impedance and voltage, respectively, and A and B are functions of the TIA gain and multiplexer channel.

Considering the fitting function, the Python software calculates the values of A and B for each channel and TIA gain, resulting in a two-dimensional array of calibration coefficients, which are sent to the PSoC, via USB, and used in the AFE normal operation. After the calibration process, an accuracy test of the circuit was conducted, and the results are shown in Fig. 10. The accuracy measurements show that the AFE circuit is capable of measuring impedances with an accuracy greater than 90%, in a range between 300 Ω and 150 kΩ , which satisfies the requirements for the multi-sensor array. However, due to fitting imperfections, the accuracy of the AFE circuit slightly decreases for impedances between 1.5 kΩ and 3 kΩ .

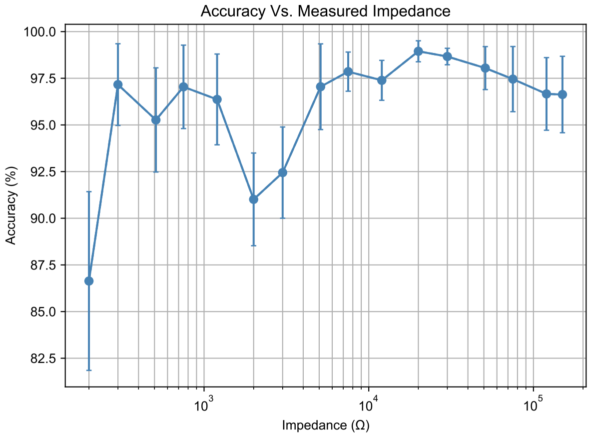

Fig. 10. Accuracy of the AFE circuit as a function of the impedance under measurement.

V. CONCLUSIONS

In this paper, an equivalent electrical model of a chemical E-Nose sensor was obtained and studied. A highly reconfigurable and flexible AFE circuit was designed, implemented and tested, which is capable of measuring impedances with an accuracy greater than 90%. Due to the unique properties and construction of the ionogel sensors, the electrical model and reconfigurable AFE circuit enable the implementation of innovative signal acquisition and processing techniques, such as spectral analysis and humidity compensation. Therefore, both the electrical model characterization and AFE circuit are useful and valuable tools that can easily be implemented in E-Nose devices, improving their performance.

REFERENCES

[1] A. Kannadan, “History of the Miasma Theory of Disease,” tech. rep., College of DuPage, 2018.

[2] D. B. Walker, J. C. Walker, P. J. Cavnar, J. L. Taylor, D. H. Pickel, S. B. Hall, and J. C. Suarez, “Naturalistic quantification of canine olfactory sensitivity,” *Applied Animal Behaviour Science*, vol. 97, pp. 241–254, may 2006.

[3] K. Persaud and G. Dodd, “Analysis of discrimination mechanisms in the mammalian olfactory system using a model nose,” *Nature*, vol. 299, no. 5881, pp. 352–355, 1982.

[4] A. Sharma, R. Kumar, I. Aier, R. Semwal, P. Tyagi, and P. Varadwaj, “Sense of Smell: Structural, Functional, Mechanistic Advancements and Challenges in Human Olfactory Research,” *Current Neuropharmacology*, vol. 17, no. 9, pp. 891–911, 2018.

[5] Y. Ren, H. S. Ramaswamy, Y. Li, C. Yuan, and X. Ren, “Classification of impact injury of apples using electronic nose coupled with multivariate statistical analyses,” *Journal of Food Process Engineering*, vol. 41, p. e12698, aug 2018.

[6] L. F. Valdez and J. M. Gutiérrez, “Chocolate Classification by an Electronic Nose with Pressure Controlled Generated Stimulation,” *Sensors 2016, Vol. 16, Page 1745*, vol. 16, p. 1745, oct 2016.

[7] N. Fens, A. H. Zwinderman, M. P. Van Der Schee, S. B. De Nijs, E. Dijkers, A. C. Roldaan, D. Cheung, E. H. Bel, and P. J. Sterk, “Exhaled Breath Profiling Enables Discrimination of Chronic Obstructive Pulmonary Disease and Asthma,” *Clin. Exp. Allergy*, vol. 180, pp. 1076–1082, dec 2012.

[8] R. van de Goor, M. van Hooren, A. M. Dingemans, B. Kremer, and K. Kross, “Training and Validating a Portable Electronic Nose for Lung Cancer Screening,” *Journal of Thoracic Oncology*, vol. 13, pp. 676–681, may 2018.

[9] M. Bruins, Z. Rahim, A. Bos, W. W. Van De Sande, H. P. Endtz, and A. Van Belkum, “Diagnosis of active tuberculosis by e-nose analysis of exhaled air,” *Tuberculosis*, vol. 93, pp. 232–238, mar 2013.

[10] A. Hussain, A. T. Semeano, S. I. Palma, A. S. Pina, J. Almeida, B. F. Medrado, A. C. Pádua, A. L. Carvalho, M. Dionísio, R. W. Li, H. Gamboa, R. V. Ulijn, J. Gruber, and A. C. Roque, “Tunable Gas Sensing Gels by Cooperative Assembly,” *Advanced Functional Materials*, vol. 27, p. 1700803, jul 2017.

[11] N. Zoric, A. Iavorschi, M. Sireteanu, G. Viziteu, and R. Ciobanu, “Design and Simulations of Idc Sensor Using Comsol Multyphysics and Dielectric Spectroscopy of LTCC Materials,” *Buletinul Agir*, no. 4, pp. 63–69, 2013.

[12] R. R. Khan and S. W. Kang, “Highly sensitive multi-channel IDC sensor array for low concentration taste detection,” *Sensors (Switzerland)*, vol. 15, pp. 13201–13221, jun 2015.

[13] C. Esteves, S. I. Palma, H. M. Costa, C. Alves, G. M. Santos, E. Ramou, A. L. Carvalho, V. Alves, and A. C. Roque, “Tackling Humidity with Designer Ionic Liquid-Based Gas Sensing Soft Materials,” *Advanced Materials*, 2022.

[14] Digilent, “USB Oscilloscope and Logic Analyzer - Digilent Analog Discovery 2.” https://digilent.com/shop/, 2021. Accessed: 2022-02-18.

[15] A. Scientific, “Technical Data for Alicat MC-Series Mass Flow Controllers.” https://www.alicat.com, 2019. Accessed: 2022-02-18.

[16] T. Connectivity, “Digital Relative Humidity sensor with Temperature output.” https://www.te.com/usa-en/home.html, 2007. Accessed: 2022-04-04.

[17] I. Technologies, “PSoC ® 5LP: CY8C58LP Family Datasheet Programmable System-on-Chip (PSoC ®) General Description.” https://www.infineon.com/cms/en/, 2014. Accessed: 2022-02-10.

2022

Design, Implementation and Test of an Ionogel Sensor-based Electronic Nose

João Santos

NOVA SCHOOL OF
SCIENCE & TECHNOLOGY